Fluorescence Quantum Yields and Anisotropies of Short-Lived Chromophores

Inaugural Dissertation

for the attainment of the title of doctor
in the Faculty of Mathematics and Natural Sciences
at the Heinrich Heine University Düsseldorf

presented by

Mahbobeh Morshedi
from Tehran, Iran

Düsseldorf, July 2024

from the institute of physical chemistry II
at the Heinrich Heine University Düsseldorf

Published by permission of the
Faculty of Mathematics and Natural Sciences at
Heinrich Heine University Düsseldorf

Supervisor: Prof. Dr. Peter Gilch
Co-supervisor: Prof. Dr. Michael Schmitt

Date of the oral examination: 19.09.2024

Declaration

I hereby declare under oath that I have independently authored this thesis, without undue assistance from third parties, adhering to the "Principles for the Safeguarding of Good Scientific Practice at Heinrich Heine University Düsseldorf". This dissertation has not been submitted to any other faculty or institution. Furthermore, I have not previously attempted to obtain a doctorate.

---------- ----------

Place, Date Mahbobeh Morshedi

To the strong women of Iran

"Woman, Life, Freedom"

Contents

Acknowledgements

First and foremost, I would like to express my gratitude to Prof. Dr. Peter Gilch for welcoming me into his research group and providing the opportunity to conduct my doctoral studies in this exciting field of Physical Chemistry. I am grateful for the trust he placed in me, which has been instrumental in my growth and development throughout this journey. I would also like to thank him for his support in attending many enriching conferences.

I extend my thanks to Prof. Dr. Michael Schmitt for being my second reviewer and for his fruitful collaboration on the 2-cyanoindole project.

I am grateful to Dr. Janina Bertling for making my first day in Germany unforgettable and to Dr. Kristoffer A. Thom for his assistance at the start of my work.

Special appreciation goes to Dr. Barbara Elza Nogueira de Faria for her support, valuable advice, and continuous encouragement throughout our friendship.

My sincere thanks go to Michilly/Michelly Popely (Michelle Rademacher), who was not only my “dear colleague” but also my “dear conference buddy” and “dear friend”. Thank you, Michilly, for your invaluable insights and the countless joyful moments we shared throughout this journey. Your presence has been a highlight of my experience, and I deeply value all the support and laughter we’ve shared.

Additional thanks go to Franziska Bergstein, Francisco van Riel Neto, Theresa Ott, Matthias Jantz, and, of course, Mila, for the joyful moments we shared. I am also grateful to Anna Reiffers for her guidance on the Kerr gate setup and her ongoing support.

Further, I appreciate my research colleagues and everyone who assisted me with my projects: Dr. Oliver Nolden for conducting experiments at the fsTA device, and for many insightful discussions and advice. I am very grateful for his supportive presence and the joyful moments we spent together. Philipp Janke for his diligent efforts and active support with numerous measurements during his bachelor thesis; Wiebke Haselbach for the experiments at the nsTA device; Simon Zimmermann for his contributions to our shared project and assistance at the Kerr gate device. Finally, I would like to express special thanks to David Kleverkamp, who was always ready with an answer to every question. I appreciate his contributions to our shared project, the helpful discussions we had, and endless fun times we shared.

Last but not least, I extend my deepest gratitude to my mother for her unwavering support and for instilling in me the virtues of patience and persistence in achieving my long-term goals. At the end, my greatest thanks go to my husband, Amirarsalan Asharion. Without his boundless encouragement, this journey would have been much more challenging. Words cannot fully express my appreciation for his enduring inspiration and incredible support throughout this process.

Publications, Presentations, Posters

Publications in Peer-Reviewed Journals

- Nolden, O., Kremper, J., Haselbach, W., Morshedi, M., Guhl, J., Schmeinck, P., Marian, C. M., Ganter, C., Gilch, P., (2022): Femtosecond Spectroscopy and Quantum Chemistry of a Linearly Coordinated Copper(I) Carbene Complex. In: *ChemPhotoChem*, 7, e202200231. DOI: 10.1002/cptc.202200231

- Morshedi, M., Nolden, O., Janke, P., Haselbach, W., Schmitt, M., Gilch, P., (2023): The Photophysics of 2-Cyanoindole Probed by Femtosecond Spectroscopy. In: *Photochem Photobiol Sci*, 22, 745-759. DOI: 10.1007/s43630-022-00348-3

- Morshedi, M., Zimmermann, S., Klaverkamp, D., Gilch, P., (2024): References for Small Fluorescence Quantum Yields. In: *J Fluoresc*, XX, XXXX-XXXX. DOI: 10.1007/s10895-024-03729-2

Conference participation

- **Poster presentation:** Morshedi, M., Nolden, O., Janke, P., Haselbach, W., Schmitt, M., Gilch, P., The Photophysics of 2-Cyanoindole probed by Femtosecond Spectroscopy, 10th Central European Conference on Photochemistry, Bad Hofgastein, Austria; 02/2022

- **Poster presentation:** Morshedi, M., Nolden, O., Janke, P., Haselbach, W., Schmitt, M., Gilch, P., The Photophysics of 2-Cyanoindole probed by Femtosecond Spectroscopy, 28th PhotoIUPAC: International Symposium on Photochemistry, Amsterdam, Netherlands;07/2022

- **Poster presentation:** Morshedi, M., Nolden, O., Janke, P., Haselbach, W., Schmitt, M., Gilch, P., Solvent Dependent Intersystem Crossing of 2-Cyanoindole, 28 Lecture Conference on Photochemistry, Düsseldorf, Germany; 09/2022

- **Short talk:** Morshedi, M., Nolden, O., Janke, P., Haselbach, W., Schmitt, M., Gilch, P., The Femtosecond PhotoPhysics of 2-Cyanoindole — a Promising Probe of Protein Hydration, 31st ICP: International Conference on Photochemistry, Sapporo, Japan; 07/2023

Abstract

In fluorescence spectroscopy, the fluorescence quantum yield Φ_{fl} serves as an important metric that quantifies the efficiency with which a fluorophore converts absorbed photons into emitted light. The relative method, commonly employed for determining fluorescence quantum yield, involves comparing the yield Φ_{fl} of a compound to that of a reference material with a known yield. In the first study of this thesis, three new reference compounds with emission spectra covering the UV/Vis range have been identified for determining low fluorescence quantum yields, with yields ranging from 10^{-5} to 10^{-4}. These include thymidine in water for the blue, dibenzoylmethane in ethanol for the green, and malachite green chloride in water for the red region of the spectrum. These substances are chosen for their ease of handling, photostability, commercial availability, and the mirror-image symmetry observed between their absorption and fluorescence spectra. This symmetry suggests that the same electronic states are involved in both the absorption and emission processes, justifying the use of the Strickler-Berg relationship. Additionally, the fluorescence excitation spectra of these compounds closely match their absorption spectra, ensuring that the emissions measured are indeed from the compounds being studied. The fluorescence quantum yields Φ_{fl} of the compounds were first determined using the relative method and then compared with the one according to the Strickler-Berg analysis in conjunction with time resolved fluorescence spectroscopy. The fluorescence quantum yield values obtained from both methods show agreement within their respective error margins.

The second study of this thesis investigates the photophysical properties of a specific copper(I) carbene complex, [1,3-bis(2,6-diisopropylphenyl)imidazol-2-ylidene]-(2-picoline)copper(I) tetrafluoroborate (abbreviated as NHCCuPy), by femtosecond spectroscopy and quantum chemistry across various solvents. Copper(I) complexes, with intriguing luminescent properties, are increasingly emerging as viable alternatives to heavy metal-based complexes like iridium and platinum, which are commonly used in organic light-emitting diodes (OLEDs). NHCCuPy exhibits significant sensitivity to environmental conditions, as evidenced by its performance in different media. While embedded in a poly(methyl methacrylate) (PMMA) matrix or processed as a powder, the complex shows a high fluorescence quantum yield. Conversely, this yield dramatically decreases when the complex is in the form of single crystals or in solution. Employing the fluorescence Kerr gate setup with high sensitivity allowed for a detailed comparative analysis of the small emissions from NHCCuPy and 2-picoline (the ligand).

The third study of this thesis is concerned with femtosecond fluorescence and transient absorption experiments on the photophysics of 2-cyanoindole in solution. The chromophore of the naturally occurring fluorescent amino acid tryptophane is indole. Therefore, unnatural amino acid derivatives with functionalized indoles are of great interest as fluorescent probes in protein studies. For instance, the fluorescence quantum yield of 2-cyanoindole is strongly sensitive to the solvent. Its fluorescence quantum yield in water is as small as $4.4 \cdot 10^{-4}$ and increases to a value of 0.057 in tetrahydrofuran. 2-Cyanoindole can, thus, represent a promising fluorescence probe in hydration studies of proteins. In water, its fluorescence decays within 8 ps, irrespective of the excitation wavelength. For short wavelength excitation (266 nm) the initial fluorescence anisotropy is close to zero. For excitation with 300 nm, it amounts to ~ 0.2. This is in accordance with the energetic proximity of two singlet states (L_a and L_b). The transition from the L_a to L_b state occurs in less than 100 fs. For all solvents studied in this work,

a bi-exponential decay was observed. In water, femtosecond transient absorption reveals that the fluorescence decay is solely due to internal conversion to the ground state. In aprotic solvents such as acetonitrile and tetrahydrofuran, the fluorescence decay is prolonged, with time constants of ~900 ps and ~2.6 ns respectively, where intersystem crossing to the triplet state contributes to the decay.

List of Abbreviations

BBO	β-barium borate
ESA	excited state absorption
FRET	Förster resonance energy transfer
FC	Frank-Condon
fs	femtosecond (10^{-15} s)
fsTA	femtosecond transient absorption
GSB	ground state bleach
IC	internal conversion
ISC	intersystem crossing
ns	nanosecond (10^{-9} s)
nsTA	nanosecond transient absorption
NOPA	non-linear optical parametric amplifier
Nd:YAG	neodymium-doped yttrium aluminum garnet; Nd:$Y_3Al_5O_{12}$
NHCCuPy	[1,3-bis(2,6-diisopropylphenyl)imidazol-2-ylidene]-(2-picoline)copper(I) tetrafluoroborate
OLED	organic light emitting diode
OPA	optical parametric amplifier
ps	picosecond (10^{-12} s)
PMMA	poly(methyl methacrylate)
SE	stimulated emission
TDM	transition dipole moment
VR	vibrationen relaxation
yield Φ_{fl}	fluorescence quantum yield

1. Motivation

Fluorescence, defined as the emission of light by a material after absorbing light, has a rich history that spans several centuries. It began in the early 16th century when the phenomenon was first observed in the blue glow of wood extracts [1]. Over the years, the understanding of fluorescence evolved significantly. An early highlight was George Stokes's seminal work in 1854 [2]. He observed how substances could absorb light at one wavelength and emit at a longer one, naming the phenomenon "fluorescence" inspired by the mineral fluorite. By the 20th century, fluorescence spectroscopy emerged as a key technique, enabling quantitative analysis of fluorescence phenomena [3]. Subsequently, the introduction of the fluorescence microscope further improved biological investigations such as the study of cellular structures [4, 5]. The field continued to evolve with the development of time resolved fluorescence spectroscopy in the latter half of the century. By the 1980s, advancements in instruments have enabled time resolved fluorescence measurements with femtosecond (fs) resolution, allowing for tracing of ultrafast processes [6, 7].

Its applications now span from fundamental sciences like photophysics, photochemistry, and photobiology to practical uses in everyday items such as text markers [8, 9] and electronic devices [10, 11]. Fluorescence spectroscopy and time resolved fluorescence spectroscopy have emerged as powerful tools to exclusively monitor the behaviors of the (singlet) excited states without interference of contributions from the ground and triplet states or photoproducts (see Chapter 1). As the spectroscopic signatures of a fluorophore can be sensitive to its environment, fluorescence signals can report on static and dynamic properties of this environment [12, 13]. Its sensitivity has also enabled detection at the single molecule level [14-17]. It is particularly useful for exploring the structure and dynamics of biological macromolecules like nucleic acids and proteins [18, 19]. In these studies, naturally occurring amino acid residues, such as tryptophan, can be employed as the reporters of local environments within proteins [13, 20]. Substituting intrinsic tryptophan residues with analogs that exhibit distinct spectroscopic properties can expand the applications of tryptophan as a fluorescence probe [21].

In fluorescence spectroscopy, the fluorescence quantum yield (Φ_{fl}) is an important parameter that measures the efficiency of light emission by fluorophores after photon absorption. For individual emitters, it offers insights into radiative transitions, along with fluorescence lifetime, spectrum, and fluorescence anisotropy [22]. Typically, the yield Φ_{fl} is determined by comparing it to reference materials with known quantum yields. However, these references often have high yield Φ_{fl} values, posing a challenge in measuring compounds with lower yield Φ_{fl}. This includes some of the key biological substances such as DNA and RNA bases, which have very small yields Φ_{fl} ($\sim 10^{-4}$) [23]. The first study of this thesis addresses this issue by identifying new reference materials that improve the reliability of Φ_{fl} measurements for compounds with low yields Φ_{fl}.

The second study of this thesis examines the photophysics of a specific copper(I) carbene complex in solution for the first time. This complex shows significant sensitivity to its environment, as evidenced by its performance across different media. When embedded in a poly(methyl methacrylate) (PMMA) matrix or processed as a powder, the complex exhibits a high fluorescence quantum yield of 0.87 [24]. However, in single crystals and solutions, this yield decreases dramatically. Among the various spectroscopic techniques employed in this work, a method termed "fluorescence Kerr gating" was utilized for fluorescence spectroscopy,

with a detailed description provided in Chapter 1. This setup was chosen for its high sensitivity in detecting small fluorescence signals.

The third study of this thesis explores the photophysics of 2-cyanoindole by femtosecond spectroscopy. Indole is the chromophore of the natural fluorescent amino acid tryptophane [12]. It was shown that the fluorescence lifetime and quantum yield of 2-cyanoindole is strongly dependent on the solvent [25], and thereby can serve as a promising probe for protein hydration studies. The fluorescence lifetime of this compound in water was not determined in this study due to the limited time resolution. Therefore, the third study of this thesis aims at the fluorescence lifetime of 2-cyanoindole in this solvent (water). Additionally, indole and its derivatives, including 2-cyanoindole, exhibit two close lying excited states, L_a and L_b [26]. This study further employed time resolved fluorescence anisotropy experiments to identify the emissive state (L_a or L_b) of 2-cyanoindole.

In these three studies, fluorescence spectroscopy serves as the common technique, highlighting its versatility and importance across various contexts. Both steady state and time resolved fluorescence spectroscopy provide exclusive information on the singlet excited states and offer insights into different photophysical aspects.

This thesis is a cumulative one and is structured into the following chapters. Chapter 1 provides a focused summary of photophysics, followed by the techniques of time resolved spectroscopy employed in this thesis. In Chapter 2, a background on fluorescence quantum yield is provided, followed by an overview on the contributions of the Kerr gate setup to the copper(I) carbene complex study. Chapter 3 provides a background on fluorescence anisotropy. References are compiled in chapter 4. The three publications resulting from this thesis, which have been published in peer-reviewed journals, are reproduced in Chapter 5.

1.1. Fundamentals of Photophysics and Time Resolved Spectroscopy

Photophysics explores the physical processes of molecules and atoms when they interact with light, encompassing the absorption and emission of light, as well as the population and depopulation of excited states. Photophysical processes are often depicted and explained with the aid of a Jablonski diagram (see Figure 1.1). This diagram was first introduced by Aleksander Jablonski in 1933 [27, 28].

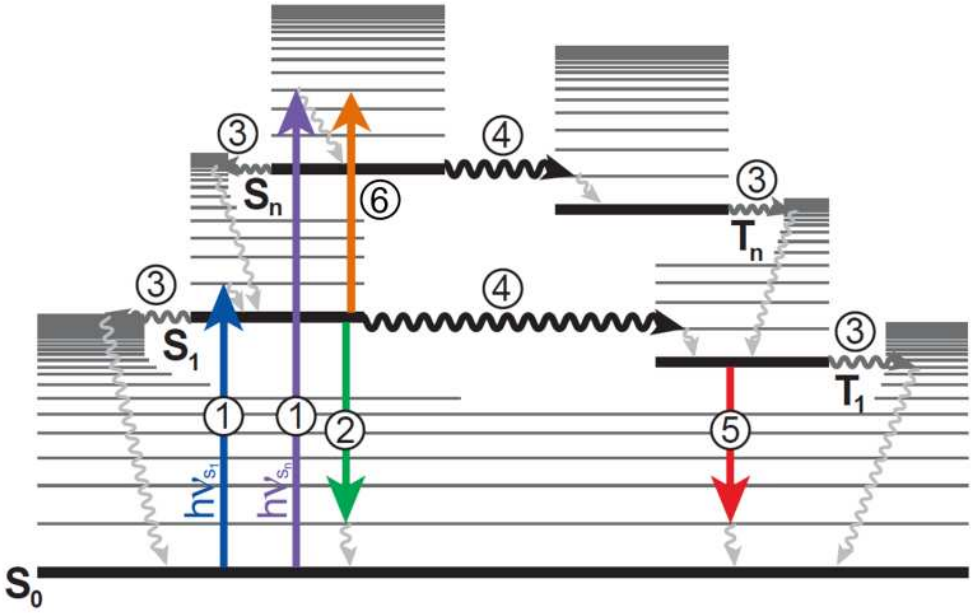

Figure 1.1. The Jablonski diagram provides a detailed visualization of key photophysical processes. It features thick horizontal lines to denote the vibrational ground states of electronic states (S_0, S_1, ..., S_n and T_1, ..., T_n), and thin, grayish horizontal lines to represent excited vibrational levels. It is commonly assumed that the ground state is a singlet one (S_0), as is often the case for organic molecules. Vertical upward arrows illustrate absorption processes. Excitation from the electronic ground state to the lowest excited state is depicted in blue (marked by ①), while excitation to higher states is shown in purple (marked by ①). Transient absorption from an excited state to upper ones is shown in orange (marked by ⑥). Downward vertical arrows illustrate radiative transitions, symbolizing fluorescence in green (marked by ②) and phosphorescence in red (marked by ⑤). Non-radiative transitions between electronic states are depicted by wavy horizontal arrows, with internal conversion labeled as ③ and intersystem crossing as ④. Additionally, angled, light gray arrows illustrate vibrational relaxation within an electronic state. Adapted from ref. [29].

The diagram displays various electronic states, including the ground state (S_0) and excited ones (S_1, …, T_1, …). In thermal equilibrium, the molecule is in the electronic ground state, which for most organic molecules is a singlet state (S_0). The absorption of a photon triggers a transition from a lower energy state, commonly S_0, to a higher state of the same multiplicity such as S_1. Typically, such electronic excitations are also accompanied by vibrational excitations within the same electronic state, a phenomenon referred to as a vibronic transition. Additionally, not only the ground state but also the excited states of the molecule are capable of absorbing photons, leading to what is known as transient absorption (TA).

Within an electronic state, different vibrational levels exist. An electronic transition typically first populates higher vibrational states, from which the molecule may relax to a lower

vibrational energy level within the same electronic state through vibrational relaxation (VR). From that level the molecule may return to the ground state through radiative decay processes. If this transition occurs from a singlet state, it is termed fluorescence [12]. Non-radiative transitions between electronic states can occur while preserving multiplicity, known as internal conversion (IC), or change the multiplicity (e.g., $S_1 \rightarrow T_1$) through intersystem crossing (ISC). Emission from triplet states is referred to as phosphorescence (radiative decay). According to Kasha's rule [30], the emission usually occurs from the lowest excited state (S_1 or T_1), because the energy gaps between higher excited states are generally smaller compared to the substantial energy gap between the lowest excited state (S_1 or T_1) and the ground state (S_0) [31]. This larger energy gap often results in slower internal conversion from $S_1 \rightarrow S_0$ or $T_1 \rightarrow S_0$ than radiative processes. Also, transitions (internal conversion) from higher to lower excited states (e.g., $S_2 \rightarrow S_1$, $T_2 \rightarrow T_1$, or $T_2 \rightarrow S_1$) typically occur much faster than radiative processes [32]. Consequently, emission spectra often reflect the energy gap between $S_1 \rightarrow S_0$ or $T_1 \rightarrow S_0$, and are usually independent of the excitation wavelength. Although Kasha's rule applies to many organic compounds [33, 34], numerous exceptions can be found [35, 36].

process	time scale
absorption	~ 1 as
VR	100 fs – 1 ps
IC	1 ps – 1 µs
ISC	1 ps – 1 s
fluorescence	1 ns – 10 ns
phosphorescence	1 µs – 1 ms

Table 1.1. Typical time scale for some photophysical processes [35].

According to Table 1.1, absorption events occur on a very short time scale, a duration which is too short for significant nuclear displacement. When a molecule absorbs a photon, the electron density is redistributed almost instantaneously. In contrast, the atomic nuclei, which have masses much greater than that of the electrons, respond more slowly to this change and initially, their relative positions remain unchanged. This phenomenon underlines the Franck-Condon (FC) principle [37, 38], which in its "classical" version states that positions and momenta of nuclei do not change during the absorption process. Prior to the absorption, the nuclei are assumed to be located at the minima of the potential energy curves and to have zero momentum. This assumption is in conflict with Heisenberg's uncertainty principle. As during the photon absorption the position of the nuclei are assumed to be constant, the transition occurs vertically (see Figure 1.2 a). The respective arrow marking this transition ends at the upper potential energy curves. This point corresponds to the turning point of a classical vibration where the momentum is zero. According to the quantum mechanical FC principle, the probability of an electronic transition between states is determined by the overlap of their vibrational wavefunctions across multiple levels. Franck-Condon factors, derived from squared overlap integrals, allow for approximations of the shapes and locations of absorption and emission bands, as well as the signal intensities and positions of spectral lines through vibronic transitions. Whereas the classical FC principle can only predict the energetic position of the absorption maxima, the quantum mechanical one yields the vibronic envelope of a transition (see Figure 1.2 b).

The emission spectrum of a molecule often appears at longer wavelengths than the absorption spectrum, a phenomenon known as the Stokes shift, which is a measure of the amount of energy that is transferred to the solvent during VR (see Figure. 1.2 c). The absorption and emission spectra commonly exhibit a so-called mirror-image relationship. This occurs due to the similarity in vibrational energy levels involved during both absorption and emission [12]. Accordingly, taking into account the Stokes shift, the fluorescence spectrum appears as a mirror-image of the absorption spectrum, shifted to lower energies (see Figure. 1.2 c).

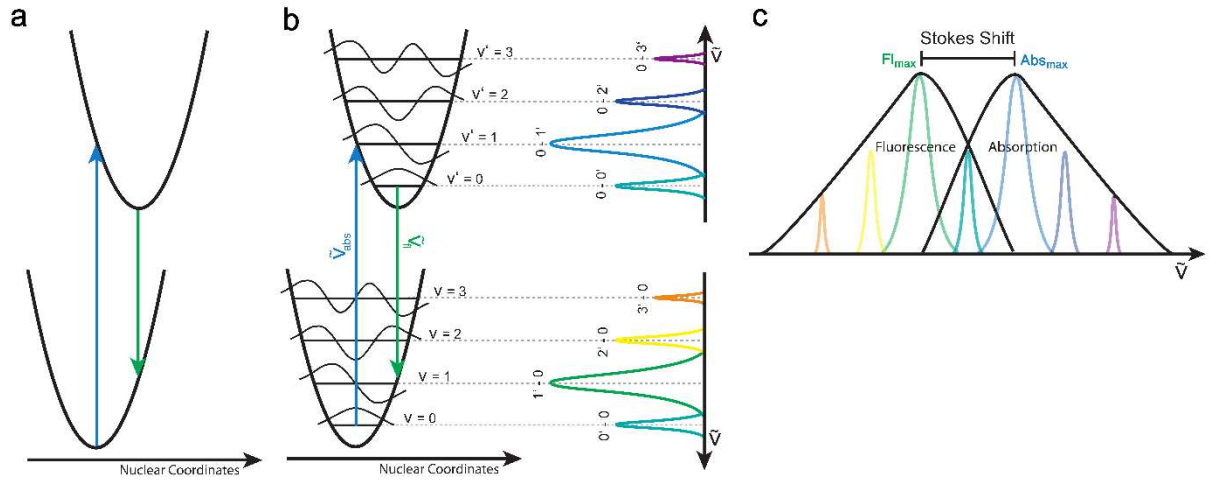

Figure. 1.2. Schematic diagram illustrating the Franck-Condon (FC) principle and Stokes shift. **a**: Classical version of FC principle. Vertical arrows represent absorption (upward) and emission (downward) transitions. The classical FC principle can only predict the energetic position of the absorption and emission maxima. **b**: Quantum mechanical FC principle. Horizontal lines denote vibrational levels within each electronic state. Vertical arrows represent absorption (upward) and emission (downward) transitions. The quantum mechanical FC principle predicts the vibronic envelope of a transition. **c**: Depiction of normalized absorption and fluorescence spectra. The spectral shift between the absorption and fluorescence peaks, known as the Stokes shift, is highlighted. A mirror-image relationship is often observed between the absorption and emission spectra, attributable to the similarity in vibrational energy levels involved during both processes. Different vibronic transitions responsible for the progressions are depicted. These progressions, illustrated by the envelopes in both spectra, may be observed or may be washed out due to the solvent contributions. Adapted from ref. [29].

Strickler-Berg relationship

The relationship between absorption and emission described by A. Einstein [28, 39] does not exactly apply to molecules in solution, as they typically exhibit broad absorption and emission bands. In such cases, the radiative rate constant, which quantifies the molecule's capability for spontaneous emission, can be correlated with the integrated absorption strength using formulas developed by Lewis and Kasha [40], Förster [41], Strickler and Berg [42], Birks and Dyson [43], and Ross [28, 44].

In this thesis, only the Strickler and Berg [42] relationship is relevant. Strickler and Berg formulated the following expression to determine the radiative rate constant k_{rad} (equations 1.1 and 1.2);

$$k_{rad} = \frac{8\pi \ln(10) c_0 n^2}{N_A} \langle \tilde{\nu}^{-3} \rangle^{-1} \int \frac{\epsilon(\tilde{\nu}) d\tilde{\nu}}{\tilde{\nu}}, \quad (1.1)$$

$$\langle \tilde{\nu}^{-3} \rangle^{-1} = \frac{\int S_{fl}(\tilde{\nu}) d\tilde{\nu}}{\int \tilde{\nu}^{-3} S_{fl}(\tilde{\nu}) d\tilde{\nu}}. \quad (1.2)$$

c_0 represents the speed of light, n is the refractive index of the solvent, and N_A is Avogadro's number. The term $\langle \tilde{\nu}^{-3} \rangle^{-1}$ is computed via equation (1.2) with the fluorescence spectrum $S_{fl}(\tilde{\nu})$ as an input. The term accounts for the cubic dependence of spontaneous emission on the wavenumber $\tilde{\nu}$. Calculating this involves integrating over the fluorescence spectrum $S_{fl}(\tilde{\nu})$ with respect to the wavenumber $\tilde{\nu}$. The term $\int \frac{\epsilon(\tilde{\nu}) d\tilde{\nu}}{\tilde{\nu}}$ represents the area integral of the absorption band. The Strickler-Berg relationship holds only when the spectral bands considered are a result of the same electronic transition (e.g., $S_0 \rightarrow S_1$ and $S_1 \rightarrow S_0$).

Solvent Effects

Based on the Franck-Condon principle, transitions into different vibrational levels within the same electronic transition—known as vibrational progressions—occur with different probabilities. Therefore, these transitions, which vary in signal strength, should be visible in both the absorption and emission spectra. In fact, this is particularly the case for spectra obtained in the gas phase [12]. However, in solution, the vibrational progressions might appear weak (be smeared out) and difficult to observe, depending on the specific characteristics of the solvent (see also Figure 1.2 c). In solutions, the visibility of vibrational progressions is determined by the strength of the interactions between the molecules of the solvent and the solute. In non-polar solvents, where only weak van der Waals forces are present, vibrational progressions are partially observed. Conversely, in polar or protic solvents, the intense dipole-dipole and hydrogen bonding interactions lead to a significant broadening of both absorption and emission spectra, making it difficult to discern vibrational progressions [12].

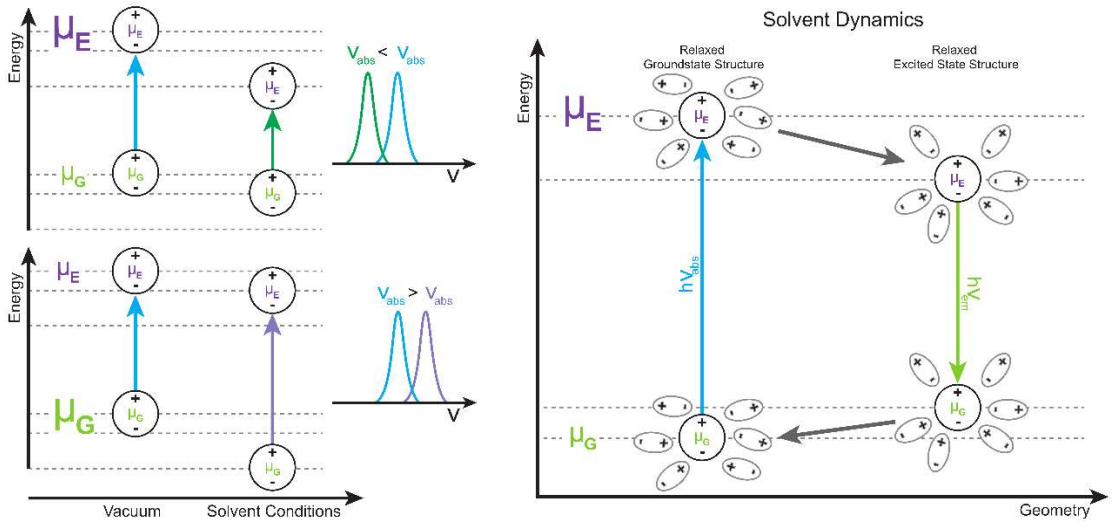

Figure 1.3. Schematic representation of solvent effect on molecular electronic states**. Left**: Schematic illustration of different solvatochromic shifts resulting from different dipole moments of ground- μ_G and excited state μ_E.

Right: Schematic representation of the dynamic solvation effects on the Stokes shift when $\mu_E > \mu_G$ in a polar solvent. Adapted from ref. [29].

Apart from influencing the shape of the absorption and emission bands, the solvent environment can further impact the position of the bands, i.e., the (absorption and emission) transition energy and thereby also the excited state lifetime. Shifts in the energy of the transition can be observed when compared to a vacuum or between solvents differing in polarity and proticity. These shifts dominantly arise from the interactions between the molecule's electric dipole moment and the dipole moments of the surrounding solvent molecules. For the ground state these stabilizations are related to solvation energy (see Figure 1.3 left). Upon excitation, the molecule's dipole moment may change, leading to different solvation energies for the ground and excited states, thereby altering their relative energies compared to those in a vacuum. This change typically results in shifts in the energy levels of the transitions. If the dipole moment of the ground state ($|\mu_G|$) is smaller than that of the excited state ($|\mu_E|$), the excited state becomes more stabilized, resulting in a bathochromic (red) shift, referred to as positive solvatochromism. Conversely, if the dipole moment of the ground state ($|\mu_G|$) exceeds that of the excited state ($|\mu_E|$), it leads to a hypsochromic (blue) shift due to greater stabilization of the ground state by the solvent molecules—a phenomenon known as negative solvatochromism [12]. The dependence of fluorescence on solvent polarity has, for instance, been widely applied in biological studies, including in the analysis of protein fluorescence [45-49]. Tryptophan, a naturally fluorescent amino acid, is extensively utilized as an intrinsic fluorescence probe in protein hydration studies [50-53]. It serves as a reporter that reveals information about the local environment of amino acid residues within proteins. For example, in polar solvents, tryptophan exhibits a red shift in fluorescence, indicating that the amino acid residue is likely on the surface of the protein, interacting with water molecules. Conversely, in non-polar surrounding, a blue-shifted fluorescence suggests that the tryptophan residue is buried within the protein, shielded from the solvent and presumably isolated by a non-polar environment [54]. Despite the extensive applications of tryptophan as a fluorescence probe, it does have limitations, including complex decay kinetics, among others [55-57]. Therefore, some derivatives of tryptophan have been developed to expand (improve) its applications. The fluorescence characteristics of these derivatives can sometimes exhibit even greater sensitivity to the solvent polarity compared to the intrinsic form [21, 58-62].

Furthermore, the proticity of the solvent also affects the energy levels of electronic transitions. Protic solvents capable of forming hydrogen bonds can significantly contribute to solvation energy, thereby changing the energies of the electronic states involved [12]. In molecules with heteroatoms, the electron density in the n-orbital is partially localized on the heteroatom and promotes the formation of H-bonds. The associated stabilization of the n-orbital causes a negative solvatochromism of $n\pi^*$ transitions with increasing solvent proticity [12].

Additionally, some chemical reactions can occur between the solute and the solvent, including excited state proton transfer reactions that involve the loss or gain of a proton. In the excited state, electron redistributions can shift electron density towards or away from functional groups, altering their pKa. This can be observed in some aromatic compounds such as phenol [63] and naphthol [64-68], where the aromatic ring systems withdraw electron density from the hydroxyl groups in the excited state, consequently increasing their acidity. These molecules are, thus, photoacids. Molecules that can accept a proton in the excited state are considered

photobases, including compounds like acridine [69]. Rapid proton transfer reactions can quickly deplete the excited state population, and thereby decreasing the excited state lifetime [70, 71].

Besides influencing the maximum of a transition band relative to the vacuum or between solvents of different polarity or proticities, solvents may also influence the position of emission bands as well as the separations between the lowest absorptions band and emission bands (Stokes shifts). This shift is typically observed in fluorescence emission by comparing the absorption and emission spectra, where the emitted wavelengths are longer than those of absorption (see Figure 1.3 right). In thermal equilibrium, solvent molecules are oriented in the most energetically favorable arrangement around the solute molecule in the ground state. Upon light absorption, the molecule becomes vertically excited (according to the Franck-Condon principle), altering its electron density distribution and concomitantly the dipole moment. Thus, in the excited state the solvent molecules are not optimally aligned. Over time, the solvent molecules reorganize to stabilize the molecule's new electronic state through a process known as dielectric relaxation. This adjustment typically takes between 100 femtoseconds and several picoseconds depending on the size of the solvent molecules [72, 73]. Since the emission process also occurs vertically, the solvent molecules initially have an energetically unfavorable orientation when the molecule returns to the ground state. Following this, the solvent molecules reorganize within the typical timeframe for dielectric relaxation. Solvent relaxation can sometimes lead to significant Stokes shifts. For instance, in proteins, tryptophan residues typically absorb light at 280 nm, while their emission is observed around 350 nm [12, 74]. Similar to the dependency of fluorescence on solvent polarity, the Stokes shift also plays an important role in numerous biological studies [75, 76].

Methods of Time Resolved Spectroscopy Applied

In this section, the methods of time resolved spectroscopy employed to obtain the presented results are listed and elaborated on. Additionally, the operating principles and the setups utilized for the experiments in this thesis are outlined. For specific descriptions of the experimental details and the results, see Chapter 5.

fs-Fluorescence Spectroscopy via Kerr Effect

Fluorescence spectroscopy with femtosecond time resolution relies on the concept of optical gates, all of which are based on optical non-linearities [77, 78]. An optical gate, in general, is an optical element that initially blocks the light path. A short pulse (switching or gate pulse) induces an optical effect that opens the gate and allows the beam to pass through. The gate light includes a variable delay line; by adjusting the length of this line, it is possible to determine when the optical gate opens, and the sample light (fluorescence) can be detected [78]. The relevant third-order non-linearity utilized to implement this gate is the optical Kerr effect [78, 79]. This effect describes how the refractive index n depends on the intensity of the (gate) light according to equation 1.3;

$$n(t) = n_0 + n_2 I(t)_g. \qquad (1.3)$$

Here, n_0 represents the conventional refractive index, and n_2 parameterizes the non-linear contribution. When exposed to a gate pulse, the non-linear refractive index of a medium in the direction parallel to the electric field vector of the gate pulse ($n_\parallel$) differs from that in the perpendicular direction ($n_\perp = n_0$), resulting in temporary birefringence within the medium [79]. In birefringent media, the optical axis serves as a reference for describing spatial orientations, where directions are defined as parallel or perpendicular to this axis [79]. If the polarization direction of the incoming fluorescence light is not exactly parallel or perpendicular to the optical axis, the perpendicular and parallel components pass through the medium at different phase velocities. This results in a phase shift after passing through the medium, which typically leads to an elliptical polarization of the light [79].

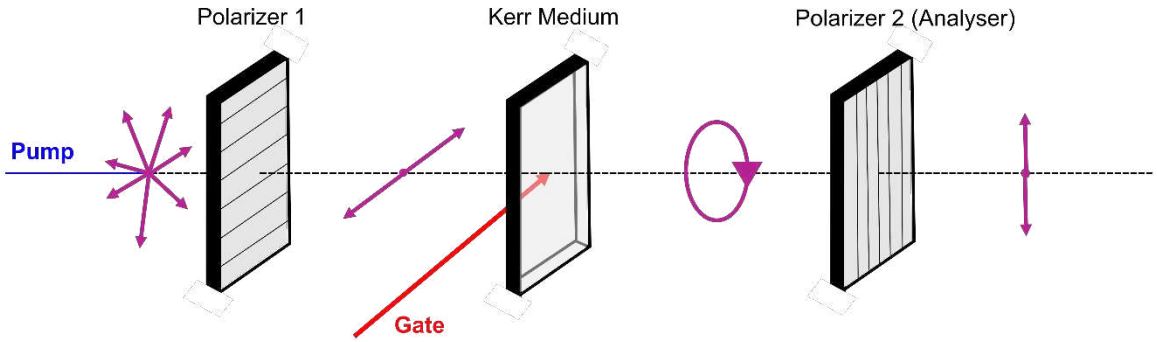

Figure 1.4. Schematic representation of an optical Kerr gate. A Kerr medium (KM) is positioned between two orthogonal wire-grid polarizers (P1 and P2). Purple arrows indicate the planes of polarization. Note that although the wire-grid polarizers are illustrated with the beam path parallel to their grid lines, the actual configuration has the beam passing perpendicularly through the grids.

Based on the optical Kerr effect, an optical gate can be realized. Initially, a polarizer selects one specific polarization direction of the fluorescence light from the excited sample (see Figure 1.4). A second polarizer, oriented perpendicularly and acting as an analyzer, blocks the path of this polarized light towards the detector. Between the polarizers, an isotropic medium (Kerr medium) is positioned for which, in its normal state, the indices obey $n_\perp = n_0 = n_\parallel$, thus preserving the polarization of the light. Upon exposure to a gate pulse, the Kerr medium becomes birefringent, temporarily rotating the polarization of the incoming light. For this time interval, some of the fluorescence light can subsequently pass through the analyzer. The relative delay between the excitation and gate light allows for detecting fluorescence decay at specific intervals.

The first optical Kerr gate was introduced in 1969 by Duguay and Hansen, who utilized a liquid Kerr media [80]. They were able to measure fluorescence decays starting from 10 ps [81]. However, their setup was constrained by the gate opening time, which is determined by the pulse duration of the gate pulse (8 ps) and the relaxation time of the liquid CS_2 (2 ps).

Initially, the use of Kerr gates in emission spectroscopy was not a primary focus; instead, their main application was in the measurement of the temporal characteristics of laser pulses using the FROG technique (frequency-resolved optical gating) [82]. Kerr gates were also

used to suppress fluorescence in optical imaging of objects [83] and time resolved resonance Raman spectroscopy [84]. At the onset of the 21st century, Kerr gates were increasingly reported in connection with emission spectroscopy, particularly in Japan by Takeda et al. [85] and Kanematsu et al. [86-88], and in Germany by Schmidt et al. [89]. The significant improvement of these setups was made by in replacing the liquid Kerr medium with optical glass. Due to the absence of rotational relaxation, the medium responds almost instantaneously [90, 91], enabling femtosecond time resolution.

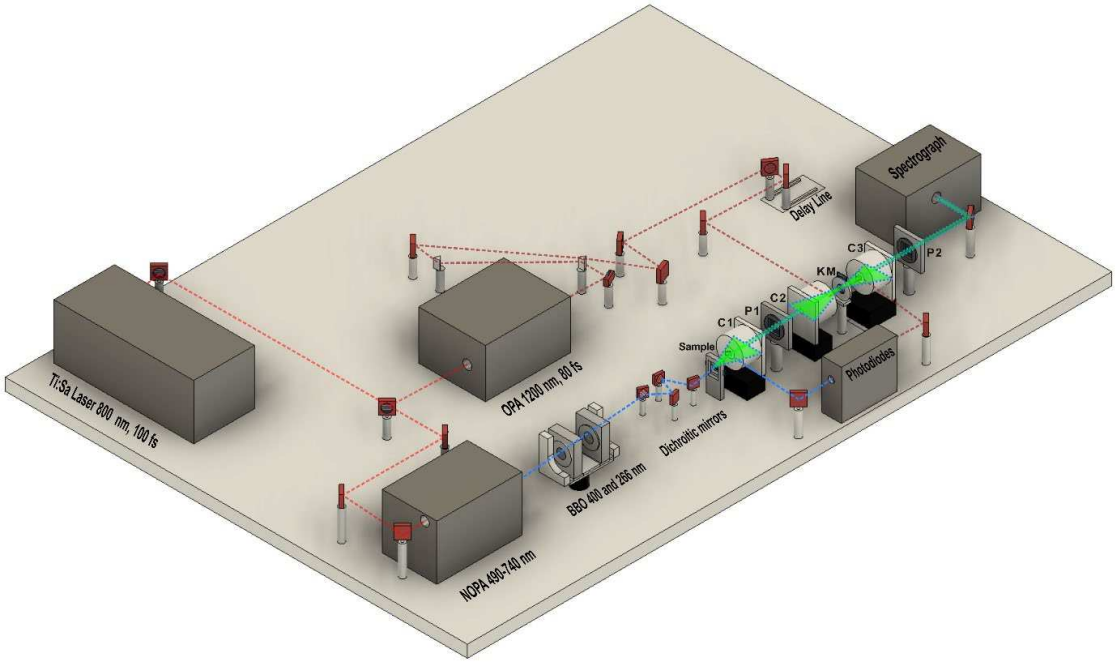

Figure 1.5. Setup for femtosecond fluorescence measurements with the optical Kerr effect. Colored lines indicate the beam paths. The fundamental of a Ti:Sa laser/amplifier is marked in light red, the excitation in blue, the gate in dark red, and fluorescence in green. Cassegrains (C1, C2, C3), polarizers (P1, P2), and Kerr medium (KM) are marked with their corresponding symbols. The positions of other components of the setup including the Ti:Sa laser/amplifier, NOPA (non-collinear optical parametric amplifier), OPA (optical parametric amplifier), nonlinear optical crystals, such as β-barium borate (BBOs), dichroitic mirrors, photodiodes, and the delay line are shown. The Shamrock 303 spectrograph coupled with an iDus 420 CCD-Camera is also indicated. Aperture and lenses are not included in the scheme.

In the femtosecond spectroscopy group of Peter Gilch, the present Kerr gate setup (see Figure 1.5) was built by Ramuna Mundt and Gerald Raoul Ryseck, based on an original design by Schmidt et al [89]. It has also been characterized in detail by Ramona Mundt [92] and Anna Reiffers [29]. The 800 nm fundamental from a Ti:Sa laser/amplifier can be converted to different pump wavelengths. Using a beam splitter, a portion of the fundamental 800 nm beam is directed through nonlinear optical crystals, such as β-barium borate (BBO), for frequency doubling (SHG, Second Harmonic Generation), resulting in a wavelength of 400 nm. This wavelength can then be further modified through sum frequency generation (SFG, Sum Frequency Generation) to produce a wavelength of 266 nm. Additionally, using another beam splitter, a portion of the fundamental beam is fed into a non-collinear optical parametric amplifier (NOPA) to generate wavelengths between ~490 and ~740 nm. These wavelengths can subsequently be frequency doubled using BBO crystals, achieving wavelengths from ~ 235 nm to ~350 nm. Four dichroic mirrors select the desired wavelength. The excitation beam is directed through a lens in a flow cell cuvette which continuously refreshes the sample. The

fluorescence light generated at the sample is collected and collimated by a Cassegrain reflector (C1). It consists of a concave and a convex spherical mirror to prevent additional chirp caused by the dispersion of the collected light. The polarization direction of the collimated beam is selected through a polarizer (P1) and then focused by another Cassegrain reflector (C2). At the focus, the beam passes through the Kerr medium. The light is then recollimated by a third Cassegrain (C3) and directed to a second polarizer (P2), or analyzer. The light is then guided towards the detector by two mirrors and a lens. The detector includes a Shamrock 303 spectrograph coupled with an iDus 420 CCD camera. Additionally, a small mirror attached to C1 directs the pump pulse towards a photodiode detector, which continuously monitors the pump intensity throughout the measurement.

The high intensity of the gate pulse can cause multi-photon absorption (MPA) in the Kerr medium, resulting in undesired emissions [86, 93]. To suppress MPA, a portion of the fundamental beam is converted to a wavelength of ~ 1200 nm using a two-stage optical parametric amplifier (OPA). This conversion can significantly reduce parasitic emission signals caused by MPA in quartz glass [89]. The gate beam (80 fs) is then reflected by two mirrors positioned on a delay line. Another mirror, along with a lens, focuses the gate beam onto a small reflective mirror attached to C2, aligning the beam to pass through the Kerr medium. An additional small mirror on C3 focuses the gate pulse towards the photodiode detector. The photodiode detectors allow for detecting data on both excitation and gate intensities, facilitating subsequent signal corrections. The timing and duration of the gate pulse relative to the excitation pulse are controlled to detect the fluorescence decay at specific intervals. This is achieved by using a single light source for both pulses, which are initially split in a semi-reflective mirror. To adjust the path length of the gate pulse, two mirrors on a delay line are moved, thereby varying the distance the pulse travels to reach the Kerr medium. By selecting various delay times between the gate and pump pulses, the optical gate can be opened at specific times after the initial impact of the pump on the sample, enabling the measurement of emission signals at specifically chosen delay times.

The spectra recorded at specific delay times t_D after excitation are indicated as $I(\lambda, t_D)_{pump/gate}$. The contributions of the background signals to these spectra need to be subtracted. Therefore, background spectra for pump only $I(\lambda)_{pump}$ and gate only $I(\lambda)_{gate}$ are recorded. The spectrum for pump only is dominated by the fluorescence leakage through the closed polarizer P2. It is linearly proportional to the intensity of the pump *P*. Using a photodiode, this intensity can be recorded for the pump only condition (P_0) and for each delay time ($P(t_D)$). In the Kerr medium, third harmonic generation (THG) of the gate light occurs throughout, with a particularly strong contribution at the interface between air and quartz glass due to the change in refractive indices. At a wavelength of ~ 400 nm, this signal can contribute to a parasitic background to the gate only spectrum ($I(\lambda)_{gate}$) and must, therefore, be subtracted in such cases. THG of the gate pulse, a third-order nonlinear process, scales cubically with the intensity of the gate pulse. This intensity was also measured for the gate only condition (G_0) and for each delay time ($G(t_D)$) using a photodiode. In the equation below (equation 1.4), the term within square brackets accounts for the correction of these background contributions [94].

$$F(\lambda, t_D) = \left[I(\lambda, t_D)_{pump/gate} - I(\lambda)_{pump} \cdot \left(\frac{P(t_D)}{P_0} \right) - I(\lambda)_{gate} \cdot \left(\frac{G(t_D)}{G_0} \right)^3 \right]$$

$$\cdot \frac{P_0}{P(t_D)} \cdot \left(\frac{G_0}{G(t_D)}\right)^2 \cdot Sens\,(\lambda) \cdot \left(\frac{\lambda}{\lambda_{Cwl}}\right)^2 \qquad (1.4)$$

Besides the background, the signal also fluctuates with intensities of the pump and gate. This can be corrected using the expressions $\frac{P_0}{P(t_D)}$ and $\left(\frac{G_0}{G(t_D)}\right)^2$ for the pump and gate intensities, respectively [94]. Since the gate efficiency varies quadratically with the gate intensity, a squared term is included to reflect this dependency [78]. To account for the spectral sensitivity of the components in the setup, the correction function $\frac{1}{Sens\,(\lambda)}$ is applied, which can be determined using a black body radiator [95, 96]. It emits an ideal spectrum ($I(\lambda)_{ideal}$) which is calculated using the following formula (equation 1.5):

$$I(\lambda)_{ideal} = \frac{2\pi C_0}{\lambda^4} \frac{1}{e^{\left(\frac{hC_0}{\lambda K_B T}\right)} - 1}. \quad (1.5)$$

According to equation 1.5, the spectrum of the radiator depends on the temperature *T*, alongside the constants for the speed of light in vacuum c_0, Planck's constant *h*, and the Boltzmann constant k_B. As a function of wavelength, this formula represents the radiation as photons per second, area and wavelength interval. The spectrum of a suitable lamp is approximated as $I(\lambda)_{ideal}$ and can be calculated using the known temperature *T* of the lamp. The lamp spectrum $I(\lambda)_{measured}$ is recorded. Its shape is affected by sensitivity curve $Sens\,(\lambda)$ of the instrument according to equation 1.6.

$$I(\lambda)_{measured} = I(\lambda)_{ideal} \cdot Sens\,(\lambda). \qquad (1.6)$$

With $Sens\,(\lambda)$ the recorded spectra can be corrected. To adjust for the wavelength dependency of the gate efficiency, a factor λ^2 is additionally applied [97]. To normalize the signals according to their order of magnitude, the correction factor is related to the central wavelength of the spectrum or the grating in the monochromator λ_{Cwl}. The data were subsequently corrected for the time zero dispersion [89], relying dispersion parameters given in ref. [98] and [99]. The solvent was also measured and corrected in the same way as the sample. The solvent contributions were then subtracted after proper scaling [94].

Time Resolved Transient UV/Vis Spectroscopy

Transient absorption spectroscopy allows to track time dependent absorption changes (ΔA) upon photoexcitation. These absorption changes can be of positive or negative signals. Positive transient absorption signals indicate increased absorption by the photo-excited sample at certain wavelengths, due to excited state absorption or ground state absorption of photoproducts (ESA; Figure 1.6 orange). Negative signals arise when the probe beam detects either reduced absorption which is known as ground state bleaching (GSB, Figure 1.6 blue), or an increase in probe intensity due to stimulated emission (SE, Figure 1.6 green). Each of these processes can contribute simultaneously to the observed transient absorption signal.

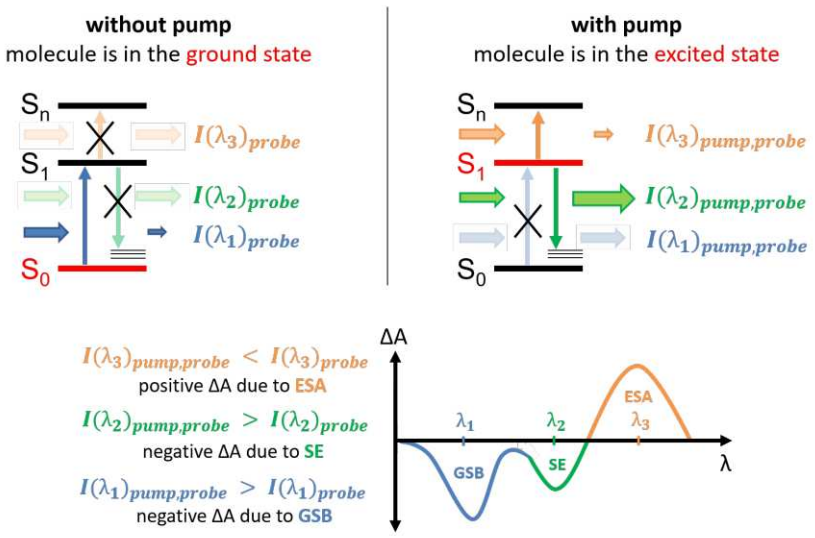

Figure 1.6. Diagram of excited state absorption, ground state bleach, and stimulated emission in fs-TA and ns-TA spectroscopy. The scheme illustrates the processes involved in fsTA spectroscopy, including excited state absorption (ESA), ground state bleach (GSB), and stimulated emission (SE). As an illustration, three wavelengths λ_1, λ_2, and λ_3 of the probe beam are shown. The diagram emphasizes changes in the intensity of these wavelengths $I(\lambda_1, \lambda_2, \lambda_3)_{probe}$ with and without photoexcitation (pump), depicted in the top right and top left respectively, to demonstrate the formation of $\Delta A(\lambda, t_D)$. Adapted from ref. [100].

Signal changes can be measured using femtosecond transient absorption spectroscopy, which covers time scales ranging from ~ 10 fs to ~10 ns. For longer delay times, extending the delay path can lead to beam broadening. Therefore, nanosecond transient absorption spectroscopy (nsTA) is used to cover the processes spanning from ~20 ns to several milliseconds.

fs-Transient UV/Vis Spectroscopy

The setup for UV/Vis absorption spectroscopy with femtosecond time resolution has been previously described in detail in other works [29, 100-104]. It operates on the pump-probe principle, which is closely related to the pump-gate principle described in the previous section. It utilizes two distinct laser beams—both derived from the same femtosecond pulsed laser source—as outlined in Figure 1.7. The pump beam is designed to photoexcite the sample, while the spectrally broad probe beam probes the absorption of the sample at a precise time interval following the photoexcitation. The same laser source used for the Kerr gate setup was employed in this setup. The process of generating the excitation wavelength for the pump beam also follows a similar method as described for the Kerr gate setup. The pump beam's excitation wavelength is set through frequency doubling and, if necessary, further modified by sum frequency generation, employing nonlinear optical crystals like β-barium borate (BBO) for these processes. With a fundamental wavelength of 800 nm from a Ti:Sa femtosecond laser, the resulting wavelengths are 400 nm and 266 nm, respectively. Other wavelengths ranging from ~470 nm to ~700 nm can be generated using non-collinear optical parametric amplification (NOPA). The output wavelengths from the NOPA can also be frequency doubled

to achieve wavelengths between ≈235 and ≈350 nm. To introduce a controlled delay between the pump and probe beams, a delay stage is placed along the path of the pump beam. This stage adjusts the length of the light path to the sample, thereby translating a physical distance into a temporal delay. It allows for time delays ranging from ~ 40 fs to ~ 4 ns. The broad probe pulse is generated through a white light generation process, where focusing the femtosecond laser beam onto a transparent medium like a CaF_2 crystal causes nonlinear processes that broaden the spectrum [105, 106]. This probe beam then passes through the continuously refreshed sample in a flow cell cuvette, is dispersed by a grating, and is ultimately detected by a photodiode array.

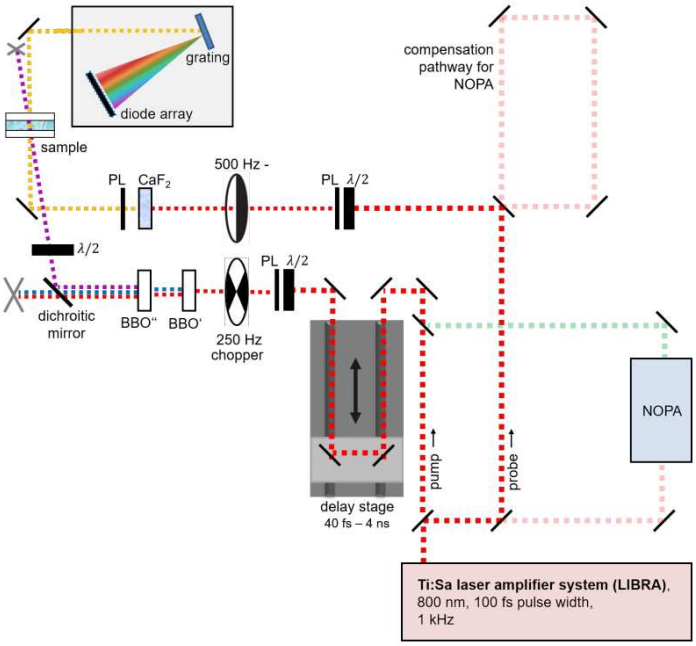

Figure 1.7. Scheme of the setup for femtosecond transient absorption measurements. The wavelengths of the pump and probe are shown with the corresponding spectral colors. The generated white light, passing through a CaF2 plate, is represented by a yellow line. Polarizers and λ/2 plates, marked as PL and λ/2 respectively, and with their combination form an attenuation unit. Lenses and apertures are not depicted in the scheme. Adapted from ref. [100].

ns-Transient UV/Vis Spectroscopy

Unlike fsTA, which uses an optical delay-based pump-probe arrangement, nsTA utilizes an electronically triggered detection system. This enables continuous and complete scanning of the time range from 20 nanoseconds to milliseconds by employing a continuous wave (CW) probe light to measure changes in light intensity after the excitation pulse is applied.

In the setup used in this thesis for ns flash photolysis, changes in the probe light's intensity over time are detected using a photomultiplier (PM). Typically, the temporal resolution of the measurement is determined either by the sampling rate of the oscilloscope, which records the signal from the PM, or by the electronic response time of the PM itself.

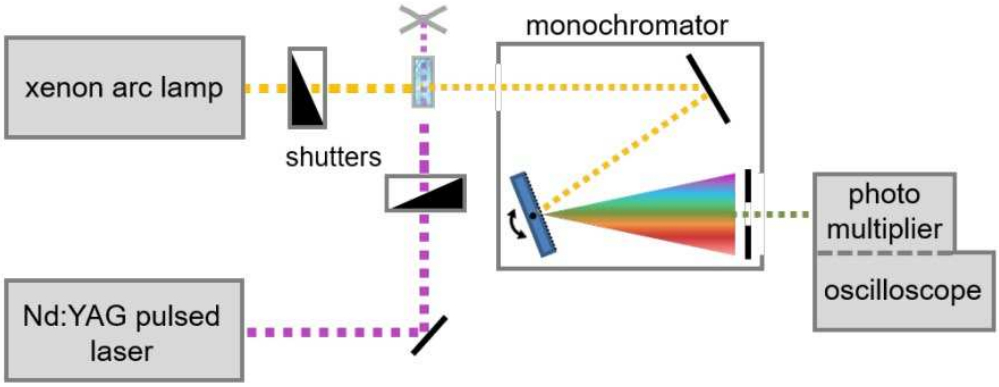

Figure 1.8. Scheme of the commercial setup for nanosecond transient absorption measurements used in this thesis. The spectrally broad light emitted by a pulsed xenon arc lamp is illustrated with a yellow line. A (scanning) monochromator is employed to select individual wavelengths at a time, which are then detected by a photomultiplier. Adapter from ref. [100].

The excitation source in this commercial setup (LP980 from Edinburgh) is a nanosecond Nd:YAG (neodymium-doped yttrium aluminum garnet; Nd:$Y_3Al_5O_{12}$) pulsed laser, which outputs a fundamental wavelength of 1064 nm (see Figure 1.8). The fourth harmonic (266 nm) is generated for the photoexcitation of the sample through nonlinear optical processes. To accommodate the need for a long (and spectrally broad) probe pulse in nsTA, a separate light source, specifically a xenon flash lamp, is employed. This lamp provides stable, high intensity white light pulses over hundreds of microseconds, making it ideal for probing.

2. Fluorescence Quantum Yields—Background

The fluorescence quantum yield (Φ_{fl}) is a key parameter in investigating the photochemical and photophysical properties of molecules and represents the ratio of emitted photons to absorbed photons. This ratio serves as an indicator of a dye's fluorescence efficiency [12]. The yield Φ_{fl} is a dimensionless number ranging from 0 to 1, or sometimes expressed as a percentage. For individual emitters, the fluorescence quantum yield provides insight into radiative transitions, in combination with the fluorescence lifetime, fluorescence spectrum, and fluorescence anisotropy [22]. The yield Φ_{fl}, along with the absorption coefficient (ε), determines the sensitivity for detecting specific analytes or targets. The product of the yield Φ_{fl} and ε, known as "brightness" [107], is crucial for evaluating and comparing the performance of fluorescent labels and dyes and thereby facilitating the design of new fluorescent probes and sensors. The yield Φ_{fl} is also essential for numerous applications in biological and medical diagnostics, including fluorescence correlation spectroscopy (FCS) and Förster resonance energy transfer (FRET) [108, 109]. Additionally, the yield Φ_{fl} plays an important role in characterizing materials used in organic light-emitting diodes (OLEDs) [10]. The yield Φ_{fl}, along with luminescence data, also facilitate the assessment of material purity [110, 111].

The term "fluorescence quantum yield" as well as a method to determine it were first introduced by Vavilov for organic dyes in solution [112]. In his work he also for the first time showed that the value of the yield Φ_{fl} can approach unity. Since then, numerous studies have been conducted to improve and refine the measurement of fluorescence quantum yields. The first relative determination of fluorescence quantum yield using a known standard was established by Parker and Rees [113], who reproduced the quantum yield value of 0.55 for quinine sulfate in 0.1 N H_2SO_4, originally reported by Melhuish through absolute determinations [114]. Most fluorescence quantum yield measurements are reported for compounds in solution. However, yields have also been determined for organic compounds in the gas phase [115-117], in crystalline states, and on solid surfaces [118-122]. Additionally, measurements for multichromophoric biomacromolecules have been reported [123-125].

In general, determinations of the yield Φ_{fl} can be categorized into absolute and relative methods [126]. Absolute techniques include determinations through calorimetric approaches or by using instruments equipped with an integrating sphere detector. Absolute calorimetric methods for determining fluorescence quantum yields involve measuring the temperature increase caused by light absorption in a sample and were commonly reported in the literature prior to the 1990s [127, 128]. An absolute method that has been utilized in more recent years is thermal lensing (see Figure 2.1) [129-133]. This technique relies on a property of laser beams as they pass through a sample of absorbing molecules. The laser typically exhibits a Gaussian intensity distribution with radially symmetric intensity [133]. Therefore, when it passes through an absorbing medium, it unevenly heats the medium due to its intensity profile [125]. This results in localized heating within the sample, creating a temperature profile. As the refractive index of the sample is temperature-dependent, this temperature gradient induces a corresponding gradient in the refractive index, thereby forming a thermal lens. This lens acts similarly to an optical lens, altering the path of the traveling beam to cause either focusing or defocusing. The development of the thermal lens over time can be observed by monitoring changes in the beam expansion and intensity, which are detected by a suitably positioned detector from a distance. The non-radiative decay, indicated by heat generation within the

sample, is quantified through the changes caused by the thermal lens, thereby enabling the calculation of the fluorescence quantum yield. This method, like other absolute calorimetric methods provides a direct measure of non-radiative decay processes in the sample. Although the setup for most of the calorimetric measurements is relatively simple compared to other methods, the precision required to detect slight temperature changes is crucial, which can pose challenges in terms of sensitivity and accuracy, especially in comparison to the conventional fluorometers [110, 125]. Therefore, this method is not very suitable for weakly emissive compounds [125]. In this technique, samples with high absorbance are often used to enhance temperature sensitivity, which can sometimes lead to issues with reabsorption. This method has the advantage of being insensitive to scattering and independent of the sample's geometry [134].

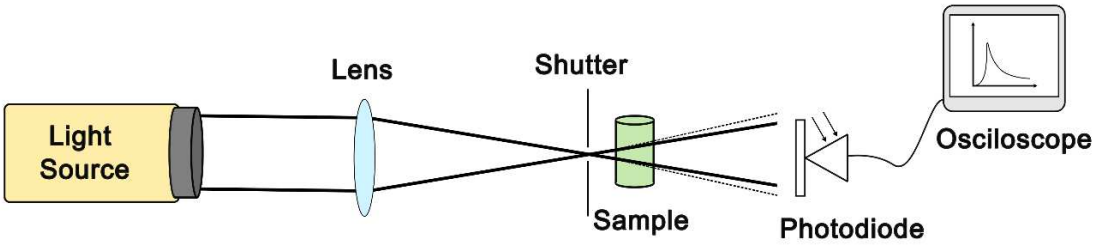

Figure. 2.1. Experimental setup for thermal lensing measurements. The diagram illustrates the path of light from a source through a lens, focusing on a sample. A shutter controls light exposure, the photodiode detects changes in light intensity. Data is analyzed and visualized using an oscilloscope connected to the photodiode. The figure was inspired by ref. [125, 135].

Nowadays, most of the absolute determinations rely on integrating sphere setups. The integrating sphere was originally introduced by de Mello et al. in 1997 [136]; however, the fundamental principle had already been published by the same group two years earlier [137, 138]. As shown in Figure 2.2, an integrating sphere setup consists of a hollow spherical cavity with its interior coated with a highly diffuse white scattering material. This setup is designed to capture light emitted by a sample in all directions. When a sample, which can be in solution or solid state, is placed inside the sphere and illuminated by a controlled light source, it absorbs light and fluoresces. The scattering coating on the sphere's interior ensures that light emitted by the sample is uniformly diffused across the sphere, allowing for a portion of the emitted light to be collected regardless of the direction of emission. Light intensity emitted by the sample, as well as the light absorbed, are measured by the detector. The fluorescence quantum yield is then calculated by comparing the intensity of the emitted light to the intensity of the absorbed light [139, 140]. In integrating sphere setups, polarization effects are effectively neutralized due to the extensive scattering and reflections within the sphere, which randomize the light's polarization [126, 138]. Similar to thermal lensing, reabsorption effects may also be problematic here and can be intensified by the multiple scattering events [110]. This can introduce inaccuracies if not properly accounted for. Additional uncertainties may arise from non-uniform coatings on either the sphere or sample holders and from variability in how samples are positioned within the sphere [126].

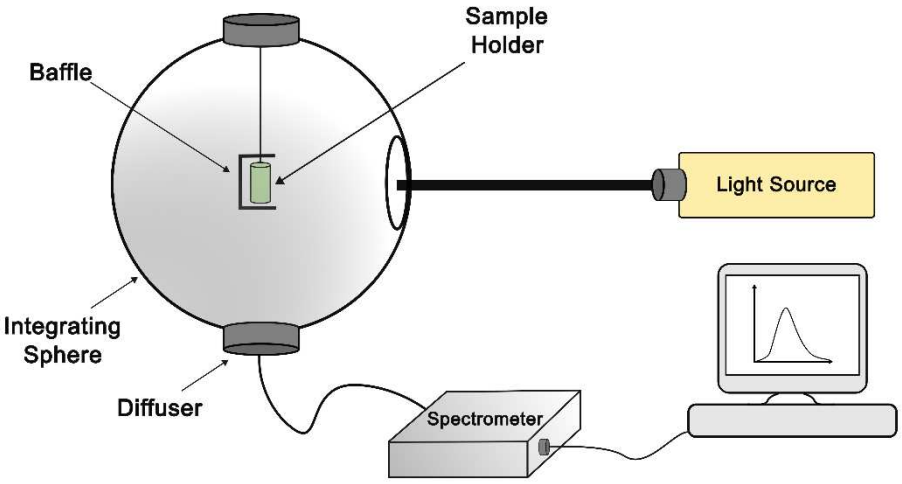

Figure 2.2. Fluorescence quantum yields determined by an integrating sphere. The setup includes a light source directed at a sample holder inside the sphere to excite the sample. Light emitted by the sample is diffused uniformly by the integrating sphere's reflective interior, ensuring that a portion of the emitted light is captured. A baffle positioned within the integrating sphere ensures that the detector does not capture the initial reflections of the incident or emitted light. The detector is mounted directly on the wall of the integrating sphere. The emitted light is then analyzed by a spectrometer connected to a computer for spectral analysis. The figure was inspired by ref. [141].

With regard to relative methods, one reported approach utilized Raman scattering signals from neat solvents to determine fluorescence quantum yields. Chekalyuk et. al. [142] proposed using the spontaneous Raman scattering signal of the solvent as an internal standard for measuring the fluorescence of highly dilute dye solutions. In their studies, they employed an attenuated laser beam to prevent saturation effects in fluorescence measurements and calibrated the fluorescence signal against the Raman scattering at the 3440 cm^{-1} water line. They employed available data for the differential Raman scattering cross-section of solvents at specific excitation wavelengths and measured the absorption cross-section of the chromophore using a conventional spectrophotometer. This approach enabled them to determine the fluorescence quantum yields of quinine sulfate, fluorescein, and rhodamine 6G in aqueous solutions. The method is quite convenient, yet its application has been limited to specific solvents and has not been applied to others. It is particularly suited to dilute solutions of strong emitters, enabling straightforward quantification of the Raman signal. Although this method may hold potential for compounds with small fluorescence quantum yields, doubts have been raised regarding the reliability of using Raman signals as calibration tools in laser-induced fluorescence measurements [125, 143].

The most commonly used method for the determination of the yield Φ_{fl} is the relative method which is readily accessible through conventional spectrofluorometers [144]. Most potential errors and sources of uncertainty mentioned for other methods also apply to this method. However, one important advantage of this approach is its effectiveness for moderately or weakly emissive compounds [125]. Common spectrofluorometers nowadays are sufficiently sensitive to accurately measure compounds with small fluorescence quantum yields in optically dilute solutions, which enhances measurement accuracy and minimizes the risk of errors associated with less sensitive equipment [125]. In this method, the fluorescence intensity of a sample is compared to that of a reference with a known quantum yield under the same experimental conditions. Reference materials with well-established fluorescence quantum

yields are, thus, essential for such measurements. However, as Brouwer [145] highlight, most of these reference compounds have high yield Φ_{fl}, typically above 0.5. This approach is practical for high-yield fluorophores but poses challenges when studying chromophores with much lower yields. In molecules with small fluorescence quantum yields, non-radiative processes, which compete with fluorescence emission, predominate. Upon photon absorption, the deactivation of the excited state is governed by the relative kinetic rate constants of various processes, a concept illustrated by the Jablonski diagram discussed in chapter 1. The fate of an excited state can be considered a random event with multiple potential outcomes, such as fluorescence, internal conversion, intersystem crossing, energy transfer to surrounding molecules, or other non-radiative processes (see Figure 2.3) [146]. The probability of each outcome is determined by the rate constant of the specific process relative to the combined rate constants of all deactivation processes. Specifically, the probability that a singlet excited state deactivates through photon emission—fluorescence—is given by the rate constant of fluorescence emission (k_{rad}) relative to the sum of the rate constants of all deactivating processes ($k_{rad}+\Sigma k_{nr}$, where Σk_{nr} encompasses all non-radiative processes) [144]. For chromophores undergoing allowed transitions, radiative rate constants k_{rad} are typically on the order of 10^8 s^{-1}, while non-radiative rate constants k_{nr} may approach the vibrational frequency, estimated at ~10^{13}-10^{14} s^{-1} [146]. Consequently, the lower boundary for the yield Φ_{fl} of the order of 10^{-6} to 10^{-5} can be approximated using the equation 2.1;

$$\Phi_{fl} = \frac{k_{rad}}{k_{rad}+k_{nr}} \qquad (2.1)$$

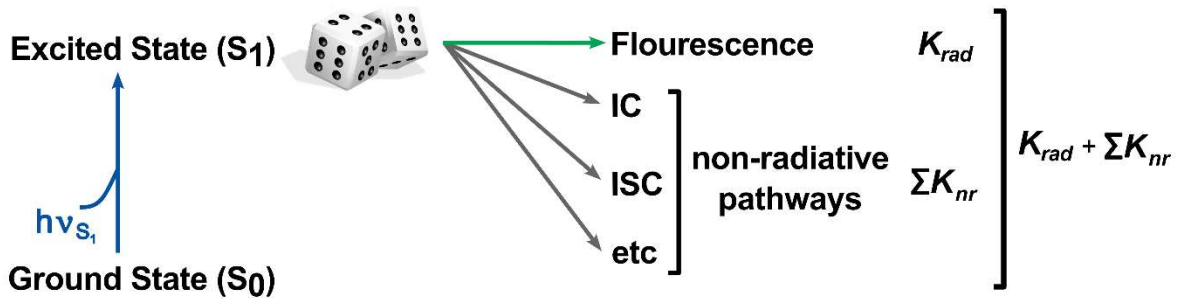

Figure 2.3. Schematic representation of the various pathways through which the first excited state may deactivate, emphasizing the stochastic nature of these processes. The probability of the excited state deactivating through fluorescence is determined by the ratio of k_{rad} to $k_{rad} + \Sigma k_{nr}$, where Σk_{nr} denotes the sum of the rate constants for all non-radiative pathways capable of deactivating S_1. The figure was inspired by ref. [144].

Applying the relative method to determine such small fluorescence quantum yields is often limited by the available reference materials, which predominantly exhibit high quantum yields. This presents a challenge, underscoring the necessity for standards with smaller, well-validated fluorescence quantum yields that span various spectral ranges. Such standards enable more accurate quantitative comparisons. By aligning the fluorescence intensities of the sample and reference within the optimal detection range, instrument measurement errors can also be minimized.

In the recently published publication entitled “References for Small Fluorescence Quantum Yields” [147], three compounds are identified with fluorescence quantum yields in the range of 10^{-5} to 10^{-4} covering the UV/Vis spectral range. The fluorescence quantum yields Φ_{fl} of the compounds were first determined using the relative method. For comparison, these yields were also calculated using the relationship between the yield, the radiative rate constant k_{rad}, and the fluorescence lifetime (τ_{fl}), as detailed in equation 2.2;

$$\Phi_{fl} = k_{rad}\tau_{fl}. \qquad (2.2)$$

The radiative rate constant k_{rad} was obtained via the Strickler-Berg relation [42] (see chapter 1), and the fluorescence lifetime τ_{fl} was measured using the time resolved fluorescence Kerr gating setup. The fluorescence quantum yield values obtained from both methods closely aligned within their respective error margins. The results of this study are summarized in a publication which is reproduced in Chapter 5.

2.1. Copper(I) Carbene Complexes

In the evolving landscape of materials science, particular emphasis has been placed on developing cost-effective and environmentally friendly alternatives to heavy metal-based complexes, like iridium and platinum, commonly used in organic light emitting diodes (OLEDs). Copper(I) complexes, with intriguing luminescent properties, are emerging as promising candidates for this replacement [148-151].

In this context, the study “Femtosecond Spectroscopy and Quantum Chemistry of a Linearly Coordinated Copper(I) Carbene Complex” [104] was conducted to investigate the photophysical characteristics of a specific copper(I) carbene complex: [1,3-bis(2,6-diisopropylphenyl)imidazol-2-ylidene]-(2-picoline)copper(I) tetrafluoroborate, referred to as NHCCuPy. This complex demonstrates significant environmental sensitivity, as evidenced by its performance in various media. When incorporated into a poly(methyl methacrylate) (PMMA) matrix or processed as a powder, the complex exhibits a high fluorescence quantum yield of 0.87 [24]. However, this yield dramatically decreases in single crystals and solutions, where it becomes orders of magnitude smaller.

This study further explores the behavior of NHCCuPy in different solvent environments, both coordinating and non-coordinating, to understand these variations in luminescence. Notably, when the complex is dissolved in solution, the quantum yield is in the order of ~ 10^{-5}, contrary to its performance in PMMA [24]. This complex includes 2-picoline as a ligand. The association of the ligand to the copper(I) ion is an equilibrium process and, thus, in solution, free 2-picoline molecules and ones bound to copper(I) may coexist. Both species may contribute to the fluorescence signal of the solution.

This study utilized both steady state and time resolved spectroscopy to investigate the photophysics of NHCCuPy in different environments. Among the techniques employed was the fluorescence Kerr gate setup, which is particularly advantageous not only for time resolved measurements but also for recording steady state fluorescence spectra. This setup was specifically chosen for its high sensitivity to very low emission levels, making it ideal for detecting potential impurities and very small fluorescence signals. This setup, as described in chapter 1, was operated with an open gate, to record the steady state fluorescence spectra in this

study. This configuration allowed for a detailed comparison of the emission properties of NHCCuPy and 2-picoline, providing insights into how each component contributes to the overall luminescence. The results of this study are summarized in a publication which is reproduced in chapter 5.

3. Fluorescence Anisotropies—Background

The term “anisotropy” was first defined by Aleksander Jablonski to describe the polarized emission observed in solutions [27, 152]. Over time, this concept has emerged as an important tool in various fields of biochemical fluorescence applications [153]. For instance, anisotropy experiments can provide insights into the size and shape of proteins [154], or assess how rigid different molecular environments are [155, 156]. This technique is applied in exploring protein dynamics and other biomolecular behaviors, revealing the impacts of structural changes or molecular interactions [157, 158]. For instance, it plays a key role in studying protein denaturation and in examining protein interactions that affect rotational behavior [159, 160]. Fluorescence anisotropy is also instrumental in clinical diagnostics, particularly in immunoassays, where it effectively measures analyte concentrations [161, 162]. Additionally, it offers detailed insights into the rotational dynamics under different environmental conditions, making it invaluable for studying membrane-bound fluorophores [12, 163, 164].

Anisotropy experiments rely on the concept of photoselective excitation of molecules using polarized light [12]. Light is an electromagnetic wave, characterized by oscillating electric and magnetic fields that are perpendicular to each other. When the electric field oscillates in a single plane and maintains a consistent orientation relative to the direction of propagation, the light is known as linearly polarized [165]. Absorption of light induces a transition from the ground electronic state (a) to an excited one (b). In quantum mechanics, one approach to approximately describe molecular electronic transitions involves the use of transition dipole moments (TDMs) $\vec{\mu}_{ab}$ [166]. Here the assumptions are made that the excitation light is polarized along the z-axis and propagates along the x-axis through a sample containing randomly oriented molecules (see Figure 3.1). The absorption probability (P_θ) depends on the square of the dot product of the electric field $\vec{E}$ and the TDM ($\left|\vec{\mu}_{ab} \cdot \vec{E}\right|^2$) and is proportional to $\cos^2(\theta)$ (see equation 3.1);

$$P_\theta \propto \left|\vec{\mu}_{ab} \cdot \vec{E}\right|^2 \propto \cos^2(\theta). \qquad (3.1)$$

Here, θ represents the angle between the transition dipole moment and the polarization direction of the electric field. The absorption probability is maximal when the alignment is parallel ($\theta = 0^\circ$) and is zero when perpendicular ($\theta = 90^\circ$). This indicates the probability that a molecule with a specific orientation will become excited. To account for the probability associated with a specific angle θ, the $\sin(\theta)$ term is included to average the probability of excitation across the ensemble. As a result, molecules whose TDMs are oriented in specific directions will experience a preferential excitation (see Figure 3.1). This phenomenon (photoselection) can be quantitively described by the equation 3.2;

$$\langle P_\theta \rangle \propto \cos^2(\theta) \cdot \sin(\theta). \qquad (3.2)$$

This selective excitation can be observed in the emission signal when polarizers are used in front of a detector. Taking into account the $\cos^2(\theta) \cdot \sin(\theta)$ distribution, the polarization characteristics of the emitted light form a dumbbell shape, as depicted in Figure 3.1, indicating that the polarization of the emitted light is symmetrically distributed around the z-axis. Molecules with TDMs closely aligned with the z-axis polarization are more likely to be excited, resulting in stronger emission signals along the z-axis. Conversely, as the orientation angle nears 90°, the emission intensity diminishes, reaching zero in the x-y plane. Accordingly, for

the conditions that the molecules do not rotate and undergo the same electronic transition during both absorption and emission, the intensity of light emitted parallel to the polarization direction of the excitation ($I_{\parallel}$) is typically three times greater than that emitted perpendicularly ($I_{\perp}$). To describe the extent of polarization of the emission, a parameter known as fluorescence anisotropy has been defined and can be quantified using the equation 3.3 [12],

$$r = \frac{I_{\parallel} - I_{\perp}}{I_{\parallel} + 2I_{\perp}}. \qquad (3.3)$$

Here, $I_{\parallel}$ and $I_{\perp}$ represent the intensities of light emitted parallel and perpendicular to the excitation polarization, respectively. The denominator in this equation represents the total fluorescence intensity (I_{total}), which includes contributions from all three Cartesian axes ($I_{total} = I_x + I_y + I_z$). Given the symmetric distribution of the emission in the xy-plane ($I_y = I_x$), the total intensity simplifies to $I_{total} = I_z + 2I_x = I_{\parallel} + 2I_{\perp}$.

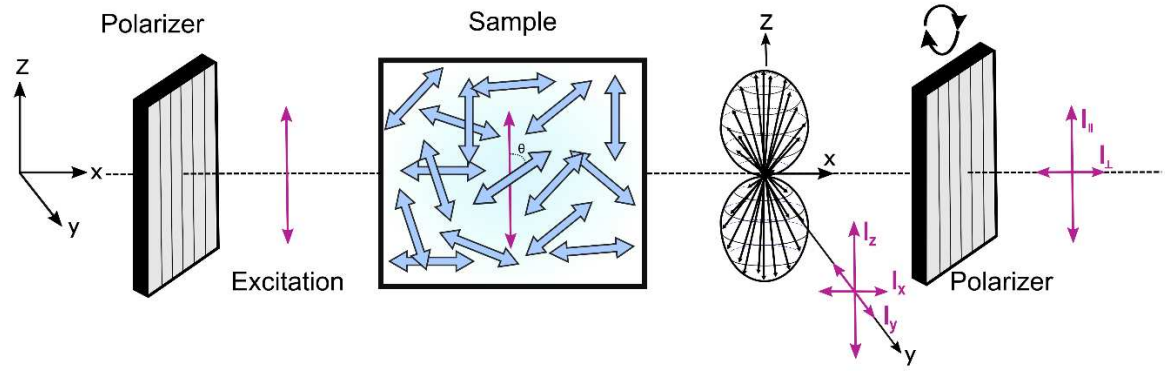

Figure 3.1. Fluorescence anisotropy measurement. Light propagates from left to right. Polarized excitation light aligned along the z-axis excites the sample. In the sample, molecules are oriented randomly. The resulting emission is symmetrically distributed around the z-axis. A rotatable polarizer allows for selective detection of the y- or z-components of the emission. The intensities $I_{\parallel}$ and $I_{\perp}$are then measured by a detector positioned behind the polarizer. The image of the dumbbell-shaped emission distribution was taken from ref. [12], and redrawn.

Assuming the molecules are immobile and undergo non-degenerate transitions, the (initial) anisotropy r can range from -0.2 to 0.4 [12]. A maximum value of 0.4 is observed when the same electronic transition is involved in both absorption and emission processes, and the angle β—the angle between the transition dipole moments for excitation and emission—is 0°. Conversely, a minimum value of -0.2 is obtained when the angle β reaches 90°, typically observed when the absorbing and emitting states are different. For the angle β =54.7°, both $I_{\parallel}$ and $I_{\perp}$ yield the same value, resulting in an anisotropy of zero. Generally, the anisotropy r is associated with the angle β according to the equation 3.4;

$$r = \frac{3cos^2(\beta) - 1}{5} \qquad (3.4)$$

When molecules can rotate between the time of absorption and emission, this rotation can lead to the depolarization of the emitted light. Rotational diffusion, characterized by random rotational movements (tumbling) of fluorophores in solution, is a common cause of

fluorescence depolarization [12]. This process causes the anisotropic distribution of excited molecules, initially aligned by photoselection, to gradually evolve towards isotropy [12, 28].

The decay of anisotropy from its initial value, r_0, due to rotational diffusion can be described by an exponential law (equation 3.5):

$$r(t) = r_0\, e^{-\frac{t}{\tau_r}} \qquad (3.5)$$

where r_0 is the initial anisotropy, t represents time, and τ_r is the rotational relaxation time, which characterizes the time scale at which the fluorophore can tumble within its environment. The time constant τ_r is estimated using the Debye-Stokes-Einstein relation (equation 3.6) [12, 28]:

$$\tau_r = \frac{V\eta}{k_b T} \qquad (3.6)$$

Here, V denotes the hydrodynamic volume of the molecule, η the viscosity of the solvent, k_b the Boltzmann constant, and T the temperature. For small molecules in solutions with low viscosity, the typical time constant is on the order of 40 ps [12]. When this time constant is shorter than the fluorescence lifetime, the fluorescence emission tends to exhibit an isotropic ensemble, resulting in a time-averaged anisotropy that approaches zero. However, for very short-lived chromophores where the fluorescence lifetime is comparatively short, the fluorescence tends to retain much of its initial polarization during the lifetime of fluorescence. With the aid of time resolved techniques, it is possible to record both the initial anisotropy r_0 as well as the decay time τ_r [167].

Besides rotational diffusion, another mechanism, among others, may also contribute to the decay of anisotropy, namely electronic excitation energy transfer [12]. In this process, energy is transferred when a molecule in an excited state (referred to as the donor) releases energy, which is then transferred to another molecule in its ground state (termed the acceptor). This transfer of energy can occur within a single molecule between different moieties or across distinct molecules. Using anisotropy measurements this transfer can be monitored [168-170].

Anisotropy measurements are also applied to study and interpret the dynamics of molecular excited states. They are particularly useful for distinguishing between different electronic transitions, which may have transition dipole moments oriented differently [171-173]. For instance, indole and its derivatives are known to have two closely lying excited states (L_a and L_b) [26, 171, 174, 175]. For most derivatives of indole, the angle between the transition dipole moments of these states can vary between 20° and 90° [26, 171, 174, 175]. Thereby, transitions between these states can lead to significant fluorescence depolarization. The dynamics of these processes can be investigated using time resolved fluorescence anisotropy [176]. In the publication "The photophysics of 2-cyanoindole probed by femtosecond spectroscopy" [177], we specifically examined the cyano derivative of indole, 2-cyanoindole, using time resolved fluorescence anisotropy to assign the emission to an excited state (L_a or L_b). The results of this study are summarized in a publication which is reproduced in Chapter 5.

4. References

1. Valeur, B. and M.N. Berberan-Santos, *A brief history of fluorescence and phosphorescence before the emergence of quantum theory.* Journal of Chemical Education, 2011. **88**(6): p. 731-738.
2. Stokes, G.G. *On the change of refrangibility of light*. in *Abstracts of the Papers Communicated to the Royal Society of London*. 1854. The Royal Society London.
3. Udenfriend, S., *Development of the spectrophotofluorometer and its commercialization.* Protein science: a publication of the Protein Society, 1995. **4**(3): p. 542.
4. Ghiran, I.C., *Introduction to fluorescence microscopy.* Light Microscopy: Methods Protocols, 2011: p. 93-136.
5. Renz, M., *Fluorescence microscopy—A historical and technical perspective.* Cytometry Part A, 2013. **83**(9): p. 767-779.
6. Shank, C., et al., *Compression of femtosecond optical pulses.* Applied Physics Letters, 1982. **40**(9): p. 761-763.
7. Weiner, A. and E. Ippen, *Femtosecond excited state relaxation of dye molecules in solution.* Chemical Physics Letters, 1985. **114**(5-6): p. 456-460.
8. Birriel, J.J. and D. King, *Fluorescence spectra of highlighter inks.* The Physics Teacher, 2018. **56**(1): p. 20-23.
9. Hoinka, N.M. and T. Fuhrmann-Lieker, *Amplified spontaneous emission in paper.* Scientific Reports, 2019. **9**(1): p. 1862.
10. Kalyani, N.T. and S. Dhoble, *Organic light emitting diodes: Energy saving lighting technology—A review.* Renewable Sustainable Energy Reviews, 2012. **16**(5): p. 2696-2723.
11. Bauri, J., R.B. Choudhary, and G. Mandal, *Recent advances in efficient emissive materials-based OLED applications: a review.* Journal of Materials Science, 2021. **56**(34): p. 18837-18866.
12. Lakowicz, J.R., *Principles of fluorescence spectroscopy*. 2006: Springer.
13. Royer, C.A., *Probing protein folding and conformational transitions with fluorescence.* Chemical Reviews, 2006. **106**(5): p. 1769-1784.
14. Jett, J.H., et al., *High-speed DNA sequencing: an approach based upon fluorescence detection of single molecules.* Journal of biomolecular structure dynamics, 1989. **7**(2): p. 301-309.
15. Weiss, S., *Fluorescence spectroscopy of single biomolecules.* Science, 1999. **283**(5408): p. 1676-1683.
16. Moerner, W. and D.P. Fromm, *Methods of single-molecule fluorescence spectroscopy and microscopy.* Review of Scientific instruments, 2003. **74**(8): p. 3597-3619.
17. Celebrano, M., et al., *Single-molecule imaging by optical absorption.* Nature Photonics, 2011. **5**(2): p. 95-98.
18. Xiong, Y., et al., *A review on recent advances in amino acid and peptide-based fluorescence and its potential applications.* New Journal of Chemistry, 2021. **45**(34): p. 15180-15194.
19. Millar, D.P., *Time-resolved fluorescence spectroscopy.* Current opinion in structural biology, 1996. **6**(5): p. 637-642.
20. Gan, X., et al., *Determination of tetracaine hydrochloride by fluorescence quenching method with some aromatic amino acids as probes.* 2012. **22**: p. 129-135.
21. Debopreeti, M., T. Thomas, and G. Feng, *Utility of 5-Cyanotryptophan Fluorescence as a Sensitive Probe of Protein Hydration.* 2016.
22. Resch-Genger, U. and K. Rurack, *Determination of the photoluminescence quantum yield of dilute dye solutions (IUPAC Technical Report).* Pure applied chemistry, 2013. **85**(10): p. 2005-2013.
23. Gustavsson, T. and D. Markovitsi, *Fundamentals of the intrinsic DNA fluorescence.* Accounts of Chemical Research, 2021. **54**(5): p. 1226-1235.
24. Liske, A., et al., *Cu–F interactions between cationic linear N-heterocyclic carbene copper (I) pyridine complexes and their counterions greatly enhance blue luminescence efficiency.* Inorganic chemistry, 2019. **58**(9): p. 5433-5445.

25. Hilaire, M.R., et al., *Solvent dependence of cyanoindole fluorescence lifetime.* Chemical physics letters, 2017. **685**: p. 133-138.
26. Abou-Hatab, S. and S. Matsika, *Theoretical investigation of positional substitution and solvent effects on n-cyanoindole fluorescent probes.* The Journal of Physical Chemistry B, 2019. **123**(34): p. 7424-7435.
27. Jablonski, A., *Efficiency of anti-Stokes fluorescence in dyes.* Nature, 1933. **131**(3319): p. 839-840.
28. Parson, W.W., *Modern optical spectroscopy*. Vol. 2. 2007: Springer.
29. Reiffers, A., *Zeitaufgelöste Spektroskopie zur Photophysik und Photochemie von Phthalimiden.* PhD thesis, Heinrich-Heine-Universität Düsseldorf, 2020.
30. Kasha, M., *Characterization of electronic transitions in complex molecules.* Discussions of the Faraday society, 1950. **9**: p. 14-19.
31. Marian, C.M., *Understanding and controlling intersystem crossing in molecules.* Annual review of physical chemistry, 2021. **72**(1): p. 617-640.
32. Ermolaev, V.L., *Ultrafast nonradiative transitions between higher excited states in organic molecules.* Russian Chemical Reviews, 2001. **70**(6): p. 471-490.
33. Itoh, T., *Fluorescence and phosphorescence from higher excited states of organic molecules.* Chemical reviews, 2012. **112**(8): p. 4541-4568.
34. Maciejewski, A., et al., *Radiationless decay of the second excited singlet states of aromatic thiones: experimental verification of the energy gap law.* Chemical physics, 1984. **87**(2): p. 295-303.
35. Klán, P. and J. Wirz, *Photochemistry of organic compounds: from concepts to practice*. 2009: John Wiley & Sons.
36. Turro, N., et al., *The effect of wavelength on organic photoreactions in solution. Reactions from upper excited states.* Chemical Reviews, 1978. **78**(2): p. 125-145.
37. Franck, J. and E. Dymond, *Elementary processes of photochemical reactions.* Transactions of the Faraday Society, 1926. **21**(February): p. 536-542.
38. Condon, E., *A theory of intensity distribution in band systems.* Physical Review, 1926. **28**(6): p. 1182.
39. Einstein, A., *Zur quantenmechanik der strahlung.* Physikalische Zeitschrift, 1917. **18**: p. 121-128.
40. Lewis, G.N. and M. Kasha, *Phosphorescence in fluid media and the reverse process of singlet-triplet absorption.* Journal of the American Chemical Society, 1945. **67**(6): p. 994-1003.
41. Förster, T., *Fluoreszenz organischer Verbindungen (G. Kortüm).* Zeitschrift Naturforschung Teil A, 1951. **6**: p. 470.
42. Strickler, S. and R.A. Berg, *Relationship between absorption intensity and fluorescence lifetime of molecules.* The Journal of chemical physics, 1962. **37**(4): p. 814-822.
43. Birks, J.B. and D. Dyson, *The relations between the fluorescence and absorption properties of organic molecules.* Proceedings of the Royal Society of London. Series A. Mathematical Physical Sciences, 1963. **275**(1360): p. 135-148.
44. Ross, R.T., *Radiative lifetime and thermodynamic potential of excited states.* Photochemistry Photobiology, 1975. **21**(6): p. 401-406.
45. Eftink, M.R., *The use of fluorescence methods to monitor unfolding transitions in proteins.* Biophysical journal, 1994. **66**(2): p. 482-501.
46. Klonis, N., et al., *Spectral properties of fluorescein in solvent-water mixtures: applications as a probe of hydrogen bonding environments in biological systems.* Photochemistry photobiology, 1998. **67**(5): p. 500-510.
47. Hawe, A., M. Sutter, and W. Jiskoot, *Extrinsic fluorescent dyes as tools for protein characterization.* Pharmaceutical research, 2008. **25**: p. 1487-1499.
48. Harano, Y., *Application of hydration thermodynamics to the evaluation of protein structures and protein-ligand binding.* Entropy, 2012. **14**(8): p. 1443-1468.
49. Klymchenko, A.S., *Solvatochromic and fluorogenic dyes as environment-sensitive probes: design and biological applications.* Accounts of chemical research, 2017. **50**(2): p. 366-375.
50. Chen, Y. and M.D. Barkley, *Toward understanding tryptophan fluorescence in proteins.* Biochemistry, 1998. **37**(28): p. 9976-9982.

51. Lotte, K., R. Plessow, and A. Brockhinke, *Static and time-resolved fluorescence investigations of tryptophan analogues–a solvent study.* Photochemical Photobiological Sciences, 2004. **3**: p. 348-359.
52. Ghisaidoobe, A.B. and S.J. Chung, *Intrinsic tryptophan fluorescence in the detection and analysis of proteins: a focus on Förster resonance energy transfer techniques.* International journal of molecular sciences, 2014. **15**(12): p. 22518-22538.
53. Pandit, S.K. and G. Das, *Fluorescent detection of Tryptophan in Physiological media: Potential Applications in Environmental Samples and Living Systems.* Sensors Actuators B: Chemical, 2024: p. 136131.
54. Albani, J., *Origin of tryptophan fluorescence lifetimes part 1. Fluorescence lifetimes origin of tryptophan free in solution.* Journal of fluorescence, 2014. **24**: p. 93-104.
55. Gudgin, E., R. Lopez-Delgado, and W.R. Ware, *The tryptophan fluorescence lifetime puzzle. A study of decay times in aqueous solution as a function of pH and buffer composition.* Canadian Journal of Chemistry, 1981. **59**(7): p. 1037-1044.
56. Petrich, J., et al., *On the origin of nonexponential fluorescence decay in tryptophan and its derivatives.* Journal of the American Chemical Society, 1983. **105**(12): p. 3824-3832.
57. Adams, P.D., et al., *Intramolecular quenching of tryptophan fluorescence by the peptide bond in cyclic hexapeptides.* Journal of the American Chemical Society, 2002. **124**(31): p. 9278-9286.
58. Guharay, J. and P.K. Sengupta, *Characterization of the fluorescence emission properties of 7-azatryptophan in reverse micellar environments.* Biochemical biophysical research communications, 1996. **219**(2): p. 388-392.
59. Wong, C.Y. and M.R. Eftink, *Biosynthetic incorporation of tryptophan analogues into staphylococcal nuclease: Effect of 5-hydroxytryptophan and 7-azatryptophan on structure and stability.* Protein science, 1997. **6**(3): p. 689-697.
60. Broos, J., F. Maddalena, and B.H. Hesp, *In vivo synthesized proteins with monoexponential fluorescence decay kinetics.* Journal of the American Chemical Society, 2004. **126**(1): p. 22-23.
61. Xu, J., et al., *Picosecond fluorescence dynamics of tryptophan and 5-fluorotryptophan in monellin: slow water–protein relaxation unmasked.* The Journal of Physical Chemistry B, 2015. **119**(11): p. 4230-4239.
62. Talukder, P., et al., *Cyanotryptophans as novel fluorescent probes for studying protein conformational changes and DNA–protein interaction.* Biochemistry, 2015. **54**(51): p. 7457-7469.
63. Feitelson, J., E. Hayon, and A. Treinin, *Photoionization of phenols in water. Effects of light intensity, oxygen, pH, and temperature.* Journal of the American Chemical Society, 1973. **95**(4): p. 1025-1029.
64. Laws, W.R. and L. Brand, *Analysis of two-state excited-state reactions. The fluorescence decay of 2-naphthol.* Journal of Physical Chemistry, 1979. **83**(7): p. 795-802.
65. Harris, C.M. and B.K. Selinger, *Acid-base properties of 1-naphthol. Proton-induced fluorescence quenching.* The Journal of Physical Chemistry, 1980. **84**(11): p. 1366-1371.
66. Bardez, E., E. Monnier, and B. Valeur, *Dynamics of excited-state reactions in reversed micelles. 2. Proton transfer involving various fluorescent probes according to their sites of solubilization.* The Journal of Physical Chemistry, 1985. **89**(23): p. 5031-5036.
67. Marciniak, B., H. Kozubek, and S. Paszyc, *Estimation of pKa* in the first excited singlet state. A physical chemistry experiment that explores acid-base properties in the excited state.* Journal of chemical education, 1992. **69**(3): p. 247.
68. Mandal, D., S.K. Pal, and K. Bhattacharyya, *Excited-state proton transfer of 1-naphthol in micelles.* The Journal of Physical Chemistry A, 1998. **102**(48): p. 9710-9714.
69. Beens, H., et al., *Effect of solvent and temperature on proton transfer reactions of excited molecules.* Discussions of the Faraday Society, 1965. **39**: p. 183-193.
70. Yu, H.T., et al., *Fluorescence quenching in indoles by excited-state proton transfer.* Journal of the American Chemical Society, 1992. **114**(22): p. 8449-8454.
71. Chen, Y., B. Liu, and M.D. Barkley, *Trifluoroethanol quenches indole fluorescence by excited-state proton transfer.* Journal of the American Chemical Society, 1995. **117**(20): p. 5608-5609.

72. Pigliucci, A., et al., *Investigation of the Influence of Solute− Solvent Interactions on the Vibrational Energy Relaxation Dynamics of Large Molecules in Liquids.* The Journal of Physical Chemistry A, 2007. **111**(28): p. 6135-6145.
73. Bagchi, B. and B. Jana, *Solvation dynamics in dipolar liquids.* Chemical Society Reviews, 2010. **39**(6): p. 1936-1954.
74. Teale, F. and G. Weber, *Ultraviolet fluorescence of the aromatic amino acids.* Biochemical Journal, 1957. **65**(3): p. 476.
75. Zhu, X., et al., *Anti-Stokes shift luminescent materials for bio-applications.* Chemical Society Reviews, 2017. **46**(4): p. 1025-1039.
76. Abeywickrama, C.S., *Large Stokes shift benzothiazolium cyanine dyes with improved intramolecular charge transfer (ICT) for cell imaging applications.* Chemical Communications, 2022. **58**(71): p. 9855-9869.
77. Rulliere, C., *Femtosecond laser pulses*. 2005: Springer.
78. Arzhantsev, S. and M. Maroncelli, *Design and characterization of a femtosecond fluorescence spectrometer based on optical Kerr gating.* Applied spectroscopy, 2005. **59**(2): p. 206-220.
79. Boyd, R.W., A.L. Gaeta, and E. Giese, *Nonlinear optics*, in *Springer Handbook of Atomic, Molecular, and Optical Physics*. 2008, Springer. p. 1097-1110.
80. Duguay, M. and J.-W. Hansen, *An ultrafast light gate.* Applied physics letters, 1969. **15**(6): p. 192-194.
81. Duguay, M. and J. Hansen, *Direct measurement of picosecond lifetimes.* Optics Communications, 1969. **1**(5): p. 254-256.
82. Trebino, R. and D.J. Kane, *Using phase retrieval to measure the intensity and phase of ultrashort pulses: frequency-resolved optical gating.* JOSA A, 1993. **10**(5): p. 1101-1111.
83. Wang, L., P.P. Ho, and R. Alfano, *Time-resolved Fourier spectrum and imaging in highly scattering media.* Applied optics, 1993. **32**(26): p. 5043-5048.
84. Matousek, P., et al., *Efficient rejection of fluorescence from Raman spectra using picosecond Kerr gating.* Applied Spectroscopy, 1999. **53**(12): p. 1485-1489.
85. Takeda, J., et al., *Time-resolved luminescence spectroscopy by the optical Kerr-gate method applicable to ultrafast relaxation processes.* Physical Review B, 2000. **62**(15): p. 10083.
86. Kinoshita, S., et al., *Efficient optical Kerr shutter for femtosecond time-resolved luminescence spectroscopy.* Review of Scientific Instruments, 2000. **71**(9): p. 3317-3322.
87. Kanematsu, Y., et al., *Femtosecond optical Kerr-gate measurement of fluorescence spectra of dye solutions.* Journal of luminescence, 2000. **87**: p. 917-919.
88. Nakamura, R. and Y. Kanematsu, *A simple and effective method for femtosecond spectral snapshots.* Journal of luminescence, 2001. **94**: p. 559-563.
89. Schmidt, B., et al., *A broadband Kerr shutter for femtosecond fluorescence spectroscopy.* Applied Physics B, 2003. **76**: p. 809-814.
90. Rentzepis, P., et al., *Picosecond emission spectroscopy of homogeneously broadened, electronically excited molecular states.* Physical Review Letters, 1970. **25**(26): p. 1742.
91. Albrecht, H.-S., et al., *Measurement of ultraviolet femtosecond pulses using the optical Kerr effect.* Applied Physics B, 1992. **55**: p. 362-364.
92. Mundt, R., *Femtosekunden-Fluoreszenzspektroskopie an kurzlebigen UV-Chromophoren.* PhD thesis, Heinrich-Heine-Universität Düsseldorf, 2016.
93. Sheik-Bahae, M., D.J. Hagan, and E.W. Van Stryland, *Dispersion and band-gap scaling of the electronic Kerr effect in solids associated with two-photon absorption.* Physical review letters, 1990. **65**(1): p. 96.
94. Mundt, R., et al., *Thioxanthone in apolar solvents: ultrafast internal conversion precedes fast intersystem crossing.* Physical Chemistry Chemical Physics, 2016. **18**(9): p. 6637-6647.
95. Planck, M., *On the law of distribution of energy in the normal spectrum.* Annalen der physik, 1901. **4**(553): p. 1.
96. Serway, R., C. Moses, and C. Moyer, *Modern Physics. Brooks*. 2004, Cole Publishing Company.
97. Tsang, T.Y., *Optical third-harmonic generation at interfaces.* Physical Review A, 1995. **52**(5): p. 4116.
98. Malitson, I.H., *Interspecimen comparison of the refractive index of fused silica.* Josa, 1965. **55**(10): p. 1205-1209.

99. Rheims, J., J. Köser, and T. Wriedt, *Refractive-index measurements in the near-IR using an Abbe refractometer.* Measurement Science Technology, 1997. **8**(6): p. 601.
100. Nolden, O., *Time-Resolved Spectroscopy on Copper(I) Carbene Complexes.* PhD thesis, Heinrich-Heine-Universität Düsseldorf, 2023.
101. Ye, T.-Q., et al., *Development of an ultrafast laser apparatus for time-resolved UV-visible and infrared spectroscopy.* Applied spectroscopy, 1996. **50**(5): p. 597-607.
102. Jeoung, S.C., et al., *Ultrafast decay dynamics of photoexcited Cu (II)(TMpy-P4) in water solvent.* Chemical physics letters, 1999. **309**(5-6): p. 369-376.
103. Villnow, T.T., *Schnelle Interkombination aromatischer Carbonylverbindungen am Beispiel von Thioxanthon und Anthrachinon.* PhD thesis, Heinrich-Heine-Universität Düsseldorf, 2015.
104. Nolden, O., et al., *Femtosecond spectroscopy and quantum chemistry of a linearly coordinated copper (I) carbene complex.* ChemPhotoChem, 2023. **7**(4): p. e202200231.
105. Satzger, H. and W. Zinth, *Visualization of transient absorption dynamics–towards a qualitative view of complex reaction kinetics.* Chemical Physics, 2003. **295**(3): p. 287-295.
106. Johnson, P.J., V.I. Prokhorenko, and R.D. Miller, *Stable UV to IR supercontinuum generation in calcium fluoride with conserved circular polarization states.* Optics Express, 2009. **17**(24): p. 21488-21496.
107. Braslavsky, S., *Glossary of terms used in photochemistry, (IUPAC Recommendations 2006).* Pure Applied Chemistry, 2007. **79**(3): p. 293-465.
108. Stryer, L., *Fluorescence energy transfer as a spectroscopic ruler.* Annual review of biochemistry, 1978. **47**(1): p. 819-846.
109. Lerner, E., et al., *Toward dynamic structural biology: Two decades of single-molecule Förster resonance energy transfer.* Science, 2018. **359**(6373): p. eaan1133.
110. Demasa, J. and G. Crosby, *The measurement of photoluminescence quantum yields. 1 A Review2.* J. Chem. Phys, 1968. **48**: p. 4726.
111. Stephen, W., *CA Parker, Photoluminescence of solutions. Elsevier Publishing Company, Amsterdam, 1968.* Analytica Chimica Acta, 1969. **44**(1): p. 247-247.
112. Vavilov, S., *The fluorescence efficiency of dye solutions.* Z Phys, 1924. **22**: p. 266-272.
113. Parker, C.A. and W. Rees, *Correction of fluorescence spectra and measurement of fluorescence quantum efficiency.* Analyst, 1960. **85**(1013): p. 587-600.
114. Melhuish, W., *The measurement of absolute quantum efficiencies of fluorescence.* New Zealand J. Sci. Technol, 1955. **37**: p. 142.
115. Hall, L., T. Hunter, and M. Stock, *Absolute fluorescence quantum yields for vapour-phase benzene and naphthalene, and comments on the non-radiative processes.* Chemical Physics Letters, 1976. **44**(1): p. 145-149.
116. Rockley, M.G., *Simple, new technique for measurement of fluorescence quantum yields: Application to benzene vapor.* Chemical Physics Letters, 1977. **50**(3): p. 427-430.
117. Sonnenschein, M., A. Amirav, and J. Jortner, *Absolute fluorescence quantum yields of large molecules in supersonic expansions.* The Journal of Physical Chemistry, 1984. **88**(19): p. 4214-4218.
118. Ateşl, S. and A. Yildiz, *Determination of the absolute quantum efficiency of the luminescence of crystalline anthracene and of meso–dimeso derivatives using photoacoustic spectroscopy.* Journal of the Chemical Society, Faraday Transactions 1: Physical Chemistry in Condensed Phases, 1983. **79**(12): p. 2853-2861.
119. Alimarin, I., V. Durnev, and V. Runov, *DETERMINATION OF LUMINESCENCE QUANTUM YIELDS OF SORBED COMPOUNDS BY PHOTOACOUSTIC-SPECTROSCOPY.* TEORETICHESKAYA I EKSPERIMENTALNAYA KHIMIYA, 1987. **23**(6): p. 705-711.
120. VieiraáFerreira, L.F. and M. áRosßrio Freixo, *Photochemistry on surfaces: fluorescence emission quantum yield evaluation of dyes adsorbed on microcrystalline cellulose.* Journal of the Chemical Society, Faraday Transactions, 1992. **88**(1): p. 15-22.
121. Haynes, D., A. Tokmakoff, and S. George, *Temperature-dependent absolute fluorescence quantum yield of C60 multilayers.* Chemical physics letters, 1993. **214**(1): p. 50-56.
122. Mirenda, M., M.G. Lagorio, and E. San Román, *Photophysics on surfaces: determination of absolute fluorescence quantum yields from reflectance spectra.* Langmuir, 2004. **20**(9): p. 3690-3697.

123. BRODY, M. and S.S. BRODY, *Internal fluorescence standards for light scattering biological material.* Photochemistry Photobiology, 1971. **13**(3): p. 293-297.
124. Kurian, E., F.G. Prendergast, and J.R. Small, *Photoacoustic analysis of proteins: volumetric signals and fluorescence quantum yields.* Biophysical journal, 1997. **73**(1): p. 466-476.
125. Rurack, K., *Fluorescence quantum yields: methods of determination and standards.* Standardization quality assurance in fluorescence measurements I: techniques, 2008: p. 101-145.
126. Würth, C., et al., *Relative and absolute determination of fluorescence quantum yields of transparent samples.* Nature protocols, 2013. **8**(8): p. 1535-1550.
127. Mardelli, M. and J. Olmsted III, *Calorimetric determination of the 9, 10-diphenyl-anthracene fluorescence quantum yield.* Journal of Photochemistry, 1977. **7**(4): p. 277-285.
128. Olmsted, J., *Calorimetric determinations of absolute fluorescence quantum yields.* Journal of Physical Chemistry, 1979. **83**(20): p. 2581-2584.
129. Bindhu, C. and S. Harilal, *Effect of the excitation source on the quantum-yield measurements of rhodamine B laser dye studied using thermal-lens technique.* Analytical Sciences, 2001. **17**(1): p. 141-144.
130. Estupiñán-López, C., C.T. Dominguez, and R. De Araujo, *Eclipsing thermal lens spectroscopy for fluorescence quantum yield measurement.* Optics express, 2013. **21**(15): p. 18592-18601.
131. Estupiñán-López, C., et al., *Quantum dots fluorescence quantum yield measured by thermal lens spectroscopy.* Quantum Dots: Applications in Biology, 2014: p. 93-101.
132. Simonelli, C., et al., *Realization of a high power optical trapping setup free from thermal lensing effects.* Optics Express, 2019. **27**(19): p. 27215-27228.
133. Vargas-Vargas, A., et al., *Dual beam transient thermal lens spectroscopy with high repetition pulsed IR-Laser Excitation: Photothermal and fluorescence quantum yields determination.* Infrared Physics Technology, 2023. **129**: p. 104561.
134. Brannon, J.H. and D. Magde, *Absolute quantum yield determination by thermal blooming. Fluorescein.* The Journal of Physical Chemistry, 1978. **82**(6): p. 705-709.
135. Magde, D., et al., *Absolute luminescence yield of cresyl violet. A standard for the red.* Journal of Physical Chemistry, 1979. **83**(6): p. 696-699.
136. de Mello, J.C., H.F. Wittmann, and R.H. Friend, *An improved experimental determination of external photoluminescence quantum efficiency.* Advanced materials, 1997. **9**(3): p. 230-232.
137. Greenham, N., et al., *Measurement of absolute photoluminescence quantum efficiencies in conjugated polymers.* Chemical physics letters, 1995. **241**(1-2): p. 89-96.
138. Fries, F. and S. Reineke, *Statistical treatment of photoluminescence quantum yield measurements.* Scientific reports, 2019. **9**(1): p. 15638.
139. Gaigalas, A.K. and L. Wang, *Measurement of the fluorescence quantum yield using a spectrometer with an integrating sphere detector.* Journal of Research of the National Institute of Standards Technology, 2008. **113**(1): p. 17.
140. Würth, C., et al., *Evaluation of a commercial integrating sphere setup for the determination of absolute photoluminescence quantum yields of dilute dye solutions.* Applied spectroscopy, 2010. **64**(7): p. 733-741.
141. Leyre, S., et al., *Absolute determination of photoluminescence quantum efficiency using an integrating sphere setup.* Review of scientific instruments, 2014. **85**(12).
142. Cheknlyuk, A., et al., *Determination of fluorescence quantum yields using a spontaneous Raman scattering line of the solvent as internal standard.* Spectroscopy Letters, 1982. **15**(5): p. 355-365.
143. Sivaprakasam, V. and D.K. Killinger, *Effect of polarization and geometric factors on quantitative laser-induced fluorescence-to-Raman intensity ratios of water samples and a new calibration technique.* JOSA B, 2003. **20**(9): p. 1980-1989.
144. Levitus, M., *Tutorial: measurement of fluorescence spectra and determination of relative fluorescence quantum yields of transparent samples.* Methods applications in fluorescence, 2020. **8**(3): p. 033001.
145. Brouwer, A.M., *Standards for photoluminescence quantum yield measurements in solution (IUPAC Technical Report).* Pure Applied Chemistry, 2011. **83**(12): p. 2213-2228.
146. Montalti, M., et al., *Handbook of photochemistry*. 2006: CRC press.

147. Morshedi, M., et al., *References for Small Fluorescence Quantum Yields.* Journal of Fluorescence, 2024: p. 1-14.
148. Deaton, J.C., et al., *E-type delayed fluorescence of a phosphine-supported Cu2 (μ-NAr2) 2 diamond core: harvesting singlet and triplet excitons in OLEDs.* Journal of the American Chemical Society, 2010. **132**(27): p. 9499-9508.
149. Hashimoto, M., et al., *Highly efficient green organic light-emitting diodes containing luminescent three-coordinate copper (I) complexes.* Journal of the American Chemical Society, 2011. **133**(27): p. 10348-10351.
150. Wada, A., et al., *Efficient luminescence from a copper (i) complex doped in organic light-emitting diodes by suppressing C–H vibrational quenching.* Chemical Communications, 2012. **48**(43): p. 5340-5342.
151. Wei, F., et al., *Efficient nondoped organic light-emitting diodes with CuI complex emitter.* Organic Electronics, 2014. **15**(11): p. 3292-3297.
152. Szudy, J., *Born 100 Years Ago: Aleksander Jablonski (1898-1980).* EPA NEWSLETTER-EUROPEAN PHOTOCHEMISTRY ASSOCIATION, 1997: p. 4-11.
153. Steiner, R.F., *Fluorescence anisotropy: theory and applications*, in *Topics in fluorescence spectroscopy: Principles*. 1991, Springer. p. 1-52.
154. González Flecha, F.L. and V. Levi, *Determination of the molecular size of BSA by fluorescence anisotropy.* Biochemistry molecular biology education, 2003. **31**(5): p. 319-322.
155. Bucci, E. and R.F. Steiner, *Anisotropy decay of fluorescence as an experimental approach to protein dynamics.* Biophysical chemistry, 1988. **30**(3): p. 199-224.
156. Gradinaru, C.C., et al., *Fluorescence anisotropy: from single molecules to live cells.* Analyst, 2010. **135**(3): p. 452-459.
157. LiCata, V.J. and A.J. Wowor, *Applications of fluorescence anisotropy to the study of protein–DNA interactions.* Methods in cell biology, 2008. **84**: p. 243-262.
158. Gijsbers, A., T. Nishigaki, and N. Sánchez-Puig, *Fluorescence anisotropy as a tool to study protein-protein interactions.* JoVE, 2016(116): p. e54640.
159. Barbero, N., et al., *Fluorescence anisotropy analysis of protein–antibody interaction.* Dyes pigments, 2009. **83**(2): p. 225-229.
160. Chullipalliyalil, K., et al., *In-vial detection of protein denaturation using intrinsic fluorescence anisotropy.* Analytical Chemistry, 2023. **95**(5): p. 2774-2782.
161. Dandliker, W., et al., *Fluorescence polarization immunoassay. Theory and experimental method.* Immunochemistry, 1973. **10**(4): p. 219-227.
162. Hicks, J., *Fluorescence immunoassay.* Human pathology, 1984. **15**(2): p. 112-116.
163. Mazzeo, B.A. and D.D. Busath, *From molecular dynamics to fluorescence anisotropy of fluorophores bound to oriented structures.* Journal of Computational Physics, 2013. **232**(1): p. 482-497.
164. Lakowicz, J., *Fluorescence spectroscopic investigations of the dynamic properties of biological membranes*, in *Spectroscopy in biochemistry*. 2018, CRC Press. p. 195-245.
165. Khonina, S.N. and I. Golub, *Optimization of focusing of linearly polarized light.* Optics Letters, 2011. **36**(3): p. 352-354.
166. Atkins, P.W. and R.S. Friedman, *Molecular quantum mechanics*. 2011: Oxford University Press, USA.
167. Gustavsson, T., et al., *Rotational diffusion of the 7-diethylamino-4-methylcoumarin C1 dye molecule in polar protic and aprotic solvents.* Photochemical Photobiological Sciences, 2003. **2**(3): p. 329-341.
168. Kim, Y., et al., *Direct measurements of energy transfer between identical chromophores in solution.* The Journal of chemical physics, 1989. **91**(12): p. 7557-7562.
169. Andrews, D.L. and G. Juzeliūnas, *The range dependence of fluorescence anisotropy in molecular energy transfer.* The Journal of chemical physics, 1991. **95**(8): p. 5513-5518.
170. Yeow, E.K., et al., *The dynamics of electronic energy transfer in novel multiporphyrin functionalized dendrimers: a time-resolved fluorescence anisotropy study.* The Journal of Physical Chemistry B, 2000. **104**(12): p. 2596-2606.
171. Valeur, B. and G. Weber, *Resolution of the fluorescence excitation spectrum of indole into the 1La and 1Lb excitation bands.* Photochemistry Photobiology, 1977. **25**(5): p. 441-444.

172. Michl, J. and E.W. Thulstrup, *Spectroscopy with polarized light: solute alignment by photoselection in liquid crystals, polymers and membranes*, in *Liquid crystals, polymers, and membranes*. 1995, VCH publishers.
173. Mullaney, J.M., et al., *Green fluorescent protein as a probe of rotational mobility within bacteriophage T4.* Journal of virological methods, 2000. **88**(1): p. 35-40.
174. Weber, G., *Fluorescence-polarization spectrum and electronic-energy transfer in tyrosine, tryptophan and related compounds.* Biochemical Journal, 1960. **75**(2): p. 335.
175. Yamamoto, Y. and J. Tanaka, *Polarized absorption spectra of crystals of indole and its related compounds.* Bulletin of the Chemical Society of Japan, 1972. **45**(5): p. 1362-1366.
176. Shen, X. and J.R. Knutson, *Femtosecond internal conversion and reorientation of 5-methoxyindole in hexadecane.* Chemical physics letters, 2001. **339**(3-4): p. 191-196.
177. Morshedi, M., et al., *The photophysics of 2-cyanoindole probed by femtosecond spectroscopy.* Photochemical Photobiological Sciences, 2023. **22**(4): p. 745-759.

5. Publications in Peer-Reviewed Journals

5.1. Femtosecond Spectroscopy and Quantum Chemistry of a Linearly Coordinated Copper(I) Carbene Complex (Publication I)

Title: Femtosecond Spectroscopy and Quantum Chemistry of a Linearly Coordinated Copper(I) Carbene Complex

Authors: Oliver Nolden, Jennifer Kremper, Wiebke Haselbach, Mahbobeh Morshedi, Jasper Guhl, Philipp Schmeinck, Christel M. Marian, Christian Ganter, Peter Gilch

Published in: ChemPhotoChem

Year: 2022

Impact Factor: 3 (2023)

My Contributions to the Publication:

- acquisition of steady state fluorescence spectra of the complex and the ligand with the fluorescence Kerr gate setup

ChemPhotoChem

Research Articles
doi.org/10.1002/cptc.202200231

Chemistry Europe
European Chemical Societies Publishing

www.chemphotochem.org

Special Collection

Femtosecond Spectroscopy and Quantum Chemistry of a Linearly Coordinated Copper(I) Carbene Complex

Oliver Nolden,[a] Jennifer Kremper,[a] Wiebke Haselbach,[a] Mahbobeh Morshedi,[a] Jasper Guhl,[b] Philipp Schmeinck,[c] Christel M. Marian,*[b] Christian Ganter,*[c] and Peter Gilch*[a]

Linearly coordinated copper(I) carbene complexes, such as [1,3-bis(2,6-diisopropylphenyl)imidazol-2-ylidene]-(2-picoline)copper(I) tetrafluoroborate (**1**), exhibit promising photophysical properties with regard to organic light emitting diode (OLED) applications. Their emission characteristics strongly depend on the surrounding (crystal, matrix, and solution). Here, the behavior of **1** in solution is scrutinized by steady state as well as femtosecond spectroscopy. In coordinating solvents, like acetonitrile and alcohols, **1** is shown to bind solvent molecules as ligands. In non-coordinating solvents, femtosecond UV/Vis absorption spectroscopy reveals a tri-exponential decay with time constants of 0.3 ps, 900 ps, and 0.7 μs. The time constants are assigned with the aid of quantum chemistry. A more complex decay is observed in coordinating solvents.

Introduction

Copper(I) complexes might provide a cheap and more earth abundant alternative for existing emitters for organic light emitting diodes (OLED) based on iridium or platinum.[1] These heavy elements, due to strong spin-orbit coupling, provide high intersystem crossing (ISC) and phosphorescent rate constants with emission quantum yields up to unity.[2] Yet, they possess clear disadvantages compared to their copper(I) analogues. In addition to economic and ecological issues,[3] undesired non-radiative deactivation of iridium or platinum complexes may occur due to the d^6 or d^8 configurations of the respective ions.[4] In copper(I) complexes with their d^{10} configuration deactivating metal centered excitations are absent. Therefore, copper(I) complexes are presently intensively investigated with regard to their application as second and third generation OLED emitters. Emitters of these generations make use of phosphorescence as well as thermally activated delayed fluorescence (TADF).[5]

For a systematic approach regarding the luminescent properties of copper(I) complexes, it is necessary to understand the elementary photophysical and photochemical processes that are involved. As for many transition metal complexes, these compounds show complicated excited state kinetics due to their high density of states and the ability for fast intersystem crossing.[6] These processes can only be traced by (ultrafast) time-resolved spectroscopy. While most copper(I) complexes being investigated are of trigonal or tetragonal geometry,[7] research on linearly coordinated complexes is still scarce. Within the class of linearly coordinated copper(I) complexes a focus was laid on those bearing N-heterocyclic carbene ligands.[7–8]

In a recent study by some of the present authors, the luminescence of a linearly coordinated copper(I) complex bearing an N-heterocyclic carbene (NHC) ligand (1,3-bis(2,6-diisopropylphenyl)imidazol-2-ylidene) as a σ-donor and 2-picoline as a π-acceptor ligand (compound **1**, Scheme 1) was investigated.[9] This complex caught our attention since as a powder and in poly(methyl methacrylate) (PMMA) matrix it

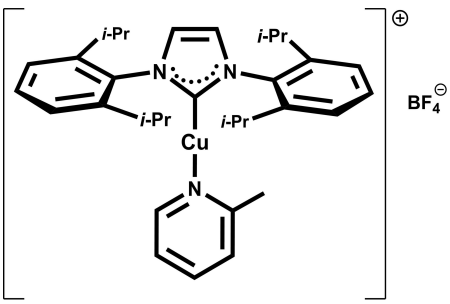

Scheme 1. Structure of complex **1**.

[a] O. Nolden, J. Kremper, W. Haselbach, M. Morshedi, Prof. Dr. P. Gilch
Institut für Physikalische Chemie
Heinrich-Heine-Universität Düsseldorf,
Universitätsstr. 1, 40225 Düsseldorf, Germany
E-mail: Gilch@hhu.de
[b] J. Guhl, Prof. Dr. C. M. Marian
Institut für Theoretische Chemie und Computerchemie
Heinrich-Heine-Universität Düsseldorf,
Universitätsstr. 1, 40225 Düsseldorf, Germany
E-mail: Christel.Marian@hhu.de
[c] P. Schmeinck, Prof. Dr. C. Ganter
Institut für Anorganische Chemie und Strukturchemie
Heinrich-Heine-Universität Düsseldorf,
Universitätsstr. 1, 40225 Düsseldorf, Germany
E-mail: Christian.Ganter@hhu.de

Supporting information for this article is available on the WWW under https://doi.org/10.1002/cptc.202200231

Special Collection An invited contribution to a Special Collection on Emissive Materials for Organic Light Emitting Diodes

exhibits emission quantum yields as high as 0.87. In single crystals and solutions of the compound, the yields are orders of magnitudes smaller. Quantum chemical computations attribute this to the presence (luminescence) or absence (no luminescence) of the coordinating counterion BF_4^-.[10] In the complex with coordinated BF_4^-, the lowest excited state is an emissive state with metal-to-ligand charge-transfer (MLCT) character. In absence of BF_4^-, a dark locally excited triplet state is the lowest one. Heretofore, the excited state kinetics of the complex have only been traced in solid state. Here, we augment this by time-resolved spectroscopy in solution covering a time range of 100 fs to 10 μs.

As the complex **1** has the tendency to bind additional ligands and to connect with earlier experiments,[9] we intended to study **1** in the non-coordinating solvent dichloromethane (DCM). Yet, in femtosecond experiments on **1** dissolved in DCM and on neat DCM the formation of a white precipitation was observed. During screening for suitable solvents pronounced changes in the absorption spectrum of **1** in weakly coordinating solvents like acetonitrile (MeCN) and 2-propanol were observed. In the course of steady state and time-resolved UV/Vis experiments, further indications for the interaction of **1** with MeCN and 2-propanol were observed. Based on these experimental observations, two structures that might form in the presence of coordinating solvents are suggested and their spectral properties computed quantum chemically. To the best of our knowledge, no study has yet discussed the coordinating interaction of linearly coordinated copper(I) complexes with solvent molecules in depth. Therefore, the findings of this study constitute an important step towards elucidating the structural interactions of linearly coordinated complexes with a solvent environment. However, due to experimental and quantum chemical ambiguities we refrain from giving a distinct answer to which species is present. In 2,2,2-trifluoroethanol (TFE) the absorption signatures of **1** resembles the one in DCM. Therefore, for the characterization of **1** in non-coordinating surroundings TFE was used. Furthermore, emission spectroscopy was applied giving indications for coordinating interactions of the counterion with the copper center in non-coordinating solvents.

Materials and Methods

Samples and general conditions: 1 was synthesized according to a previously published protocol and completely characterized.[9] The purity of **1** was verified by ^{1}H-NMR, ^{13}C{1H}-NMR, ESI mass spectrometry and elemental analysis (see SI, Figure S1). The analytical data obtained agree well with the literature.[9] 2-Picoline, tetrabutylammonium tetrafluoroborate and tris(bipyridine)ruthenium(II) chloride were supplied by Sigma Aldrich, dichloromethane (Fisher Chemical, HPLC gradient grade), tetrahydrofurane (Sigma Aldrich, inhibitor free, >99.8%), 2,2,2-trifluorethanol (Apollo Scientific, >99%), acetonitrile (ChemSolute, HPLC gradient grade), 2-propanol (Sigma Aldrich, 99.9%) were used as solvents. If not mentioned otherwise all measurements were performed under argon or nitrogen atmosphere. All measurements were performed at room temperature (~20 °C).

Steady state spectroscopy: The UV/Vis absorption spectra were recorded with a two-beam Lambda 19 spectrometer from Perkin Elmer GmbH using standard 1-cm- or 1-mm-path-length fused silica cells. Unless otherwise noted the fluorescence was recorded in right-angle detection with a FluoroMax-4 from Horiba Scientific. The sample absorption at the excitation wavelength was ~0.05 for a path length of 1 cm to avoid inner filter effects. As references for the determination of the emission quantum yields thymidine in water ($\Phi_{lum} = 1.32 \cdot 10^{-4}$[11]) and tris(bipyridine)ruthenium(II) chloride in water ($\Phi_{lum,air} = 0.028$[12]) were employed. For the comparison of the emission of **1** and 2-picoline a fluorescence Kerr gate instrument as described in Ref. [13] was used. The instrument was operated with an open gate, i.e. steady state spectra were obtained. Samples were excited by 266 nm laser pulses obtained by frequency tripling of 800 nm femtosecond pulses. All emission spectra were corrected for the spectral sensitivities of the respective instruments. In order to convert the fluorescence spectra recorded with constant wavelength band pass into the wavenumber representation, intensities were multiplied by the respective wavelength squared.[14]

Femtosecond transient absorption spectroscopy: The femtosecond transient absorption (fsTA) setup has been described elsewhere in detail.[15] A 1 kHz Ti:Sa laser amplifier system (Coherent Libra) served as pulse source. The output wavelength is 800 nm and the pulse duration is 100 fs. To yield 266 nm pump pulses, the 800 nm laser output was frequency tripled using β-barium borate crystals. The pump pulse energy at the sample was adjusted to ~1 μJ and the beam had a focal diameter of 160 μm (full width at half maximum (FWHM)) on the sample. The absorption change was probed with a white light continuum generated in CaF_2 with a diameter of 100 μm on the sample. The relative polarization of the pump and probe beam was set to the magic angle. The time resolution was ~180 fs. The spectra were recorded at 139 time delay settings between −1 to 1 ps on a linear and from 1 ps to 3.4 ns on a logarithmic time scale. For every delay setting, 2000 spectra were recorded and the data were averaged over 4 succeeding delay scans. The instrumental shift of time zero with wavelength was determined via the optical Kerr effect and corrected for. To remove signal contributions of the solvent and to account for time-zero femtosecond artifacts, a separate measurement of the solvent was subtracted with proper scaling depending on the absorption of the sample solution.[16] The solution was pumped through a fused silica flow cell (custom made, Hellma Analytics) with 1 mm path length. The samples absorption at the excitation wavelength was set to 0.7 per mm.

Nanosecond transient absorption spectroscopy: The nanosecond transient absorption (nsTA) data were acquired with a laser flash photolysis spectrometer LP980 from Edinburgh Instruments in a right-angle geometry. The fourth harmonic (266 nm) of the output wavelength of a Nd:YAG laser (Spitlight 600, InnoLas) with a repetition rate of 5 Hz and a pulse duration of 12 ns (FWHM) was utilized for photoexcitation. The diameter of the pump beam was ~8 mm. The average pulse energy amounted to 2 mJ. A pulsed xenon lamp (Osram XBO 150 W/CR OFR) was used as a probe beam. The transmitted probe light was detected by a photomultiplier (Hamamatsu, PMT-900) after being dispersed by a grating monochromator. To obtain transient spectra, every 5 nm kinetic traces were recorded and averaged over 64 acquisitions. The solution was pumped through a fused silica flow cell (Hellma Analytics) with a path length of 5 mm in pump and 10 mm in probe direction. The samples absorption at the excitation wavelength was set to 1.6 per cm.

Data analysis: Wavelength and time dependent data were analyzed globally using a multi-exponential trial function convoluted with the instrumental response function (IRF, Eq. (1)):[17]

$$\Delta A(\lambda, t) = IRF \otimes \sum_{i=1}^{n} \Delta A_i(\lambda) \cdot e^{-\frac{t}{\tau_i}}. \quad (1)$$

The fit yields a decay associated difference spectrum (DADS) $\Delta A_i(\lambda)$ for each time constant τ_i.

Quantum chemical calculations: The optimized geometries were obtained from Kohn-Sham density functional theory (DFT) for the ground state, from time dependent-DFT (TD-DFT) for the singlet excited states and from the Tamm-Dancoff approximation (TDA-TDDFT) for triplet excited states. A PBE0 functional, the GD3 dispersion correction, and a def2-SV(P) basis set for all atoms as implemented in Gaussian were used.[18] The copper core was treated with a cc-pVDZ-PP basis set in conjunction with the Stuttgart-Köln MCDHF RSC ecp.[19] Solvent effects were accounted for with the standard IEF-PCM.[20] Its point charges were exported from Gaussian to Turbomole, to be used for the DFT/MRCI calculations.[21] The DFT/MRCI calculations used the optimized geometry, including the point charges, and employed the R2018 Hamiltonian,[22] the same basis, but the BH-LYP functional.[22–23] For the calculation of ISC rate constants in the Condon approximation, the spin-orbit coupling (SOC) matrix elements were calculated via SPOCK, and the vibrational overlap via VIBES.[24] Based on the computed oscillator strengths f_i, absorption coefficient spectra $\varepsilon_i(\tilde{\nu})$ were obtained. Herein, the relation between the spectral integral covering an electronic transition band and f_i according to Equation (2)[25] was employed.

$$f_i = \frac{4\varepsilon_0 m_e c_0^2}{e_0^2} \cdot \frac{\ln 10}{N_A} \int_0^\infty \varepsilon_i(\tilde{\nu}) d\tilde{\nu} \quad (2)$$

In the equation, ε_0 is the vacuum electric permittivity, m_e the electron mass, c_0 the speed of light in vacuum, e_0 the elementary charge, and N_A the Avogadro constant. The band $\varepsilon_i(\tilde{\nu})$ was modelled with a Gaussian. Its width (FWHM) was chosen to match approximately the experimental one.

Results

Steady state measurements

1 dissolved in DCM, TFE, MeCN and 2-propanol features an absorption band lowest in energy with a maximum around 260 nm (see Figure 1 and S3 in the supporting information (SI)). The band is strongly affected by the solvent. In DCM, the highest peak absorption coefficient (~18000 $M^{-1}cm^{-1}$) is recorded and the band is structureless. The spectrum of **1** in TFE resembles the one in DCM. For MeCN and 2-propanol as solvents, the absorption is blue-shifted compared to DCM. Furthermore, peak absorption coefficients are smaller and a vibrational progression becomes discernable. This progression is very similar to the one of the free 2-picoline ligand (see Figure 1a).

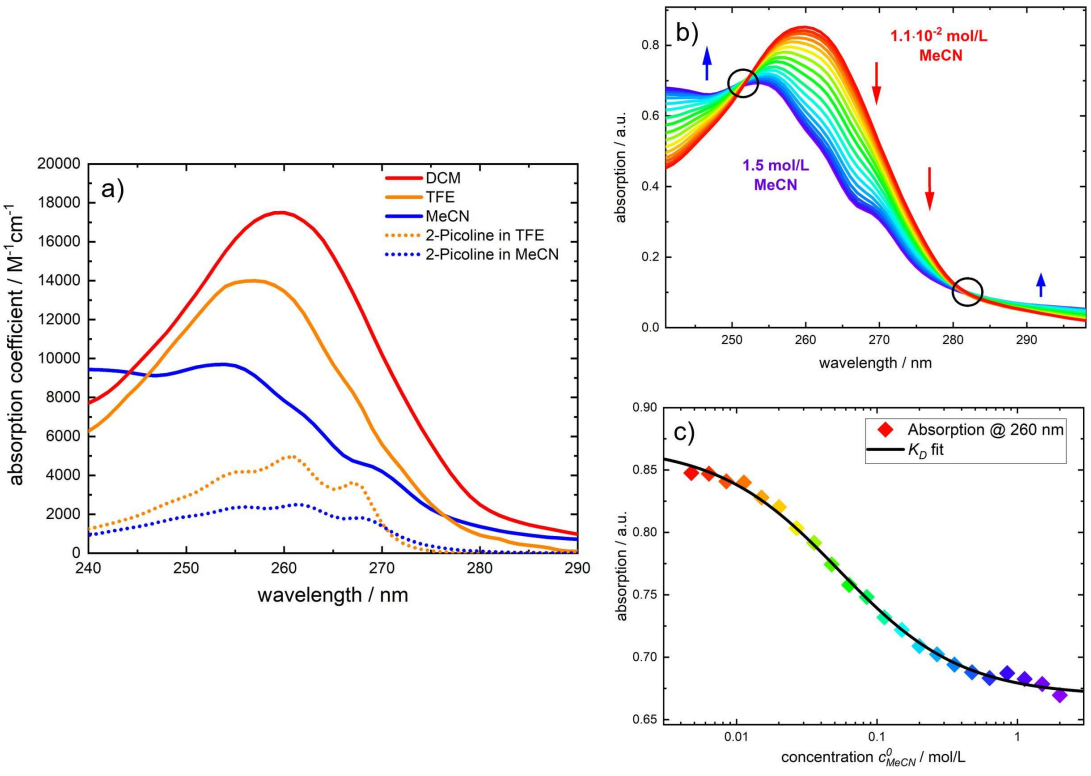

Figure 1. Absorption properties of **1** in different solvents. a) Absorption spectra (absorption coefficients as a function of wavelength) of **1** in DCM (red), TFE (orange), and MeCN (blue). The respective spectra of 2-picoline in TFE and MeCN (orange and blue dotted respectively) are shown for comparison. b) Impact of the addition of MeCN to absorption spectra of **1** dissolved in DCM. The initial concentration c_1^0 of **1** amounted to $5 \cdot 10^{-5}$ M and remains constant throughout the experiment. Initial MeCN concentrations c_{MeCN}^0 ranged from $0.8 \cdot 10^{-2}$ M (red) to 2 M (blue). Circles mark isosbestic points. c) Dependence of the absorption at 260 nm on the initial concentration of MeCN c_{MeCN}^0 (values from Figure 1b). The diamonds mark experimental values, the line a fit as described in the text based on eq 3–6.

These differences might originate from a "simple" solvatochromic effect or from a chemical reaction with the solvent (e.g. coordination). A titration experiment favors the latter interpretation (see Figure 1b). For very low MeCN concentration, the spectrum of **1** in DCM is recorded. Upon MeCN addition the absorption decreases between 255 nm and 280 nm and increases beyond that region. Clear isosbestic points are seen at 255 nm and 280 nm. Singular value decomposition shows that only two singular values are necessary to describe the behavior. This and the isosbestic points suggest an equilibrium of two species. To quantify the chemical equilibrium, a fit of the concentration dependence based on Equations (3–6) was performed. In this treatment, the addition of one equivalent of MeCN is assumed.

$$K_D = \frac{c_1 \cdot c_{MeCN}}{c_{1-MeCN}} \tag{3}$$

$$c_1 + c_{1-MeCN} = c_1^0 \tag{4}$$

$$c_{MeCN} + c_{1-MeCN} = c_{MeCN}^0 \tag{5}$$

$$A = (\varepsilon_{1-MeCN} \cdot c_{1-MeCN} + \varepsilon_1 \cdot c_1) \cdot d \tag{6}$$

In these equations, K_D is the dissociation constant of **1** coordinated by MeCN (**1**-MeCN). c_1, c_{MeCN}, and c_{1-MeCN} are the equilibrium concentrations of compound **1**, MeCN, and the complex **1**-MeCN, respectively. c_1^0 and c_{MeCN}^0 are the initial concentrations of **1** and MeCN (prior to equilibration). The absorption A depends on the concentrations c_1 and c_{1-MeCN} and the respective absorption coefficients ε_1 and ε_{1-MeCN} as well as the path length $d = 1$ cm. A fit based on these equations provides a good description of the experimental behavior at 260 nm (see Figure 1c). During this fit only two parameters were varied, namely the dissociation constant K_D and the absorption coefficient of **1**-MeCN. According to this fit, the dissociation constant K_D equals 0.05 ± 0.006 M and ε_{1-MeCN} equals 13415 ± 33 $M^{-1}cm^{-1}$. An analysis based on the assumption that **1** binds two equivalents of MeCN and releases one equivalent of 2-picoline was also performed (see Scheme 2 and SI, Figure S2 and Eq. S1–S4). The respective diagram reveals systematic deviations between experimental results and the fit. We, thus, favor the addition of one equivalent. Similar observations were made for a titration experiment using 2-propanol as a solvent for **1**. The titration experiment and respective fitting (based on one equivalent of 2-propanol) yields a K_D value of ~2 M (see SI, Figure S3). This indicates a less favored reaction of **1** with 2-propanol compared to MeCN.

The titration experiment shows that **1** and MeCN react to form a novel complex. Experiments with **1** and 2-picoline have revealed the tendency of **1** to transform into a trigonal complex with two ligands in addition to the NHC ligand.[9] In the present context, two MeCN molecules might coordinate (Scheme 2, structure **2a**) and replace the 2-picoline ligand. Alternatively, one MeCN molecule might additionally coordinate to the Cu atom in complex **1**, leading to the trigonal planar species **2b** (see Scheme 2). In order to better understand which species are present, we attempted to synthesize and investigate the bis-acetonitrile complex **2a** by performing the synthetic procedure for **1** without adding 2-picoline and replacing the solvent THF with MeCN. However, all attempts to obtain **2a** in analytically pure form failed due to its instability. In solution, it undergoes a rapid conversion to the bis(NHC) copper(I) tetrafluoroborate and presumably one equivalent of tetrakis(MeCN)-copper(I) tetrafluoroborate. The former one can be detected by ^{1}H-NMR-spectroscopy and ESI mass spectrometry (see SI, Figure S4). However, this finding indicates that **2a** cannot be present in significant concentrations in solution of **1** in MeCN, since its conversion products are not observed in those solutions. Based on this argument together with the results from the titration experiment (see Figure 1b), we assume that compound **2b** is the only other species present in solution of **1** in MeCN under the given conditions.

Also, the emission spectra of **1** are solvent dependent (see Figure 2). In MeCN it exhibits a maximum of emission around 350 nm while in the non-coordinating solvents the emission curves show a maximum around 500 nm in line with previous measurements of **1** in PMMA films.[9] Contrary to the measurement in PMMA in which the luminescence quantum yield is

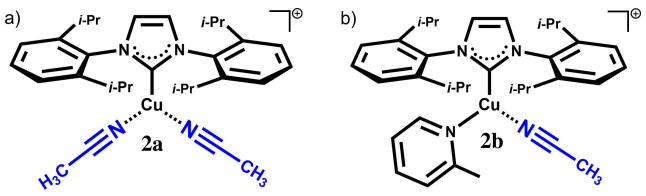

Scheme 2. Proposed structures of **1** in MeCN with a) two MeCN molecules replacing one 2-picoline (**2a**) b) one MeCN coordinating to **1** forming the trigonal complex **2b**.

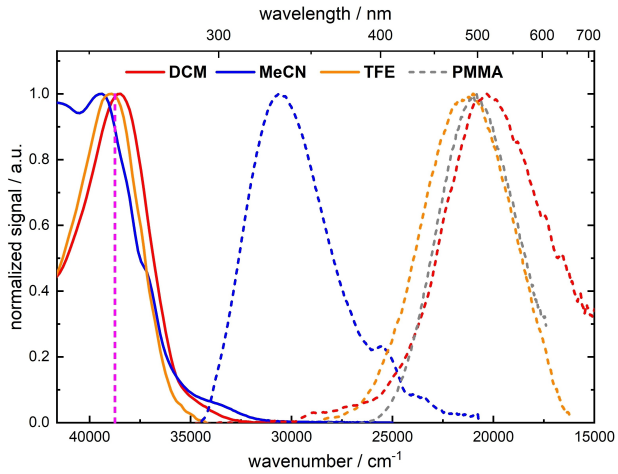

Figure 2. Emission spectroscopy on **1** in different solvents and PMMA. Normalized absorption spectra (solid lines) and emission spectra (dashed lines) are shown for **1** in DCM (smoothed, red), TFE (smoothed, orange), MeCN (smoothed; blue) and PMMA (grey). For the recording of the emission spectra the excitation wavelength was set to 260 nm as marked as magenta vertical line in the absorption spectra. Due to the low overall signal level and the diminishing spectral sensitivity between 600 and 700 nm, the shape of the emission spectra there might deviate from the "true" form.

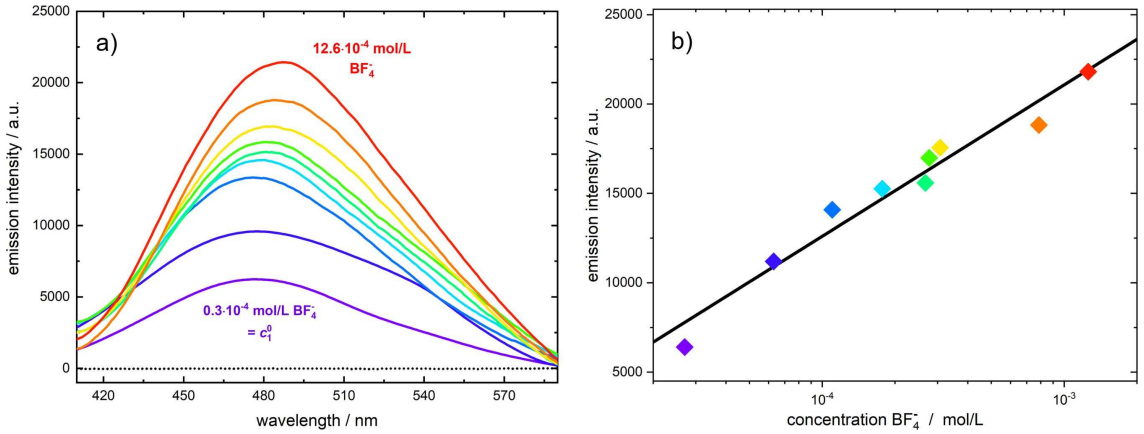

Figure 3. Impact of the addition of BF_4^- salt to the emission spectra of **1** dissolved in DCM. a) Emission spectra of **1** in DCM solution with increasing amount of counterion BF_4^- ranging from $0.3 \cdot 10^{-4}$ M (purple; equals initial concentration of compound **1**) to $12.6 \cdot 10^{-4}$ M (red). Tetrabutylammonium tetrafluoroborate was used as BF_4^- salt. Attempts to record an emission spectrum of a tetrabutylammonium tetrafluoroborate DCM solution under identical conditions resulted in a signal of essentially zero as depicted by the black dotted line. b) Plot of the emission intensity dependence on the concentration of BF_4^- ions (values from Figure 3a).

0.87,[9] **1** in MeCN solutions features an apparent quantum yield of approx. 10^{-5}. It is worth mentioning that the emission maximum of **1** in MeCN is similar to that of 2-picoline in MeCN (328 nm and 324 nm, respectively; see SI, Figure S5). For identical absorption at the excitation wavelength, the emission signal of **1** dissolved in MeCN amounts to ~0.03 of the 2-picoline signal. Assuming that in MeCN one equivalent of 2-picoline would be released if **2a** was formed (see above) and accounting for inner filter effects one would expect a reduction by 0.3. Thus, also emission spectroscopy disfavors the presence of compound **2a**.

Earlier studies on **1** as a powder had suggested that emission of **1** is mostly due to a species in which the counterion BF_4^- interacts with **1**. To check whether this is also responsible for the emission in solution, spectra as a function of the BF_4^- concentration were recorded (see Figure 3). It is clearly visible that the emission increases with the addition of the counterion BF_4^-. This suggests that as in solid state and polymer matrices the interaction of **1** with BF_4^- increases the luminescence.[9] Furthermore, comparing the apparent quantum yield of luminescence of **1** in DCM ($\Phi_{lum} \approx 10^{-5}$) with **1** in PMMA ($\Phi_{lum} \approx 0.87$[9]) it can be derived that only a small amount of **1** is present as luminescent BF_4^- coordinated complex (see Scheme 3). The increase of the emission signal with BF_4^- concentration does not saturate in the accessible range. Therefore, no dissociation constant K_D and emission quantum yield for the **1**–BF_4^- complex can be derived.

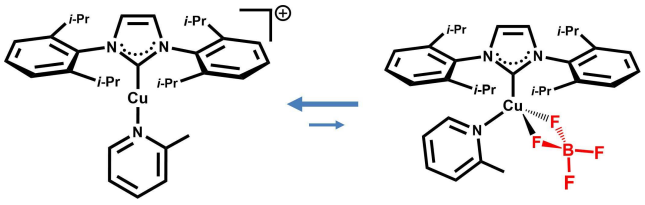

Scheme 3. Equilibrium between BF_4^--coordinated and uncoordinated species of **1** in non-coordinating solvents. The equilibrium is expected to be predominantly on the linear species (left).

Time-resolved measurements

Time-resolved UV/Vis absorption spectroscopy was conducted using femtosecond (100 fs–3 ns) as well as nanosecond (100 ns–10 µs) transient absorption techniques. The combined results from both techniques for **1** in TFE are shown as contour plots in Figure 4. Due to aforementioned difficulties with DCM and 266 nm laser pulses, here, results are only shown for TFE as a solvent. However, one successful scan on **1** dissolved in DCM reveals very similar spectro-temporal signatures as **1** dissolved in TFE (see SI, Figure S6). This further underlines DCM and TFE are both non-coordinating.

Negative signal contributions originating from stimulated emission (SE) or ground state bleach (GSB) are not observed and throughout the whole time frame and for all wavelengths positive signals of excited state absorption (ESA) are detected. Directly after photoexcitation a strong ESA signal covering the complete detection range shows maxima at ~350 and 620 nm. Within less than one picosecond this signature gives way to one which is essentially flat with a shallow maximum at ~550 nm. On a time scale of ~1 ns, the fsTA signal is seen to rise. In the course of this rise a difference spectrum with peaks at ~350, 450, and 550 nm forms. This distinctive pattern also appears in the nsTA experiment. This experiment reveals a microsecond lifetime for the carrier of this signature. "Late" femtosecond and "early" nanosecond spectra overlay favorably. This indicates that no kinetic component is missed due to the gap in the temporal coverage between 4–100 ns.

A global fit analysis was performed on the data to evaluate the kinetics of **1**. The data are fitted satisfactorily using three time constants, with $\tau_1 = 0.3$ ps, $\tau_2 = 900$ ps, $\tau_3 = 0.68$ µs. The resulting decay associated difference spectra ($DADS_{1\text{-}3}$) are shown in Figure 5. Additionally, the DADS for an 'infinite' delay

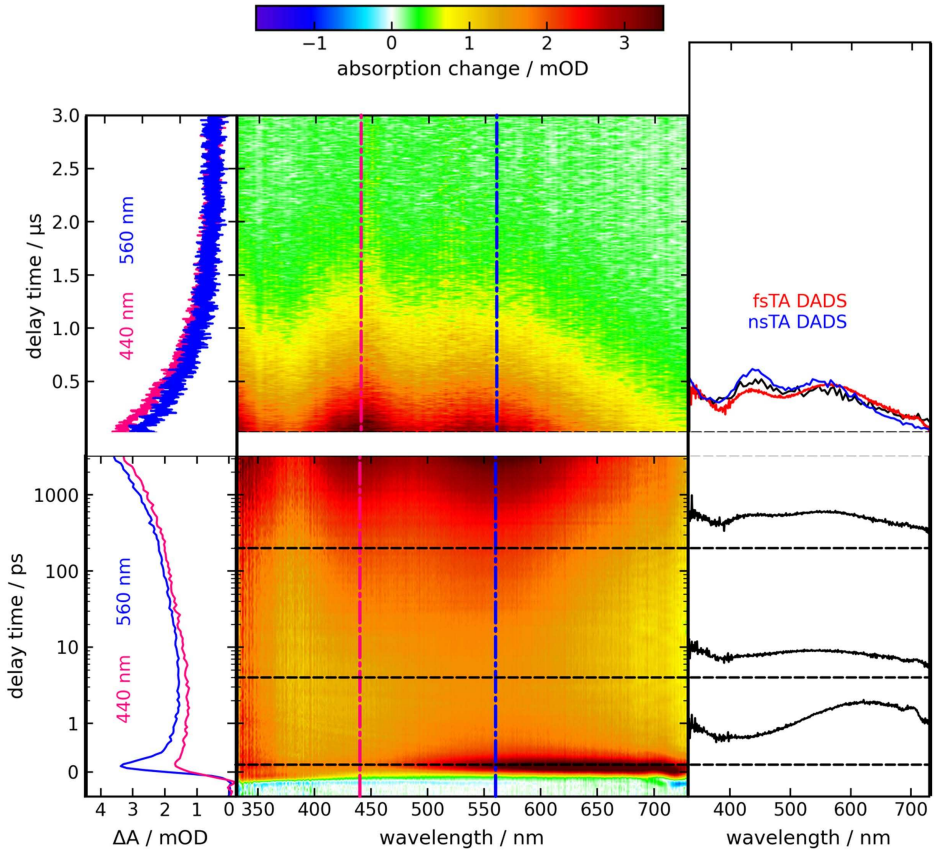

Figure 4. Time-resolved spectroscopy data acquired for **1** in TFE. The excitation was tuned to 266 nm. In the contour representation (central), the difference absorption signal is color-coded. Vertical lines mark spectral positions for the time traces plotted on the left while horizontal lines mark certain delay times for the difference spectra plotted on the right. The last decay associated difference spectrum (DADS) from the fsTA experiment is compared to the DADS obtained from the nsTA experiment.

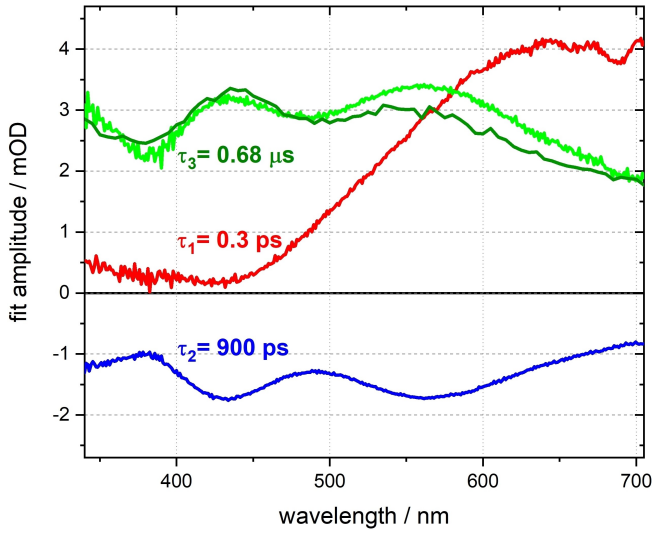

Figure 5. Decay associated difference spectra obtained from the fsTA and nsTA experiments of **1** in TFE. The bright green line shows the DADS for an infinite delay time from fsTA experiment, dark green shows the DADS for the time constant from the nsTA experiment of $\tau_3 = 0.68$ µs.

time, accounting for remaining signature in the fsTA experiment at a delay time of ~4 ns, is compared with the DADS resulting from the decay observed in the nsTA experiment. The similarity of these spectra confirms the above statement that no process is missed due to the temporal gap.

The respective $DADS_1$ shows a minor positive amplitude around 350 nm with a minimum around 450 nm followed by a rise for longer wavelengths peaking at 650 nm. Those positive amplitudes reveal a decay of the ESA signal, indicating that a transient species with strong absorption at 650 nm deactivates into a state that shows less absorption. As the transient spectra between 1 and 100 ps are almost without any features, contributions from a rising signal are absent. The $DADS_2$ is negative throughout the complete spectral range. It, thus, describes a spectrally broad signal rise. Minima at ~350, 430, and 560 nm coincide with the maxima in the $DADS_3$. Thus, the buildup of a species is described. The $DADS_3$ describes the decay of this species presumably to the ground state. Comparable kinetics are observed for **1** in DCM. The respective results of the global fit analysis and respective $DADS_{1\text{-}3}$ are shown in Figure S7.

Femtosecond and nanosecond time-resolved experiments were also performed on **1** dissolved in MeCN (see Figure 6). As for the time-resolved experiments of **1** in TFE or DCM, no negative signal contributions are observed. However, the spectro-temporal behavior of **1** in MeCN is very distinct from

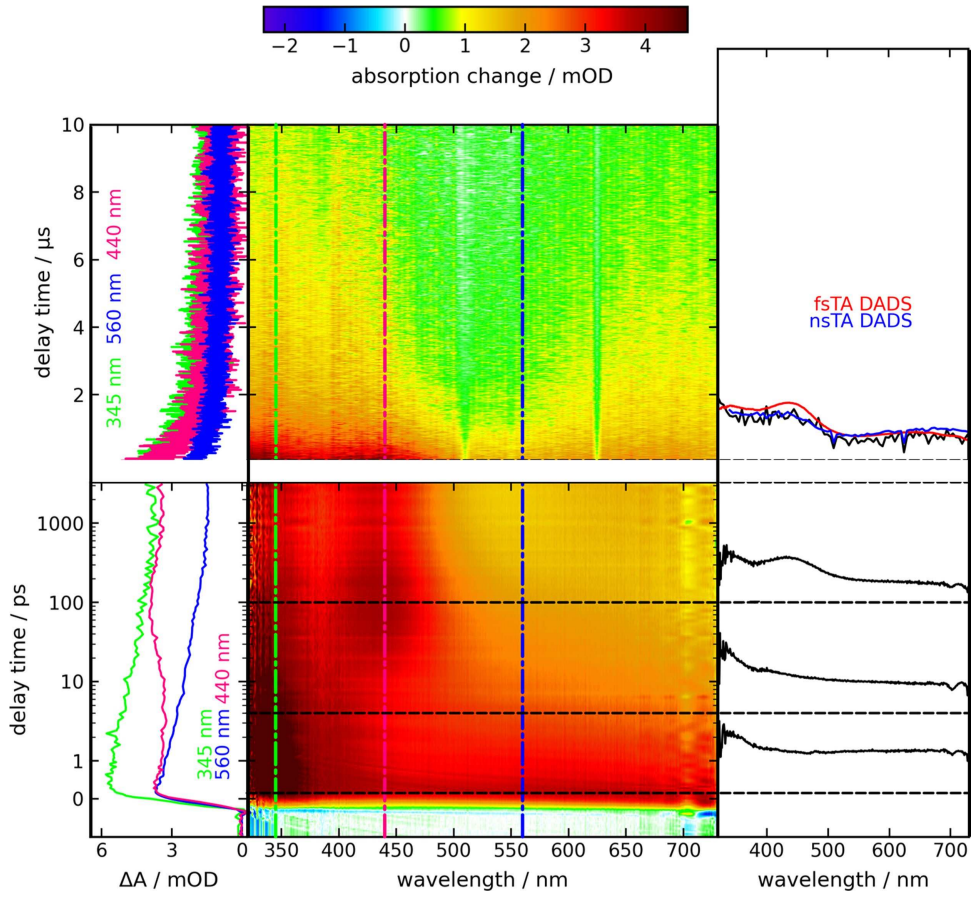

Figure 6. Time-resolved spectroscopy data acquired for **1** in MeCN. The excitation was tuned to 266 nm. In the contour representation (central), the difference absorption signal is color-coded. Vertical lines mark spectral positions for the time traces plotted on the left while horizontal lines mark certain delay times for the difference spectra plotted on the right. The last decay associated difference spectrum (DADS) from the fsTA experiment is compared to the only DADS received from the nsTA experiment.

the one of **1** in TFE or DCM. Right after excitation, two broad ESA bands are observed. One peaks around 330 nm, the other one at ~650 nm. In contrast to the feature at 330 nm, which shows a slower decay of around 10 ps, the broad band at ~650 nm decays within picoseconds. Another ESA band peaking at 440 nm appears around 100 ps. This band decays together with the band at 330 nm into a slightly less pronounced ESA feature. The decay of this signature is then observed in the nsTA experiment. Again, "late" femtosecond and "early" nanosecond spectra overlay favorably indicating that no kinetic component is missed due to the gap in the temporal coverage between 4–100 ns.

In a global analysis, data could be fit satisfactorily using four time constants with $\tau_1 = 2.6$ ps, $\tau_2 = 40$ ps, $\tau_3 = 235$ ps, and $\tau_4 = 2.5$ µs. Respective $DADS_{1\text{-}4}$ are shown in Figure 7. The first $DADS_1$ only bears positive amplitudes indicating that a positive transient absorption signal is decreasing with the respective time constant of 2.6 ps. For the band peaking at ~700 nm, the transient absorption signal decrease is more pronounced than for the one at 330 nm. This indicates that the subsequent species, which forms with τ_1 and decays with $\tau_2 = 40$ ps, shows higher transient absorption in the region below 500 nm and less above 500 nm as it is seen for the respective spectrum

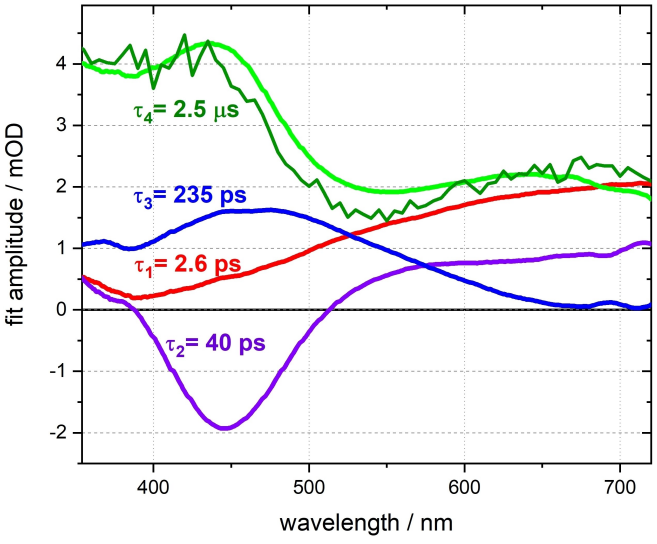

Figure 7. Decay associated difference spectra obtained from fsTA and nsTA experiment of **1** in MeCN. The bright green line shows the DADS for an infinite delay time from fsTA experiment, dark green shows the DADS for the sole decay time constant of the nsTA experiment of $\tau_4 = 2.5$ µs.

around 5–10 ps. The $DADS_2$ shows a distinct minimum at 450 nm. This minimum mirrors a maximum in the $DADS_3$ and thus indicates a rise due to the formation of another species. $DADS_3$ shows a maximum at 450 nm and a signal close to zero at ~650 nm. Although the transient spectra look quite similar for 100 ps and 3 ns, this indicates that except for the region at around 600 nm there is a change in absorption between the third and fourth temporal feature mostly at ~450 nm. The last $DADS_4$ eventually shows maxima at 350, 440, and 650 nm. Further, it bears the highest amplitudes on the complete detection range compared to $DADS_{1-3}$. The $DADS_4$ describes the decay of the last transient species being present presumably to the ground state.

Quantum chemical calculations

The spectroscopic experiments have indicated clearly that **1** reacts with coordinating solvents like MeCN. The product of this coordination was suggested to adopt structures **2a** or **2b**. In the following, quantum chemically computed absorption coefficient spectra of these species are compared with the experimental ones. Further, the absorption coefficient spectrum obtained by subtracting the one of 2-picoline from the one of **1** in MeCN ($\varepsilon_{1\text{-}MeCN}(\lambda) - \varepsilon_{2\text{-}picoline}(\lambda)$) is shown as a hypothetical experimental spectrum for **2a** assuming the quantitative formation of **2a** for **1** in MeCN (see Figure 8). Computed geometrical parameters are summarized in the SI (see Table S1 to S14 and separate .xyz files).

From the three species considered, compound **1** in DCM shows the highest agreement with the experimental spectrum with regard to their spectral shape and signal strength. In DCM (Figure 8a), it is expected that **1** is present in a linear geometry with little interaction between complex and solvent. The weak band with a maximum around 300 nm in the computed spectrum arises from the S_1 absorption at the S_0 equilibrium geometry. Earlier work revealed, however, that the spectral position of this transition experiences a blue shift and its oscillator strength diminishes when the torsional angle between the two ligands is increased.[10] Sampling of the torsional conformations is therefore expected to bring the red edge of the computed spectrum into better agreement with the experimental spectrum, which features a shoulder in the long wavelength regime. Similar considerations apply to the low-energy bands of the trigonal complexes **2a** and **2b** in acetonitrile as solvent. As can be seen in Figure 8b, the experimentally observed absorption maximum at 254 nm is well reproduced by the calculations for both, **2a** and **2b**. However, more or less pronounced discrepancies between experimental and calculated spectra are observed for the spectral regions at higher or lower wavelengths than 254 nm for both structures. Thus, an unequivocal decision which of the two species **2a** or **2b** is present cannot be made on this basis.

Furthermore, the change in total energy of **2b** in DCM relative to the linear complex **1** in DCM and a distant MeCN molecule was calculated. In DCM, a slightly positive energy value of 1.0 kJ/mol was found, which signals a thermally neutral addition within chemical accuracy. This is in line with the weak binding affinity, i.e. large K_D value. The coordinative bonding of MeCN to the copper center leads to a marked weakening of the Cu–N(2-picoline) bond in the electronic ground state. This is reflected in an elongation of this bond from 190 pm to 202 pm. In MeCN solution, the addition of MeCN is also slightly endothermic with a calculated energy of 1.9 kJ/mol.

The stability of **2b** with respect to the ejection of the MeCN ligand was also investigated (see Figure 9). The lowest excited states of **2b**, the S_{MLCT}/T_{MLCT} are 48.0/50.7 kJ/mol more favorable than their counterparts for **1**. The energy gain is, however, not reflected in a stronger Cu–N(nitrile) bond. Electron density is transferred into an antibonding Cu-MeCN orbital (see Figure 9 and S8), and the bond is slightly elongated by 2 pm (from 197 to 199 pm). In contrast, the Cu–N(2-picoline) bond length

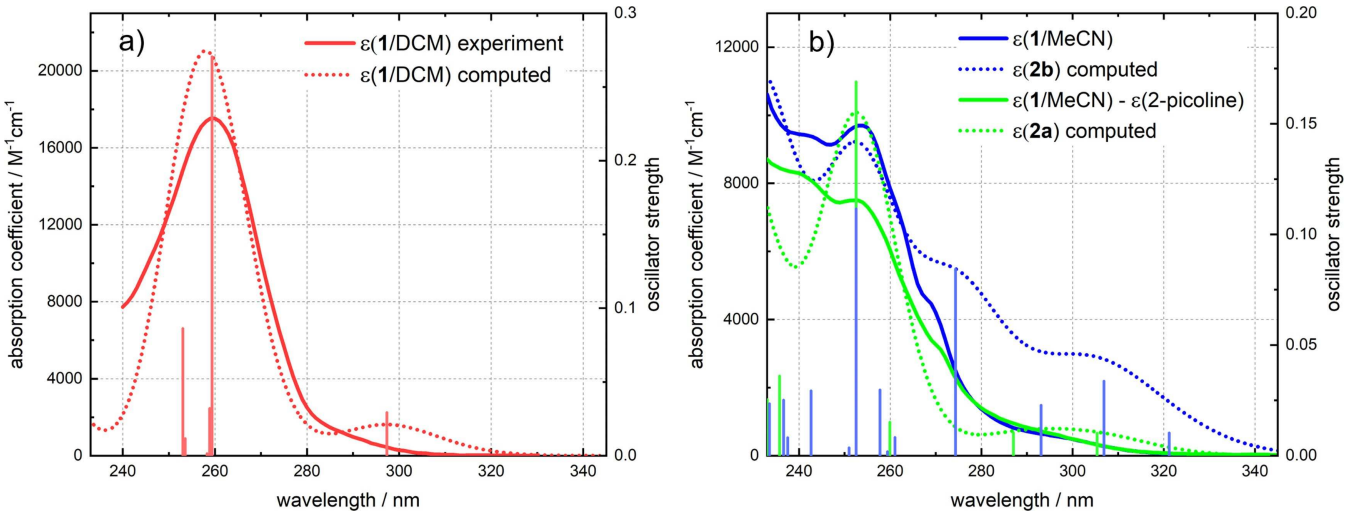

Figure 8. Comparison of calculated UV/Vis absorption coefficient spectra (dashed lines, left y-axis), including the oscillator strengths of each transition (vertical lines, right y-axis) of **1**, **2a** and **2b** with experimental spectra (solid lines) of a) **1** in DCM (red), b) **1** in MeCN (blue) and a hypothetical spectrum of **2a** that is obtained by subtracting the absorption coefficient spectrum of **1** in MeCN by the one of 2-picoline ($\varepsilon_{1\text{-}MeCN}(\lambda) - \varepsilon_{2\text{-}picoline}(\lambda)$, green).

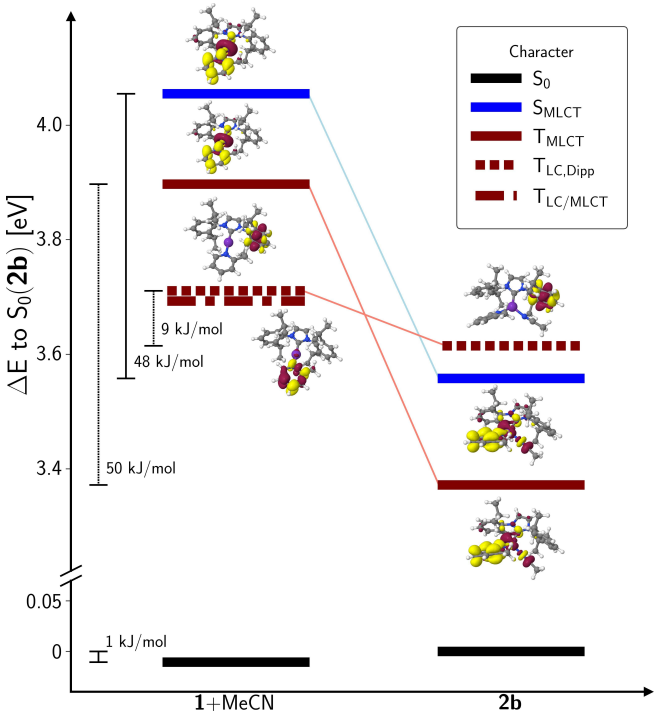

Figure 9. Total adiabatic energies of lowest excited states for complex **1** and **2b** in DCM relative to the ground state of **2b**. To compare with **2b**, the ground state energy of one MeCN molecule in DCM was added to the energy of complex **1**. The respective electron difference densities are shown next to each bar. Separately, an enlarged version of the densities is provided in the SI (Figure S8).

shrinks from 202 pm in the electronic ground state of **2b** to 189/187 pm in the S_{MLCT}/T_{MLCT} states where the copper coordination adopts a nearly T-shaped structure. The corresponding bond lengths of **1** amount to 185/184 pm in the S_{MLCT}/T_{MLCT} states. With regard to a potential substitution of the 2-picoline ligand by MeCN (formation of structure **2a**), the computations suggest that this is unlikely in the excited state. The Cu–N(2-picoline) bond is strengthened upon excitation.

Previous examinations had shown that the excited states of **1** decay from the S_{MLCT} state through a $T_{LC/MLCT}$ intermediate into a local triplet excitation on a diisopropylphenyl (Dipp) moiety.[10] In our present study, we added the GD3 dispersion correction and a continuum solvation, in total increasing the excitation energies. The $T_{LC,Dipp}$ state is affected most by dispersion interactions, lying now almost isoenergetic to the $T_{LC/MLCT}$ state. Yet, solvent coordination affects it to a lesser extent. The $T_{LC,Dipp}$ state is lowered by 9.3 kJ/mol upon MeCN addition, not enough to constitute the adiabatically lowest excited state of the threefold coordinated complex **2b**. The intermediate $T_{LC/MLCT}$ state that is responsible for the efficient ISC from the S_{MLCT} state to the triplet manifold in **1**, gains MLCT character in **2b** and thus mixes with the T_{MLCT} state. This mixture explains why no minimum structure could be found for the T_2 state of **2b** despite substantial effort. The considerable impact of MeCN addition on the relative energies and geometrical structures of the excited states further corroborates the experimental observations that the steady state and the transient spectra change markedly.

Discussion

Steady state spectroscopy of **1** in solution has indicated that **1** may react with solvent molecules. In non-coordinating solvents like TFE or DCM complex **1**, that is linear in its crystal structure,[9] is most likely present in a linear geometry as well. In coordinating solvents like MeCN, experiments show clear indication for a chemical reaction (e.g. coordination) between solvent and complex. Based on joint spectroscopic and quantum chemical data, suggestions on the structure of the complex are given. Furthermore, time-resolved UV/Vis spectroscopy was applied on **1** in TFE, DCM and MeCN. In the case of non-coordinating solvents, findings are compared to quantum chemical computations reported here, extending previous reports on **1**.[10,26] As a result, a consistent picture of the photokinetics of **1** upon excitation to its longest wavelength absorption maximum is obtained. In both cases (i.e. in coordinating and non-coordinating solvents), **1** shows involved photokinetics.

From steady state measurements, clear indications are found for an equilibrium chemical reaction for **1** in MeCN leading to the potential products **2a** or **2b**. Based upon experimental evidence (vide supra) we consider **2b** to be the species formed in this equilibrium. On the other hand, our quantum chemical calculations are not conclusive as to which species is formed.

Considering the electron pair donicity (i.e. Gutmann's donor number (*DN*)) of 2-picoline and MeCN as a measure for their coordinating affinity[27] with MeCN bearing a value of 14.1 kcal/mol[27] and 3-picoline, 4-picoline as well as pyridine[1] showing values of 39.0, 34.0 and 33.1 kcal/mol respectively,[27–28] one would expect 2-picoline to show a stronger affinity to the copper center than MeCN does. This again favors compound **2b** over **2a**. Quantum chemical calculations revealed that in the ground state the coordination of MeCN on **1** is neither favored nor disfavored energetically. This is in line with the large experimental K_D value. In the excited state, the addition is clearly favorable, ruling out the ligand release in the excited state. Due to these ambiguities, a definitive structure cannot be assigned to **1** dissolved in MeCN. Therefore, we refrain from an interpretation of the time-resolved measurements on **1** in MeCN.

Steady state experiments of **1** in TFE or DCM show that emission occurs at similar wavelengths as in solid or PMMA environment. In those environments a coordinating interaction of the counterion BF_4^- is proposed that gives rise to a high quantum yield of emission ($\Phi_{lum} \approx 0.87$ in PMMA).[9] However, the apparent quantum yield of emission that was determined for **1** in DCM is in the order of 10^{-5}. Therefore, we assume that **1** in DCM or TFE is mostly present as a linear complex (see

[1] For the sake of comparison and due to the absence of suitable DN value for 2-picoline, respective values for closely related derivatives are given.

Scheme 3), that shows virtually no emission in solution. The non-coordinating behavior of TFE is considered reasonable due to its low electron pair donicity, expressible with a negligible value of DN.[29] Based on that we further conclude that the signatures received from transient absorption measurements in TFE and DCM represent dominantly the linear species of **1**.

Assuming a consecutive model, we suggest a kinetic scheme (see Figure 10) taking into account three observable transient states. Species associated difference spectra[30] based on this model are depicted in the SI (Figure S9). Assignments of states and processes rely on quantum chemical computations on **1**. In contrast to previous reports,[10,26] the R2018 Hamiltonian, specially designed for metal complexes, a solvent continuum, and dispersion corrections were used. The latter have a large impact on the molecular geometry, shortening the H_{Me}–$C_{Ar,ipr}$ bond lengths from 339 and 362 pm to 313 and 315 pm, respectively. After photoexcitation into the absorption maximum, which is dominantly made up of the $S_2 \leftarrow S_0$ transition, internal conversion (IC) into the S_1 minimum is assumed to be fast and to occur within the time resolution of the instrument (~100 fs). According to DFT/MRCI calculations the S_1 state is a singlet state with $d_\sigma \rightarrow \pi_{Py}$ MLCT character where Cu d_σ electron density is transferred to the 2-picoline ligand. With regard to the adiabatic energy, four triplet states lie below the S_1 state. Based on this energetic ordering, states are referred to as T_1-T_4 in the following. The T_1 state (3.69 eV) shows both ligand centered (LC, mainly on the 2-picoline ligand) and MLCT character ($T_{LC/MLCT}$) and constitutes the corresponding triplet state to the S_2 state. States T_2 and T_3 (3.71 eV) originate from excitations localized on the Dipp moieties of the NHC ligand ($T_{LC,Dipp}$) while the T_4 state (3.90 eV) has the same excited state character as the S_1 state (T_{MLCT}). Computed ISC rate constants for the transitions $S_1 \rightarrow T_{1,2,3,4}$ will now be compared with experimental findings. The highest ISC rate constant is observed for the transition to the $T_{LC/MLCT}$ state with a value of $k_{ISC,LC/MLCT} = 5.3 \cdot 10^{11}\ s^{-1}$. This rate constant follows from a large spin-orbit coupling between the S_{MLCT} and the $T_{LC/MLCT}$ states. In both excitations, copper d-orbitals are involved. These orbitals differ in magnetic quantum number which is responsible for the large spin-orbit coupling. The second highest ISC rate constant is calculated for the transition to the two states $T_{LC,Dipp}$ with $k_{ISC,LC,Dipp} = 2.1 \cdot 10^{8}\ s^{-1}$, followed by ISC into T_{MLCT} with $k_{ISC,MLCT} = 3.2 \cdot 10^{7}\ s^{-1}$. The computed radiative rate constant k_{rad} of the S_1 state amounts to only $8.4 \cdot 10^{6}\ s^{-1}$. As all ISC rate constants are orders of magnitudes higher, a very small fluorescence quantum yield is expected. This matches the experimental observation. Based on the above ISC rate constants, the $T_{LC/MLCT}$ state owns the highest probability to be populated following S_{MLCT} excitation. The inverse of $k_{ISC,LC/MLCT}$ is 2 ps, which is somewhat larger than the observed time constant τ_1 of 300 fs. According to the computations, the $T_{LC/MLCT}$ state is the lowest triplet state in terms of adiabatic energy. Yet, these computations predict the $T_{LC,Dipp}$ state to be isoenergetic with this state within 20 meV. So it cannot be excluded that the $T_{LC,Dipp}$ state is in fact the one lowest in energy. Time-resolved spectroscopy strongly favors this. After the τ_1 process, assigned to the ISC transition into $T_{LC/MLCT}$, two processes with time constants $\tau_2 = 900$ ps and $\tau_3 = 0.68$ µs are observed. If the τ_1 process populated the lowest triplet state, only one further process ought to occur. We, thus, assign the τ_2 process to a transition between the $T_{LC/MLCT}$ state and the $T_{LC,Dipp}$ state. According to the experiment, the latter one ought to be the one lowest in energy. This lifetime of $\tau_2 = 900$ ps seems long if one takes the near degeneracy of the two states into consideration. However, these states differ strongly in character and thereby also in equilibrium geometries. This ought to result in a large reorganization energy λ and thus a substantial barrier

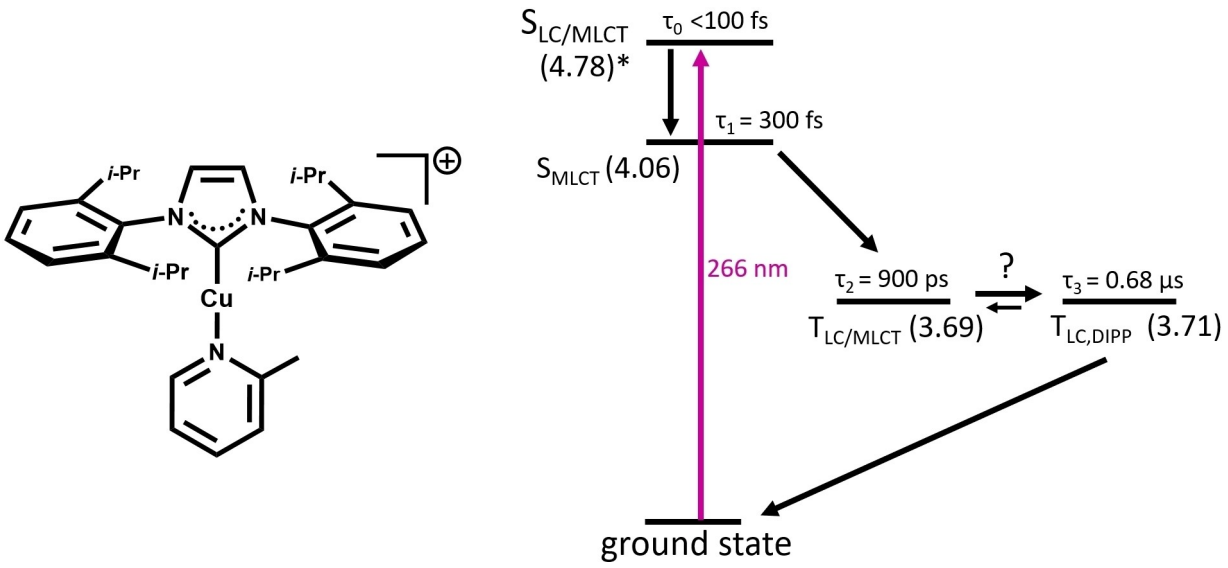

Figure 10. Kinetic scheme of **1** in TFE. The time constants were received from the fs- and nsTA experiments. The electronic state assignment was done on the basis of quantum chemical calculations on the linear complex. The values in brackets show the adiabatic energies of the respective states in eV relative to the S_0 minimum. The value marked with a star shows the vertical energy of the $S_{LC/MLCT}$ state.

(of ~λ/4) for the IC transition between the two states.[31] An equilibration of the two states cannot be excluded.

In any case, a long-lived upper triplet state, as observed here, bears the potential for luminescent application. For instance, HIGHrISC fluorophores for OLEDs make use of such long-lived upper triplet states.[32] In the HIGHrISC approach – also known as hot exciton – an upper triplet state that lies energetically close to the S_1 state is used for efficient triplet harvesting via reverse intersystem crossing (rISC). The lowest populated triplet state, $T_{LC,Dipp}$ exhibits a lifetime of 0.68 µs, which is a typical value for such complexes.[33] With a calculated phosphorescence rate constant of 0.36 s^{-1} emission from $T_{LC,Dipp}$ state is outcompeted by non-radiative deactivation processes. This underlines the hypothesis that the emission that is observed originates not directly from **1** but from a coordinated counterion derivative as it is proposed in Ref. [9].

Conclusion

The steady state absorption and emission behavior of a linear copper(I) carbene complex (compound **1**) has been studied in non-coordinating solvents, such as DCM and TFE, as well as in coordinating solvents, such as MeCN and 2-propanol. The investigation yielded a distinct behavior depending on the type of solvent (i.e. coordinating or non-coordinating). In coordinating solvents, clear indications were found for a chemical equilibrium reaction between **1** and the respective solvent. Based on steady state experiments and quantum chemical computations, suggestions on the resulting compound are provided. Furthermore, for both TFE and MeCN, femtosecond time-resolved transient absorption spectroscopy was applied, yielding involved photokinetics. In the case of TFE, a consistent picture on the compound's photokinetics could be obtained with the help of quantum chemical computations. In the course of the study, a long-lived upper triplet state has been detected, making **1** a potential candidate for HIGHrISC applications.

Acknowledgements

This work has been supported by the Deutsche Forschungsgemeinschaft (DFG, German Research Foundation), Project number 396890929 (GRK 2482). We thank our colleague Thomas J. J. Müller (Heinrich Heine University Düsseldorf, Institute of Organic Chemistry) for suggesting TFE as a suitable solvent. Open Access funding enabled and organized by Projekt DEAL.

Conflict of Interest

The authors declare no conflict of interest.

Data Availability Statement

The data that support the findings of this study are available from the corresponding author upon reasonable request.

Keywords: time-resolved spectroscopy · copper(I) complexes · thermally activated delayed fluorescence (TADF) · quantum chemistry · solvent effects

[1] a) J. C. Deaton, S. C. Switalski, D. Y. Kondakov, R. H. Young, T. D. Pawlik, D. J. Giesen, S. B. Harkins, A. J. M. Miller, S. F. Mickenberg, J. C. Peters, *J. Am. Chem. Soc.* **2010**, *132*, 9499–9508; b) M. Hashimoto, S. Igawa, M. Yashima, I. Kawata, M. Hoshino, M. Osawa, *J. Am. Chem. Soc.* **2011**, *133*, 10348–10351; c) F. Wei, T. Zhang, X. Liu, X. Li, N. Jiang, Z. Liu, Z. Bian, Y. Zhao, Z. Lu, C. Huang, *Org. Electron.* **2014**, *15*, 3292–3297; d) A. Wada, Q. Zhang, T. Yasuda, I. Takasu, S. Enomoto, C. Adachi, *Chem. Commun.* **2012**, *48*, 5340–5342; e) F. B. Dias, T. J. Penfold, A. P. Monkman, *Methods Appl. Fluoresc.* **2017**, *5*, 012001.

[2] M. Kleinschmidt, C. van Wüllen, C. M. Marian, *J. Chem. Phys.* **2015**, *142*, 094301.

[3] D. Volz, M. Wallesch, C. Fléchon, M. Danz, A. Verma, J. M. Navarro, D. M. Zink, S. Bräse, T. Baumann, *Green Chem.* **2015**, *17*, 1988–2011.

[4] V. Yam, A. Chan, E. Hong, *Nat. Chem. Rev.* **2020**, *4*.

[5] a) A. F. Rausch, H. H. H. Homeier, H. Yersin, in *Photophysics of Organometallics* (Ed.: A. J. Lees), Springer Berlin Heidelberg, Berlin, Heidelberg, **2010**, pp. 193–235; b) C. L. Linfoot, M. J. Leitl, P. Richardson, A. F. Rausch, O. Chepelin, F. J. White, H. Yersin, N. Robertson, *Inorg. Chem.* **2014**, *53*, 10854–10861; c) P.-T. Chou, Y. Chi, M.-W. Chung, C.-C. Lin, *Coord. Chem. Rev.* **2011**, *255*, 2653–2665; d) P. Data, A. Kurowska, S. Pluczyk, P. Zassowski, P. Pander, R. Jedrysiak, M. Czwartosz, L. Otulakowski, J. Suwinski, M. Lapkowski, A. P. Monkman, *J. Phys. Chem. C* **2016**, *120*, 2070–2078; e) J. Eng, T. J. Penfold, *Chem. Rec.* **2020**, *20*, 831–856.

[6] a) A. n. Vlček, *Coord. Chem. Rev.* **2000**, *200–202*, 933–978; b) J. A. Weinstein, in *Applied Photochemistry* (Eds.: R. C. Evans, P. Douglas, H. D. Burrow), Springer Netherlands, Dordrecht, **2013**, pp. 105–148.

[7] a) S. Shi, L. R. Collins, M. F. Mahon, P. I. Djurovich, M. E. Thompson, M. K. Whittlesey, *Dalton Trans.* **2017**, *46*, 745–752; b) J. Li, L. Wang, Z. Zhao, X. Li, X. Yu, P. Huo, Q. Jin, Z. Liu, Z. Bian, C. Huang, *Angew. Chem. Int. Ed.* **2020**, *59*, 8210–8217; *Angew. Chem.* **2020**, *132*, 8287–8294.

[8] a) H. Yersin, R. Czerwieniec, M. Z. Shafikov, A. F. Suleymanova, in *Highly Efficient OLEDs*, **2018**, pp. 1–60; b) O. S. Wenger, *J. Am. Chem. Soc.* **2018**, *140*, 13522–13533; c) N. Armaroli, G. Accorsi, F. Cardinali, A. Listorti, in *Photochemistry and Photophysics of Coordination Compounds I* (Eds.: V. Balzani, S. Campagna), Springer Berlin Heidelberg, Berlin, Heidelberg, **2007**, pp. 69–115; d) M. J. Leitl, D. M. Zink, A. Schinabeck, T. Baumann, D. Volz, H. Yersin, *Top. Curr. Chem.* **2016**, *374*, 25; e) D. Di, A. Romanov, L. Yang, J. Richter, J. Rivett, S. Jones, T. Thomas, M. Abdi-Jalebi, R. Friend, M. Linnolahti, M. Bochmann, D. Credgington, *Science* **2017**, *356*, 159–163; f) M. Gernert, U. Müller, M. Haehnel, J. Pflaum, A. Steffen, *Chem. Eur. J.* **2017**, *23*, 2206–2216; g) S. Shi, M. C. Jung, C. Coburn, A. Tadle, D. Sylvinson, M. R. P. I. Djurovich, S. R. Forrest, M. E. Thompson, *J. Am. Chem. Soc.* **2019**, *141*, 3576–3588; h) R. Hamze, S. Shi, S. C. Kapper, D. S. Muthiah Ravinson, L. Estergreen, M.-C. Jung, A. C. Tadle, R. Haiges, P. I. Djurovich, J. L. Peltier, R. Jazzar, G. Bertrand, S. E. Bradforth, M. E. Thompson, *J. Am. Chem. Soc.* **2019**, *141*, 8616–8626; i) R. Hamze, J. L. Peltier, D. Sylvinson, M. Jung, J. Cardenas, R. Haiges, M. Soleilhavoup, R. Jazzar, P. I. Djurovich, G. Bertrand, M. E. Thompson, *Science* **2019**, *363*, 601–606; j) M. Gernert, L. Balles-Wolf, F. Kerner, U. Müller, A. Schmiedel, M. Holzapfel, C. M. Marian, J. Pflaum, C. Lambert, A. Steffen, *J. Am. Chem. Soc.* **2020**, *142*, 8897–8909; k) T. Hölzel, A. Belyaev, M. Terzi, L. Stenzel, M. Gernert, C. M. Marian, A. Steffen, C. Ganter, *Inorg. Chem.* **2021**, *60*, 18529–18543; l) A. Ruduss, B. Turovska, S. Belyakov, K. A. Stucere, A. Vembris, K. Traskovskis, *Inorg. Chem.* **2022**, *61*, 2174–2185; m) X.-F. Song, Z.-W. Li, W.-K. Chen, Y.-J. Gao, G. Cui, *Inorg. Chem.* **2022**, *61*, 7673–7681.

[9] A. Liske, L. Wallbaum, T. Hölzel, J. Föller, M. Gernert, B. Hupp, C. Ganter, C. M. Marian, A. Steffen, *Inorg. Chem.* **2019**, *58*, 5433–5445.

[10] J. Föller, C. Ganter, A. Steffen, C. M. Marian, *Inorg. Chem.* **2019**, *58*, 5446–5456.

[11] D. Onidas, D. Markovitsi, S. Marguet, A. Sharonov, T. Gustavsson, *J. Phys. Chem. B* **2002**, *106*, 11367–11374.
[12] K. Suzuki, A. Kobayashi, S. Kaneko, K. Takehira, T. Yoshihara, H. Ishida, Y. Shiina, S. Oishi, S. Tobita, *Phys. Chem. Chem. Phys.* **2009**, *11*, 9850–9860.
[13] a) B. Schmidt, S. Laimgruber, W. Zinth, P. Gilch, *Appl. Phys. B* **2003**, *76*, 809–814; b) A. Reiffers, C. Torres Ziegenbein, L. Schubert, J. Diekmann, K. A. Thom, R. Kühnemuth, A. Griesbeck, O. Weingart, P. Gilch, *Phys. Chem. Chem. Phys.* **2019**, *21*, 4839–4853.
[14] J. Mooney, P. Kambhampati, *J. Phys. Chem. Lett.* **2013**, *4*, 3316–3318.
[15] S. Fröbel, L. Buschhaus, T. Villnow, O. Weingart, P. Gilch, *Phys. Chem. Chem. Phys.* **2015**, *17*, 376–386.
[16] M. Lorenc, M. Ziolek, R. Naskrecki, J. Karolczak, J. Kubicki, A. Maciejewski, *Appl. Phys. B* **2002**, *74*, 19–27.
[17] H. Satzger, W. Zinth, *Chem. Phys.* **2003**, *295*, 287–295.
[18] a) M. J. Frisch, G. W. Trucks, H. B. Schlegel, G. E. Scuseria, M. A. Robb, J. R. Cheeseman, G. Scalmani, V. Barone, G. A. Petersson, H. Nakatsuji, X. Li, M. Caricato, A. V. Marenich, J. Bloino, B. G. Janesko, R. Gomperts, B. Mennucci, H. P. Hratchian, J. V. Ortiz, A. F. Izmaylov, J. L. Sonnenberg, D. Williams-Young, F. Ding, F. Lipparini, F. Egidi, J. Goings, B. Peng, A. Petrone, T. Henderson, D. Ranasinghe, V. G. Zakrzewski, J. Gao, N. Rega, G. Zheng, W. Liang, M. Hada, M. Ehara, K. Toyota, R. Fukuda, J. Hasegawa, M. Ishida, T. Nakajima, Y. Honda, O. Kitao, H. Nakai, T. Vreven, K. a. Throssell, Gaussian 16, Revision A.03, Gaussian, Inc., Wallingford CT, **2016**; b) C. Adamo, V. Barone, *J. Chem. Phys.* **1999**, *110*, 6158–6170; c) S. Grimme, J. Antony, S. Ehrlich, H. Krieg, *J. Chem. Phys.* **2010**, *132*; d) A. Schäfer, H. Horn, R. Ahlrichs, *J. Chem. Phys.* **1992**, *97*, 2571–2577.
[19] a) K. A. Peterson, C. Puzzarini, *Theor. Chem. Acc.* **2005**, *114*, 283–296; b) D. Figgen, G. Rauhut, M. Dolg, H. Stoll, *Chem. Phys.* **2005**, *311*, 227–244.
[20] J. Tomasi, B. Mennucci, R. Cammi, *Chem. Rev.* **2005**, *105*, 2999–3094.
[21] a) R. Ahlrichs, M. Bär, M. Häser, H. Horn, C. Kölmel, *Chem. Phys. Lett.* **1989**, *162*, 165–169; b) R. Ahlrichs, M. K. Armbruster, R. A. Bachorz, M. Bär, H. P. Baron, R. Bauernschmitt, F. A. Bischoff, S. Böcker, N. Crawford, P. Deglmann, TURBOMOLE 6.3, University of Karlsruhe and Forschungszentrum Karlsruhe GmbH, TURBOMOLE GmbH, **2010**.
[22] A. Heil, M. Kleinschmidt, C. M. Marian, *J. Chem. Phys.* **2018**, *149*.
[23] a) S. Grimme, M. Waletzke, *J. Chem. Phys.* **1999**, *111*, 5645–5655; b) A. D. Becke, *J. Chem. Phys.* **1993**, *98*, 1372–1377.
[24] a) M. Kleinschmidt, J. Tatchen, C. M. Marian, *J. Chem. Phys.* **2006**, *124*, 124101; b) M. Etinski, J. Tatchen, C. M. Marian, *J. Chem. Phys.* **2011**, *134*, 154105.
[25] B. Valeur, M. N. Berberan-Santos, in *Molecular Fluorescence, Vol. 2*, **2012**, pp. 31–51.
[26] N. Lüdtke, J. Föller, C. M. Marian, *Phys. Chem. Chem. Phys.* **2020**, *22*, 23530–23544.
[27] V. Gutmann, *Coord. Chem. Rev.* **1967**, *2*, 239–256.
[28] F. Cataldo, *Eur. Chem. Bull.* **2015**, *2015*, 92–97.
[29] J. A. Marinsky, Y. Marcus, in *Ion Exchange and Solvent Extraction: A Series of Advances, Volume 13*, CRC Press, Boca Raton, **2021**.
[30] I. H. M. van Stokkum, D. S. Larsen, R. van Grondelle, *Biochim. Biophys. Acta, Bioenerg.* **2004**, *1652*, 82–104.
[31] A. Nitzan, in *Chemical Dynamics in Condensed Phase – The Spin-Boson Model*, Oxford University Press, Oxford, New York, **2006**.
[32] K. A. Thom, F. Wieser, K. Diestelhorst, A. Reiffers, C. Czekelius, M. Kleinschmidt, M. Bracker, C. M. Marian, P. Gilch, *J. Phys. Chem. Lett.* **2021**, *12*, 5703–5709.
[33] B. Hupp, C. Schiller, C. Lenczyk, M. Stanoppi, K. Edkins, A. Lorbach, A. Steffen, *Inorg. Chem.* **2017**, *56*, 8996–9008.

Manuscript received: August 18, 2022
Revised manuscript received: December 2, 2022
Accepted manuscript online: December 12, 2022
Version of record online: December 29, 2022

5.2. The Photophysics of 2-Cyanoindole Probed by Femtosecond Spectroscopy (Publication II)

Title: The Photophysics of 2-Cyanoindole Probed by Femtosecond Spectroscopy

Authors: Mahbobeh Morshedi, Oliver Nolden, Philipp Janke, Wiebke Haselbach, Michael Schmitt, Peter Gilch

Published in: Photochemical and Photobiological Sciences

Year: 2023

Impact Factor: 2.7 (2023)

My Contributions to the Publication:

- acquisition of time resolved fluorescence/anisotropy spectra
- analysis of time resolved fluorescence/anisotropy spectral results and generating the corresponding figures
- conducting the literature research
- composition of parts of the manuscript

Photochemical & Photobiological Sciences (2023) 22:745–759
https://doi.org/10.1007/s43630-022-00348-3

ORIGINAL PAPERS

The photophysics of 2-cyanoindole probed by femtosecond spectroscopy

Mahbobeh Morshedi[1] · Oliver Nolden[1] · Philipp Janke[1] · Wiebke Haselbach[1] · Michael Schmitt[1] · Peter Gilch[1]

Received: 16 September 2022 / Accepted: 24 November 2022 / Published online: 10 December 2022

Abstract

The photophysics of 2-cyanoindole (2-CI) in solution (water, 2,2,2-trifluoroethanol, acetonitrile, and tetrahydrofuran) was investigated by steady-state as well as time resolved fluorescence and absorption spectroscopy. The fluorescence quantum yield of 2-cyanoindole is strongly sensitive to the solvent. In water the quantum yield is as low as 4.4×10^{-4}. In tetrahydrofuran, it amounts to a yield of 0.057. For 2-CI dissolved in water, a bi-exponential fluorescence decay with time constants of ~1 ps and ~8 ps is observed. For short wavelength excitation (266 nm) the initial fluorescence anisotropy is close to zero. For excitation with 310 nm it amounts to 0.2. In water, femtosecond transient absorption reveals that the fluorescence decay is solely due to internal conversion to the ground state. In aprotic solvents, the fluorescence decay takes much longer (acetonitrile: ~900 ps, tetrahydrofuran: ~2.6 ns) and intersystem crossing contributes.

Graphical abstract

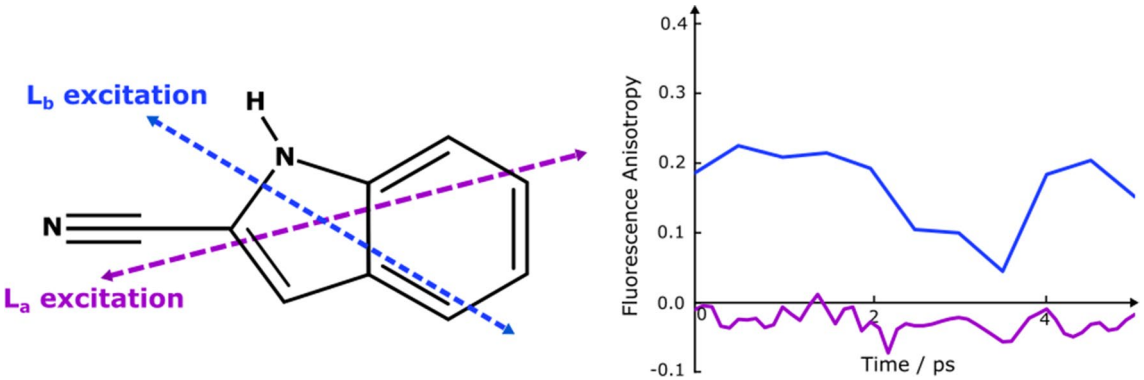

Keywords 2-Cyanoindole · Photophysics · Solvent effects · Time resolved spectroscopy · Fluorescence anisotropy · Triplet state

1 Introduction

The side chain of the amino acid tryptophan consists of the hetero-aromatic indole moiety. This moiety contributes strongly to the intrinsic fluorescence of proteins [1]. Substitution of the indole moiety may alter its fluorescence properties which can be exploited, for instance, in biophysical studies on proteins and peptides [2–6]. The cyano-substituent is hereby of particular interest. It exhibits strong negative inductive and mesomeric (resonance)

This publication is dedicated to Prof. Silvia E. Braslavsky, a pioneer in photobiology and photobiophysics, on the occasion of her 80th birthday.

✉ Peter Gilch
gilch@hhu.de

[1] Institut für Physikalische Chemie, Heinrich-Heine-Universität Düsseldorf, Universitätsstr. 1, 40225 Düsseldorf, Germany

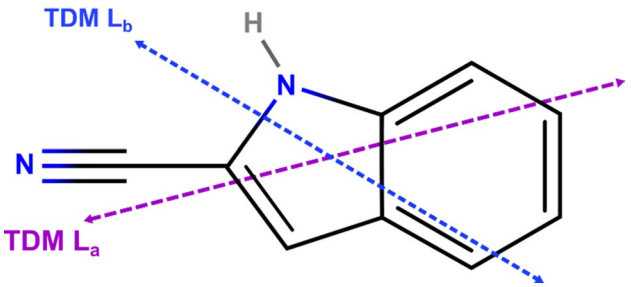

Scheme 1 Chemical structure of the molecule 2-CI. Purple and blue dashed arrows indicate the orientation of the transition dipole moments (TDM) of the L_a and L_b states [10]

effects on the chromophore [7]. It may, thus, substantially alter the electronic structure of indole. Due to its size, a cyano-substituent causes only a small steric effect [8]. Some cyanoindoles exhibit strongly solvent dependent fluorescence lifetimes and quantum yields [9]. For the title compound 2-cyanoindole (2-CI, structure in Scheme 1) dissolved in tetrahydrofuran (THF), a fluorescence lifetime of 2.9 ns was measured [9]. Dissolving the compound in dimethylsulfoxide (DMSO) reduces the lifetime to 0.4 ns. For water as a solvent, only an upper boundary of 0.05 ns for the lifetime was reported (see also ref. [10]). Due to this dependence, the fluorescence of 2-CI and other cyanoindoles can serve as a sensor of the local environment of an amino acid residue in a protein. The cyano-group further offers the possibility to probe this environment via vibrational spectroscopy [11–14].

Here, femtosecond fluorescence and UV/Vis absorption experiments on the photophysics of 2-CI are reported. The experiments aim at the fluorescence lifetime of 2-CI in water for which heretofore only an upper boundary has been reported (see above). Via time-dependent fluorescence anisotropy measurement, information on the emissive state (L_a or L_b) [15] is retrieved. With femtosecond UV/Vis absorption, transient states populated in the course of the fluorescence decay are detected. It is shown that in aprotic solvents intersystem crossing (ISC) contributes substantially to the decay. Experiments were conducted using solutions of 2-CI in water, 2,2,2-trifluoroethanol (TFE), acetonitrile (MeCN), and tetrahydrofuran (THF). TFE was selected to study the effect of the proticity on the photophysics. Like water, it is a protic solvent albeit with a lower dielectric constant. MeCN is a strongly polar but aprotic solvent and THF represents a solvent of moderate to small polarity.

2 Experimental section

2.1 Samples

2-CI (≥ 99.89%) was purchased from Chem Scene, thymidine (≥ 99.0%) from Sigma-Aldrich, water (HPLC gradient grade) from Fisher Chemical, 2,2,2-trifluoroethanol (99%) from Carbolution Chemicals, acetonitrile (≥ 99.9%) from Honeywell, tetrahydrofuran (≥ 99.9%) from Sigma-Aldrich. All chemicals were used as supplied. All measurements were performed at room temperature (~ 20 °C).

2.2 Steady-state measurements

Steady-state absorption spectra were measured with a Lambda 19 spectrometer from Perkin Elmer. Fluorescence spectra were recorded on a FluoroMax-4 (Horiba Scientific). The excitation wavelength was set to 260 nm. 1 cm fused silica cuvettes (Hellma Analytics) were employed for these measurements. To determine the fluorescence quantum yields Φ_{fl}, thymidine in water served as reference ($\Phi_{fl} = 1.32 \times 10^{-4}$ [16]). Fluorescence excitation spectra were obtained by detecting the fluorescence signal around 340 nm. For both, emission and excitation spectra, the optical densities were kept below 0.05 (per cm) to avoid inner filter effect. Spectra were corrected for the spectral sensitivity of the instrument.

2.3 Time resolved fluorescence measurements

A femtosecond fluorescence Kerr gating was used to trace the decay of 2-CI in water for 266 and 310 nm excitation pulses. A detailed description for this setup was given before [17, 18]. A Ti:Sa laser amplifier system (Libra, Coherent) served as pulse source with a repetition rate of 1 kHz, 100 fs pulse duration and a wavelength of 800 nm. To generate 266 nm pump pulses, a part of the output was first converted to a wavelength of 400 nm by frequency doubling (in a BBO crystal type I, 29°, 1 mm). Subsequently, from the doubled and the fundamental, the sum frequency was generated to yield a wavelength of 266 nm (in another BBO crystal, type II, 55.5°, 0.5 mm). The beam diameter was 80 µm (full width half maximum, FWHM) and the energy per pulse amounted to 1.1 µJ at the sample location. For the generation of 310 nm excitation pulses, a part of the output was fed in to a TOPAS-White non-collinear optical parametric amplifier system. The TOPAS was set to generate pulses peaking at 620 nm. By frequency doubling (BBO crystal, type I, 37°, 0.15 mm), they were converted to the pump wavelength of 310 nm with an energy per pulse of 0.9 µJ. The instrumental response function (IRF) was about 430 and 440 fs (FWHM) for 266 and 310 nm excitation light, respectively. The rather long IRF times can (partially) be attributed to the group velocity mismatch of fluorescence and gate light in the Kerr medium [19]. The optical gate operated as described before [18]. For the experiment with 266 nm excitation pulse, the integration time for each spectrum was set to 2.5 s. To record each scan, there were 50 steps from − 2 to 5 ps on a linear scale, then 35 steps on a logarithmic one up to 35 ps. For

this measurement, a total of 12 scans were averaged. For the measurement with 310 nm excitation pump, the integration time was set to 1 s. Each scan covered a time range of 40 ps which consisted of 80 equidistant steps. For this measurement, a total of 40 scans were averaged. The solutions were circulated by a peristaltic pump (REGLO Analog MS-2/8 from ISMATEC®) through a flow cell (custom made QX, Hellma Analytics) with 1 mm path length. Measurements on solutions of 2-CI (concentrations of ~ 24 µM and ~ 32 µM for the excitation of 266 and 310 nm light, respectively) as well as the neat solvent were performed. Solvent signals were subtracted from the solution ones after proper scaling.

2.4 Time resolved fluorescence anisotropy measurements

Measurements of the fluorescence anisotropy for both 266 and 310 nm excitation pulses were performed on the Kerr gate set up as well. To this end, a fluorescence signal $S_{||}(\lambda, t)$ with the pump pulse parallel to the first polarizer of the Kerr gate was recorded. Then the polarization of the pump light was rotated by 90° with a half-wave plate. Care was taken to ensure the same excitation energy for both polarizations were employed. The anisotropy was then calculated via [1]

$$r(\lambda, t) = \frac{S_{||}(\lambda, t) - S_{\perp}(\lambda, t)}{S_{||}(\lambda, t) + 2S_{\perp}(\lambda, t)}. \quad (1)$$

Thymidine in water was chosen for the calibrations of the set up. To record the parallel signal $S_{||}(\lambda, t)$ the solution was excited at 266 nm and the integration time amounted to 1 s. The time range covered was 7 ps. The range was divided in 70 equidistant steps. It was averaged over 13 delay line scans. The perpendicular signal $S_{\perp}(\lambda, t)$ was recorded with the same settings. Thymidine solution had a concentration of ~ 16 µM. The resulting anisotropy value from Eq. (1) was calculated. The initial anisotropy for thymidine in water was determined to be 0.31 ± 0.01. It compares favorably with the value of 0.35 reported by Gustavsson et al. [20]. For the anisotropy experiment on 2-CI solutions with 266 nm excitation, the same settings were applied to the parallel and perpendicular measurements. The integration time for each spectrum was set to 2.5 s. For recording each scan, there were 50 steps from − 2 to 5 ps linearly, then 35 steps on a logarithmic scale up to 35 ps. In total, 12 scans were averaged. To record the anisotropy measurement for the solution of 2-CI with 310 nm excitation light, the integration time amounted to 1 s. Each scan covered a time range of 40 ps which consisted of 80 linearly steps. For this measurement, a total of 7 scans were averaged. Time resolved anisotropy experiments were recorded as a function of detection wavelength and delay time, however, only one selected wavelength was shown (see result section). For dissolved 2-CI (concentrations of ~ 20 µM and ~ 30 µM for the excitation of 266 and 310 nm light, respectively) and the neat solvent data sets were recorded. After proper scaling the solvent signals were subtracted.

2.5 Femtosecond transient absorption

The experimental setup for femtosecond transient absorption measurements was described in depth elsewhere [21–23]. Briefly, for all measurements, a 1 kHz Ti:Sa femtosecond laser amplifier system (Libra, Coherent) was used to obtain the frequency-tripled output (266 nm) as pump pulses. The beam had a diameter of 160 µm on the sample position and the pump pulse energy at the sample was adjusted to ~ 1 µJ. Absorption changes were probed by a single-filament white light continuum generated in CaF_2 with a diameter of 100 µm on the sample. The relative orientation of pump and probe polarization time was set at the magic angle. The instrumental response time was ~180 fs (FWHM). Each scan consisted of 139 steps, from –1 to 1 ps being equidistant on a linear time scale and between 1 ps and 3.4 ns on a logarithmic time scale. 2000 spectra were recorded and a total of 4 scans were averaged for the measurement. Using a flow cell (Hellma, Suprasil) with 1 mm optical path length, sample solutions were circulated over the course of a measurement. The absorption of samples was set to ~ 0.7 per mm at the excitation wavelength. The solvent signal was recorded as a separate measurement and subtracted with proper scaling [24]. The instrumental time zero shift was determined as a function of wavelength via the optical Kerr effect and corrected for.

2.6 Nanosecond transient absorption spectroscopy

A detailed description of the setup is given elsewhere [18]. Nanosecond transient absorption spectra were acquired using an Edinburgh Instruments LP980 spectrometer in a right-angle geometry. The fourth harmonic (266 nm) pulses from a Nd:YAG laser (Spitlight 600, Innolas, 5 Hz repetition rate, pulse duration of 12 ns (FWHM)) served as the excitation. The beam had a diameter of ~8 mm. The average pulse energy was set to 2 mJ. As a probe beam a pulsed xenon lamp (Osram XBO 150 W/CR OFR) was utilized. A photomultiplier (Hamamatsu, PMT-900) was used to detect the transmitted probe light after being dispersed by a grating monochromator. Every 5 nm, kinetic traces were acquired and averaged over 64 acquisitions to obtain transient spectra. The sample solution was circulated by a peristaltic pump (REGLO Analog MS-2/8 from ISMATEC®) through a rectangular flow cell. In the direction of the pump its length amounted to 5 mm, in the probe direction to 10 mm. The samples absorption at the excitation wavelength amount to 1.6 per cm.

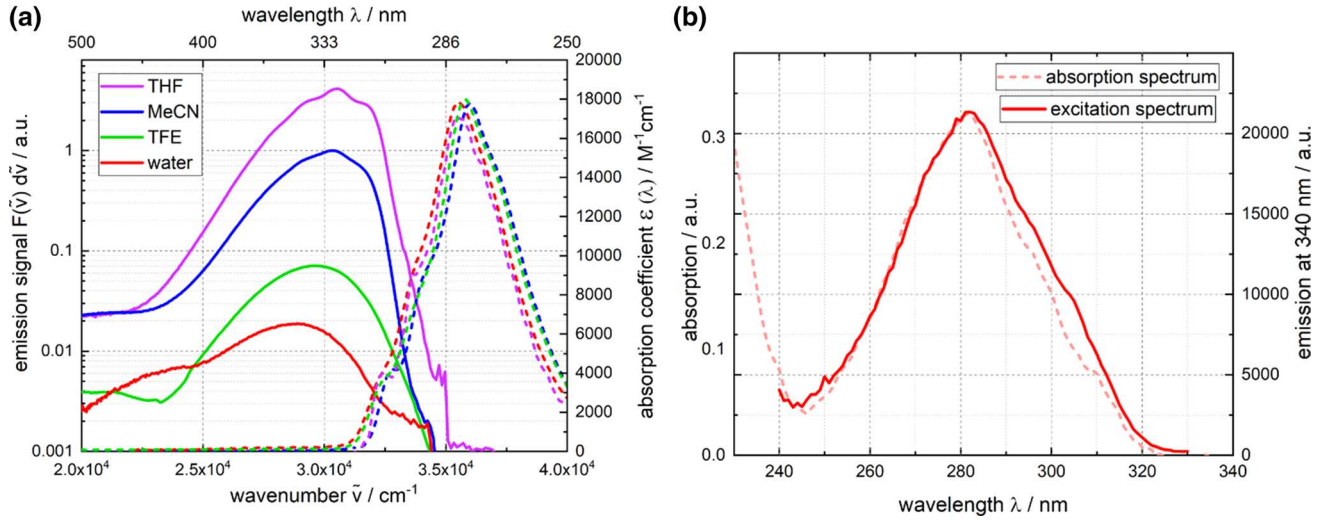

Fig. 1 **a** Fluorescence (logarithmic y-axis, solid lines) and absorption (coefficients, dashed lines) spectra of 2-CI in different solvents. The excitation wavelength for the fluorescence spectra was tuned to 260 nm. Fluorescence spectra are scaled so that their integrals are proportional to their fluorescence quantum yields Φ_{fl}. **b** Fluorescence excitation of 2-CI in comparison with its absorption spectrum. For the excitation spectrum the signal was probed at 340 nm

2.7 Data analysis

The measured data sets $S(\lambda, t)$ were analyzed globally with multi-exponential fit function convoluted with the instrumental response function (IRF):

$$S(\lambda, t) = IRF \otimes \sum_{i=1}^{n} S_i(\lambda) \cdot e^{-\frac{t}{\tau_i}}. \quad (2)$$

The procedure yields time constants τ_i, decay associated spectra $S_i(\lambda)$ (DAS, in the case of fluorescence measurements) and decay associated difference spectra (DADS, in the case of absorption measurements) [25, 26]. A spectrum $S_i(\lambda)$ parametrizes the spectral changes in the course of a process with time constant τ_i. For $S_i(\lambda) > 0$, it describes a signal decay and for $S_i(\lambda) < 0$ a rise. The sum of the spectra $S_i(\lambda)$, $\sum_{i=1}^{n} S_i(\lambda)$, equals the signal at time zero.

3 Results

3.1 Steady state spectroscopy of 2-CI in different solvents

The absorption band of 2-CI lowest in energy is located at wavenumbers larger than 30,000 cm^{-1} (see Fig. 1, Table 1 and ref. [9]). The band consists of a shoulder around 32,500 cm^{-1} and a maximum at 35,500 cm^{-1}. The absorption band features a weak positive solvatochromism, i.e., it shifts to smaller wavenumbers with increasing solvent polarity. Peak absorption coefficients ε_{max} determined here are in the range 17,000–18,000 M^{-1} cm^{-1} and depend only slightly on the solvent (see also Table 1). The present value for water of 17,800 M^{-1} cm^{-1} is somewhat higher than the value of 16,000 M^{-1} cm^{-1} reported earlier [9].

Table 1 Photophysical properties of 2-CI derived from steady-state experiments

	Water	TFE	MeCN	THF
λ_{abs}/nm	282	279	280	282
ε_{max}/ M^{-1} cm^{-1}	17,800 ± 120	17,050	17,800 ± 700	17,200 ± 570
λ_{em}/nm	342	333	329	328
Φ_{fl}	4.4×10^{-4}	1.3×10^{-3}	1.5×10^{-2}	5.7×10^{-2}
k_{rad}/s^{-1}	0.61×10^{8}	0.40×10^{8}	0.17×10^{8}	0.23×10^{8}
τ_{fl}^{SB}/ps	7	32	850	2500

Absorption maxima λ_{abs} of the absorption band lowest in energy are listed. Absorption coefficients ε_{max} correspond to the strongest absorption maxima. Wavelengths λ_{abs} and λ_{em} are retrieved from spectra obtained with constant wavelength bandpass. Experimental fluorescence quantum yields Φ_{fl} were determined with thymidine in water as a reference ($\Phi_{fl} = 1.32 \times 10^{-4}$ [16]). The radiative rate constants k_{rad} were determined via a Strickler–Berg analysis as described in the text. The last row gives predicted fluorescence lifetimes τ_{fl}^{SB}, whereby $\tau_{fl}^{SB} = \frac{\Phi_{fl}}{K_{RAD}}$

The fluorescence emission spectra of 2-CI in the different solvents peak around 30,000 cm^{-1} (see Fig. 1 and Table 1). As the absorption spectra they are subject to a weak positive solvatochromism. The impact of the solvent on the fluorescence quantum yield Φ_{fl} is pronounced. In water, it amounts to 4.4×10^{-4}. In THF, it is two orders of magnitude higher. This dependence is in agreement with previous studies

[9]. The fluorescence excitation spectra overlay favorably with the properly rescaled absorption spectrum exemplified in Fig. 1b for 2-CI in water. 2-CI, thus, obeys the Kasha-Vavilov rule [27].

To arrive at a first estimate for the excited state lifetime, particularly for 2-CI in water, a Strickler–Berg analysis was undertaken [28, 29]. For 2-CI, such an analysis is hampered by overlapping electronic transitions around 30,000 cm^{-1}. According to quantum chemical calculations [15] and gas phase spectroscopy [10] two $\pi\pi^*$ transitions termed L_a and L_b are located in this energetic region. For 2-CI, the L_b transition was found to be lowest in energy. The L_b transition features a smaller oscillator strength ($f = 0.092$) than the L_a one ($f = 0.307$) [15]. To isolate the L_b contribution to the band around 30,000 cm^{-1}, a procedure developed earlier [30] was used. The procedure rests on the assumption that a mirror image relation [29] exists between the fluorescence spectrum and that part of the absorption spectrum from which the fluorescence originates. Thus, the 2-CI fluorescence spectrum plotted on a wavenumber axis was flipped and shifted to overlay with the onset of the absorption spectrum (see Fig. 2). Hereby, the "trivial" frequency dependences of spontaneous emission (fluorescence) and absorption [29] was taken into account. The height of the flipped and shifted spectrum was scaled so that it approximately matches the absorption coefficient spectrum of 2-CI. The spectrum generated thereby entered the Strickler–Berg analysis. The radiative rate constants k_{rad} obtained are of the order of 0.5×10^8 s^{-1} (see Table 1). With these rate constants and the fluorescence quantum yields Φ_{fl}, fluorescence lifetimes τ_{fl}^{SB} can be predicted, according to $\tau_{fl}^{SB} = \frac{\Phi_{fl}}{k_{rad}}$. The lifetimes obtained for 2-CI in THF ($\tau_{fl}^{SB} = 2500$ ps) and in MeCN ($\tau_{fl}^{SB} = 850$ ps) compare favorably with the ones measured directly (2900 and 900 ps [9]). The lifetimes for the other two solvents will be considered in conjunction with the time resolved measurements.

3.2 Time resolved fluorescence spectroscopy of 2-CI in water

In previous studies on the 2-CI fluorescence [9, 10], its decay in water was not reported due to the limited time resolution of the instruments. Here, the decay is traced by femtosecond fluorescence Kerr gating [17, 18]. In these experiments, solutions of 2-CI in water were excited at 266 and 310 nm. For 266 nm excitation, 2-CI should predominately be promoted to the L_a state, the 310 nm excitation should favor L_b excitation [15]. 266 nm excitation causes a fluorescence signal peaking at 341 nm (Fig. 3) which is close to the value of the steady-state spectrum (cf. Fig. 1). The signal decays to zero on the 10 ps time scale. Closer inspection reveals a slight red-shift and broadening within ~ 1 ps. To retrieve time

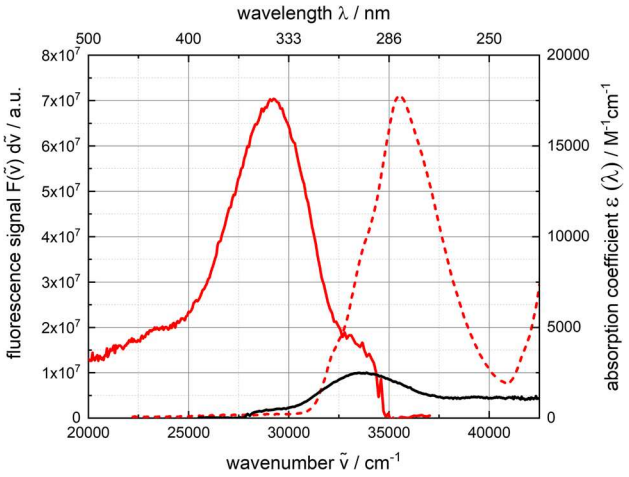

Fig. 2 Identification of the L_b band in the absorption spectrum of 2-CI in water. A synthetic absorption spectrum of the L_b state (black) was generated from the fluorescence spectrum (red) and compared with the experimental absorption spectrum (dotted red line). For details, see text

constants, the spectro-temporal behavior of the fluorescence was subject to a global analysis. A multi-exponential ansatz convoluted with instrumental response function served as a trial function. Two exponential terms proved necessary for a satisfactory fit of the measurement. The time constants retrieved are τ_{fl_1}=1.5 ps and τ_{fl_2}=7.9 ps (see Table 2). The value of τ_{fl_2} is close to the estimate based on the Strickler–Berg treatment (see above). The decay associated spectrum DAS_1 for the time constant τ_{fl_1} peaks at 328 nm and its height amounts to only ~ 1/3 of the one of DAS_2 which peaks at 351 nm (Fig. 5). By adjusting the polarization of the excitation light parallel and perpendicular positions, the time dependent anisotropy $r(t)$ was recorded. The anisotropy is close to zero throughout the time range covered.

Excitation of 2-CI in water with 310 nm pulses results in a time dependent fluorescence signal similar to the one for 266 nm excitation (Fig. 4). The emission again peaks around 341 nm and decays on the 10 ps time scale. The time constants retrieved by the global analysis amount to τ_{fl_1}= 2.5 ps and τ_{fl_2}= 7.6 ps and are, thus, close to the values for the 266 nm excitation. Also, the DAS exhibit similar shapes and relative heights (cf. Fig. 5). The time dependent anisotropy $r(t)$ does differ from the 266 nm experiment. Its initial value is 0.2. Within ~ 5 ps it decays to zero. However, after a few picoseconds the $r(t)$ curve fluctuates strongly since the fluorescence signals contributing go to zero as well. Therefore, this decay behavior of the anisotropy should not be interpreted.

Measurements with both excitation wavelengths revealed a bi-exponential decay when analyzing them with multi-exponential trial function. It is well known that on the picosecond time scale fluorescence spectra red-shift due to dielectric relaxation (dynamic Stokes shift) [31]. Such a shift

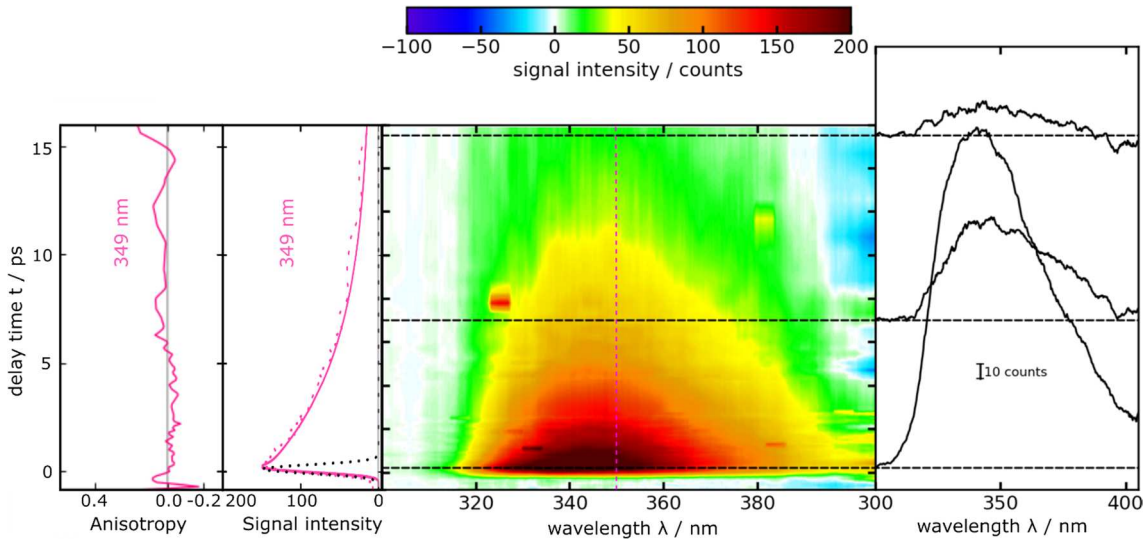

Fig. 3 Femtosecond transient fluorescence on 2-CI in water (~24 µM) as a function of detection wavelength λ and delay time t. The solution was excited at 266 nm. In the central contour representation, reddish hue represents large fluorescence signals. One representative time trace (349 nm) as well as a fit are shown on the left. The dotted black line represents the IRF as obtained from Raman scattering of the solvent. Selected spectra are depicted on the right. Their vertical positions correspond to the respective delay time. On the very left, the anisotropy as a function of time is plotted. The selected detection wavelength was 349 nm. The signal does not show a significant wavelength dependence

can "feign" a multi-exponential decay if the data set is analyzed with the trial function used here [32]. Thus, to clarify whether the bi-exponential decay is genuine, a second ansatz for the analysis was used. A normalized spectrally integrated fluorescence signal $I_{fl}(t)$ was computed according to

$$I_{fl}(t) = \frac{\int \frac{S_{fl}(\tilde{\nu},t)}{\tilde{\nu}^3} d\tilde{\nu}}{\int \frac{S_{fl}(\tilde{\nu},0)}{\tilde{\nu}^3} d\tilde{\nu}}. \quad (3)$$

Hereby, $S_{fl}(\tilde{\nu}, t)$ is the wavenumber $\tilde{\nu}$ and time t dependent fluorescence signal. $S_{fl}(\tilde{\nu}, 0)$ is this signal at time zero. The division by $\tilde{\nu}^3$ cancels the trivial wavenumber or frequency dependence [29]. The average time dependent emission wavenumber $\langle\tilde{\nu}\rangle(t)$ was computed via

$$\langle\tilde{\nu}\rangle(t) = \frac{\int \frac{S_{fl}(\tilde{\nu},t)}{\tilde{\nu}^3} \tilde{\nu} d\tilde{\nu}}{\int \frac{S_{fl}(\tilde{\nu},t)}{\tilde{\nu}^3} d\tilde{\nu}}. \quad (4)$$

As the above description has shown, the signals $S_{fl}(\tilde{\nu}, t)$ are very similar for excitation wavelengths of 266 and 310 nm. The 266 nm measurement offers a larger spectral coverage and a higher signal to noise ratio. The analysis was, thus, performed on the 266 nm measurement.

The time dependence of the spectrally integrated signal $I_{fl}(t)$ (Fig. 6) is very similar to wavelength resolved time traces depicted in Fig. 3. Indeed, a bi-exponential fit of $I_{fl}(t)$ taking the IRF into account yields time constants $\tau_{fl_1}^{int}$=1.5 ps (relative amplitude 0.4) and $\tau_{fl_2}^{int}$=8 ps (0.6) which are very close to those determined by the above global analysis. The average fluorescence wavenumber at time zero $\langle\tilde{\nu}\rangle(0)$ amounts to 29,300 cm^{-1}. It shifts to 27,900 cm^{-1} for "infinite" times. According to a single exponential fit, the time constant for this shift is 0.33 ps. This time constant is close to the average solvent relaxation time of water (0.4 ps [31]).

3.3 Time resolved UV/Vis absorption spectroscopy of 2-CI in different solvents

Obviously, time resolved fluorescence spectroscopy cannot reveal which states are populated in the course of the depletion of the primarily excited singlet state. Therefore, also time resolved UV/Vis absorption experiments were

Table 2 Summary of time constants for the decay of 2-CI in various solvents for the excitation with 266 nm

	Water	TFE	MeCN	THF
τ_1/ps	0.9	1.4	2.8	5.3
τ_2/ps	8.3	29	640	2600
τ_{fl_1}/ps	1.5 ± 0.4			
τ_{fl_2}/ps	7.9 ± 0.5			
τ_3/µs			1.56	1.56

τ_1, τ_2 obtained from femtosecond UV/Vis absorption measurements and τ_3 from nanosecond transient absorption experiments. τ_{fl_1} and τ_{fl_2} were retrieved from fs transient fluorescence measurements

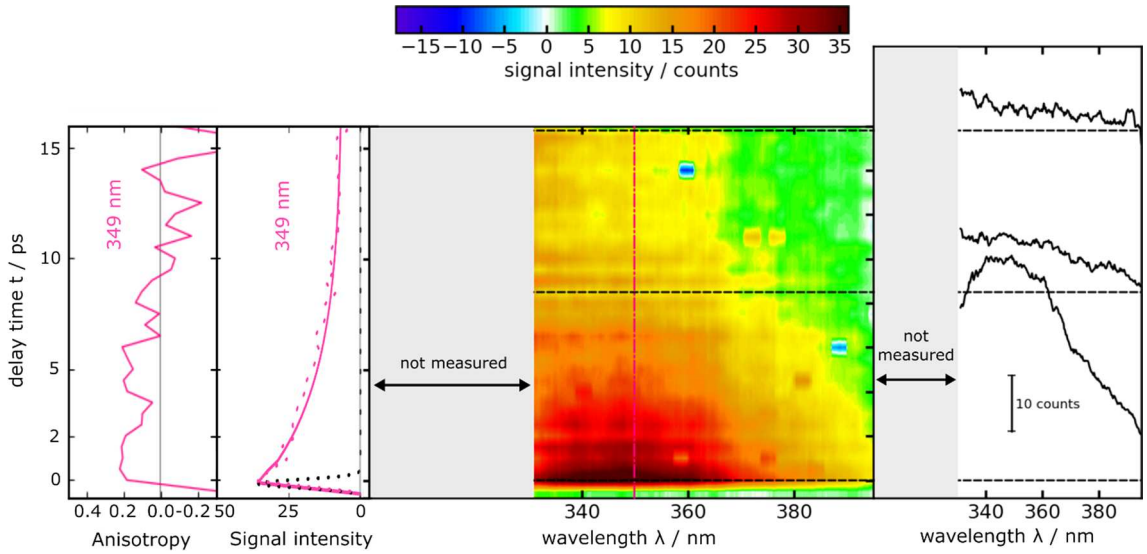

Fig. 4 Femtosecond transient fluorescence on 2-CI in water (~ 32 µM) as a function of detection wavelength and delay time. The solution was excited at 310 nm. For the description of the representation see Fig. 3

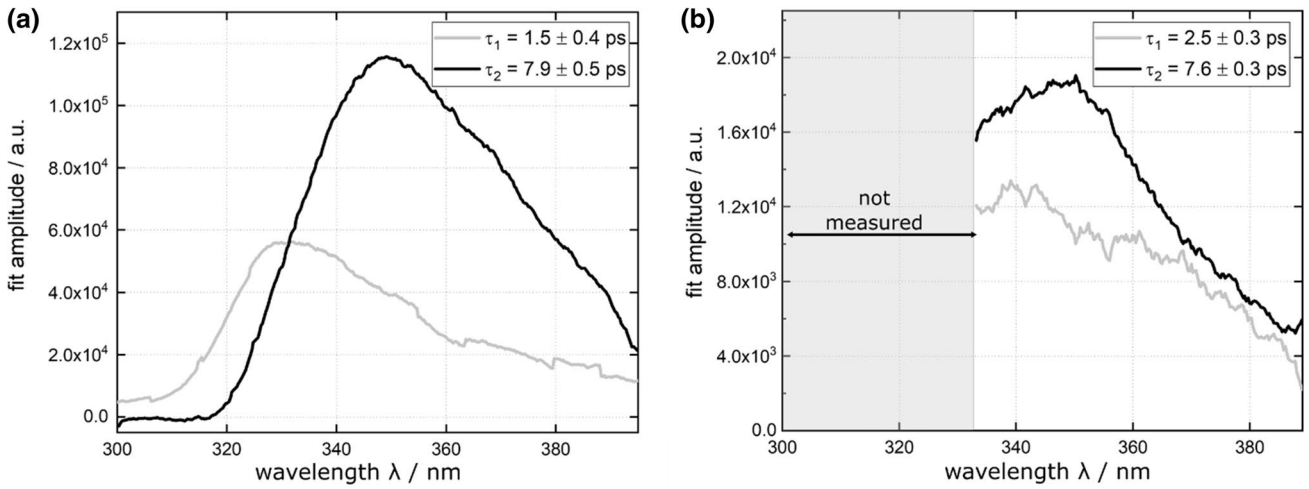

Fig. 5 Decay associated spectra derived from the fluorescence decays of 2-CI in water **a** for the excitation with 266 nm depicted in Fig. 3 and **b** for the excitation with 310 nm depicted in Fig. 4. The time constants derived from global fits are indicated

conducted. According to the above fluorescence experiments, the excitation wavelength has little impact on the decay kinetics. Therefore, for all absorption experiments, the excitation was tuned to 266 nm. For 2-CI in water, the excitation results in positive absorption changes throughout the spectral range covered (Fig. 7). No negative signals due to ground state bleach (GSB) or stimulated emission (SE) are recorded. The absence of GSB is due to small vanishing absorption coefficients of 2-CI in this range, cf. Fig. 1. The SE signal is expected in the spectral region of the fluorescence. Its absence indicates that it is overcompensated by excited state absorption (ESA). The ESA at time zero is characterized by peaks at 440 nm and ~ 750 nm. Within ~ 1 ps a slight signal decrease around 435 nm and a weak increase around 570 nm is observed. This results in a less structured difference spectrum. The overall signal decays to essentially zero on the 10 ps time scale.

The behavior in another protic solvent, namely TFE, is similar (Fig. 7). Around time zero the ESA peaks mentioned before at ~ 430 and 720 nm are observed. In addition, a positive difference absorption feature increasing toward the UV is discernible. Again, minor signal changes within a few picoseconds are recorded. The overall signal decay is slower than in water occurring with 20–30 ps. After that decay a weak absorption band peaking at 405 nm persists until the end of time range covered (3 ns).

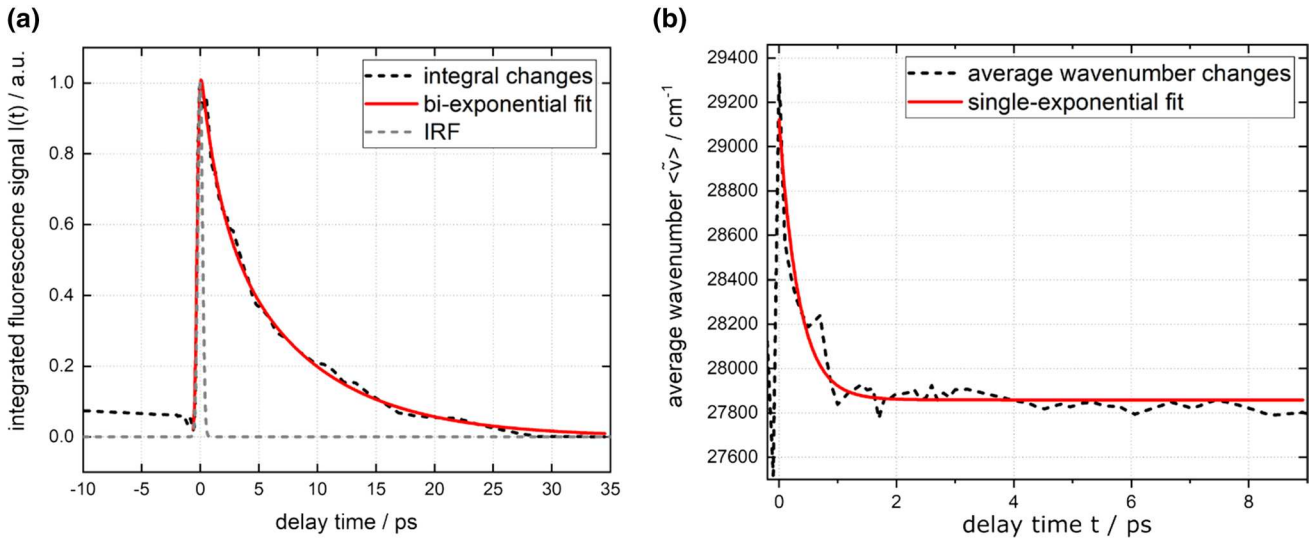

Fig. 6 Analysis of the fluorescence signal depicted in Fig. 3 using spectral integrals. **a** The spectrally integrated fluorescence signal $I_{fl}(t)$ (cf. Equation (3)) is plotted as a function of time (dotted black line). The red line represents the result of bi-exponential fit which takes the IRF into account. **b** The evolution of the average emission wavenumber $\langle\tilde{\nu}\rangle(t)$ (cf. Equation (4), dotted black line) and the result of a single-exponential fit (solid red line)

In the aprotic solvents MeCN and THF, similar spectral signatures as in the protic ones are observed around time zero (Fig. 8). Again, small spectral changes occur within a few picoseconds. The decay of the initial signature now takes much longer and occurs on the nanosecond time range. This is in line with the solvent dependence of the fluorescence lifetime reported earlier [9]. Importantly, on this time scale also a signal increase around 410 nm is observed. This rise is due to the population of a longer lived transient species—presumably the triplet state of 2-CI. According to the transient spectra at 3 ns, the species features an absorption peak at 420 nm and a shoulder at 380 nm. The same signature was observed in a nanosecond transient absorption experiment (Fig. 8). According to these experiments, the species exhibits a lifetime in the microsecond range in deoxygenated solutions (1.56 µs for 2-CI in MeCN as well as THF) which is in line with the tentative triplet assignment [33].

For a quantitative comparison of the 2-CI transient absorption in different solvents, the same analysis approach as for time resolved fluorescence was adopted. Measurements in all solvents could be fitted with a tri-exponential trial function. Hereby, one time constant was set to infinity to account for the signal persisting longer than 3 ns ("offset" in the following). The first time constant τ_1 ranges between 0.9 ps (water) and 5.3 ps (THF), see Table 2. The value for water is close to one determined by time resolved fluorescence spectroscopy (τ_{fl_1}=1.5 ps). The respective decay associated difference spectra $DADS_1$ are similar to each other with maxima around 460 nm and minima at 560 nm (Fig. 9). The minima are more pronounced in protic solvent. Relative to the other DADS the amplitudes are smaller and, thus, $DADS_1$ parametrizes small spectral changes. The second time constant τ_2 spreads between 8.3 ps (water) to 2600 ps (THF). The value for water is again very close to fluorescence time constant τ_{fl_2}=7.9 ps. The values for MeCN (τ_2 =640 ps) and THF (τ_2=2600 ps) are close to the reported fluorescence lifetimes (900 and 2900 ps [9]). In the $DADS_2$ maxima are located at 420, 560, and ~ 720 nm for the protic solvents. In the aprotic solvents, minima are found at 410 nm. These negative features parametrize the rise due to the population of a species with "infinite" lifetime. Accordingly, in the $DADS_3$ positive bands around 410 nm are seen for the aprotic solvents. For the protic ones, a weak if any signature is seen here.

4 Discussion

The essential experimental findings of this study are the first report of the fluorescence decay of 2-CI in water, the anisotropy of this fluorescence, the bi-exponential decay of the singlet state in all solvents considered as well as the population of the triplet state in aprotic solvents. Steady state (Strickler–Berg analysis) as well as time resolved fluorescence and absorption spectroscopy reveal a fluorescence lifetime of ~ 8 ps for 2-CI in water. In the Strickler–Berg analysis, one only arrives at this value when isolating the L_b contribution to the absorption band lowest in energy (cf. Fig. 2). This gives strong evidence that the emission originates from the L_b state. As all lifetimes derived via Strickler–Berg match the ones measured directly (cf. Tables 1 and 2), emission

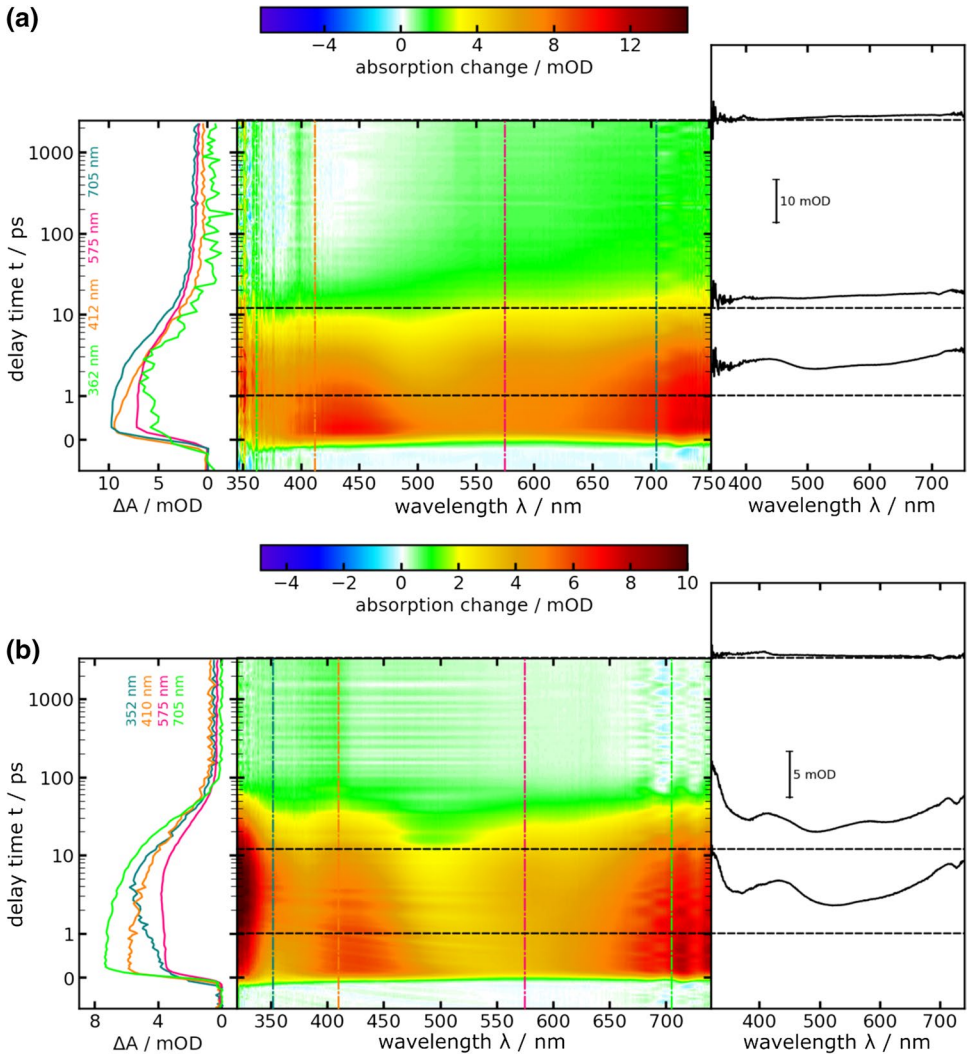

Fig. 7 Femtosecond UV/Vis absorption as a function of detection wavelength λ and delay time t on 2-CI in protic solvents. The solutions were excited at 266 nm. In the central contour representation, reddish hue stands for positive difference absorption due to ESA. The time axis is linear until 1 ps and logarithmic thereafter. Representative time traces are plotted on the left (vertical dashed lines in the contour plot indicate their spectral position). Selected difference spectra are depicted on the right. Their vertical positions (horizontal dashed lines) correspond to the respective delay time. **a** Solvent water, 2-CI concentration of 10 µM. **b** Solvent TFE, 2-CI concentration of 6.7 µM. For the measurement of 2-CI in water, the scattering of the second order excitation light from 532 to 553 nm was removed and spectra were interpolated in between

seems to occur from the L_b state in all solvents. The L_b lifetime decreases with increasing solvent polarity and proticity. The impact of the latter is particularly pronounced as a comparison of the behavior in MeCN (aprotic) and TFE (protic) shows. In MeCN (dielectric constant of 35.9 [33]) the lifetime is around 900 ps. In TFE with its smaller dielectric constant (26.7 [33]) the lifetime is around 30 ps.

The fluorescence anisotropy experiment confirms the emission out of the L_b state. With 266 nm excitation the (initial) anisotropy of the transient fluorescence is close to zero. As rotational depolarization occurs on a much longer time scale [34, 35] than the IRF time (~430 fs) of the experiment, this anisotropy value has to be related to non-parallel transition dipoles for excitation and emission. An initial anisotropy of zero implies that the two transition dipoles span an angle of 54.7° [34]. According to quantum chemical computations, the angle between the transition dipoles of the L_a and L_b states are very close to this value, namely 57° [15]. According to these computations, the 266 nm excitation addresses the L_a state. Within our IRF time (~430 fs), an internal conversion (IC) transition to the L_b state seems to occur from which all fluorescence detected here originates. Such a short transition time is in agreement with recent measurement on tryptophan, for which the $L_a \rightarrow L_b$ transition was shown to occur within less than 50 fs [36]. A similar transition time was derived from fluorescence anisotropy measurements on 5-methoxyindole [37]. The anisotropy of zero implies that also in terms of adiabatic energies the L_b state is the lowest. Thus, no L_a-L_b state switching occurs (situation as described by Fig. 8a in ref. [15]). Hebestreit et al. [10] have calculated the excited state dipole moments of the L_a and L_b state, respectively, and compared them to the experimental values from electronic Stark spectroscopy. They found a considerably smaller dipole moment for the L_a (3.44D) compared to the L_b state (4.95D) in 2-CI. This behavior is strikingly different from that of the other substituted indoles and also from the parent indole, in which the dipole moment of the L_a state is always larger than of the L_b

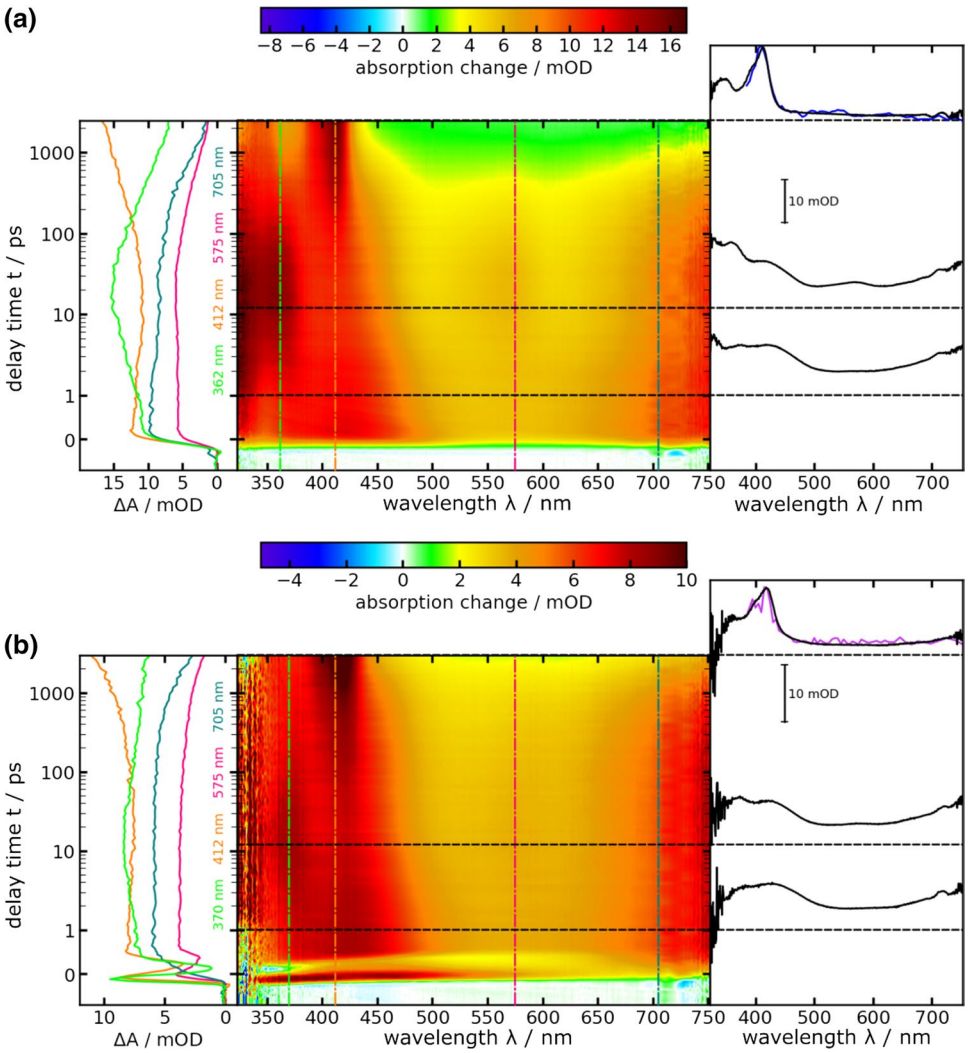

Fig. 8 Femtosecond UV/Vis absorption as a function of detection wavelength λ and delay time t on 2-CI in aprotic solvents. The solution was excited at 266 nm. For the description of the representation see Fig. 7. **a** Solvent MeCN, 2-CI concentration of 7.2 µM. **b** Solvent THF, 2-CI concentration of 11 µM. Overlaid with the spectra at 3 ns are the spectra from nanosecond transient absorption experiments (blue and purple). Neat THF exhibits strong signals around time zero which cannot be completely removed by subtraction. This explains the time zero pattern

state. Even for the structurally very similar 3- [38], 4- [39], and 5-CI [40] the L_a dipole moment is the larger one, leading to state inversion upon solvation in strongly polar solvents. It can thus be stated safely that it is the small dipole moment of the L_a state in 2-CI, which impedes state switching here. One has, however, to keep in mind that the notation of L_a and L_b for the excited ππ* states is somehow misleading, since the states tend to mix considerably and the original notation, introduced by Platt for cata-condensed hydrocarbons [41] and later extended to indole by Weber [42] is difficult to employ, the closer both ππ* states are located.

For 310 nm excitation, the (initial) anisotropy amounts to ~ 0.2. For this excitation wavelength, the L_b state is predominately excited [15] and from this state emission ought to occur. Thus, only one transition dipole is involved and the initial anisotropy should amount to 0.4 [34]. The observation that the experimental value is smaller than this prediction could be due to two reasons. (i) Even in chromophores with no overlapping electronic transitions the initial anisotropies are commonly somewhat smaller than 0.4 [1]. This matches our observation on the anisotropy behavior of thymidine in water which was investigated for calibration purposes (see Experimental Section). For thymidine, an initial anisotropy of 0.4 is expected. Our measurement yielded a value of ~ 0.3 in good agreement with an earlier study [20]. (ii) The L_a and L_b transition partially overlap and the L_a transition exhibit a much larger oscillator strength. Therefore, it is very likely that with the 310 nm excitation the L_b state is not excited exclusively. As discussed above a partial L_a excitation ought to shift the anisotropy toward zero. Presumably both contributions are responsible for the value of 0.2 for the 310 nm excitation.

These anisotropy experiments give clear evidence that for 2-CI in water the L_b state is populated within less than ~ 100 fs irrespective of the excitation wavelength. The similarity of the transient absorption signatures around time zero and the above Strickler–Berg argument strongly suggest that this also implies for all other solvents. The depopulation of the L_b state (time constant τ_2) occurs within ~ 8 ps to ~ 2500 ps, depending on the solvent. This depopulation

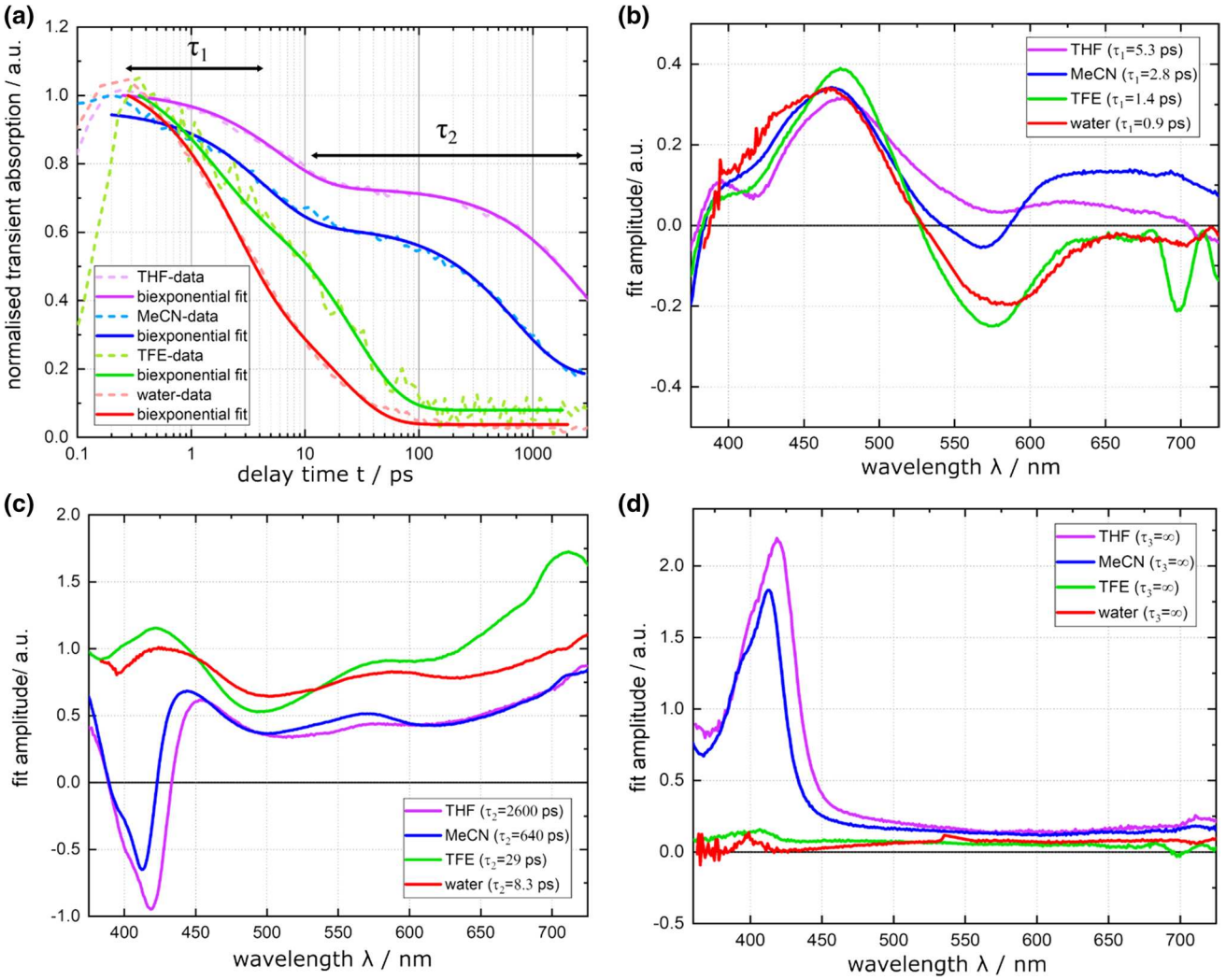

Fig. 9 Global analysis of the femtosecond UV/Vis absorption measurements on 2-CI in the four solvents as depicted in Figs. 7 and 8. **a** Time traces for a detection wavelength of 450 nm. The dashed lines are experimental values, the lines describe the fit results. The black arrows mark the spread of the time constants τ_1 and τ_2. **b** Decay associated difference spectra for the time constant τ_1, $DADS_1$. **c** $DADS_2$. **d** $DADS_3$, offset

goes along with the fluorescence decay. The solvent dependence of the time constant τ_2 can be rationalized by a crossing of the L_b state with a $^1\pi\sigma^*$ one as put forth by Domcke and Sobolewski [43, 44]. The $^1\pi\sigma^*$ state gets stabilized in polar solvents, thereby reducing the barrier for the IC transition. The present results indicate that in addition to the polarity also the proticity of the solvents has a huge impact on the lifetime τ_2. Gas phase data have shown that 2-CI forms binary cluster with water. Water seems to act as a hydrogen bond acceptor in this cluster [45]. For the isolated 3-CI-$(H_2O)_1$ cluster a direct lifetime measurement shows a distinct shortening of the fluorescence lifetime from 9.8 ns (monomer) to 3.6 ns (1:1 water cluster) [38]. Determination of fluorescence lifetimes for different cluster sizes and different solvent clusters are on the way to resolve the problem of how the solvent influences the fate of the excited state.

Prior to that a process with the time constant τ_1 of a few picoseconds occurs in all solvents. The analysis based on band integrals (cf. Fig. 6) excludes a dynamic Stokes shift as the underlying mechanism. Also, for the other solvents, the dynamic Stokes shift is an unlikely explanation. In acetonitrile, for instance, the time constant τ_1 amounts to 2.8 ps as compared to 0.9 ps for water, despite the fact that dielectric relaxation in acetonitrile is even faster than in water [31]. The underlying process might be vibrational cooling which is known to occur on the picosecond time scale [46, 47]. Yet, also vibrational cooling ought to retain the band integral [47–49]. Furthermore, for 2-CI in water, the τ_1 process is

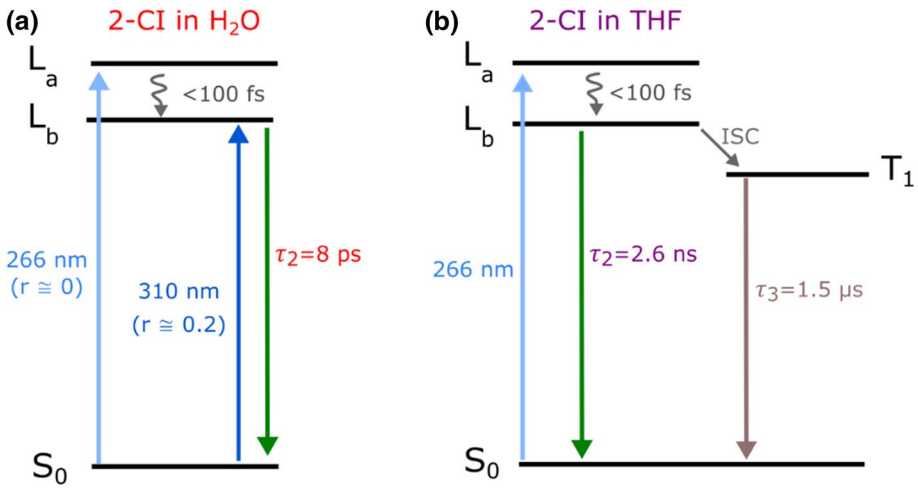

Fig. 10 Jablonski diagram of the excited state deactivation kinetics of 2-CI **a** in water and **b** THF

observed for 266 and 310 nm excitation. The 266 nm excitation deposits ~ 5000 cm^{-1} more vibrational excess energy in the molecule than the 310 nm one. If the τ_1 process were related to vibrational cooling, it should be less pronounced for 310 nm excitation. As this is not the case (cf. Fig. 5), vibrational cooling as the underlying process seems unlikely. Considering the rigid structure of 2-CI, different conformers and thereby a kinetic heterogeneity do not seem to be a plausible explanation. Aggregation can also cause such a heterogeneity [50, 51]. Yet, aggregation is expected to be solvent dependent [52–55]. As a bi-exponential behavior with similar relative amplitudes is observed in all solvents considered, also aggregation is not a probable explanation. Thus, at present, no consistent assignment can be given.

The assignment of the time constant τ_3 is less involved. The respective transient peaks around 420 nm (cf. Fig. 8) which are close to the absorption peak of the indole triplet in water [56–60]. In the respective experiments on indole [57], the triplet signature was accompanied by the ones of the indole cation and the solvated electron. In the femto- and nanosecond experiments on 2-CI these signatures are absent. This might be related with the strong electron withdrawing character of the cyano substituent. The measured time constant τ_3 for 2-CI in MeCN and THF is well in line with triplet lifetimes in general [33]. For indole and derivatives lifetimes in the range 12–50 µs were reported [56–58, 60, 61]. The value of ~ 2 µs is, thus, on the shorter side. We assign the species decaying with the time constant τ_3 to the triplet state of 2-CI. The signal of this state is nearly negligible in water as well as TFE and much larger in MeCN and THF (see $DADS_3$ in Fig. 9). As at present, no difference absorption coefficients of the 2-CI triplet are available, the triplet quantum yield Φ_T cannot be quantified. Assuming that the difference absorption coefficients are similar in all solvents and normalizing to identical excitation conditions, one can derive the following relative yields (with respect to MeCN): water (0.008), TFE (0.034), MeCN (1), and THF (0.7). Thus, triplet yields scale approximately as the lifetimes τ_2. This suggests that the rate constant (k_{ISC}) for intersystem crossing is similar in all solvents. In protic solvents, ISC is outcompeted by IC.

5 Conclusion

Femtosecond transient fluorescence experiments on 2-CI in water revealed a fluorescence decay of ~8 ps for both excitation wavelengths of 266 and 310 nm (see Fig. 10). This is a result of the ultrafast depletion of the L_a state in less than 100 fs. The respective anisotropy experiments provided strong evidence of the origin of this emission from the L_b state, regardless of the excitation wavelength. In time resolved transient absorption measurements, for all solvents, a bi-exponential decay was observed. The longer of the two (τ_2) proved to be strongly solvent dependent. In aprotic solvents (MeCN and THF), intersystem crossing to the triplet state contributes to the singlet decay. The triplet assignment was confirmed by nanosecond transient absorption experiments. The relative triplet yields are proportional to the lifetime τ_2. Quantum chemical computations aiming at the nature of the τ_1 process including channels through the $^1\pi\sigma^*$ state are under way.

Acknowledgements This work has been supported by the Deutsche Forschungsgemeinschaft (DFG, German Research Foundation), project numbers 396890929 (GRK 2482, "ModISC") and SCHM1043/14-1.

Funding Open Access funding enabled and organized by Projekt DEAL.

Data availability The datasets generated during and/or analysed during the current study are available from the corresponding author on reasonable request.

Declarations

Conflict of interest On behalf of all authors, the corresponding author states that there is no conflict of interest.

References

1. Lakowicz, J. R. (2006). *Principles of Fluorescence Spectroscopy* (3rd ed.). Springer.
2. Beechem, J. M., & Brand, L. (1985). Time-resolved fluorescence of proteins. *Annual review of biochemistry, 54*(1), 43–71. https://doi.org/10.1146/annurev.bi.54.070185.000355
3. Chen, Y., Liu, B., Yu, H.-T., & Barkley, M. D. (1996). The peptide bond quenches indole fluorescence. *Journal of the American Chemical Society, 118*(39), 9271–9278. https://doi.org/10.1021/ja961307u
4. Hu, J. J., He, P. Y., & Li, Y. M. (2021). Chemical modifications of tryptophan residues in peptides and proteins. *Journal of Peptide Science, 27*(1), e3286. https://doi.org/10.1002/psc.3286
5. Ladokhin, A. S. (2000). Fluorescence spectroscopy in peptide and protein analysis. *Encyclopedia of analytical chemistry* (pp. 5762–5779). John Wiley & Sons.
6. Xiong, Y., Shi, C., Li, L., Tang, Y., Zhang, X., Liao, S., Zhang, B., Sun, C., & Ren, C. (2021). A review on recent advances in amino acid and peptide-based fluorescence and its potential applications. *New Journal of Chemistry, 45*, 15180–15194. https://doi.org/10.1039/D1NJ02230J
7. Hansch, C., Leo, A., & Taft, R. W. (1991). A survey of Hammett substituent constants and resonance and field parameters. *Chemical Reviews, 91*(2), 165–195. https://doi.org/10.1021/cr00002a004
8. Talukder, P., Chen, S., Roy, B., Yakovchuk, P., Spiering, M. M., Alam, M. P., Madathil, M. M., Bhattacharya, C., Benkovic, S. J., & Hecht, S. M. (2015). Cyanotryptophans as novel fluorescent probes for studying protein conformational changes and DNA–Protein interaction. *Biochemistry, 54*(51), 7457–7469. https://doi.org/10.1021/acs.biochem.5b01085
9. Hilaire, M. R., Mukherjee, D., Troxler, T., & Gai, F. (2017). Solvent dependence of cyanoindole fluorescence lifetime. *Chemical Physics Letters, 685*, 133–138. https://doi.org/10.1016/j.cplett.2017.07.038
10. Hebestreit, M. L., Lartian, H., Henrichs, C., Kühnemuth, R., Meerts, W. L., & Schmitt, M. (2021). Excited state dipole moments and lifetimes of 2-cyanoindole from rotationally resolved electronic Stark spectroscopy. *Physical Chemistry Chemical Physics, 23*(17), 10196–10204. https://doi.org/10.1039/D1CP00097G
11. Ma, J., Pazos, I. M., Zhang, W., Culik, R. M., & Gai, F. (2015). Site-specific infrared probes of proteins. *Annual Review of Physical Chemistry, 66*, 357.
12. Liu, J., Feng, R.-R., Zhou, L., Gai, F., & Zhang, W. (2022). Photoenhancement of the C≡ N stretching vibration intensity of aromatic nitriles. *The Journal of Physical Chemistry Letters, 13*, 9745–9751. https://doi.org/10.1021/acs.jpclett.2c02418
13. Van Wilderen, L., Brunst, H., Gustmann, H., Wachtveitl, J., Broos, J., & Bredenbeck, J. (2018). Cyano-tryptophans as dual infrared and fluorescence spectroscopic labels to assess structural dynamics in proteins. *Physical Chemistry Chemical Physics, 20*(30), 19906–19915. https://doi.org/10.1039/C8CP00846A
14. Ahmed, I. A., Acharyya, A., Eng, C. M., Rodgers, J. M., DeGrado, W. F., Jo, H., & Gai, F. (2019). 4-Cyanoindole-2′-deoxyribonucleoside as a dual fluorescence and infrared probe of DNA structure and dynamics. *Molecules, 24*(3), 602. https://doi.org/10.3390/molecules24030602
15. Abou-Hatab, S., & Matsika, S. (2019). Theoretical investigation of positional substitution and solvent effects on n-Cyanoindole fluorescent probes. *The Journal of Physical Chemistry B, 123*(34), 7424–7435. https://doi.org/10.1021/acs.jpcb.9b05961
16. Onidas, D., Markovitsi, D., Marguet, S., Sharonov, A., & Gustavsson, T. (2002). Fluorescence properties of DNA nucleosides and nucleotides: A refined steady-state and femtosecond investigation. *The Journal of Physical Chemistry B, 106*(43), 11367–11374. https://doi.org/10.1021/jp026063g
17. Schmidt, B., Laimgruber, S., Zinth, W., & Gilch, P. (2003). A broadband Kerr shutter for femtosecond fluorescence spectroscopy. *Applied Physics B-Lasers and Optics, 76*(8), 809. https://doi.org/10.1007/s00340-003-1230-7
18. Haselbach, W., Kaminski, J. M., Kloeters, L. N., Müller, T. J. J., Weingart, O., Marian, C. M., Gilch, P., & Nogueira de Faria, B. E. (2022). Investigating a TADF emitter by time resolved near infrared spectroscopy. *Chemistry-A European Journal*. https://doi.org/10.1002/chem.202202809.
19. Kozma, I. Z., Krok, P., & Riedle, E. (2005). Direct measurement of the group-velocity mismatch and derivation of the refractive-index dispersion for a variety of solvents in the ultraviolet. *Journal of the Optical Society of America B, 22*(7), 1479–1485. https://doi.org/10.1364/JOSAB.22.001479
20. Gustavsson, T., Sharonov, A., & Markovitsi, D. (2002). Thymine, thymidine and thymidine 5′-monophosphate studied by femtosecond fluorescence upconversion spectroscopy. *Chemical Physics Letters, 351*(3), 195–200. https://doi.org/10.1016/S0009-2614(01)01375-6
21. Laimgruber, S., Schachenmayr, H., Schmidt, B., Zinth, W., & Gilch, P. (2006). A femtosecond stimulated Raman spectrograph for the near ultraviolet. *Applied Physics B, 85*(4), 557–564. https://doi.org/10.1007/s00340-006-2386-8
22. Laimgruber, S., Schmierer, T., Gilch, P., Kiewisch, K., & Neugebauer, J. (2008). The ketene intermediate in the photochemistry of ortho-nitrobenzaldehyde. *Physical Chemistry Chemical Physics, 10*(26), 3872–3882. https://doi.org/10.1039/B800616D
23. Fröbel, S., Buschhaus, L., Villnow, T., Weingart, O., & Gilch, P. (2015). The photoformation of a phthalide: A ketene intermediate traced by FSRS. *Physical Chemistry Chemical Physics, 17*(1), 376–386. https://doi.org/10.1039/C4CP03351E
24. Lorenc, M., Ziolek, M., Naskrecki, R., Karolczak, J., Kubicki, J., & Maciejewski, A. (2002). Artifacts in femtosecond transient absorption spectroscopy. *Applied Physics B, 74*(1), 19–27. https://doi.org/10.1007/s003400100750
25. Satzger, H., & Zinth, W. (2003). Visualization of transient absorption dynamics–towards a qualitative view of complex reaction kinetics. *Chemical Physics, 295*(3), 287–295. https://doi.org/10.1016/j.chemphys.2003.08.012
26. van Stokkum, I. H., Larsen, D. S., & Van Grondelle, R. (2004). Global and target analysis of time-resolved spectra. *Biochimica et Biophysica Acta -Bioenergetics, 1657*(2–3), 82–104. https://doi.org/10.1016/j.bbabio.2004.04.011

27. Klán, P., & Wirz, J. (2009). *Photochemistry of Organic Compounds. From Concepts to Practice*. Wiley.
28. Strickler, S. J., & Berg, R. A. (1962). Relationship between absorption intensity and fluoresence lifetime of molecules. *The Journal of Chemical Physics, 37*, 814–822. https://doi.org/10.1063/1.1733166
29. Parson, W. W. (2009). *Modern Optical Spectroscopy, With Exercises and Examples from Biophysics and Biochemistry* (Student). Springer.
30. Reiffers, A., Torres Ziegenbein, C., Schubert, L., Diekmann, J., Thom, K. A., Kühnemuth, R., Griesbeck, A., Weingart, O., & Gilch, P. (2019). On the large apparent Stokes shift of phthalimides. *Physical Chemistry Chemical Physics, 21*(9), 4839–4853. https://doi.org/10.1039/C8CP07795A
31. Bagchi, B., & Jana, B. (2010). Solvation dynamics in dipolar liquids. *Chemical Society Reviews, 39*(6), 1936–1954. https://doi.org/10.1039/B902048A
32. Marciniak, H., & Lochbrunner, S. (2014). On the interpretation of decay associated spectra in the presence of time dependent spectral shifts. *Chemical Physics Letters, 609*, 184–188. https://doi.org/10.1016/j.cplett.2014.05.006
33. Montalti, M., & Murov, S. L. (2006). *Handbook of photochemistry*. Taylor & Francis.
34. Kawski, A. (1993). Fluorescence anisotropy: Theory and applications of rotational depolarization. *Critical Reviews in Analytical Chemistry, 23*(6), 459–529. https://doi.org/10.1080/10408349308051654
35. Sahoo, H. (2022). Optical spectroscopic and microscopic techniques. *Springer Singapore*. https://doi.org/10.1007/978-981-16-4550-1
36. Jaiswal, V. K., Kabaciński, P., Nogueira de Faria, B. E., Gentile, M., de Paula, A. M., Borrego-Varillas, R., Nenov, A., Conti, I., Cerullo, G., & Garavelli, M. (2022). Environment-driven coherent population transfer governs the ultrafast photophysics of tryptophan. *Journal of the American Chemical Society*. https://doi.org/10.1021/jacs.2c04565
37. Shen, X., & Knutson, J. R. (2001). Femtosecond internal conversion and reorientation of 5-methoxyindole in hexadecane. *Chemical Physics Letters, 339*(3–4), 191–196. https://doi.org/10.1016/S0009-2614(01)00325-6
38. Schneider, M., Hebestreit, M.-L., Lindic, M. M., Parsian, H., Torres-Boy, A. Y., Álvarez-Valtierra, L., Meerts, W. L., Kühnemuth, R., & Schmitt, M. (2018). Rotationally resolved electronic spectroscopy of 3-cyanoindole and the 3-cyanoindole–water complex. *Physical Chemistry Chemical Physics, 20*(36), 23441–23452. https://doi.org/10.1039/C8CP04020F
39. Hebestreit, M.-L., Schneider, M., Lartian, H., Betz, V., Heinrich, M., Lindic, M., Choi, M. Y., & Schmitt, M. (2019). Structures, dipole moments and excited state lifetime of isolated 4-cyanoindole in its ground and lowest electronically excited singlet states. *Physical Chemistry Chemical Physics, 21*(27), 14766–14774. https://doi.org/10.1039/C9CP01618J
40. Oeltermann, O., Brand, C., Engels, B., Tatchen, J., & Schmitt, M. (2012). The structure of 5-cyanoindole in the ground and the lowest electronically excited singlet states, deduced from rotationally resolved electronic spectroscopy and ab initio theory. *Physical Chemistry Chemical Physics, 14*(29), 10266–10270. https://doi.org/10.1039/C2CP41094J
41. Platt, J. R. (1949). Classification of spectra of cata-condensed hydrocarbons. *The Journal of chemical physics, 17*(5), 484–495. https://doi.org/10.1063/1.1747293
42. Weber, G. (1960). Fluorescence-polarization spectrum and electronic-energy transfer in tyrosine, tryptophan and related compounds. *Biochemical Journal, 75*(2), 335.
43. Sobolewski, A. L., & Domcke, W. (1999). Ab initio investigations on the photophysics of indole. *Chemical Physics Letters, 315*(3–4), 293–298. https://doi.org/10.1016/S0009-2614(99)01249-X
44. Soboleski, A., Domcke, W., Dedonder-Lardeux, C., & Jouvet, C. (2002). Excited-state hydrogen detachment and hydrogen transfer driven by repulsive $^1\pi\sigma^*$ states: A new paradigm for nonradiative decay in aromatic biomolecules. *Physical Chemistry Chemical Physics, 4*, 1093–1100. https://doi.org/10.1039/B110941N
45. Henrichs, C., Zimmermann, S., Hebestreit, M.-L., & Schmitt, M. (2021). Excited state structure of isolated 2-cyanoindole and the binary 2-cyanoindole-(H2O) 1 cluster from a combined Franck-Condon and rotational constants fit. *Journal of Molecular Structure, 1233*, 130055. https://doi.org/10.1016/j.molstruc.2021.130055
46. Elsaesser, T., & Kaiser, W. (1991). Vibrational and vibronic relaxation of large polyatomic-molecules in liquids. *Annual Review of Physical Chemistry, 42*, 83–107. https://doi.org/10.1146/annurev.pc.42.100191.000503
47. Kovalenko, S. A., Schanz, R., Hennig, H., & Ernsting, N. P. (2001). Cooling dynamics of an optically excited molecular probe in solution from femtosecond broadband transient absorption spectroscopy. *Journal of Chemical Physics, 115*(7), 3256–3273. https://doi.org/10.1063/1.1380696
48. Schmierer, T., Schreier, W. J., Koller, F. O., Schrader, T. E., & Gilch, P. (2009). Impact of vibrational excitation on the kinetics of a nascent ketene. *Physical Chemistry Chemical Physics, 11*(48), 11596–11607. https://doi.org/10.1039/B915451E
49. Joens, J. A. (1993). Sum rule methods for the approximation of continuous electronic absorption spectra. *The Journal of Physical Chemistry, 97*(11), 2527–2534. https://doi.org/10.1021/j100113a011
50. Barzda, V., de Grauw, C. J., Vroom, J., Kleima, F. J., van Grondelle, R., van Amerongen, H., & Gerritsen, H. C. (2001). Fluorescence lifetime heterogeneity in aggregates of LHCII revealed by time-resolved microscopy. *Biophysical Journal, 81*(1), 538–546. https://doi.org/10.1016/S0006-3495(01)75720-7
51. Yan, Z.-Q., Yang, Z.-Y., Wang, H., Li, A.-W., Wang, L.-P., Yang, H., & Gao, B.-R. (2011). Study of aggregation induced emission of cyano-substituted oligo (p-phenylenevinylene) by femtosecond time resolved fluorescence. *Spectrochimica Acta Part A: Molecular Biomolecular Spectroscopy, 78*(5), 1640–1645. https://doi.org/10.1016/j.saa.2011.01.056
52. Nath, S., Pal, H., & Sapre, A. V. (2000). Effect of solvent polarity on the aggregation of C60. *Chemical Physics Letters, 327*(3–4), 143–148. https://doi.org/10.1016/S0009-2614(00)00863-0
53. Huang, H., Liang, C. H., & Penner-Hahn, J. E. (1998). X-Ray absorption spectroscopy of dimethylcuprates: Evidence for solvent-dependent aggregation. *Angewandte Chemie International Edition, 37*(11), 1564–1566. https://doi.org/10.1002/(SICI)1521-3773(19980619)37:11%3C1564::AID-ANIE1564%3E3.0.CO;2-5
54. Wang, S., & Bazan, G. C. (2004). Solvent-dependent aggregation of a water-soluble poly (fluorene) controls energy transfer to chromophore-labeled DNA. *Chemical Communications, 21*, 2508–2509. https://doi.org/10.1039/B410002F
55. Gao, B.-R., Wang, H.-Y., Hao, Y.-W., Fu, L.-M., Fang, H.-H., Jiang, Y., Wang, L., Chen, Q.-D., Xia, H., & Pan, L.-Y. (2010). Time-resolved fluorescence study of aggregation-induced emission enhancement by restriction of intramolecular charge transfer state. *The Journal of Physical Chemistry B, 114*(1), 128–134. https://doi.org/10.1021/jp909063d
56. Fischer, C. J., Gafni, A., Steel, D. G., & Schauerte, J. A. (2002). The triplet-state lifetime of indole in aqueous and viscous environments: significance to the interpretation of room temperature phosphorescence in proteins. *Journal of the American Chemical Society, 35*, 10359–10366. https://doi.org/10.1021/ja016609x
57. Bent, D. V., & Hayon, E. (1975). Excited state chemistry of aromatic amino acids and related peptides. III. Tryptophan. *Journal*

of the American Chemical Society, 97(10), 2612–2619. https://doi.org/10.1021/ja00843a004
58. Kowalska-Baron, A., Chan, M., Gałęcki, K., & Wysocki, S. (2012). Photophysics of indole, tryptophan and N-acetyl-L-tryptophanamide (NATA): Heavy atom effect. *Spectrochimica Acta Part A: Molecular Biomolecular Spectroscopy, 98*, 282–289. https://doi.org/10.1016/j.saa.2012.08.017
59. Galley, W. C., & Purkey, R. M. (1970). Role of heterogeneity of the solvation site in electronic spectra in solution. *Proceedings of the National Academy of Sciences, 67*(3), 1116–1121. https://doi.org/10.1073/pnas.67.3.1116
60. Pernot, C., & Lindqvist, L. JJo. P. (1976). Laser photolysis of indole in cyclohexane. *Joural of Photochemistry, 6*(3), 215–220. https://doi.org/10.1016/0047-2670(76)85066-6
61. Kowalska-Baron, A., Choudhary, P., & Montes, D. (2011). The effect of immobilization in the PVA films on the fluorescence and phosphorescence lifetime of indole and its derivatives. *Biotechnology Food Science, 2*, 3–14. https://doi.org/10.34658/bfs.2011.75.2.3-14

5.3. References for Small Fluorescence Quantum Yields (Publication III)

Title: References for Small Fluorescence Quantum Yields

Authors: Mahbobeh Morshedi, Simon L. Zimmermann, David Klaverkamp, Peter Gilch

Published in: Journal of Fluorescence

Year: 2024

Impact Factor: 2.6 (2023)

My Contributions to the Publication:

- acquisition of steady state and time resolved spectra
- analysis of spectral results and generating the corresponding figures
- computation of fluorescence quantum yields
- conducting the literature research
- composition of the manuscript (original draft)

Journal of Fluorescence
https://doi.org/10.1007/s10895-024-03729-2

RESEARCH

References for Small Fluorescence Quantum Yields

Mahbobeh Morshedi[1] · **Simon L. Zimmermann**[1] · **David Klaverkamp**[1] · **Peter Gilch**[1]

Received: 14 March 2024 / Accepted: 11 April 2024

Abstract

Three compounds with fluorescence quantum yields in the range of 10^{-5} to 10^{-4} and emission spectra covering the UV/Vis spectral range are suggested as new references for the determination of small fluorescence quantum yields. The compounds are thymidine (dT) in water, dibenzoylmethane (DBM) in ethanol, and malachite green chloride (MG) in water, representing the blue, green, and red regions of the spectrum, respectively. All compounds are easily handled, photostable, and commercially available. Furthermore, these compounds exhibit a mirror-image symmetry between their absorption and fluorescence spectra. This symmetry, along with closely aligned fluorescence excitation and absorption spectra, confirms that the observed emissions originate from the compounds themselves. The fluorescence quantum yields were determined via a relative approach as well as Strickler-Berg analysis in conjunction with time resolved fluorescence spectroscopy. Within the respective error margins, the two approaches yielded identical results.

Graphical Abstract

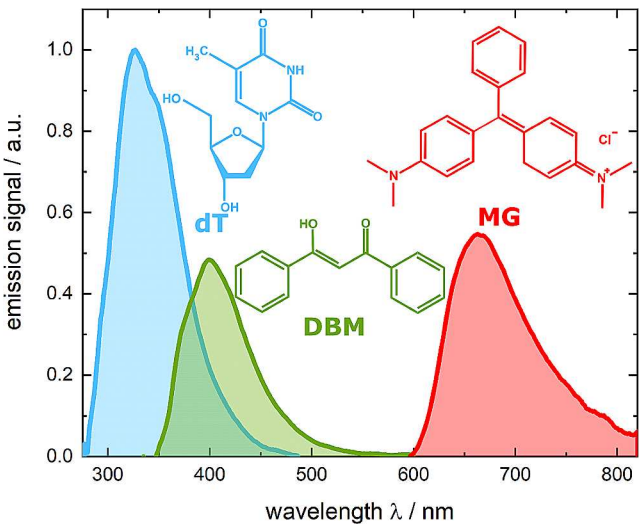

Keywords Fluorescence quantum yield · Time resolved spectroscopy · Strickler-Berg analysis · Thymidine · Dibenzoylmethane · Malachite green chloride

✉ Peter Gilch
gilch@hhu.de

Mahbobeh Morshedi
morshedi@hhu.de

Simon L. Zimmermann
simon.zimmermann@hhu.de

David Klaverkamp
david.klaverkamp@hhu.de

[1] Institut für Physikalische Chemie, Heinrich-Heine-Universität Düsseldorf, Universitätsstr. 1, 40225 Düsseldorf, Germany

Published online: 15 May 2024

Introduction

The fluorescence quantum yield $\Phi_{fl.}$ is a key parameter of molecular chromophores. It is given by the ratio of the number of photons emitted *via* fluorescence to the number of photons absorbed by a chromophore. From this definition, it is immediately clear that the yield $\Phi_{fl.}$ is a crucial figure of merit in fluorescence applications. For instance, optical brighteners [1, 2], ingredients of text markers [3, 4], emitters for organic light-emitting diodes (OLEDs) [5, 6], and fluorescence labels for modern microscopy [7] ought to feature yields $\Phi_{fl.}$ close to one. Furthermore, based on these yields, reliable estimates of lifetimes of primary molecular excitations can be made [8]. This gives important first glimpses on the photophysics and photochemistry of a chromophore and facilitates the planning of time resolved spectroscopy [9]. Additionally, precise determinations of the yield $\Phi_{fl.}$ are essential for the quantitative interpretation of Förster resonance energy transfer (FRET) experiments [10, 11].

It is, thus, no surprise that various techniques to determine these yields have been developed. They can be divided into absolute and relative ones. In absolute calorimetric approaches [12, 13], small temperature increases caused by the illumination of a sample are recorded. The temperature increase is approximately proportional to 1-$\Phi_{fl.}$. Calorimetric determinations can mostly be found in the pre-1990s literature. Nowadays, absolute determinations often make use of integrating spheres [14, 15]. With these spheres, signals proportional to the emitted and absorbed light fluxes are recorded. The ratio of these quantities is approximately equal to the yield $\Phi_{fl.}$. Contrary to the absolute methods, for which not so common set-ups are required, relative determinations rely on a widely-used instrument, namely a fluorescence spectrometer. In a relative determination, the spectrally integrated fluorescence signal of a sample is compared with the respective integral of a suitable reference (cf. Equation (4)) [16, 17]. Often solutions of dye molecules serve as a reference [18]. References based on the Raman scattering of neat solvents have also been reported [19].

Therefore, reference materials with approved and certified fluorescence quantum yields are particularly important for many users of fluorescence methods. According to Brouwer [20], the majority of these reference compounds have high fluorescence quantum yields $\Phi_{fl.}$, commonly exceeding 0.5. Many chromophores exhibit yields $\Phi_{fl.}$ many orders of magnitude smaller. Based on the relation (Eq. (1)) between the yield $\Phi_{fl.}$ and rate constants for the radiative (k_{rad}) as well as the non-radiative decay (k_{nr})

$$\Phi_{fl} = \frac{k_{rad}}{k_{rad} + k_{nr}} \tag{1}$$

a lower boundary for this yield can be estimated. We hereby restrict ourselves to organic chromophores with allowed lowest energy singlet transitions. For such chromophores, the radiative rate constant k_{rad} is of the order of 10^8 s^{-1} [9]. Internal conversion (IC) [21, 22], intersystem crossing (ISC) [21, 23–25], excitation energy (EET) [26] as well as electron transfer (ET) [27, 28], and photochemical transformations [28] can lead to non-radiative decays. The upper limit for rate constants of all of these processes results from nuclear motions [21, 29]. Characteristic frequencies of these motions are the ones of molecular vibrations with values of $\sim 10^{13}$-10^{14} s^{-1} [21, 30]. Thus, molecules with allowed transitions and ultrafast non-radiative decays, i.e., k_{nr}=10^{13}-10^{14} s^{-1}, will exhibit fluorescence quantum yields $\Phi_{fl.}$ of the order of 10^{-6}-10^{-5}. Obviously, for molecules with (partially) forbidden transitions, even smaller values may be found. Fluorescence quantum yields $\Phi_{fl.}$ many orders of magnitude smaller than one were indeed often observed experimentally. DNA and RNA bases, for instance, feature yields of $\sim 10^{-4}$ [31]. Photoreactive molecules like *trans*-azobenzene ($\sim 10^{-7}$ [32]), *cis*-stilbene ($\sim 10^{-5}$ in acetonitrile [33]), and rhodopsin ($\sim 10^{-5}$ [34]) exhibit even smaller yields. Triplet sensitizers like xanthone ($\sim 10^{-4}$ in ethanol [35]) and thioxanthone ($\sim 10^{-5}$ in cyclohexane [36]) are also examples for chromophores with very small yields. These examples emphasize the important role of compounds with small fluorescence quantum yields in diverse fields and underscore the need for establishing new reference materials to precisely quantify these yields. Relative determinations of such small fluorescence quantum yields are hampered by the predominance of references with yields of the order of one. As any quantitative comparison, the relative determination of these yields is facilitated if sample and reference exhibit similar signal strengths [37]. This similarity ensures that the measured fluorescence intensities are within the dynamic range of the instrument, thereby reducing errors associated with instrument sensitivity and signal detection limits [38, 39].

Here, we suggest and characterize three references with yields in the range of 10^{-5}-10^{-4} and emission spectra covering the UV/Vis range. Fluorescence quantum yields $\Phi_{fl.}$ of the compounds were determined with the relative approach as well as utilizing the relation between this yield, the radiative rate constant k_{rad}, and the fluorescence lifetime $\tau_{fl.}$ (Eq. (2)) [8],

$$\Phi_{fl} = k_{rad}\tau_{fl.} \tag{2}$$

The radiative rate constant k_{rad} was retrieved from absorption and fluorescence emission spectra *via* the Strickler-Berg relation (cf. Equations (5) and (6)) [40, 41]. This relation can be applied provided that the same pair of electronic states is involved in the absorption and the emission

process. Furthermore, the Condon approximation must be valid [42]. A mirror-image relationship between absorption and emission spectra is an indicator that these conditions are fulfilled [21]. Thus, molecules not obeying this relation were discarded. The fluorescence lifetime $\tau_{fl.}$ was measured using fluorescence Kerr gating [36, 43]. For the weakly fluorescent samples considered here, signals of impurities might surmount the ones of the nominal sample [44]. Matching absorption and fluorescence excitation spectra indicate that the fluorescence indeed (predominately) stems from the sample and not an impurity. Thus, for all samples this was investigated. In addition to these fundamental criteria, also practical ones were considered. Chromophores and solvents commercially available in high purities were selected. The chemical and photochemical stability of chromophores in the given solvent were also a criterium.

Based on these criteria, the following three chromophore/solvent combinations were identified and characterized. The combinations are thymidine (dT) in water, dibenzoylmethane (DBM) in ethanol, and malachite green chloride (MG) in water (see Fig. 1). In this order, they cover the blue, green, and red regions of the UV/Vis range.

For dT in water, previous determinations yielded a fluorescence quantum yield $\Phi_{\mathrm{fl.}}$ of the order of 10^{-4} [45, 46]. For the other two chromophores, reported lifetimes in the range of 100 fs – 1 ps [47–51] suggested yields of the same magnitude. We will also report on a molecule, namely *N, N*-dimethyl-4-nitroaniline (DpNA), which was discarded as determinations based on the relative approach and the one based on the Strickler-Berg analysis in combination with a lifetime measurement did not match.

Following common practice in fluorescence spectroscopy and for ease of handling, solutions were *not* de-oxygenated. Oxygen quenching should essentially not affect yields $\Phi_{\mathrm{fl.}}$ of the compounds listed in Fig. 1. Assuming diffusion limited oxygen quenching (rate constant $k_q \sim 10^{10}\ \mathrm{M^{-1}\ s^{-1}}$ [9]) and inserting a typical concentration of dissolved oxygen ($[O_2] \sim 10^{-3}\ \mathrm{M}$ [9]), one arrives at a time constant τ_{O_2} for oxygen quenching of the order of 100 ns. This is many orders of magnitude longer than the fluorescence lifetimes $\tau_{fl.}$ measured for the compounds in Fig. 1. Thus, oxygen quenching will not affect their fluorescence lifetimes, and according to Eq. (2), the yield $\Phi_{\mathrm{fl.}}$. However, oxygen quenching may affect the yields of the references employed in the relative determinations. The respective compounds feature fluorescence lifetimes $\tau_{fl.}$ in the 1–10 ns range which is closer to the lifetime τ_{O_2}. To avoid systematic errors, references with reported fluorescence quantum yields for aerated solutions were employed.

Experimental Section

Samples

Thymidine (≥ 99.0%) (CAS ID: 50-89-5), L-tyrosine (≥ 99.8%), and malachite green chloride (≥ 90.0%) (CAS ID: 569-64-2) were purchased from Sigma-Aldrich, dibenzoylmethane (99.01%) (CAS ID: 120-46-7) from BLDpharm, coumarin-1 (99.9%) from Acros Organics, rhodamine 101 from Radiant Dyes Laser & Accessories GmbH, *N, N*-dimethyl-4-nitroaniline (≥ 98%) from Tokyo Chemical Industry, water (HPLC gradient grade) from Fisher Chemical, ethanol (≥ 99.8%) from Sigma-Aldrich, and acetonitrile (HPLC gradient grade) from Chem Solute. All measurements were performed at room temperature (~ 20 °C).

Steady State Measurements

Steady state absorption spectra were recorded using Lambda 19 and 1050 + spectrometers from Perkin Elmer. Fluorescence spectra were measured with a FluoroMax-4 (Horiba Scientific). Spectra were corrected for the spectral sensitivity of the instrument. For all steady state measurements, fused

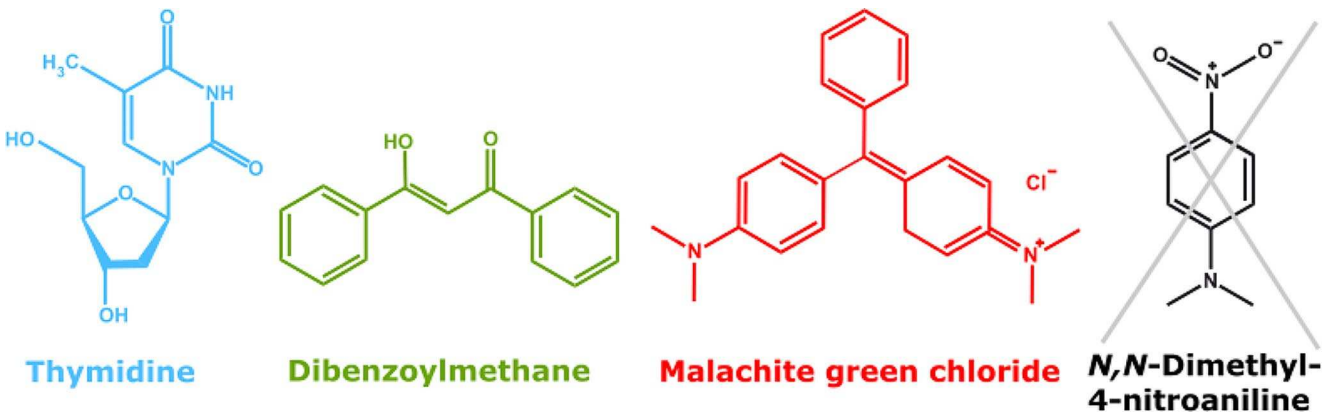

Fig. 1 Chemical structures of thymidine, dibenzoylmethane, malachite green chloride, and *N, N*-dimethyl-4-nitroaniline. The first three molecules plotted in different colors are suggested as references, the last one was discarded

silica cells (from Hellma Analytics) with a path length of 1 cm were employed. In the steady state fluorescence experiments, the sample absorption at the excitation wavelength was kept at ≤ 0.05 for a path length of 1 cm. The small absorption values avoid inner filter effects, i.e. re-absorption of emitted fluorescence, and more importantly ensures a linear scaling between the absorption values and the fluorescence signals. Equation (4) for the relative determination of the fluorescence quantum yields is based on such a scaling. The excitation and emission bandpasses were set to 5 nm for the steady state measurements of all compounds and their respective references. Also, the other settings of the fluorescence spectrometer were identical for samples and references. For the relative determination of the fluorescence quantum yields $\Phi_{fl.}$ of DpNA in acetonitrile, dT in water, DBM in ethanol, and MG in water, the following references were used, respectively: coumarin 1 (C-1) in de-oxygenated water ($\Phi^r_{fl} = 0.055$, note that the value is not significantly affected by oxygen [52]), tyrosine (Ty) in aerated water ($\Phi^r_{fl} = 0.21 \pm 0.01$ [53, 54]), C-1 in de-oxygenated water ($\Phi^r_{fl} = 0.055$ [52]), and rhodamine 101 (Rh 101) in aerated ethanol ($\Phi^r_{fl} = 0.913 \pm 0.046$ [55]). The samples and their respective references were excited at wavelengths close to their absorption maxima, while care was taken to ensure the coverage of their entire emission spectra. The region (~5 nm) around the excitation was avoided. The fluorescence spectra of all samples and their respective references were corrected for the Raman effect by subtracting a suitably scaled spectrum of the solvent, which was recorded under identical conditions.

Time Resolved Fluorescence Measurements

The setup was described in detail elsewhere before [36, 43]. A 1 kHz Ti:Sa laser amplifier system (Coherent Libra) was employed as a pulse source. Its output has a wavelength of 800 nm and a pulse duration of ~100 fs (full width half maximum, FWHM). For the experiment on DpNA in acetonitrile, the excitation wavelength was set to 400 nm. To this end, a portion of the output was converted (in a BBO crystal type I, 29°, 1 mm) to a wavelength of 400 nm by frequency doubling. The beam had an energy per pulse of 1 µJ at the sample location. For the experiments on dT in water and DBM in EtOH, the excitation wavelength was set to 266 nm. To this end, a portion of the output was initially converted (in a BBO crystal type I, 29°, 1 mm) to a wavelength of 400 nm by frequency doubling. Subsequently, the sum frequency was generated (in another BBO crystal, type II, 55.5°, 0.5 mm) to obtain a wavelength of 266 nm from the frequency doubled and the fundamental beam. At the sample location the beam had a diameter of 80 µm (FWHM) and a pulse energy of 1 µJ. For the measurement on MG in water, the excitation wavelength was tuned to 580 nm. To this end, a part of the output was directed to a TOPAS-White non-collinear optical parametric amplifier system. The TOPAS was set to generate pulses peaking at 580 nm with an energy of 0.9 µJ per pulse. The generation of the gate pulses and the operation of the Kerr gate followed the description in ref. [36]. The width of the instrumental response function (IRF), as obtained from Raman scattering of the solvent, was about 250, 270 and 220 fs (FWHM) for 400, 266 and 580 nm excitation light, respectively. For the experiment on DpNA in acetonitrile, the integration time was set to 1 s. Between −5 and 3 ps, the delay time was varied linearly in 60 steps. A total of 13 scans were averaged. For the measurement on dT in water, the integration time for each spectrum was set to 1 s. One scan consisted of 30 equidistant steps between −2 and 3 ps. A total of 14 scans were averaged. For the experiment on DBM in EtOH, the integration time of 2 s was set for each spectrum. In each scan, there were 60 equidistant steps on a linear time axis from −2 to 3 ps. 22 scans were averaged. For the experiment on MG in water, the integration time was set to 1 s. Between −2 and 3 ps, the delay time was varied linearly in 60 steps. A total of 110 scans were averaged. The solutions were circulated through a flow cell (custom made QX, Hellma Analytics) with a path length of 1 mm by a peristaltic pump (REGLO Analog MS-2/8 from ISMATEC®). Signals on solutions of DpNA, dT, DBM, and MG (concentrations of ~0.5 mM, ~1 mM, ~1.3 mM, and ~70 µM, respectively) as well as the neat solvent were recorded. The solvent contributions were subtracted after proper scaling. All time resolved spectra were corrected for the spectral sensitivity of the instrument.

Data Analysis

Time resolved data sets *S(λ, t)* were analyzed globally with a multi-exponential fit function convoluted with the instrumental response function (IRF),

$$S(\lambda, t) = IRF \otimes \sum_{i=1}^{n} S_i(\lambda) \cdot e^{-\frac{t}{\tau_i}}. \quad (3)$$

The fit yields time constants τ_i and decay associated spectra $S_i(\lambda)$ (DAS) [56, 57].

Estimates of Error Margins

For the determination of the statistical error of the yield Φ^{rel}_{fl} (measured by the relative method) and absorption coefficient (ε), multiple independent measurements were performed and the mean value was calculated [58]. The corresponding error margins denote the standard deviations from the mean [58]. The error margins of the reference yield

Φ_{fl}^{r}, if available, were accounted for by error propagation. To determine the error of the radiative rate constant k_{rad}, the error of the respective integrals (see Eq. (5)) entered an error propagation analysis [58]. The error margins in the time constants $\tau_{fl.}$ represent the deviations of the fit from the fluorescence decay data. These margins are determined through exhaustive search error analysis, utilizing the chi-squared (χ^2) statistics to evaluate the quality of the fit by taking into account the correlation among all the fit parameters [59]. The quoted error in the fluorescence quantum yield Φ_{fl}^{SB} (determined through the time resolved method) reflects the propagated errors associated with both the radiative rate constant k_{rad} and the fluorescence lifetime $\tau_{fl.}$.

Results and Discussion

DpNA and its derivative 4-nitroaniline were shown to undergo ultrafast IC with sub-picosecond time constants [60, 61]. Thus, a fluorescence quantum yield $\Phi_{\mathrm{fl.}}$ of the desired magnitude is to be expected. DpNA in acetonitrile exhibits a structureless absorption band lowest in transition energy peaking around 394 nm (see Fig. 2). The fluorescence spectrum peaks at 480 nm. The spectra converted into the transition dipole representation [41, 62] reveal that the mirror-image relationship holds approximately (see Fig. S1 in the Online Resource). The fluorescence excitation spectrum slightly deviates from the properly scaled absorption spectrum shown in Fig. 2b for DpNA in acetonitrile. Its absorption coefficient $\varepsilon_{\max}$ was determined to be $(2.30 \pm 0.08) \times 10^4\ \mathrm{M^{-1}cm^{-1}}$, which is in line with the previously reported value of $2.42 \times 10^4\ \mathrm{M^{-1}cm^{-1}}$ [63]. For the relative determination of the fluorescence quantum yield, DpNA dissolved in acetonitrile was excited close to the maximum at 400 nm (see Fig. 2). The resulting fluorescence signal was compared to the one of C-1 in water. The fluorescence quantum yield based on the relative approach Φ_{fl}^{rel} was computed using Eq. (4) [8]

$$\Phi_{fl}^{rel} = \Phi_{fl}^{r} \frac{\int S_{fl}^{s}(\lambda)\, d\lambda}{\int S_{fl}^{r}(\lambda)\, d\lambda} \frac{A^{r}}{A^{s}} \left(\frac{n^{s}}{n^{r}}\right)^{2}. \tag{4}$$

Here, Φ_{fl}^{r} is the fluorescence quantum yield of the reference, $\int S_{fl}^{s,r}(\lambda)\, d\lambda$ are the spectral integrals of the fluorescence for sample and reference. $A^{s,r} < 0.05$ are the absorptions of sample and reference at the excitation wavelength, and $n^{s,r}$ denotes the refractive index of the solvent of the sample or the reference. Values complied in ref. [52, 64] were inserted. With these inputs, a yield Φ_{fl}^{rel} of $(5.12 \pm 0.06) \times 10^{-5}$ results for DpNA in acetonitrile.

Using the spectra depicted in Fig. 2, a Strickler-Berg analysis was conducted. In this analysis, the radiative rate constant k_{rad} is obtained from spectral integrals (covering a part) of the absorption spectrum and the fluorescence spectrum (Eqs. (5, 6)) [40, 41],

$$k_{rad} = \frac{8\pi \ln(10)\, c_0 n^2}{N_A} \left\langle \tilde{\nu}^{-3} \right\rangle^{-1} \int \frac{\varepsilon(\tilde{\nu})\, d\tilde{\nu}}{\tilde{\nu}}, \tag{5}$$

$$\left\langle \tilde{\nu}^{-3} \right\rangle^{-1} = \frac{\int S_{fl}(\tilde{\nu})\, d\tilde{\nu}}{\int \tilde{\nu}^{-3} S_{fl}(\tilde{\nu})\, d\tilde{\nu}}. \tag{6}$$

Here, c_0 is the speed of light, n the refractive index of the solvent, and N_A Avogadro´s number. The factor $\left\langle \tilde{\nu}^{-3} \right\rangle^{-1}$ accounts for the cubic dependence of the spontaneous emission on the wavenumber $\tilde{\nu}$. Its evaluation involves integrals covering the fluorescence spectrum $S_{fl}\left(\tilde{\nu}\right)$ as a function of the wavenumber $\tilde{\nu}$. The fluorescence spectra $S_{fl}^{\lambda}(\lambda)$ were recorded as a function of the wavelength λ and with a constant wavelength bandpass (5 nm). For the conversion to wavenumber axis, the spectrum $S_{fl}^{\lambda}(\lambda)$ was multiplied by the wavelength λ squared, $S_{fl}\left(\tilde{\nu}\right) \sim S_{fl}^{\lambda}(\lambda)\, \lambda^2$ [8]. The molar decadic absorption $\varepsilon(\tilde{\nu})$ as a function of the wavenumber $\tilde{\nu}$ enters the integral $\int \frac{\varepsilon(\tilde{\nu}) d\tilde{\nu}}{\tilde{\nu}}$. It is crucial that this integral only covers the part of the spectrum $\varepsilon(\tilde{\nu})$ associated with the transition to the lowest excited singlet state. The respective range is marked in Fig. 2. The respective evaluation affords a radiative rate constant k_{rad} of $(1.72 \pm 0.08) \times 10^8\ \mathrm{s^{-1}}$.

In the fluorescence Kerr gating experiment, a solution of DpNA dissolved in acetonitrile was excited with femtosecond pulses centered at 400 nm (Fig. 3). Time resolved spectra closely match the shape of the steady state one, with a peak around 480 nm. Within one picosecond, almost all the emission signal has vanished (Fig. 3). The experimental results were subject to a global analysis using a single-exponential convoluted with the IRF as a trial function (see Experimental section). The procedure affords a fluorescence lifetime $\tau_{fl.}$ of 590 ± 190 fs. In a previous study a time constant of 630 fs was reported [61]. Multiplying this lifetime with the radiative rate constant determined above results in a fluorescence quantum yield Φ_{fl}^{SB} of $(1.01 \pm 0.3) \times 10^{-4}$ (see Eq. (2)). This value is approximately twice the yield Φ_{fl}^{rel} determined by the relative approach. Due to this discrepancy, DpNA was discarded as a reference.

Semi-empirical quantum chemical computations [66] and transient absorption experiments [61] performed by Ernsting et al. can rationalize this discrepancy. For the closely related molecule 4-nitroaniline, these computations predict an ultrafast (< 100 fs) decrease of the oscillator strength f and thereby the radiative rate constant k_{rad} after photo-excitation. In transient absorption experiments with a time resolution of ~ 50 fs, which compares to ~ 250 fs in the fluorescence experiments reported here, such an ultrafast

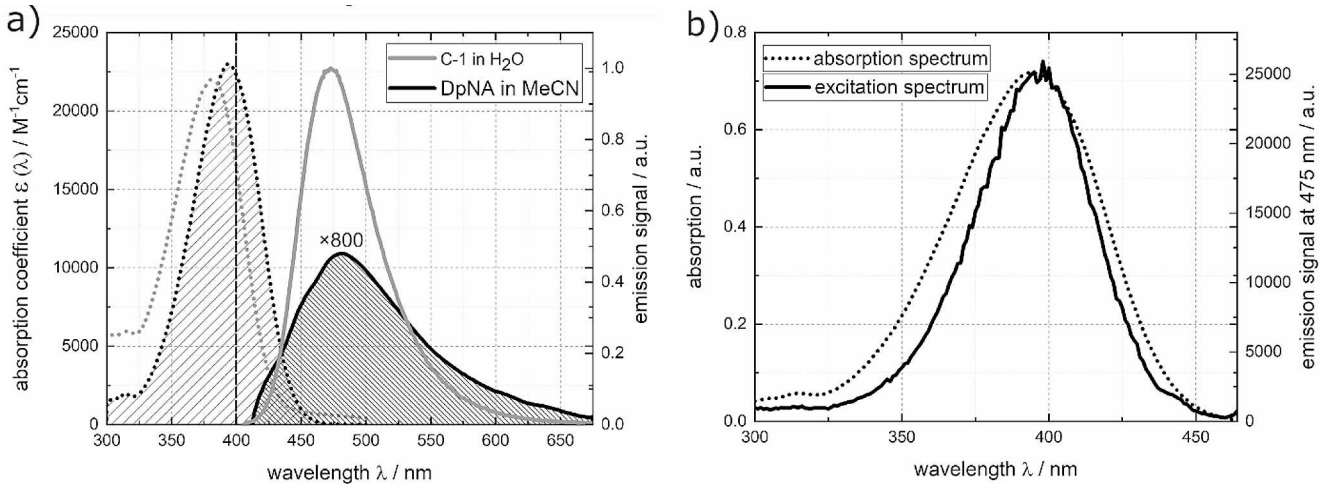

Fig. 2 (**a**) Absorption (coefficient, black dotted line) and fluorescence (smoothed black solid line) spectra of DpNA in acetonitrile. Absorption (coefficient, gray dotted line scaled according to ref. [65]) and fluorescence (gray solid line) spectra of the reference dye C-1 in water are included. The excitation wavelength at 400 nm is marked in the absorption spectra. The emission spectra were recorded with constant wavelength bandpass (5 nm). The fluorescence spectra are scaled such that their integrals are proportional to their respective fluorescence quantum yields. For the sake of comparison, the fluorescence spectrum of DpNA was multiplied by a factor of 800. The relevant ranges used for the Strickler-Berg analysis are highlighted in the absorption and emission spectra. (**b**) Fluorescence excitation spectrum of DpNA in comparison with its absorption spectrum. For the excitation spectrum the signal was probed at 475 nm

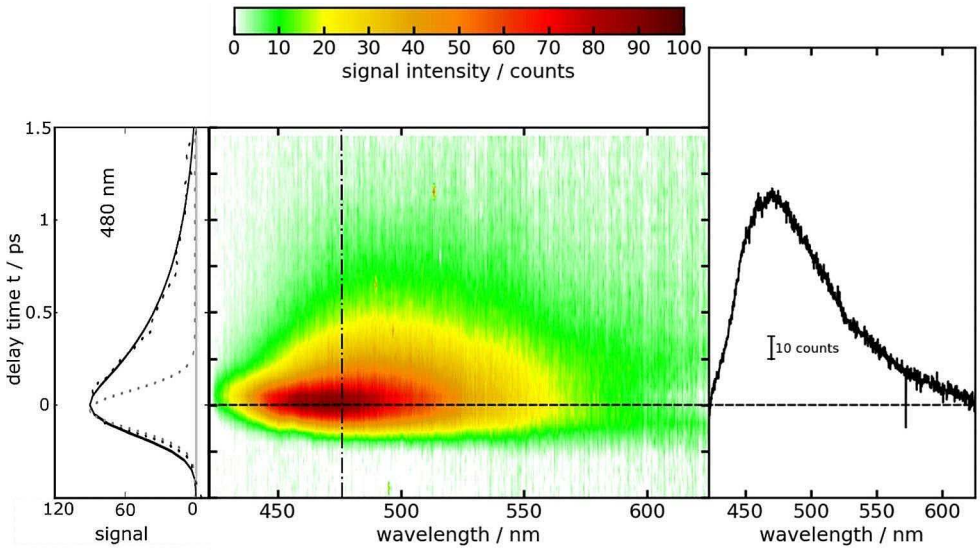

Fig. 3 Femtosecond transient fluorescence on DpNA in acetonitrile (~0.5 mM) as a function of detection wavelength λ and delay time t. The solution was excited at 400 nm. In the central contour representation, reddish hue represents large fluorescence signals. One representative time trace (480 nm) as well as a fit are shown on the left. The dotted gray line represents the IRF

decrease was observed for DpNA in acetonitrile [61]. Notably, a decrease by a factor of ~0.5 is observed. Such a non-Condon effect is not incorporated into the (standard) Strickler-Berg approach. If the reduction of the radiative rate constant k_{rad} by a factor of 0.5 is taken into account, the yields Φ_{fl}^{rel} and Φ_{fl}^{SB} match. Despite this, DpNA was discarded since for the other chromophores described below, matching values were obtained without such complications.

Blue Region of the UV/Vis Spectrum – dT in Water

The photophysics of thymidine has been extensively studied due to its fundamental role as a DNA building block [46, 67, 68]. These studies have shown that dT undergoes ultrafast internal conversion in a couple of 100 fs [69, 70]. Previous studies provide values for the fluorescence quantum yield of dT in the order of 10^{-4} [45, 46]. In this study, we aimed to reproduce these reported values. dT in water exhibits a structureless absorption band lowest in transition energy peaking around 267 nm (see Fig. 4). The fluorescence spectrum peaks at 330 nm. The spectra converted into the transition dipole representation reveal an approximate mirror-image relationship (see Fig. S2 in the Online Resource). The fluorescence excitation spectrum overlays favorably with the properly scaled absorption spectrum (Fig. 4b). Its absorption coefficient ε_{max} was determined to

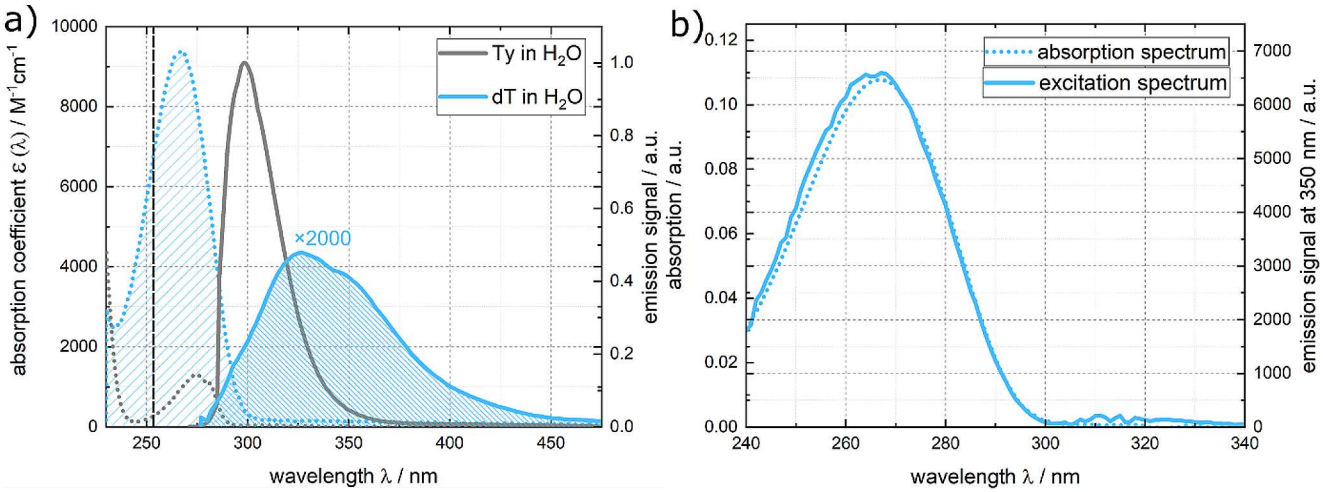

Fig. 4 (**a**) Absorption (coefficient, blue dotted line) and fluorescence (smoothed blue solid line) spectra of dT in water. Absorption (coefficient, gray dotted line scaled according to ref. [71]) and fluorescence (gray solid line) spectra of the reference dye Ty in water are included. The excitation wavelength at 255 nm is marked in the absorption spectra. The emission spectra were recorded with constant wavelength bandpass (5 nm). The fluorescence spectra are scaled such that their integrals are proportional to their respective fluorescence quantum yields. For the sake of comparison, the fluorescence spectrum of dT was multiplied by a factor of 2000. The relevant ranges used for the Strickler-Berg analysis are highlighted in the absorption and emission spectra. (**b**) Fluorescence excitation spectrum of dT in comparison with its absorption spectrum. For the excitation spectrum the signal was probed at 350 nm

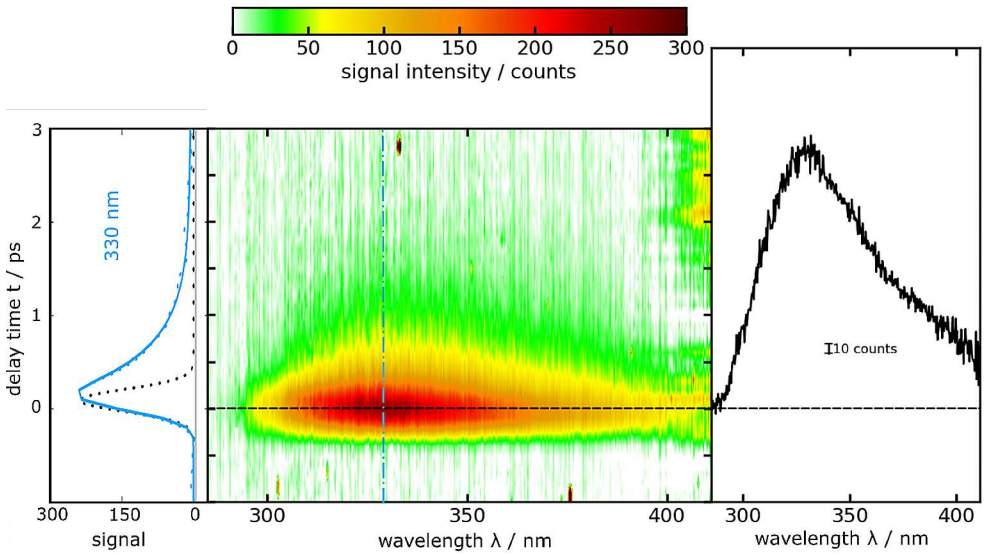

Fig. 5 Femtosecond transient fluorescence on dT in water (~1 mM) as a function of detection wavelength λ and delay time t. The solution was excited at 266 nm. In the central contour representation, reddish hue represents large fluorescence signals. One representative time trace (330 nm) as well as a single-exponential fit are shown on the left. The dotted black line represents the IRF

be $(9.4 \pm 0.1) \times 10^3$ $M^{-1}cm^{-1}$, which is somewhat smaller than the previously reported value of 9.7×10^3 $M^{-1}cm^{-1}$ [46]. For a relative determination of the fluorescence quantum yield, dT dissolved in water was excited close to the maximum at 255 nm (see Fig. 4). The resulting fluorescence signal was compared to that of Ty in water. Using Eq. (4), the relative fluorescence quantum yield Φ_{fl}^{rel} was calculated, relying on values compiled in ref. [54, 64]. From these inputs, a yield Φ_{fl}^{rel} of $(1.3 \pm 0.09) \times 10^{-4}$ for dT in water was obtained.

Using the spectra shown in Fig. 4, a Strickler-Berg analysis was performed. The relevant ranges for this analysis are highlighted in Fig. 4. This evaluation yielded a radiative rate constant k_{rad} of $(2.30 \pm 0.03) \times 10^8$ s^{-1} (see Eq. (5)).

A solution of dT in water was excited using femtosecond pulses centered at 266 nm and the resulting emission signal was probed using fluorescence Kerr gating (Fig. 5). The time resolved spectra closely resemble the shape of the steady state spectrum, exhibiting a peak around 330 nm. Within one picosecond, almost all the emission signal has vanished (Fig. 5). To determine the fluorescence lifetime $\tau_{fl.}$ of dT, a global fit of the data was performed. This analysis employed both single- and bi-exponential trial functions, convoluted with the IRF (see Experimental section). The

single-exponential fit for dT in water resulted in a fluorescence lifetime $\tau_{fl.}$ of 480 ± 140 fs. The bi-exponential fit afforded lifetimes of $\tau_1 \approx 240$ fs and $\tau_2 \approx$ 580 fs (Fig. 6). An average fluorescence lifetime $\langle \tau_{fl.} \rangle$ was derived using the Eq. (7),

$$\langle \tau_{fl} \rangle = \frac{\int DAS_1 \cdot \tau_1 + \int DAS_2 \cdot \tau_2}{\int DAS_1 + \int DAS_2}. \quad (7)$$

Here, $\int DAS_1$ and $\int DAS_2$ represent the spectral integrals of both decay associated spectra which are depicted in Fig. 6. This equation (Eq. 7) yields an average fluorescence lifetime of $\langle \tau_{fl.} \rangle = 408 \pm 190$ fs, which is somewhat smaller than the time constant obtained from the single-exponential fit. Time constants in a similar (470–700 fs) range have been reported in prior studies [46, 69, 72]. Multiplying the lifetime obtained from the single-exponential fit with the above radiative rate constant results in a fluorescence quantum yield Φ_{fl}^{SB} of $(1.11 \pm 0.3) \times 10^{-4}$ (see Eq. (2)). Inserting the average fluorescence lifetime into the same equation (Eq. 2), results in a marginally lower fluorescence quantum yield Φ_{fl}^{SB} of $(0.938 \pm 0.4) \times 10^{-4}$. However, both Φ_{fl}^{SB} values obtained here closely align with the yield Φ_{fl}^{rel} determined by the relative approach.

Green Region of the UV/Vis Spectrum – DBM in Ethanol

DBM undergoes ultrafast intramolecular proton transfer [73] upon photo-excitation. While the fluorescence quantum yield for DBM has not been quantified before, its fluorescence lifetime was found to be in the sub-picosecond range [47]. DBM in ethanol displays a structureless absorption band lowest in transition energy peaking around 340 nm (see Fig. 7). The fluorescence spectrum peaks at 400 nm. The spectra converted into the transition dipole representation reveal an approximate mirror-image relationship (see Fig. S3 in the Online Resource). The fluorescence excitation spectrum closely aligns with the properly scaled absorption spectrum for DBM in ethanol, as shown in Fig. 7b. The peak absorption coefficient ε_{max} of $(2.71 \pm 0.04) \times 10^4$ $M^{-1}cm^{-1}$ at 340 nm determined here is close to a value of 2.5×10^4 $M^{-1}cm^{-1}$ reported earlier [74]. To determine the fluorescence quantum yield of DBM relatively, a solution of DBM in ethanol was excited close to the maximum at 330 nm (see Fig. 7). The observed fluorescence signal was compared to the fluorescence of C-1 in water. Employing Eq. (4) and incorporating reference values [52, 64], the relative fluorescence quantum yield Φ_{fl}^{rel} was determined to be $(6.88 \pm 0.05) \times 10^{-5}$ for DBM in ethanol.

Utilizing the spectra presented in Fig. 7, a Strickler-Berg analysis was conducted. The relevant ranges for this analysis are highlighted in Fig. 7. From this analysis, a radiative rate constant k_{rad} of $(2.37 \pm 0.04) \times 10^8$ s^{-1} was derived (see Eq. (5)).

In the fluorescence Kerr gating experiment, femtosecond pulses centered at 266 nm were used to excite a solution of DBM dissolved in ethanol (Fig. 8). The time resolved spectra were found to closely resemble the shape of the steady state spectrum, with a peak observed around 400 nm. Within half a picosecond, nearly all the emission signal has vanished (Fig. 8). The results of the experiment were subject to a global analysis, where a single-exponential convoluted with the IRF was employed as a trial function (see Experimental Section). This analysis afforded a fluorescence lifetime $\tau_{fl.}$ of 290 ± 80 fs. A previous study reported a time constant of 240 fs [47]. By multiplying this lifetime by the radiative

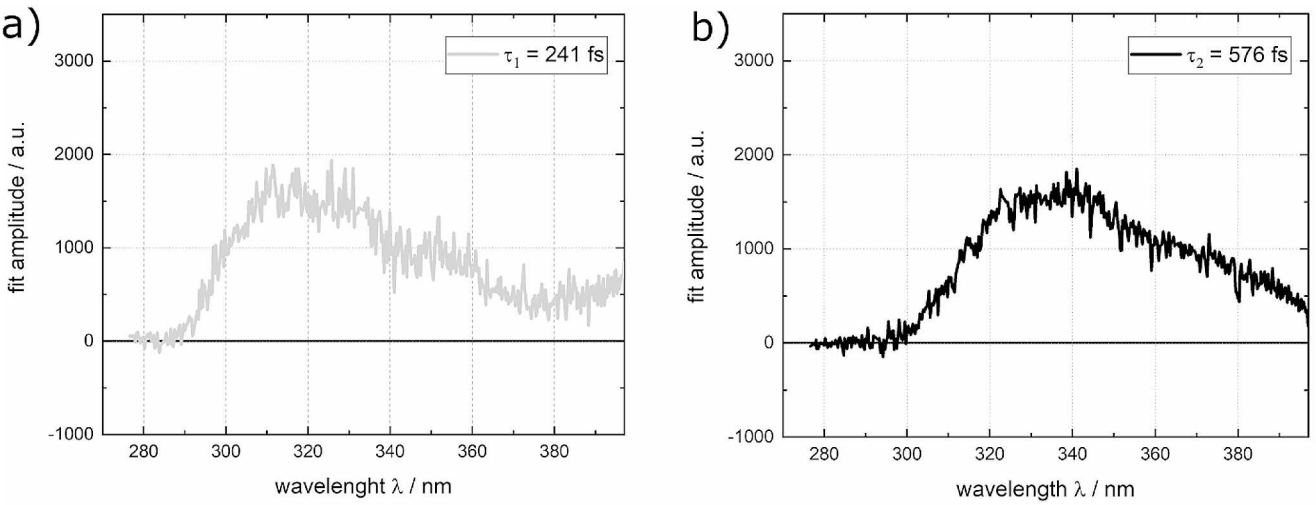

Fig. 6 Decay associated spectra (DAS) retrieved from the measurement on dT in water depicted in Fig. 5 using a bi-exponential trial function

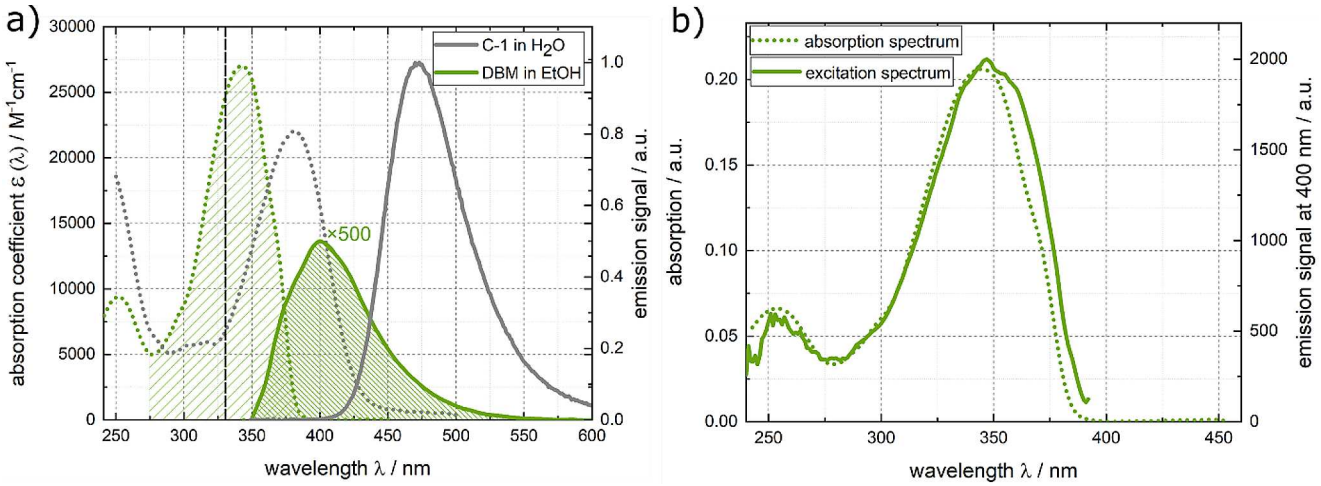

Fig. 7 (**a**) Absorption (coefficient, green dotted line) and fluorescence (smoothed green solid line) spectra of DBM in ethanol. Absorption (coefficient, gray dotted line scaled according to ref. [65]) and fluorescence (gray solid line) spectra of the reference dye C-1 in water are included. The excitation wavelength at 330 nm is marked in the absorption spectra. The emission spectra were recorded with constant wavelength bandpass (5 nm). The fluorescence spectra are scaled such that their integrals are proportional to their respective fluorescence quantum yields. For the sake of comparison, the fluorescence spectrum of DBM was multiplied by a factor of 500. The relevant ranges used for the Strickler-Berg analysis are highlighted in the absorption and emission spectra. (**b**) Fluorescence excitation spectrum of DBM in comparison with its absorption spectrum. For the excitation spectrum the signal was probed at 400 nm

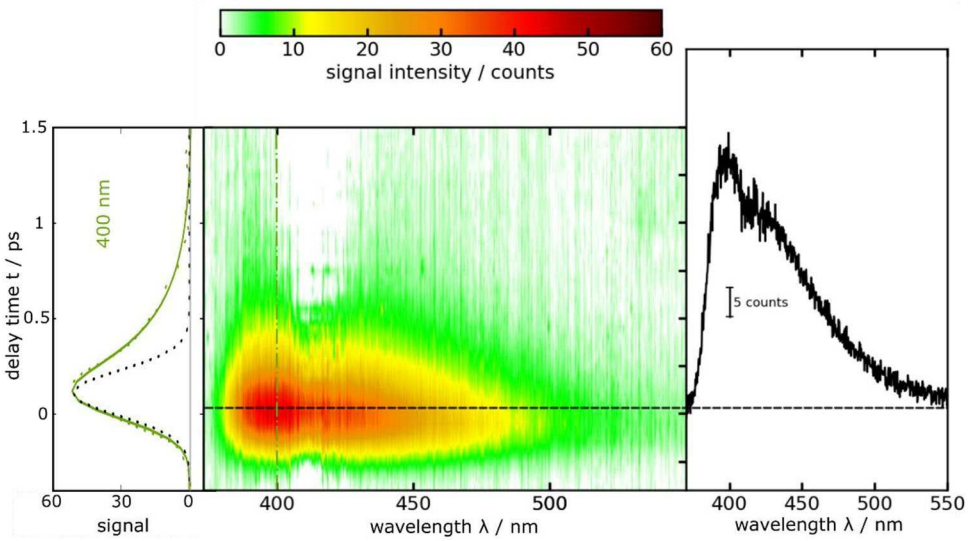

Fig. 8 Femtosecond transient fluorescence on DBM in ethanol (~ 1.3 mM) as a function of detection wavelength λ and delay time t. The solution was excited at 266 nm. In the central contour representation, reddish hue represents large fluorescence signals. One representative time trace (400 nm) as well as a fit are shown on the left. The dotted black line represents the IRF

rate constant k_{rad}, a fluorescence quantum yield Φ_{fl}^{SB} of $(6.92 \pm 1.9) \times 10^{-5}$ was calculated (see Eq. (2)).

Red Region of the UV/Vis Spectrum – MG in Water

MG, a triphenylmethane dye, exhibits pronounced visible absorption bands and has a very low fluorescence quantum yield ($\leq 10^{-4}$) in low-viscosity liquid solutions [75, 76]. Prior studies have shown that MG undergoes ultrafast internal conversion [49, 76–79]. MG in water exhibits an band lowest in transition energy peaking around 618 nm (see Fig. 9). The fluorescence spectrum peaks at 670 nm. An approximate mirror-image relationship is disclosed upon converting the spectra into the transition dipole representation (see Fig. S4 in the Online Resource). The fluorescence excitation spectrum for MG in water closely matches the properly rescaled absorption spectrum (see Fig. 9b). The peak absorption coefficient ε_{max} of $(1.43 \pm 0.01) \times 10^5\ M^{-1}cm^{-1}$ at 618 nm determined here is in line with the value of $1.40 \times 10^5\ M^{-1}\ cm^{-1}$ reported earlier [80, 81]. For a relative determination of its fluorescence quantum yield, MG dissolved in water was excited at 535 nm (see Fig. 9). The resulting fluorescence signal was compared to the one of Rh 101 in

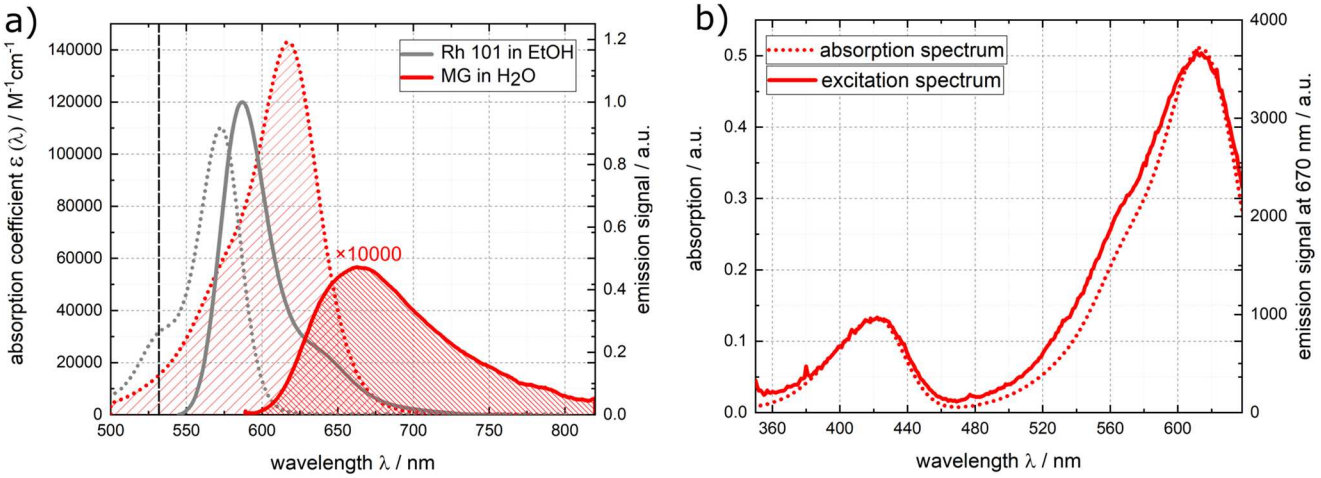

Fig. 9 (**a**) Absorption (coefficient, red dotted line) and fluorescence (smoothed red solid line) spectra of MG in water. Absorption (coefficient, gray dotted line scaled according to ref. [82]) and fluorescence (gray solid line) spectra of the reference dye Rh 101 in ethanol are included. The excitation wavelength at 535 nm is marked in the absorption spectra. The emission spectra were recorded with constant wavelength bandpass (5 nm). The fluorescence spectra are scaled such that their integrals are proportional to their respective fluorescence quantum yields. For the sake of comparison, the fluorescence spectrum of MG was multiplied by a factor of 10,000. The relevant ranges used for the Strickler-Berg analysis are highlighted in the absorption and emission spectra. (**b**) Fluorescence excitation spectrum of MG in comparison with its absorption spectrum. For the excitation spectrum the signal was probed at 670 nm

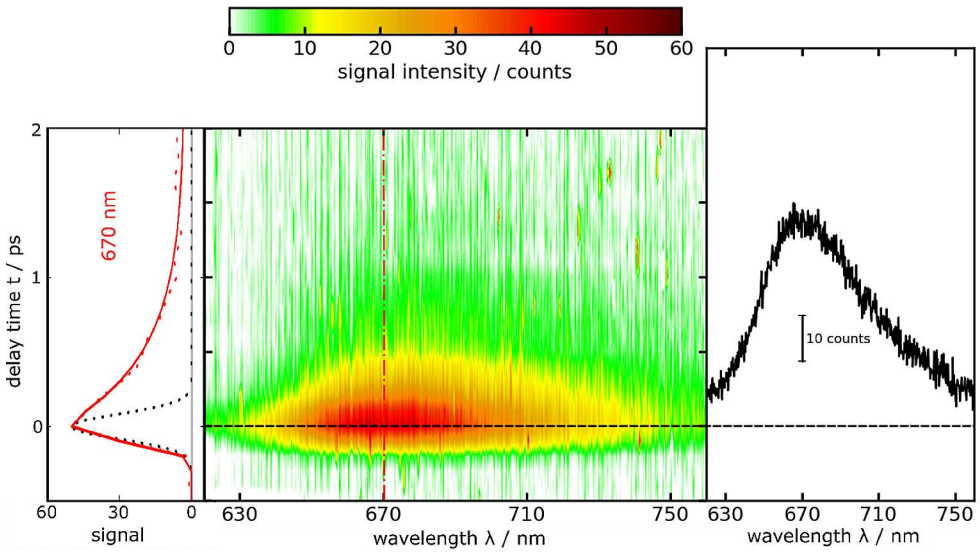

Fig. 10 Femtosecond transient fluorescence on MG in water (~ 70 µM) as a function of detection wavelength λ and delay time t. The solution was excited at 580 nm. In the central contour representation, reddish hue represents large fluorescence signals. One representative time trace (670 nm) as well as a fit are shown on the left. The dotted black line represents the IRF

ethanol. The fluorescence quantum yield based on the relative approach Φ_{fl}^{rel} was computed using Eq. (4). Values compiled in ref. [55, 64] were inserted. With these inputs, a yield Φ_{fl}^{rel} of $(9.67 \pm 0.5) \times 10^{-5}$ results for MG in water.

Using the spectra depicted in Fig. 9, a Strickler-Berg analysis was conducted. The ranges are marked in Fig. 9. The evaluation affords a radiative rate constant k_{rad} of $(2.18 \pm 0.05) \times 10^{8}$ s^{-1} (see Eq. (5)).

In the fluorescence Kerr gating experiment, femtosecond pulses with a center wavelength of 580 nm were utilized to excite a solution of MG in water (Fig. 10). The resulting time resolved spectra closely matched the steady state spectrum in shape, peaking around 670 nm. Almost the entire emission signal disappeared within one picosecond (Fig. 10). A global analysis was conducted utilizing a single-exponential function convoluted with the IRF as the trial function. This procedure yielded a fluorescence lifetime $\tau_{fl.}$ of 450 ± 160 fs. Prior studies reported time constants in a similar (520–660 fs) range [48–51]. By multiplying this lifetime by the radiative rate constant k_{rad}, a fluorescence quantum yield Φ_{fl}^{SB} of $(9.86 \pm 3.5) \times 10^{-5}$ was calculated (see Eq. (2)).

Table 1 Fluorescence quantum yields determined in this work in comparison with the earlier reports

	Φ_{fl}^{rel} from relative method	Φ_{fl}^{SB} from $k_{rad} \times \tau_{fl.}$	Φ_{fl} from prior studies
dT in water	$(1.3 \pm 0.09) \times 10^{-4}$	$(1.11 \pm 0.3) \times 10^{-4}$ [a] $(0.938 \pm 0.4) \times 10^{-4}$ [b]	1.32×10^{-4} [46], 1×10^{-4} [45]
DBM in ethanol	$(6.88 \pm 0.05) \times 10^{-5}$ [c]	$(6.92 \pm 1.9) \times 10^{-5}$	Almost non-fluorescent in solution [73, 83, 84]
MG in water	$(9.67 \pm 0.5) \times 10^{-5}$	$(9.86 \pm 3.5) \times 10^{-5}$	$< 10^{-4}$ [75], $\sim 10^{-4}$ [76]

a Based on a single-exponential fit

b Based on a bi-exponential fit

c No error margins for the yield Φ_{fl}^{r} were available

Conclusion

In this study, we propose three compounds as new references for determining small fluorescence quantum yields in the UV/Vis spectral range, with yields ranging from 10^{-5} to 10^{-4}. These compounds are thymidine in water for the blue region, dibenzoylmethane in ethanol for the green region, and malachite green chloride in water for the red region of the spectrum. Each of these compounds is easily handled, photostable, commercially available, and demonstrates a mirror-image symmetry between its absorption and fluorescence spectra. This symmetry indicates the involvement of the same electronic states in absorption and emission processes, thereby supporting the application of the Strickler-Berg relation. Furthermore, the fluorescence excitation spectra of all compounds closely align with their respective absorption spectra, confirming that the observed emissions originate from the compounds under study. The fluorescence quantum yields determined using both the relative and time resolved techniques, exhibit satisfactory agreement within their respective error margins (see Table 1). However, the error margins for the fluorescence quantum yields obtained via the time resolved technique are slightly larger, mainly due to the error in the fluorescence lifetimes (Table 1). Our findings for the fluorescence quantum yield of dT, obtained through both methods, align well with previous studies, suggesting the reliability of our results for the other compounds. It is worth noting that no value for DBM and only an upper boundary for the yield $\Phi_{fl.}$ of MG were reported previously. Here, the fluorescence quantum yields for both compounds were precisely determined.

Supplementary Information The online version contains supplementary material available at https://doi.org/10.1007/s10895-024-03729-2.

Author Contributions Mahbobeh Morshedi: sample preparation, acquisition of steady state and time resolved spectra, analysis of spectral results, computation of quantum yields, composition and editing of manuscript and figures. Simon L. Zimmermann: sample preparation, acquisition of steady state spectra, analysis of spectral results, computation of quantum yields, editing of manuscript and figures. David Klaverkamp: error analysis, editing of manuscript and figures. Peter Gilch: conceptualization, supervision, composition and editing of manuscript.

Funding This work has been supported by the Deutsche Forschungsgemeinschaft (DFG, German Research Foundation), Project number 396890929 (GRK 2482, "ModISC"). David Klaverkamp is grateful for a Kekulé scholarship from the Fonds der Chemischen Industrie. Open Access funding enabled and organized by Projekt DEAL.

Data Availability The datasets generated during and/or analysed during the current study are available from the corresponding author on reasonable request.

Declarations

Ethical Approval Not applicable.

Competing Interests The authors declare no competing interests.

References

1. Wong K-L, Bünzli J-CG, Tanner PA (2020) Quantum yield and brightness. J Lumin 224:117256. https://doi.org/10.1016/j.jlumin.2020.117256
2. Braslavsky SE (2007) Glossary of terms used in photochemistry, (IUPAC recommendations 2006). Pure Appl Chem 79:293–465. https://doi.org/10.1351/pac200779030293
3. Birriel JJ, King D (2018) Fluorescence spectra of highlighter inks. Phys Teach 56:20–23. https://doi.org/10.1119/1.5018682
4. Hoinka NM, Fuhrmann-Lieker T (2019) Amplified spontaneous emission in paper. Sci Rep 9:1862. https://doi.org/10.1038/s41598-018-38438-x

5. Kalyani NT, Dhoble S (2012) Organic light emitting diodes: Energy saving lighting technology—A review. Renew Sustain Energy Rev 16:2696–2723. https://doi.org/10.1016/j.rser.2012.02.021
6. Bauri J, Choudhary RB, Mandal G (2021) Recent advances in efficient emissive materials-based OLED applications: a review. J Mater Sci 1–30. https://doi.org/10.1007/s10853-021-06503-y
7. Suzuki T, Matsuzaki T, Hagiwara H, Aoki T, Takata K (2007) Recent advances in fluorescent labeling techniques for fluorescence microscopy. Acta Histochem Cytochem 40:131–137. https://doi.org/10.1267/ahc.07023
8. Lakowicz J (2006) In principles of fluorescence spectroscopy. Springer, Boston
9. Montalti M, Credi A, Prodi L, Gandolfi MT (2006) Handbook of photochemistry. CRC
10. Stryer L (1978) Fluorescence energy transfer as a spectroscopic ruler. Annu Rev Biochem 47:819–846. https://doi.org/10.1146/annurev.bi.47.070178.004131
11. Lerner E, Cordes T, Ingargiola A, Alhadid Y, Chung S, Michalet X, Weiss S (2018) Toward dynamic structural biology: two decades of single-molecule Förster resonance energy transfer. Science 359:eaan1133. https://doi.org/10.1126/science.aan1133
12. Mardelli M, Olmsted J III (1977) Calorimetric determination of the 9, 10-diphenyl-anthracene fluorescence quantum yield. J Photochem 7:277–285. https://doi.org/10.1016/0047-2670(77)85005-3
13. Olmsted J (1979) Calorimetric determinations of absolute fluorescence quantum yields. J Phys Chem 83:2581–2584. https://doi.org/10.1021/j100483a006
14. Gaigalas AK, Wang L (2008) Measurement of the fluorescence quantum yield using a spectrometer with an integrating sphere detector. J Res Natl Inst Stand Technol 113:17. https://doi.org/10.6028/jres.113.004
15. Würth C, Lochmann C, Spieles M, Pauli J, Hoffmann K, Schüttrigkeit T, Franzl T, Resch-Genger U (2010) Evaluation of a commercial integrating sphere setup for the determination of absolute photoluminescence quantum yields of dilute dye solutions. Appl Spectrosc 64:733–741. https://doi.org/10.1366/000370210791666390
16. Würth C, Grabolle M, Pauli J, Spieles M, Resch-Genger U (2013) Relative and absolute determination of fluorescence quantum yields of transparent samples. Nat Protoc 8:1535–1550. https://doi.org/10.1038/nprot.2013.087
17. Levitus M (2020) Tutorial: measurement of fluorescence spectra and determination of relative fluorescence quantum yields of transparent samples. Methods Appl Fluoresc 8:033001. https://doi.org/10.1088/2050-6120/ab7e10
18. Resch-Genger U, Rurack K (2013) Determination of the photoluminescence quantum yield of dilute dye solutions (IUPAC technical report). Pure Appl Chem 85. https://doi.org/10.1351/pac-rep-12-03-03
19. Cheknlyuk A, Fadeev V, Georgiev G, Kalkanjiev T, Nickolov Z (1982) Determination of fluorescence quantum yields using a spontaneous Raman scattering line of the solvent as internal standard. Spectrosc Lett 15:355–365. https://doi.org/10.1080/00387018208067999
20. Brouwer AM (2011) Standards for photoluminescence quantum yield measurements in solution (IUPAC technical report). Pure Appl Chem 83:2213–2228. https://doi.org/10.1351/PAC-REP-10-09-31
21. Klán P, Wirz J (2009) Photochemistry of organic compounds: from concepts to practice. John Wiley & Sons, UK
22. Niu Y, Peng Q, Deng C, Gao X, Shuai Z (2010) Theory of excited state decays and optical spectra: application to polyatomic molecules. J Phys Chem A 114:7817–7831. https://doi.org/10.1021/jp101568f
23. Etinski M, Tatchen J, Marian CM (2011) Time-dependent approaches for the calculation of intersystem crossing rates. J Chem Phys 134. https://doi.org/10.1063/1.3575582
24. Penfold TJ, Gindensperger E, Daniel C, Marian CM (2018) Spin-vibronic mechanism for intersystem crossing. Chem Rev 118:6975–7025. https://doi.org/10.1021/acs.chemrev.7b00617
25. Marian CM (2021) Understanding and controlling intersystem crossing in molecules. Annu Rev Phys Chem 72:617–640. https://doi.org/10.1146/annurev-physchem-061020-053433
26. Scholes GD (2003) Long-range resonance energy transfer in molecular systems. Annu Rev Phys Chem 54:57–87. https://doi.org/10.1146/annurev.physchem.54.011002.103746
27. Turro NJ, Ramamurthy V, Scaiano JC (2010) Modern molecular photochemistry of organic molecules. University Science Books, Sausalito
28. Kumpulainen T, Lang B, Rosspeintner A, Vauthey E (2017) Ultrafast elementary photochemical processes of organic molecules in liquid solution. Chem Rev 117:10826–10939. https://doi.org/10.1021/acs.chemrev.6b00491
29. Nitzan A (2006) Chemical dynamics in condensed phases: relaxation, transfer and reactions in condensed molecular systems. Oxford University Press, Oxford
30. Schrader B (2008) Infrared and Raman spectroscopy: methods and applications. Wiley, UK
31. Gustavsson T, Markovitsi D (2021) Fundamentals of the intrinsic DNA fluorescence. Acc Chem Res 54:1226–1235. https://doi.org/10.1021/acs.accounts.0c00603
32. Fujino T, Arzhantsev SY, Tahara T (2001) Femtosecond time-resolved fluorescence study of photoisomerization of trans-azobenzene. J Phys Chem A 105:8123–8129. https://doi.org/10.1021/jp0110713
33. Sajadi M, Dobryakov A, Garbin E, Ernsting N, Kovalenko S (2010) Time-resolved fluorescence spectra of cis-stilbene in hexane and acetonitrile. Chem Phys Lett 489:44–47. https://doi.org/10.1016/j.cplett.2010.02.034
34. Kochendoerfer GG, Mathies RA (1996) Spontaneous emission study of the femtosecond isomerization dynamics of rhodopsin. J Phys Chem 100:14526–14532. https://doi.org/10.1021/jp960509
35. Heinz B, Schmidt B, Root C, Satzger H, Milota F, Fierz B, Kiefhaber T, Zinth W, Gilch P (2006) On the unusual fluorescence properties of xanthone in water. PCCP 8:3432–3439. https://doi.org/10.1039/B603560D
36. Mundt R, Villnow T, Ziegenbein CT, Gilch P, Marian C, Rai-Constapel V (2016) Thioxanthone in apolar solvents: ultrafast internal conversion precedes fast intersystem crossing. PCCP 18:6637–6647. https://doi.org/10.1039/C5CP06849E
37. Rurack K (2008) Fluorescence quantum yields: methods of determination and standards. In: Resch-Genger U (ed) Standardization and Quality Assurance in fluorescence measurements I: techniques. Springer, Berlin, pp 101–145
38. Resch-Genger U, DeRose PC (2010) Fluorescence standards: Classification, terminology, and recommendations on their selection, use, and production (IUPAC Technical Report). Pure Appl Chem 82:2315–2335. https://doi.org/10.1351/PAC-REP-09-09-02
39. Resch-Genger U, Hoffmann K, Nietfeld W, Engel A, Neukammer Ja, Nitschke R, Ebert B, Macdonald R (2005) How to improve quality assurance in fluorometry: fluorescence-inherent sources of error and suited fluorescence standards. J Fluoresc 15:337–362. https://doi.org/10.1007/s10895-005-2630-3
40. Strickler S, Berg RA (1962) Relationship between absorption intensity and fluorescence lifetime of molecules. J Chem Phys 37:814–822. https://doi.org/10.1063/1.1733166
41. Parson WW (2007) Modern optical spectroscopy. Springer, Berlin

42. Mustroph H (2016) Potential-energy surfaces, the Born–Oppenheimer approximations, and the Franck–Condon principle: back to the roots. ChemPhysChem 17:2616–2629. https://doi.org/10.1002/cphc.201600243
43. Schmidt B, Laimgruber S, Zinth W, Gilch P (2003) A broadband Kerr shutter for femtosecond fluorescence spectroscopy. Appl Phys B 76:809–814. https://doi.org/10.1007/s00340-003-1230-7
44. Ciesielska B, Łukaszewicz A, Celewicz L, Maciejewski A, Kubicki J (2007) Method of determination of emission properties of very weakly emitting species ensuring elimination of emission of impurities. Appl Spectrosc 61:102–109. https://doi.org/10.1366/000370207779701389
45. Callis PR (1983) Electronic states and luminescence of nucleic acid systems. Annu Rev Phys Chem 34:329–357. https://doi.org/10.1146/annurev.pc.34.100183.001553
46. Onidas D, Markovitsi D, Marguet S, Sharonov A, Gustavsson T (2002) Fluorescence properties of DNA nucleosides and nucleotides: a refined steady-state and femtosecond investigation. J Phys Chem B 106:11367–11374. https://doi.org/10.1021/jp026063g
47. Stanimirov SS, Trifonov AA, Buchvarov IC (2021) Discovering of the L ligand impact on luminescence enhancement of Eu(dibenzoylmethane)$_3$. L_x complexes employing transient absorption spectroscopy. Spectrochim Acta Part Mol Biomol Spectrosc 258:119832. https://doi.org/10.1016/j.saa.2021.119832
48. Nagasawa Y, Ando Y, Okada T (1999) Solvent dependence of ultrafast ground state recovery of the triphenylmethane dyes, brilliant green and malachite green. Chem Phys Lett 312:161–168. https://doi.org/10.1016/S0009-2614(99)00901-X
49. Yoshizawa M, Suzuki K, Kubo A, Saikan S (1998) Femtosecond study of S_2 fluorescence in malachite green in solutions. Chem Phys Lett 290:43–48. https://doi.org/10.1016/S0009-2614(98)00483-7
50. Rafiq S, Yadav R, Sen P (2010) Microviscosity inside a nanocavity: a femtosecond fluorescence up-conversion study of malachite green. J Phys Chem B 114:13988–13994. https://doi.org/10.1021/jp1037238
51. Toyo A, Sugihara K, Nagasawa Y (2021) Nonradiative decay and vibrational dephasing of malachite green in trehalose glass monitored by femtosecond time-resolved transient absorption spectroscopy. Cryobiol Cryotechnol 67:115–119. https://doi.org/10.20585/cryobolcryotechnol.67.2_115
52. Jones G, Jackson WR, Choi CY, Bergmark WR (1985) Solvent effects on emission yield and lifetime for coumarin laser dyes. Requirements for a rotatory decay mechanism. J Phys Chem 89:294–300. https://doi.org/10.1021/j100248a024
53. White A (1959) Effect of pH on fluorescence of tyrosine, tryptophan and related compounds. Biochem J 71:217. https://doi.org/10.1042/bj0710217
54. Teale F, Weber G (1957) Ultraviolet fluorescence of the aromatic amino acids. Biochem J 65:476. https://doi.org/10.1042/bj0650476
55. Rurack K, Spieles M (2011) Fluorescence quantum yields of a series of red and near-infrared dyes emitting at 600–1000 nm. Anal Chem 83:1232–1242. https://doi.org/10.1021/ac101329h
56. Satzger H, Zinth W (2003) Visualization of transient absorption dynamics–towards a qualitative view of complex reaction kinetics. Chem Phys 295:287–295. https://doi.org/10.1016/j.chemphys.2003.08.012
57. van Stokkum IH, Larsen DS, Van Grondelle R (2004) Global and target analysis of time-resolved spectra. Biochim et Biophys Acta -Bioenergetics 1657:82–104. https://doi.org/10.1016/j.bbabio.2004.04.011
58. Bevington PR, Robinson DK, Blair JM, Mallinckrodt AJ, McKay S (1993) Data reduction and error analysis for the physical sciences. Computers Phys 7:415–416. https://doi.org/10.1119/1.17439
59. Beechem JM, Gratton E, Ameloot M, Knutson JR, Brand L (2002) Top fluorescence spectroscopy: principles 241–305. https://doi.org/10.1007/0-306-47058-6_5. The global analysis of fluorescence intensity and anisotropy decay data: second-generation theory and programs
60. Thomsen C, Thøgersen J, Keiding S (1998) Ultrafast charge-transfer dynamics: studies of p-nitroaniline in water and dioxane. J Phys Chem A 102:1062–1067. https://doi.org/10.1021/jp972492g
61. Kovalenko S, Schanz R, Hennig H, Ernsting N (2001) Cooling dynamics of an optically excited molecular probe in solution from femtosecond broadband transient absorption spectroscopy. J Chem Phys 115:3256–3273. https://doi.org/10.1063/1.1380696
62. Angulo G, Grampp G, Rosspeintner A (2006) Recalling the appropriate representation of electronic spectra. Spectrochimica Acta Part A: Mol Biomol Spectrosc 65:727–731. https://doi.org/10.1016/j.saa.2006.01.007
63. Al-Yasari A, Van Steerteghem N, Kearns H, El Moll H, Faulds K, Wright JA, Brunschwig BS, Clays K, Fielden J (2017) Organoimido-polyoxometalate nonlinear optical chromophores: a structural, spectroscopic, and computational study. Inorg Chem 56:10181–10194. https://doi.org/10.1021/acs.inorgchem.7b00708
64. Kozma IZ, Krok P, Riedle E (2005) Direct measurement of the group-velocity mismatch and derivation of the refractive-index dispersion for a variety of solvents in the ultraviolet. JOSA B 22:1479–1485. https://doi.org/10.1364/JOSAB.22.001479
65. Baleeva NS, Zaitseva SO, Mineev KS, Khavroshechkina AV, Zagudaylova MB, Baranov MS (2019) Enamine–azide [2+3]-cycloaddition as a method to introduce functional groups into fluorescent dyes. Tetrahedron Lett 60:456–459. https://doi.org/10.1016/j.tetlet.2019.01.007
66. Farztdinov VM, Schanz R, Kovalenko SA, Ernsting NP (2000) Relaxation of optically excited p-nitroaniline: Semiempirical quantum-chemical calculations compared to femtosecond experimental results. J Phys Chem A 104:11486–11496. https://doi.org/10.1021/jp001690w
67. Middleton CT, de La Harpe K, Su C, Law YK, Crespo-Hernández CE, Kohler B (2009) DNA excited-state dynamics: from single bases to the double helix. Annu Rev Phys Chem 60:217–239. https://doi.org/10.1146/annurev.physchem.59.032607.093719
68. Gustavsson T, Improta R, Markovitsi D (2010) DNA/RNA: building blocks of life under UV irradiation. J Phys Chem Lett 1:2025–2030. https://doi.org/10.1021/jz1004973
69. Pecourt J-ML, Peon J, Kohler B (2001) DNA excited-state dynamics: Ultrafast internal conversion and vibrational cooling in a series of nucleosides. J Am Chem Soc 123:10370–10378. https://doi.org/10.1021/ja0161453
70. Crespo-Hernández CE, Cohen B, Hare PM, Kohler B (2004) Ultrafast excited-state dynamics in nucleic acids. Chem Rev 104:1977–2020. https://doi.org/10.1021/cr0206770
71. Scappini F, Casadei F, Zamboni R, Monti S, Giorgianni P, Capobianco M (2007) Laboratory simulation of UV irradiation from the Sun on amino acids. I: irradiation of tyrosine. Int J Astrobiol 6:123–129. https://doi.org/10.1017/S1473550407003588
72. Peon J, Zewail AH (2001) DNA/RNA nucleotides and nucleosides: direct measurement of excited-state lifetimes by femtosecond fluorescence up-conversion. Chem Phys Lett 348:255–262. https://doi.org/10.1016/S0009-2614(01)01128-9
73. Verma PK, Koch F, Steinbacher A, Nuernberger P, Brixner T (2014) Ultrafast UV-induced photoisomerization of intramolecularly H-bonded symmetric β-diketones. J Am Chem Soc 136:14981–14989. https://doi.org/10.1021/ja508059p
74. Zawadiak J, Mrzyczek M (2014) Super-strong bathochromic and hyperchromic effects of methoxy-substituted aromatic

bis (1,3-diketones). Mendeleev Commun 1:45–46. https://doi.org/10.1016/j.mencom.2013.12.015
75. Ippen EP, Shank C, Bergman A (1976) Picosecond recovery dynamics of malachite green. Chem Phys Lett 38:611–614. https://doi.org/10.1016/0009-2614(76)80053-X
76. Zhou Y, Gurzadyan GG, Ni W, Gelin MF, Sun L (2020) Upper excited state photophysics of malachite green in solution and films. J Phys Chem B 124:4293–4302. https://doi.org/10.1021/acs.jpcb.0c01737
77. Abedin KM, Ye JY, Inouye H, Hattori T, Sumi H, Nakatsuka H (1995) Diffusive torsional dynamics of malachite green molecules in solid matrices probed by fluorescence decay. J Chem Phys 103:6414–6425. https://doi.org/10.1063/1.470420
78. Laptenok SP, Addison K, Heisler IA, Meech SR (2014) Excited state structural dynamics in higher lying electronic states: S2 state of malachite green. Chem Phys Lett 607:43–46. https://doi.org/10.1016/j.cplett.2014.05.050
79. Bhasikuttan AC, Sapre AV, Okada T (2003) Ultrafast relaxation dynamics from the S_2 state of malachite green studied with femtosecond upconversion spectroscopy. J Phys Chem A 107:3030–3035. https://doi.org/10.1021/jp034486s
80. Nakashima K, Duhamel J, Winnik M (1993) Photophysical processes on a latex surface: electronic energy transfer from rhodamine dyes to malachite green. J Phys Chem 97:10702–10707. https://doi.org/10.1021/j100143a029
81. Maxwell EJ, Tong WG (2016) Sensitive detection of malachite green and crystal violet by nonlinear laser wave mixing and capillary electrophoresis. J Chromatogr B 1020:29–35. https://doi.org/10.1016/j.jchromb.2016.02.040
82. Beija M, Afonso CA, Martinho JM (2009) Synthesis and applications of rhodamine derivatives as fluorescent probes. Chem Soc Rev 38:2410–2433. https://doi.org/10.1039/B901612K
83. Tobita S, Ohba J, Nakagawa K, Shizuka H (1995) Recovery mechanism of the reaction intermediate produced by photoinduced cleavage of the intramolecular hydrogen bond of dibenzoylmethane. J Photochem Photobiol Chem 92:61–67. https://doi.org/10.1016/1010-6030(95)04158-X
84. Zhang G, Evans RE, Campbell KA, Fraser CL (2009) Role of boron in the polymer chemistry and photophysical properties of difluoroboron–dibenzoylmethane polylactide. Macromolecules 42:8627–8633. https://doi.org/10.1021/ma9019043

A. Appendix

ChemPhotoChem

Supporting Information

Femtosecond Spectroscopy and Quantum Chemistry of a Linearly Coordinated Copper(I) Carbene Complex

Oliver Nolden, Jennifer Kremper, Wiebke Haselbach, Mahbobeh Morshedi, Jasper Guhl, Philipp Schmeinck, Christel M. Marian,* Christian Ganter,* and Peter Gilch*

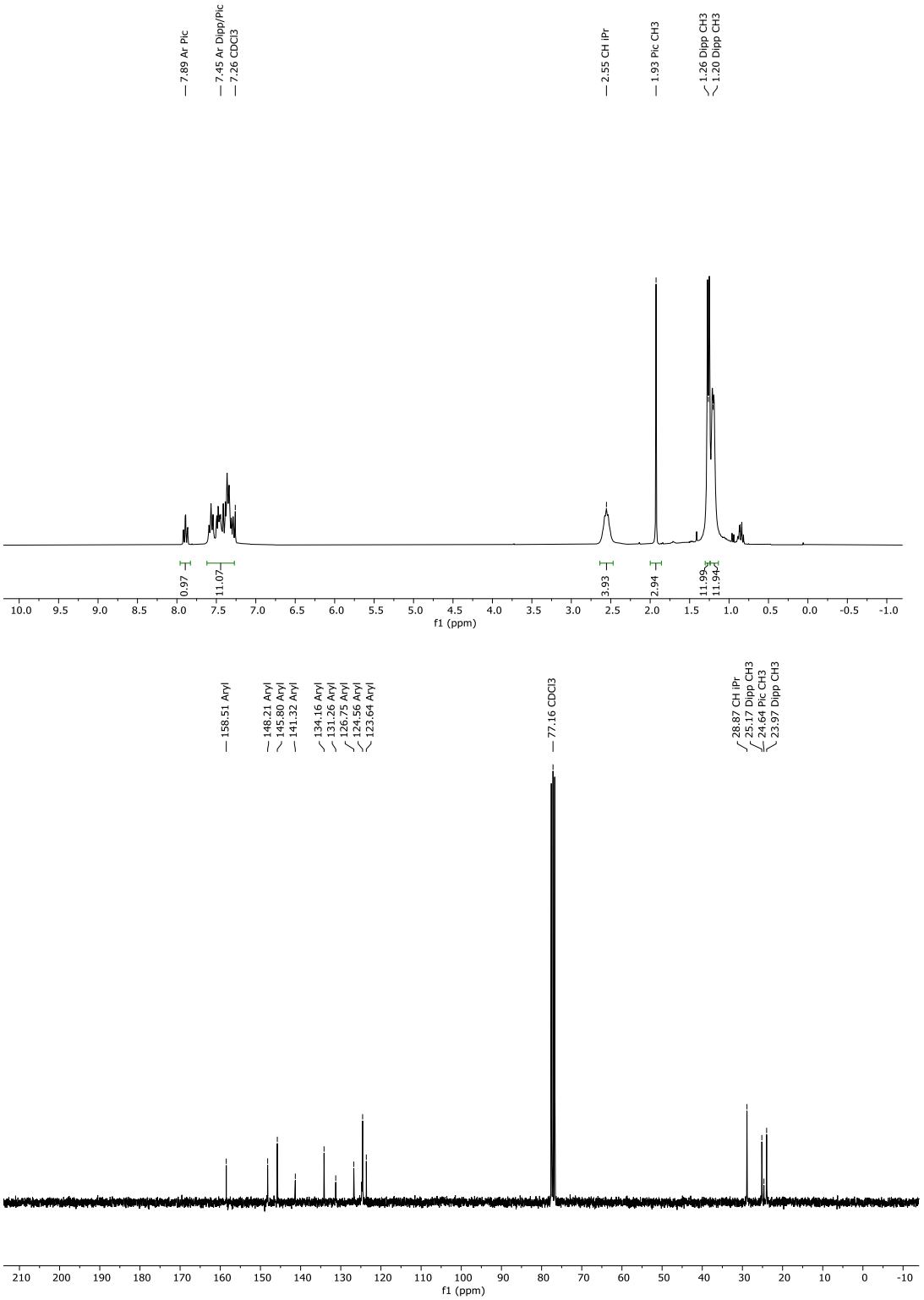

Figure S1: The purity of **1** was verified by ^{1}H-NMR (top), ^{13}C{1H}-NMR (bottom), ESI mass spectrometry and elemental analysis. The analytical data obtained agrees well with the literature [2]. ^{1}H-NMR (300 MHz, $CDCl_3$): δ = 7.89 (ddd, J_{HH} = 7.8/1.6 Hz, 1H, Pic), 7.62-7.27 (m, 11H, Aryl Pic/Dipp), 2.55 (sept, 4H, *i*Pr CH), 1.93 (s, 3H, Pic-CH_3), 1.26 (d, 12H, $^{3}J_{HH}$ = 6.7 Hz, Dipp CH_3), 1.22 (d, 12H, $^{3}J_{HH}$ = 6.8 Hz, Dipp CH3), ^{13}C{1H}-NMR (75 MHz, $CDCl_3$): δ 158.5 (s, aryl C), 148.2 (s, aryl C), 145.8 (s, aryl C), 141.3 (s, aryl C), 134.2 (s, aryl C), 131.3 (s, aryl C), 126.8 (s, aryl C), 124.6 (s, aryl C), 123.6 (s, aryl C), 28.9 (s, *i*Pr CH), 25.2 (s, Dipp CH_3), 24.6 (s, Pic-CH_3), 24.0 (s, Dipp CH_3). MALDI-TOF: m/z 544.2 ([M]+, 31%), Elem anal. Calcd. for $C_{33}H_{44}BCuF_4N_3$ (632.08): C, 62.71; H, 6.86; N, 6.65. Found: C, 62.45; H, 6.71; N, 6.53.

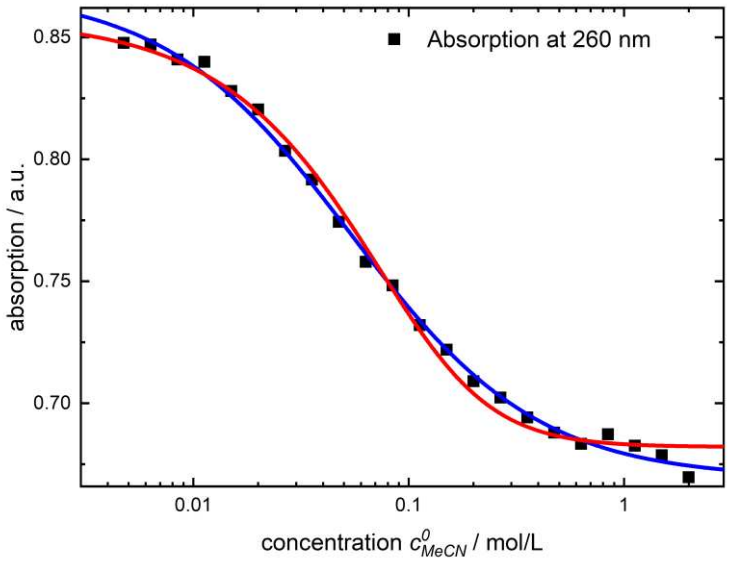

Figure S2. Dependence of the absorption at 260 nm on the initial concentration of MeCN $\boldsymbol{c^0_{MeCN}}$ (values from Figure 1b). The squares mark experimental values, the red line a fit as based on eq. S1-S4, the blue line a fit as based on eq. 3-6 (main part). For concentrations $\boldsymbol{c^0_{MeCN}}$ between 0.01 and 0.1 mol/L and beyond 1 mol/L the fit (blue, eq. S1-S4) overestimates experimental values, for $\boldsymbol{c^0_{MeCN}}$ between 0.1 and 1 mol/L experimental values are underestimated.

The fit that is applied in Figure S2 is based on eq. S1-S4. In these equations, K_D is the dissociation constant of **1** coordinated by two molecules of MeCN (**1**-2MeCN). c_1, c_{MeCN}, $c_{1\text{-}2MeCN}$, and $c_{2\text{-}picoline}$ are the equilibrium concentrations of compound **1**, MeCN, and the complex **1**-2MeCN. $\boldsymbol{c^0_1}$ and $\boldsymbol{c^0_{MeCN}}$ are the initial concentrations of **1** and MeCN (prior to equilibration). The absorption A depends on the concentrations $\boldsymbol{c_1}$, $\boldsymbol{c_{1-2MeCN}}$, and $\boldsymbol{c_{2-picoline}}$ and the respective absorption coefficients $\boldsymbol{\varepsilon_1}$, $\boldsymbol{\varepsilon_{1-2MeCN}}$, and $\boldsymbol{\varepsilon_{2-picoline}}$ as well as the path length d = 1 cm. During this fit three parameters were varied, namely the dissociation constant K_D, the absorption coefficient of **1**-2MeCN $\varepsilon_{1\text{-}2MeCN}$, and the absorption coefficient for 2-picoline in DCM $\varepsilon_{2\text{-}picoline}$. According to this fit the dissociation constant K_D equals 148 M, the absorption coefficient for 2-picoline in DCM $\varepsilon_{2\text{-}picoline}$ 1201 $M^{-1}cm^{-1}$, and the absorption coefficient of for the hypothetical complex with two MeCN molecules $\varepsilon_{1\text{-}2MeCN}$ 12784 $M^{-1}cm^{-1}$.

$$K_D = \frac{c_{\mathbf{1}} \cdot (c_{MeCN})^2}{c_{\mathbf{1}-2MeCN} \cdot c_{2-picoline}} \tag{S1}$$

$$c_{\mathbf{1}} + c_{\mathbf{1}-2MeCN} = c_{\mathbf{1}}^0 \tag{S2}$$

$$c_{MeCN} \approx c_{MeCN}^0 \tag{S3}$$

$$A = (\varepsilon_{\mathbf{1}-2MeCN} \cdot c_{\mathbf{1}-2MeCN} + \varepsilon_{\mathbf{1}} \cdot c_{\mathbf{1}} + \varepsilon_{2-picoline} \cdot c_{2-picoline}) \cdot d \tag{S4}$$

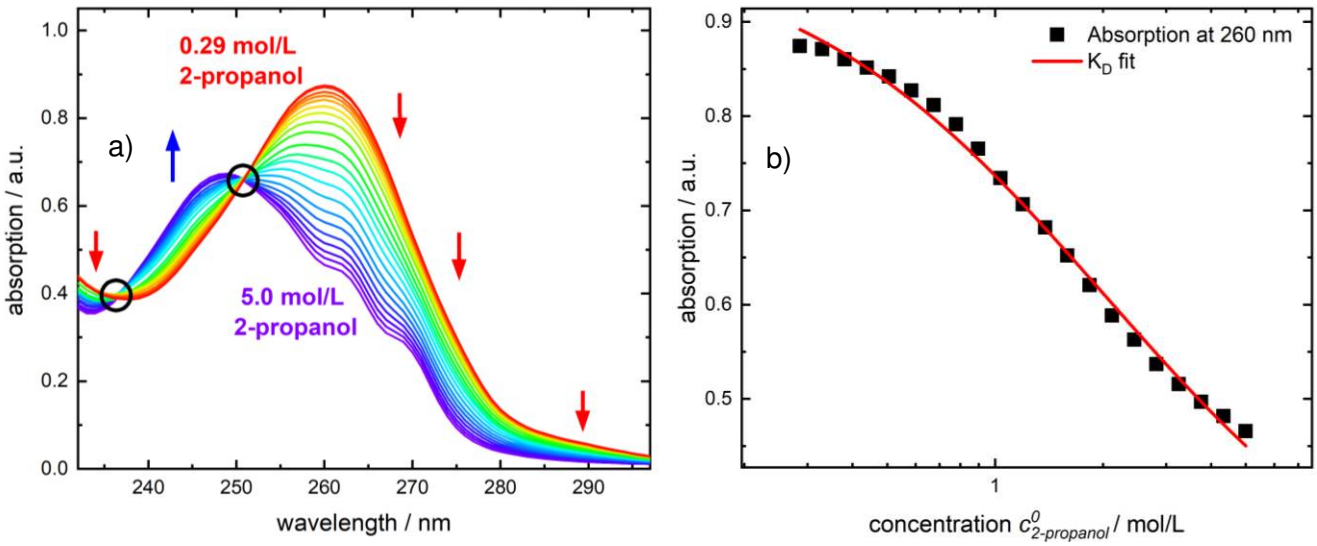

Figure S3. UV/Vis absorption behavior of **1** in 2-propanol. a) Impact of the addition of 2-propanol to absorption spectra of **1** dissolved in DCM. The initial concentration $\boldsymbol{c_1^0}$ of **1** amounted to $5 \cdot 10^{-5}$ M and remains constant throughout the experiment. Initial 2-propanol concentrations $\boldsymbol{c_{2-propanol}^0}$ ranged from 0.29 M (red) to 5 M (blue). Circles mark isosbestic points. b) Dependence of the absorption at 260 nm on the initial concentration of 2-propanol $\boldsymbol{c_{2-propanol}^0}$ (values from Figure S3a). The squares mark experimental values, the line a fit as discribed in the main part based on eq. 3-6. During this fit two parameters were varied, namely the dissociation constant K_D and the absorption coefficient of **1**-2-propanol in DCM $\varepsilon_{1\text{-}2\text{-propanol}}$. According to this fit the dissociation constant K_D equals 2 M and the absorption coefficient **1**-2-propanol $\varepsilon_{1\text{-}2\text{-propanol}}$ 4140 $M^{-1}cm^{-1}$.

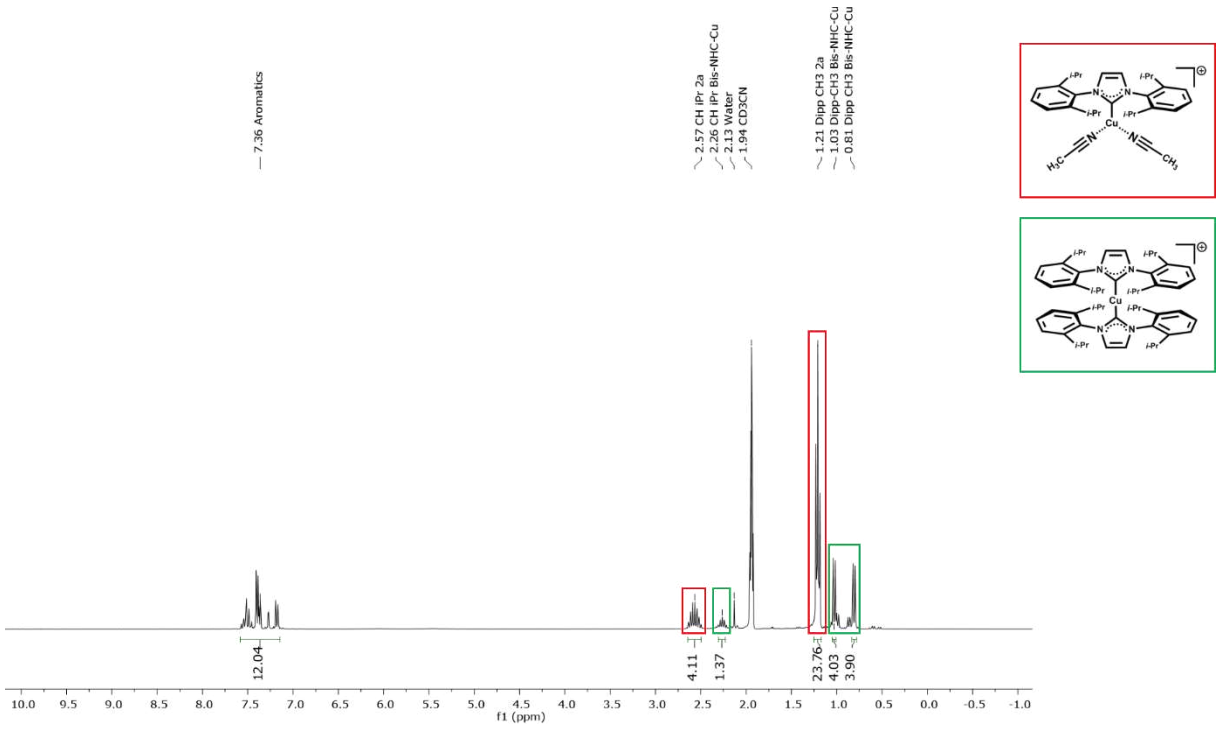

Figure S4**.** Proton NMR spectrum of the reaction mixture of the attempted synthesis of **2a** in MeCN-d^3. For this spectrum, the synthesis was performed directly in MeCN-d^3 in order to measure it with as little time loss as possible, which is why the signal for the complexated MeCN lies within the residual proton signal of the NMR solvent, to which this spectrum is also referenced. It shows two species, one being the expected **2a**, the other being the bis(NHC)-copper(I) tetrafluoroborate. Their presence is also indicated by mass spectrometry, although **2a** is not detected itself, only the mono(MeCN)-copper(I) complex. (MS (ESI(+), MeCN): m/z = 839 $[IPr\text{-}Cu\text{-}IPr]^+$, 492 $[IPr\text{-}Cu\text{-}MeCN]^+$, 388 $[IPr]^+$.

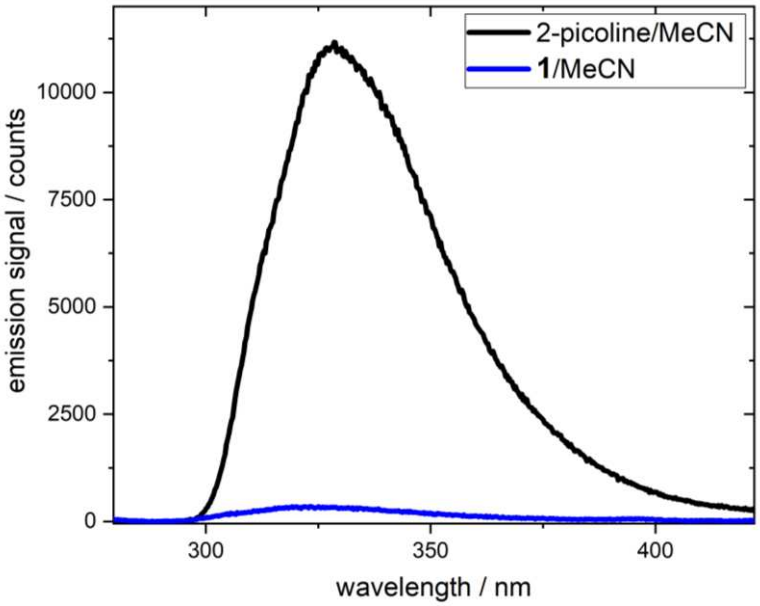

Figure S5. Comparison of the emission of similarly concentrated MeCN solutions of **1** (blue) and 2-picoline (black). The data were recorded using the Kerr setup described in the main part.

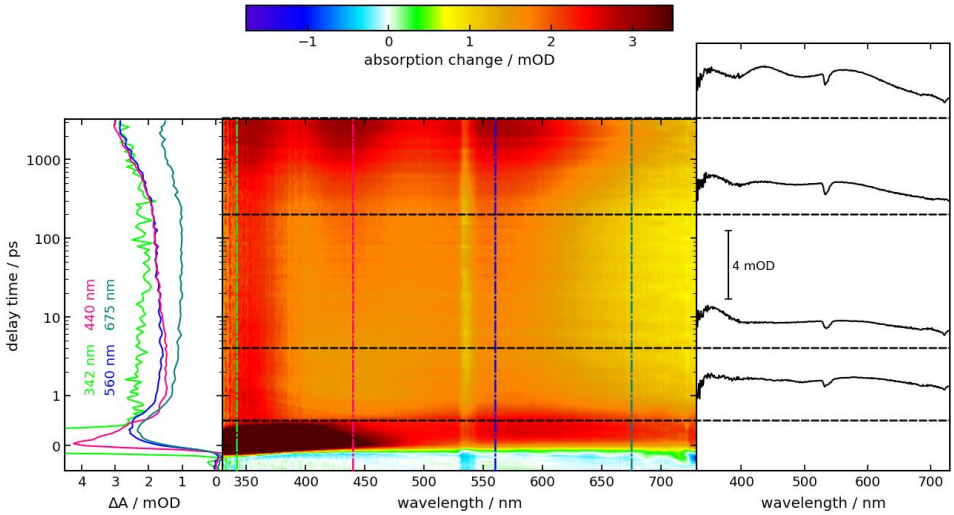

Figure S6. Time-resolved spectroscopy data aquired for **1** in DCM from fsTA experiment. The excitation was tuned to 266 nm. In the contour representation (central) the difference absorption signal is color-coded. Vertical lines mark spectral positions for the time traces plotted on the left while horizontal lines mark certain delay times for the difference spectra plotted on the right.

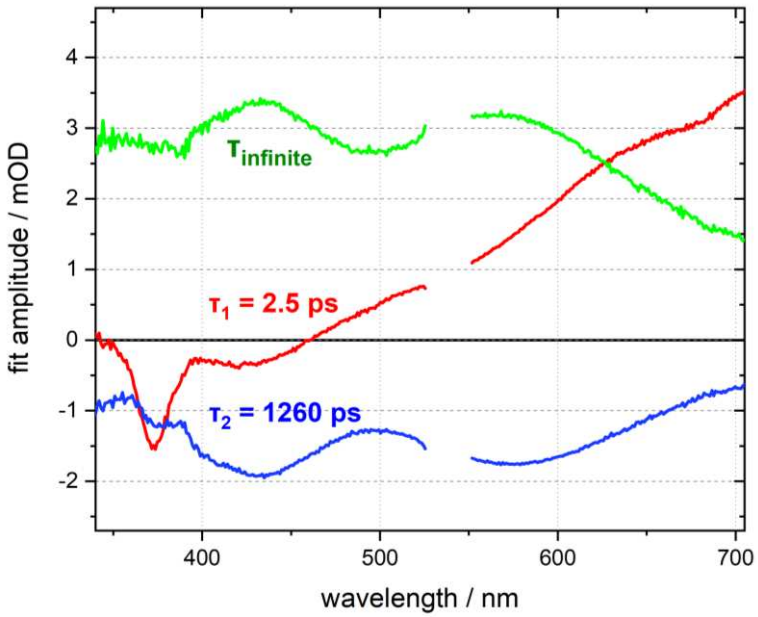

Figure S7: Decay associated difference spectra obtained from fsTA experiment of **1** in DCM. Due to strong solvent contributions around time zero that could not be fully corrected for, the first time constant of 2.5 ps and the respective DADS are less reliable.

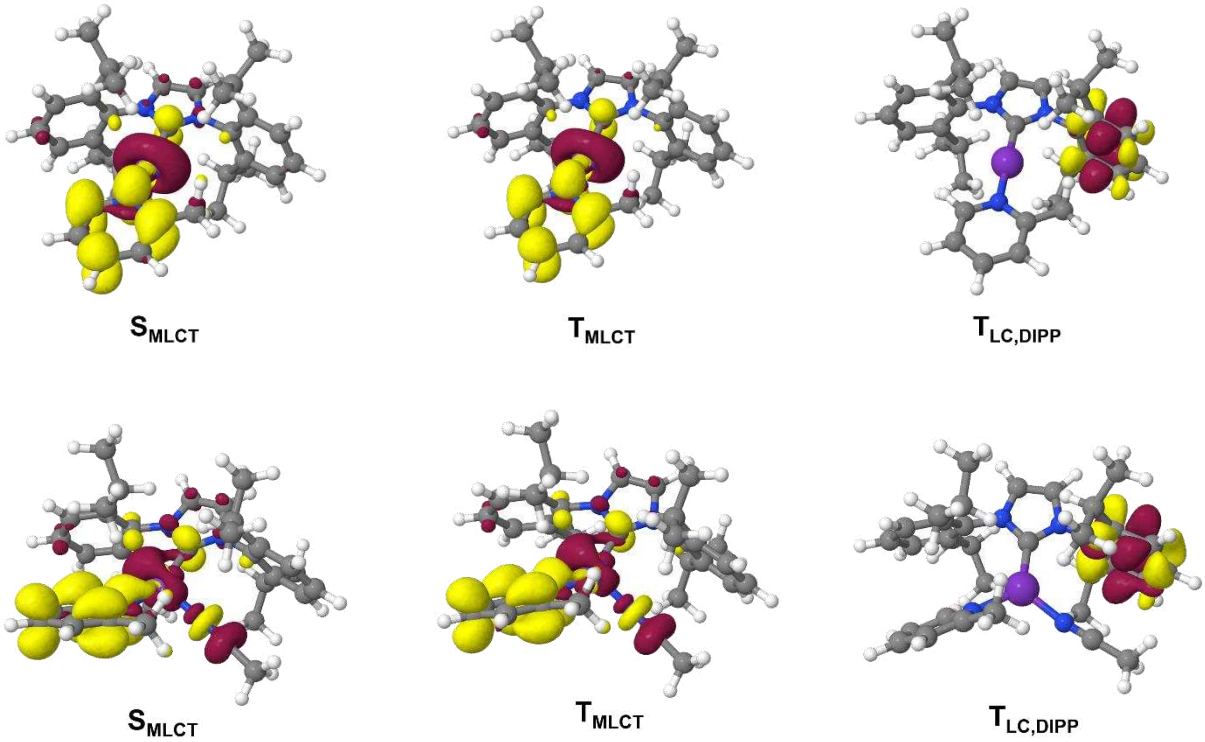

Figure S8: Electron difference densities for the S_{MLCT}, T_{MLCT}, and $T_{LC,DIPP}$ states of **1** (top) and **2b** (bottom).

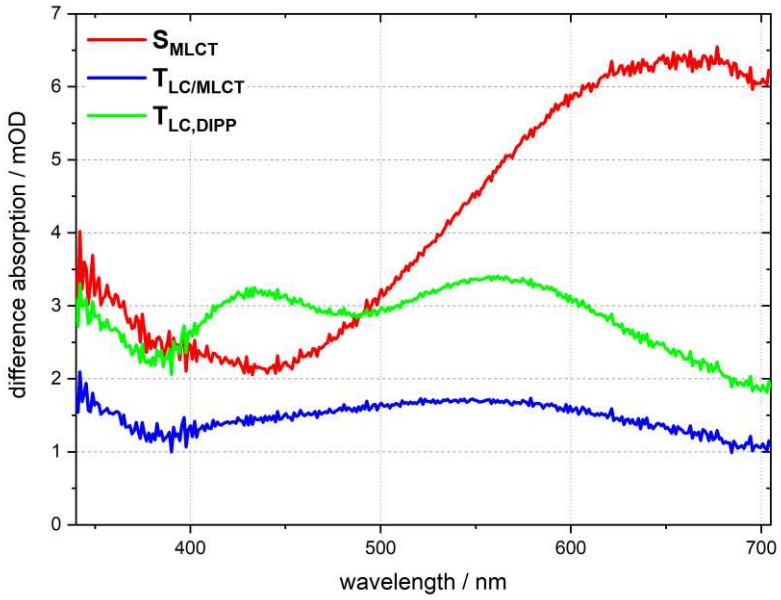

Figure S9: Species-associated difference spectra (SADS) obtained from fsTA experiment of **1** in TFE.

As expected for a consecutive model with largely differing time constants, the SADS [1] are essentially identical to difference spectra at specific delay times. The first SADS (i.e. for the S_{MLCT} state) is identical with the spectra at time zero. The second SADS (i.e. for the $T_{LC/MLCT}$ state) is identical with the spectra around a delay time of 10-100 ps, while the third SADS (i.e. for the $T_{LC,Dipp}$ state) is identical with the spectra from 4 ns onwards. Due to the absence of GSB in the transient data, yields for the population of each excited state could not be determined. Thus, the SADS were constructed assuming yields of 100% for each transition.

Table S1: Cartesian coordinates (in Å) for the S_0 geometries of compound **1** in DCM

C	0.903679	4.401519	-0.447257
C	-0.295125	5.100018	-0.328500
C	-1.406743	4.497918	0.255504
C	-1.341755	3.188559	0.743138
C	-0.113743	2.516360	0.622136
C	1.021153	3.089753	0.024342
N	-0.027964	1.165870	1.091701
C	-0.306534	0.097613	0.312827
N	-0.113554	-0.971301	1.117696
C	0.279046	-0.583047	2.382297
C	0.334253	0.776781	2.365469
C	-0.312563	-2.316762	0.668654
C	0.775369	-2.998182	0.096717
C	0.539252	-4.287845	-0.390422
C	-0.725528	-4.864555	-0.305968
C	-1.782989	-4.163013	0.266708
C	-1.600223	-2.869901	0.768564
C	2.138408	-2.349064	-0.053629
C	3.272890	-3.243895	0.445421
C	-2.769598	-2.092991	1.343652
C	-3.739207	-1.684174	0.231678
C	2.305639	2.308019	-0.174343
C	2.465468	1.930423	-1.650061
C	-2.575801	2.510282	1.306682
C	-3.252433	3.334456	2.402027
C	-3.481388	-2.861162	2.457948
C	-3.548607	2.171250	0.173185
C	3.532526	3.051548	0.353930
C	2.361488	-1.916474	-1.505499
H	0.481930	-1.302338	3.172248
H	0.595545	1.496339	3.137765
H	-2.772109	-4.627092	0.317654
H	1.356675	-4.849256	-0.851391
H	-0.889974	-5.873465	-0.695726
H	-2.346041	5.053764	0.325184
H	1.762164	4.883120	-0.924083
H	-0.366488	6.125173	-0.704000
H	-2.376579	-1.164181	1.789589
H	-2.262844	1.557037	1.764231
H	2.225176	1.367689	0.395861
H	2.150123	-1.435590	0.564010
H	-4.420953	1.617152	0.561800
H	-3.058855	1.542833	-0.593161
H	-3.915253	3.088200	-0.321891
H	-2.547542	3.570426	3.217809
H	-4.098694	2.770728	2.831880
H	-3.653368	4.286219	2.011324
H	-2.778035	-3.143495	3.260183
H	-3.956452	-3.783774	2.080807
H	-4.275847	-2.236239	2.901849
H	-3.228141	-1.068616	-0.530293
H	-4.572514	-1.088004	0.642941
H	-4.165882	-2.569408	-0.272845
H	1.576558	-1.210534	-1.831519
H	2.344750	-2.786287	-2.186337
H	3.336780	-1.410724	-1.615970
H	3.381788	-4.152852	-0.171791
H	3.104824	-3.558450	1.489853
H	4.231430	-2.698231	0.400867
H	3.412431	3.313922	1.419250
H	3.721122	3.983197	-0.207800
H	4.431228	2.418016	0.255542
H	2.564120	2.830982	-2.282102
H	1.590299	1.357550	-2.007674
H	3.364219	1.306191	-1.796887
Cu	-0.837437	0.075276	-1.482305
N	-1.364420	0.042411	-3.306895
C	-2.141256	0.079837	-5.964384
C	-1.516101	1.208331	-3.957716
C	-1.589015	-1.125772	-3.947509
C	-1.981807	-1.125616	-5.287139
C	-1.903144	1.274738	-5.287853
H	-1.316393	2.115681	-3.380268
C	-1.399463	-2.390379	-3.171502
H	-2.160743	-2.077704	-5.791661
H	-2.013841	2.245099	-5.776325
H	-2.448904	0.085760	-7.013967
H	-1.611093	-3.275261	-3.790040
H	-2.065090	-2.415256	-2.290790
H	-0.363975	-2.469330	-2.795746

Table S2: Cartesian coordinates (in Å) for the S_0 geometries of compound **1** in MeCN

C	0.909792	4.408058	-0.433738
C	-0.289266	5.106759	-0.317525
C	-1.403432	4.503313	0.260351
C	-1.341004	3.191983	0.743353
C	-0.113251	2.519163	0.624029
C	1.024577	3.094547	0.033779
N	-0.029706	1.167373	1.089671
C	-0.308889	0.100255	0.309063
N	-0.115819	-0.969494	1.113182
C	0.277511	-0.583051	2.378165
C	0.332636	0.776603	2.363009
C	-0.313428	-2.314443	0.662637
C	0.773138	-2.991538	0.083203
C	0.537750	-4.280355	-0.406938
C	-0.725141	-4.860565	-0.317622
C	-1.781196	-4.163695	0.263676
C	-1.598823	-2.871726	0.768649
C	2.134570	-2.339890	-0.069996
C	3.268693	-3.227955	0.442014
C	-2.766293	-2.098518	1.352325
C	-3.735954	-1.677828	0.244852
C	2.309367	2.312567	-0.161574
C	2.471922	1.933468	-1.636581
C	-2.576779	2.513042	1.302048
C	-3.252293	3.333140	2.401095
C	-3.478729	-2.875397	2.460000
C	-3.549298	2.181382	0.166257
C	3.535497	3.056111	0.368151
C	2.361622	-1.920241	-1.524879
H	0.480643	-1.303218	3.167181
H	0.594151	1.495109	3.136149
H	-2.769031	-4.630161	0.317775
H	1.353913	-4.837637	-0.875298
H	-0.889506	-5.868099	-0.711011
H	-2.342678	5.059584	0.328247
H	1.770312	4.890645	-0.905904
H	-0.358872	6.133008	-0.690453
H	-2.371204	-1.174787	1.806611
H	-2.265995	1.557143	1.755228
H	2.227801	1.373037	0.409628
H	2.142341	-1.420781	0.539041
H	-4.421672	1.625077	0.551722
H	-3.915301	3.101314	-0.323814
H	-2.547483	3.561602	3.219187
H	-4.100763	2.769241	2.826434
H	-3.649491	4.288399	2.014976
H	-2.774915	-3.167061	3.258589
H	-3.957422	-3.792719	2.074459
H	-4.270429	-2.251851	2.910749
H	-3.224292	-1.055677	-0.511231
H	-4.568101	-1.084383	0.662509
H	-4.163481	-2.557913	-0.267959
H	1.575965	-1.219386	-1.859804
H	2.349804	-2.795899	-2.198283
H	3.335837	-1.412454	-1.635594
H	3.377610	-4.145169	-0.163003
H	3.099012	-3.527901	1.490538
H	4.227208	-2.682671	0.391481
H	3.413540	3.319016	1.433172
H	3.725579	3.987082	-0.194352
H	4.433717	2.421519	0.271857
H	2.572599	2.833548	-2.269093
H	1.596916	1.361296	-1.995238
H	3.370490	1.308178	-1.780343
Cu	-0.841635	0.075957	-1.486084
N	-1.368854	0.034222	-3.311197
C	-2.135184	0.057789	-5.972004
C	-1.510174	1.196413	-3.970815
C	-1.599432	-1.136828	-3.944290
C	-1.986776	-1.143881	-5.285484
C	-1.891842	1.255827	-5.302945
H	-1.306558	2.106368	-3.399086
C	-1.422850	-2.396809	-3.158065
H	-2.169942	-2.098369	-5.783908
H	-1.994177	2.223475	-5.798534
H	-2.438553	0.058259	-7.022837
H	-1.639143	-3.284656	-3.770688
H	-2.092541	-2.408951	-2.280235
H	-0.389500	-2.480653	-2.777632

Table S3: Cartesian coordinates (in Å) for the S_0 geometries of compound **2a** in DCM

Cu	0.672682	0.706269	0.102012
N	2.245140	1.031018	-0.996783
C	-0.364579	-0.912686	0.035661
N	-1.576561	-1.159864	0.590492
C	-2.005721	-2.446766	0.332322
C	-1.027669	-3.033586	-0.408911
N	-0.045068	-2.078480	-0.578154
C	-2.286814	-0.189598	1.366578
C	-2.099041	-0.182898	2.759123
C	-2.760685	0.806587	3.493899
C	-3.573286	1.744776	2.860961
C	-3.737321	1.714117	1.478556
C	-3.096712	0.743918	0.699588
C	-1.163595	-1.160667	3.445060
C	0.140358	-0.458090	3.833580
C	-3.242195	0.750443	-0.810094
C	-4.706445	0.723460	-1.250631
C	1.177936	-2.256674	-1.299722
C	1.177061	-2.022674	-2.685584
C	2.398765	-2.133486	-3.357148
C	3.565497	-2.464309	-2.670518
C	3.533237	-2.693141	-1.297666
C	2.335492	-2.595595	-0.580635
C	-0.079074	-1.590328	-3.419056
C	-0.073757	-0.071594	-3.617425
C	2.319071	-2.807433	0.921427
C	2.892691	-4.169079	1.317033
C	-0.278623	-2.327135	-4.742960
C	3.044609	-1.663535	1.634048
C	-2.496108	1.944504	-1.411224
C	-1.813676	-1.852096	4.643418
H	-0.946566	-4.034452	-0.826927
H	-2.956965	-2.828332	0.696468
H	2.444125	-1.949842	-4.434191
H	4.458820	-2.945653	-0.772244
H	4.512101	-2.543573	-3.213569
H	-4.370936	2.463736	0.995505
H	-2.632517	0.852103	4.579308
H	-4.081035	2.512535	3.452601
H	-0.944899	-1.831521	-2.779837
H	-2.766370	-0.164248	-1.201321
H	-0.902864	-1.948395	2.718900
H	1.268561	-2.787346	1.256029
H	-2.552611	1.923338	-2.513681
H	-1.430740	1.928945	-1.120600
H	-2.928100	2.899686	-1.062475
H	-5.236596	-0.145929	-0.824657
H	-4.771058	0.659614	-2.351019
H	-5.243717	1.636513	-0.938880
H	-0.264350	-3.421543	-4.599731
H	0.501426	-2.068426	-5.480424
H	-1.252206	-2.051414	-5.184280
H	0.006406	0.451545	-2.649200
H	-1.003450	0.259522	-4.113416
H	0.780745	0.239618	-4.245468
H	2.592271	-0.689364	1.375918
H	4.111036	-1.628194	1.348077
H	2.986189	-1.789856	2.729297
H	3.963738	-4.250734	1.060522
H	2.357072	-4.991026	0.811115
H	2.799541	-4.318407	2.407129
H	-2.749974	-2.359481	4.352931
H	-2.049365	-1.138261	5.452209
H	-1.128148	-2.610221	5.060749
H	-0.047845	0.356269	4.556685
H	0.628631	-0.020996	2.945732
H	0.843218	-1.172753	4.297409
C	3.116113	1.114176	-1.750921
C	4.194826	1.230006	-2.708416
H	4.880557	0.373493	-2.606303
H	4.750076	2.166250	-2.535351
H	3.780128	1.239996	-3.730043
C	-0.199777	2.985188	1.995501
C	-0.741810	3.943528	2.933557
H	-0.114630	4.849115	2.958335
H	-0.774201	3.494063	3.939652
H	-1.765529	4.214938	2.629148
N	0.221090	2.207424	1.252300

Table S4: Cartesian coordinates (in Å) for the S_0 geometries of compound **2b** in DCM

C	0.855324	4.239279	-0.827039
C	-0.389722	4.834044	-1.009034
C	-1.549680	4.185390	-0.590746
C	-1.491870	2.925474	0.012919
C	-0.221183	2.342741	0.166882
C	0.967956	2.978256	-0.229397
N	-0.129580	1.034199	0.738348
C	-0.031257	-0.095397	-0.005623
N	0.089845	-1.082079	0.917768
C	0.072597	-0.582898	2.206281
C	-0.062333	0.764221	2.092455
C	0.313839	-2.452692	0.571387
C	1.634982	-2.927318	0.576985
C	1.840873	-4.268352	0.231381
C	0.772356	-5.087292	-0.117878
C	-0.526035	-4.579874	-0.141827
C	-0.785541	-3.249435	0.199343
C	2.817540	-2.032783	0.899470
C	3.595655	-2.538502	2.115494
C	-2.193356	-2.682255	0.183748
C	-3.116914	-3.379291	-0.812218
C	2.324989	2.318761	-0.065058
C	2.837892	1.799118	-1.410661
C	-2.751516	2.193530	0.440495
C	-3.816186	3.119202	1.026152
C	-2.805409	-2.693862	1.588735
C	-3.312465	1.370351	-0.722775
C	3.344834	3.241143	0.603377
C	3.723029	-1.862310	-0.322992
H	0.167074	-1.224249	3.079681
H	-0.114748	1.548556	2.843945
H	-1.349116	-5.235184	-0.435535
H	2.856788	-4.674597	0.226598
H	0.951647	-6.133176	-0.385196
H	-2.517454	4.670282	-0.740747
H	1.756156	4.762966	-1.159235
H	-0.458493	5.818372	-1.481683
H	-2.112077	-1.627472	-0.132587
H	-2.468414	1.481288	1.234082
H	2.198582	1.444264	0.594572
H	2.431464	-1.032031	1.151800
H	-4.204727	0.803672	-0.402502
H	-2.560005	0.655215	-1.093748
H	-3.599541	2.024546	-1.565836
H	-3.405879	3.747158	1.835875
H	-4.644628	2.520377	1.442428
H	-4.249270	3.786533	0.260614
H	-2.187174	-2.133207	2.309529
H	-2.906397	-3.729772	1.958815
H	-3.809557	-2.234225	1.574041
H	-2.656085	-3.450502	-1.812447
H	-4.059020	-2.812499	-0.907967
H	-3.381975	-4.399842	-0.484109
H	3.157400	-1.453762	-1.177665
H	4.169800	-2.824297	-0.632381
H	4.548539	-1.165257	-0.094454
H	4.042423	-3.530938	1.926968
H	2.941965	-2.623706	3.000925
H	4.416944	-1.842518	2.360957
H	2.969297	3.618844	1.569994
H	3.591367	4.110887	-0.030481
H	4.284295	2.692353	0.790570
H	2.966852	2.624120	-2.134024
H	2.132109	1.067165	-1.845035
H	3.811395	1.293361	-1.286664
Cu	-0.079491	-0.309757	-1.913016
N	-1.004200	0.848968	-3.284730
C	-2.339925	2.585779	-4.995510
C	-0.604855	2.120093	-3.423461
C	-2.070556	0.411859	-3.983272
C	-2.757472	1.265674	-4.849862
C	-1.237596	3.024860	-4.266188
H	0.252538	2.427927	-2.818074
C	-2.491210	-1.007032	-3.769465
H	-3.620240	0.887644	-5.403839
H	-0.871934	4.051859	-4.334243
H	-2.872685	3.263917	-5.668526
H	-3.330982	-1.285614	-4.423584
H	-2.805064	-1.158216	-2.721226
H	-1.647834	-1.693108	-3.957758
N	0.763845	-1.870694	-2.759992
C	1.249001	-2.873330	-3.067783
C	1.860496	-4.132158	-3.438131
H	1.199406	-4.962061	-3.140208
H	2.824778	-4.242224	-2.915464
H	2.028276	-4.169178	-4.526866

Table S5: Cartesian coordinates (in Å) for the S_0 geometries of compound **2b** in MeCN

C	0.853465	4.236314	-0.832317
C	-0.391673	4.830798	-1.014776
C	-1.551347	4.183358	-0.593425
C	-1.493038	2.924754	0.013083
C	-0.222270	2.342143	0.167421
C	0.966437	2.976717	-0.231556
N	-0.130427	1.034535	0.740579
C	-0.031942	-0.095543	-0.002683
N	0.088723	-1.081594	0.921408
C	0.071253	-0.581592	2.209638
C	-0.063468	0.765496	2.094941
C	0.312150	-2.452083	0.574291
C	1.633329	-2.926690	0.576329
C	1.838974	-4.266512	0.225662
C	0.770077	-5.084444	-0.125004
C	-0.528596	-4.577455	-0.143870
C	-0.787742	-3.248173	0.202216
C	2.816118	-2.032858	0.899737
C	3.595194	-2.542171	2.113612
C	-2.195637	-2.681181	0.190751
C	-3.119693	-3.372861	-0.808449
C	2.323604	2.317600	-0.067119
C	2.837576	1.799474	-1.412903
C	-2.752149	2.192993	0.442384
C	-3.818249	3.119296	1.024293
C	-2.806314	-2.700572	1.596226
C	-3.311308	1.365425	-0.718604
C	3.342324	3.240195	0.602709
C	3.720818	-1.858975	-0.322818
H	0.165605	-1.222021	3.083667
H	-0.115999	1.550152	2.846057
H	-1.351808	-5.231664	-0.439649
H	2.855053	-4.672251	0.215742
H	0.949491	-6.128490	-0.399143
H	-2.519243	4.667758	-0.744433
H	1.753966	4.758440	-1.167925
H	-0.460904	5.813209	-1.491340
H	-2.115022	-1.624757	-0.119728
H	-2.468814	1.483695	1.238391
H	2.197614	1.442652	0.591856
H	2.430339	-1.032898	1.155554
H	-4.200821	0.795572	-0.396323
H	-2.556560	0.652245	-1.088503
H	-3.601562	2.016834	-1.562797
H	-3.409257	3.749219	1.833228
H	-4.646567	2.520542	1.440985
H	-4.250752	3.784454	0.256468
H	-2.186542	-2.144971	2.319678
H	-2.908260	-3.738764	1.959927
H	-3.809837	-2.239410	1.585071
H	-2.659262	-3.437987	-1.809216
H	-4.061803	-2.805414	-0.900311
H	-3.383760	-4.395542	-0.486118
H	3.154135	-1.449927	-1.176502
H	4.168723	-2.819645	-0.634616
H	4.544881	-1.160570	-0.093011
H	4.041074	-3.534344	1.921323
H	2.942096	-2.628941	2.999411
H	4.417021	-1.846994	2.359801
H	2.966447	3.614500	1.570599
H	3.586828	4.111767	-0.029538
H	4.282560	2.692098	0.788193
H	2.965750	2.624964	-2.135847
H	2.132626	1.067039	-1.847745
H	3.811362	1.294377	-1.288398
Cu	-0.078959	-0.311598	-1.909698
N	-1.001125	0.846877	-3.283881
C	-2.330755	2.583039	-5.000048
C	-0.595372	2.115341	-3.428879
C	-2.070843	0.412005	-3.978735
C	-2.754558	1.265581	-4.848289
C	-1.225015	3.019843	-4.274249
H	0.265055	2.421159	-2.826849
C	-2.499231	-1.003270	-3.756948
H	-3.619780	0.889390	-5.399609
H	-0.854362	4.044715	-4.347326
H	-2.861243	3.260963	-5.675056
H	-3.334596	-1.283608	-4.415924
H	-2.823321	-1.143627	-2.710308
H	-1.657220	-1.694689	-3.931376
N	0.767173	-1.869331	-2.759124
C	1.255092	-2.869800	-3.069746
C	1.870750	-4.125267	-3.443617
H	1.195305	-4.956511	-3.184440
H	2.816671	-4.251164	-2.891825
H	2.073843	-4.142066	-4.526766

Table S6: Cartesian coordinates (in Å), for the S_{MLCT} geometries of compound **1** in DCM

C	0.743789	4.124790	-0.878367
C	-0.490629	4.769594	-0.862493
C	-1.569779	4.221393	-0.173189
C	-1.440057	3.016484	0.523425
C	-0.175993	2.394283	0.496020
C	0.932105	2.916300	-0.201009
N	-0.046964	1.099752	1.104862
C	-0.312622	0.013755	0.364030
N	-0.119851	-1.044007	1.162361
C	0.269683	-0.625185	2.418500
C	0.317043	0.738796	2.383653
C	-0.305289	-2.393244	0.709383
C	0.785613	-3.049638	0.114244
C	0.565879	-4.348775	-0.354763
C	-0.684329	-4.950541	-0.237838
C	-1.746033	-4.266369	0.348299
C	-1.582494	-2.965225	0.834336
C	2.150111	-2.401164	-0.023157
C	3.190368	-3.125202	0.835401
C	-2.748010	-2.224693	1.462277
C	-3.913613	-2.077671	0.481970
C	2.259966	2.187586	-0.268701
C	2.491652	1.620837	-1.672466
C	-2.631314	2.391186	1.222930
C	-3.306903	3.362854	2.192002
C	-3.186975	-2.895986	2.766000
C	-3.628215	1.844217	0.196997
C	3.425218	3.074927	0.173045
C	2.590110	-2.315284	-1.486217
H	0.476997	-1.330059	3.220336
H	0.574005	1.469785	3.146600
H	-2.722821	-4.752193	0.426199
H	1.387024	-4.899070	-0.822776
H	-0.834500	-5.967146	-0.612714
H	-2.534540	4.735520	-0.187404
H	1.573321	4.564685	-1.438408
H	-0.616762	5.710659	-1.405314
H	-2.412107	-1.206218	1.719061
H	-2.271154	1.537061	1.820258
H	2.220751	1.334724	0.429179
H	2.079896	-1.367706	0.354821
H	-4.480358	1.359624	0.703936
H	-3.162266	1.085221	-0.460766
H	-4.020379	2.648574	-0.449307
H	-2.587132	3.754050	2.931020
H	-4.115963	2.847976	2.737961
H	-3.756483	4.221228	1.663514
H	-2.350908	-2.957233	3.484137
H	-3.555167	-3.921265	2.584480
H	-4.004045	-2.321554	3.236414
H	-3.593805	-1.577457	-0.449224
H	-4.718142	-1.472007	0.934027
H	-4.342084	-3.058068	0.209837
H	1.844406	-1.781614	-2.101554
H	2.736614	-3.317400	-1.925747
H	3.547052	-1.770524	-1.564377
H	3.328561	-4.168671	0.501108
H	2.888268	-3.145474	1.896797
H	4.167100	-2.615492	0.764782
H	3.259548	3.474111	1.188163
H	3.571184	3.928614	-0.511292
H	4.361503	2.490918	0.180963
H	2.538965	2.424034	-2.428167
H	1.680960	0.929885	-1.975580
H	3.436715	1.052362	-1.710477
Cu	-0.817426	0.233295	-1.454003
N	-1.264633	0.554715	-3.206870
C	-1.952044	0.943121	-5.906081
C	-1.268094	1.825428	-3.761633
C	-1.604188	-0.534379	-4.007801
C	-1.941582	-0.348165	-5.326212
C	-1.600183	2.034392	-5.074877
H	-0.991182	2.647300	-3.093395
C	-1.561360	-1.856493	-3.314266
H	-2.203112	-1.227100	-5.923285
H	-1.587090	3.056915	-5.463072
H	-2.220226	1.089740	-6.953397
H	-1.855133	-2.682068	-3.980998
H	-2.249848	-1.884109	-2.441522
H	-0.542247	-2.090402	-2.936927

Table S7: Cartesian coordinates (in Å) the S_{MLCT} geometries of compound **2b** in DCM

C	0.746305	4.310034	-0.768396
C	-0.539673	4.776312	-1.035468
C	-1.654161	4.020755	-0.686910
C	-1.513479	2.782284	-0.051700
C	-0.203321	2.344626	0.209695
C	0.946342	3.077472	-0.140491
N	-0.024176	1.057657	0.817441
C	0.042157	-0.069701	0.084378
N	0.197684	-1.066749	0.975436
C	0.233086	-0.565820	2.263005
C	0.090466	0.783670	2.163076
C	0.340755	-2.451628	0.633824
C	1.635230	-2.992753	0.617167
C	1.757992	-4.345876	0.279424
C	0.636815	-5.106874	-0.035103
C	-0.632843	-4.530553	-0.034344
C	-0.812846	-3.184499	0.296041
C	2.871539	-2.157391	0.895981
C	3.696584	-2.729440	2.049695
C	-2.189014	-2.541077	0.292486
C	-3.166726	-3.204691	-0.673837
C	2.342063	2.527434	0.089608
C	2.880504	1.890770	-1.196472
C	-2.734627	1.958079	0.310047
C	-3.635759	2.698907	1.300375
C	-2.776632	-2.488170	1.707175
C	-3.506059	1.531968	-0.942117
C	3.311664	3.575922	0.633909
C	3.710701	-1.989395	-0.374026
H	0.364578	-1.212592	3.127621
H	0.062620	1.564989	2.918771
H	-1.496055	-5.143295	-0.302656
H	2.748872	-4.808487	0.254034
H	0.752012	-6.163114	-0.295924
H	-2.654284	4.396704	-0.919082
H	1.608184	4.913403	-1.064261
H	-0.673031	5.740389	-1.534648
H	-2.065143	-1.498302	-0.051645
H	-2.392255	1.038109	0.812859
H	2.272614	1.727914	0.846572
H	2.547348	-1.148457	1.198208
H	-4.343493	0.867038	-0.667632
H	-2.858528	0.992868	-1.657086
H	-3.922989	2.403620	-1.476317
H	-3.082779	2.973046	2.215271
H	-4.487390	2.059635	1.591541
H	-4.045432	3.624366	0.858814
H	-2.119327	-1.946831	2.407597
H	-2.927972	-3.508879	2.100738
H	-3.754189	-1.975007	1.695837
H	-2.730849	-3.313242	-1.681664
H	-4.078166	-2.589022	-0.760510
H	-3.478317	-4.204151	-0.323621
H	3.119854	-1.524863	-1.182320
H	4.090402	-2.960817	-0.738338
H	4.580983	-1.339851	-0.174946
H	4.098244	-3.728869	1.806645
H	3.089525	-2.820509	2.967018
H	4.553765	-2.069280	2.268654
H	2.912620	4.057677	1.542916
H	3.524458	4.365315	-0.107675
H	4.273427	3.099618	0.890740
H	2.945724	2.635446	-2.009312
H	2.232754	1.065218	-1.543640
H	3.887710	1.470982	-1.028756
Cu	-0.290279	-0.011630	-1.826282
N	-0.845358	0.753788	-3.463625
C	-2.254815	2.486538	-5.211859
C	-0.573327	2.115901	-3.523325
C	-1.825069	0.253958	-4.319577
C	-2.509078	1.091936	-5.168937
C	-1.248388	2.976387	-4.353222
H	0.226333	2.482803	-2.871046
C	-2.099870	-1.211528	-4.249110
H	-3.269838	0.652171	-5.821392
H	-0.975491	4.035920	-4.339906
H	-2.803832	3.142986	-5.888902
H	-2.973349	-1.480371	-4.863021
H	-2.301155	-1.530199	-3.205928
H	-1.237259	-1.808884	-4.598834
N	0.437348	-1.762894	-2.419940
C	0.888418	-2.744763	-2.816376
C	1.446979	-3.973907	-3.330675
H	0.761406	-4.807203	-3.108513
H	2.418546	-4.167640	-2.848643
H	1.584506	-3.886108	-4.420729

Table S8: Cartesian coordinates (in Å) for the T_{MLCT} geometries of compound **1** in DCM

C	0.745389	4.127369	-0.878323
C	-0.489205	4.771871	-0.864126
C	-1.568978	4.222317	-0.177104
C	-1.439579	3.016370	0.518356
C	-0.175468	2.394961	0.493394
C	0.932847	2.918158	-0.201620
N	-0.047610	1.099552	1.098972
C	-0.314934	0.012432	0.357796
N	-0.120964	-1.044779	1.158561
C	0.270179	-0.624726	2.414178
C	0.317696	0.738758	2.377812
C	-0.306328	-2.393802	0.707367
C	0.784338	-3.050879	0.112480
C	0.564470	-4.350171	-0.356240
C	-0.685813	-4.951816	-0.238947
C	-1.747397	-4.267289	0.347093
C	-1.583611	-2.965742	0.832112
C	2.149082	-2.402460	-0.023724
C	3.189339	-3.129248	0.832465
C	-2.748356	-2.224591	1.460824
C	-3.916646	-2.079908	0.483469
C	2.261013	2.189669	-0.269387
C	2.496446	1.629125	-1.675085
C	-2.632322	2.390606	1.215138
C	-3.302147	3.358314	2.192124
C	-3.183804	-2.893549	2.766958
C	-3.632908	1.854184	0.187256
C	3.424848	3.074738	0.180406
C	2.588672	-2.311787	-1.486560
H	0.478167	-1.328867	3.216468
H	0.575660	1.470347	3.139842
H	-2.724157	-4.753122	0.425724
H	1.385589	-4.900781	-0.824004
H	-0.836065	-5.968643	-0.613270
H	-2.534140	4.735816	-0.192035
H	1.575926	4.568049	-1.436391
H	-0.614736	5.713584	-1.406058
H	-2.412153	-1.205414	1.714317
H	-2.274258	1.530855	1.805609
H	2.219478	1.333252	0.424024
H	2.079057	-1.370018	0.357037
H	-4.484216	1.366014	0.692290
H	-3.168203	1.101055	-0.478435
H	-4.026343	2.664825	-0.450544
H	-2.579710	3.740393	2.933330
H	-4.113503	2.843821	2.735138
H	-3.747470	4.223041	1.670307
H	-2.345856	-2.953372	3.483026
H	-3.552210	-3.919263	2.588171
H	-3.999774	-2.318499	3.238577
H	-3.599619	-1.579060	-0.448326
H	-4.720917	-1.475232	0.937383
H	-4.344514	-3.060970	0.212625
H	1.845194	-1.770364	-2.097842
H	2.729623	-3.312366	-1.931490
H	3.548270	-1.771359	-1.562684
H	3.327880	-4.171638	0.494922
H	2.886953	-3.152989	1.893726
H	4.166037	-2.619157	0.763831
H	3.256686	3.467927	1.197504
H	3.571974	3.932685	-0.498423
H	4.361563	2.491305	0.187153
H	2.548000	2.435980	-2.426707
H	1.684921	0.940810	-1.982325
H	3.441093	1.059747	-1.712431
Cu	-0.825890	0.225175	-1.458626
N	-1.265051	0.548485	-3.203153
C	-1.950957	0.937778	-5.898099
C	-1.276969	1.818584	-3.751602
C	-1.601003	-0.539689	-4.002664
C	-1.937035	-0.351959	-5.323007
C	-1.607793	2.028546	-5.066183
H	-1.005318	2.640124	-3.080554
C	-1.555098	-1.858517	-3.306157
H	-2.194963	-1.230892	-5.921492
H	-1.599710	3.051839	-5.452091
H	-2.218639	1.085484	-6.945593
H	-1.852262	-2.686631	-3.967900
H	-2.239325	-1.879935	-2.429386
H	-0.534089	-2.088622	-2.931496

Table S9: Cartesian coordinates (in Å) the T_{MLCT} geometries of compound **2b** in DCM

C	0.792505	4.250075	-0.797804
C	-0.474126	4.746279	-1.097373
C	-1.615043	4.023073	-0.764671
C	-1.519941	2.786443	-0.117676
C	-0.227990	2.319127	0.179779
C	0.946585	3.019604	-0.152589
N	-0.090868	1.029843	0.794820
C	0.009084	-0.093789	0.059087
N	0.153463	-1.092685	0.950316
C	0.139091	-0.598467	2.240509
C	-0.016578	0.750292	2.141989
C	0.357834	-2.467572	0.598745
C	1.675947	-2.949126	0.568821
C	1.858317	-4.292008	0.218038
C	0.771639	-5.101362	-0.097657
C	-0.523026	-4.584883	-0.080643
C	-0.761691	-3.251768	0.265921
C	2.874898	-2.067562	0.866560
C	3.657386	-2.575204	2.079552
C	-2.167779	-2.681522	0.303386
C	-3.106980	-3.325767	-0.713775
C	2.324619	2.444088	0.119723
C	2.900666	1.810526	-1.151072
C	-2.768897	2.005768	0.244304
C	-3.558587	2.720774	1.343770
C	-2.749206	-2.771813	1.718828
C	-3.636504	1.725271	-0.984507
C	3.289489	3.472722	0.709084
C	3.772412	-1.923853	-0.365372
H	0.249193	-1.247563	3.106158
H	-0.077876	1.527230	2.900290
H	-1.360263	-5.234422	-0.345487
H	2.869344	-4.708265	0.184790
H	0.934014	-6.148509	-0.369808
H	-2.600151	4.424068	-1.018230
H	1.676428	4.827790	-1.080140
H	-0.572237	5.708311	-1.608618
H	-2.100251	-1.610030	0.044035
H	-2.455905	1.029220	0.650606
H	2.216882	1.639604	0.866828
H	2.508423	-1.058024	1.114352
H	-4.483484	1.072345	-0.710277
H	-3.054800	1.227699	-1.779416
H	-4.053823	2.654816	-1.409522
H	-2.940811	2.874683	2.245598
H	-4.442901	2.124690	1.629709
H	-3.912276	3.709231	1.000494
H	-2.116743	-2.248173	2.455427
H	-2.837205	-3.826669	2.034003
H	-3.755083	-2.317658	1.750564
H	-2.660524	-3.343341	-1.722719
H	-4.049020	-2.753975	-0.766412
H	-3.368114	-4.361468	-0.434786
H	3.209262	-1.516614	-1.222675
H	4.204779	-2.894504	-0.666935
H	4.607934	-1.234697	-0.151411
H	4.085927	-3.576020	1.893981
H	3.012362	-2.642564	2.972668
H	4.491877	-1.890008	2.309416
H	2.866719	3.947927	1.610749
H	3.535754	4.268997	-0.014571
H	4.236414	2.980973	0.991002
H	3.005498	2.560476	-1.954915
H	2.256042	0.995535	-1.527486
H	3.895501	1.375883	-0.950800
Cu	-0.283518	-0.015172	-1.858022
N	-0.917683	0.816837	-3.408953
C	-2.170095	2.505886	-5.304723
C	-0.407432	2.076168	-3.711742
C	-2.018223	0.366142	-4.143345
C	-2.638442	1.192282	-5.049430
C	-1.010693	2.919763	-4.607088
H	0.495659	2.376383	-3.170936
C	-2.493714	-1.013501	-3.832393
H	-3.514423	0.807490	-5.581019
H	-0.568735	3.906106	-4.776978
H	-2.663218	3.152171	-6.032601
H	-3.416259	-1.253345	-4.383329
H	-2.709023	-1.122256	-2.747875
H	-1.735907	-1.779746	-4.081000
N	0.511391	-1.705602	-2.496541
C	0.952048	-2.691169	-2.895230
C	1.501772	-3.924969	-3.407431
H	0.794143	-4.746923	-3.213838
H	2.454452	-4.141295	-2.898223
H	1.672794	-3.829424	-4.491985

Table S10: Cartesian coordinates (in Å) for the $T_{LC,Dipp}$ geometries of compound **1** in DCM

C	1.181622	4.490587	0.452897
C	-0.037927	5.103459	0.174670
C	-1.235087	4.438010	0.424822
C	-1.240481	3.147231	0.964504
C	0.005414	2.559649	1.240398
C	1.231112	3.200976	0.991833
N	0.028532	1.223373	1.754751
C	0.031917	0.132205	0.957973
N	0.051924	-0.914006	1.812916
C	0.057592	-0.492474	3.125426
C	0.042863	0.868638	3.089368
C	0.050594	-2.267721	1.348165
C	1.269955	-2.856496	1.039101
C	1.235264	-4.247949	0.468152
C	0.012772	-4.888892	0.243205
C	-1.182510	-4.274621	0.559190
C	-1.198191	-2.882929	1.131608
C	2.595704	-2.168573	1.178059
C	3.549664	-2.951635	2.088983
C	-2.514052	-2.194482	1.331439
C	-3.191846	-1.914037	-0.018770
C	2.557171	2.500901	1.222110
C	3.115943	1.989601	-0.109629
C	-2.544311	2.401607	1.176723
C	-3.551216	3.204978	2.000151
C	-3.441643	-2.985476	2.262776
C	-3.131561	1.971653	-0.170715
C	3.572400	3.375765	1.956672
C	3.224834	-1.913700	-0.198943
H	0.072846	-1.190750	3.958918
H	0.042909	1.610074	3.884920
H	-2.132327	-4.790660	0.405975
H	2.177346	-4.751369	0.244653
H	0.007154	-5.900498	-0.174762
H	-2.183592	4.928858	0.188784
H	2.112161	5.023312	0.238596
H	-0.054885	6.112374	-0.248241
H	-2.325006	-1.218308	1.808995
H	-2.322398	1.482431	1.743828
H	2.369390	1.619131	1.857269
H	2.426795	-1.184634	1.646611
H	-4.046262	1.371205	-0.022743
H	-2.408708	1.356646	-0.737502
H	-3.391348	2.848999	-0.789651
H	-3.124451	3.502662	2.973464
H	-4.453375	2.598301	2.192009
H	-3.873840	4.120967	1.474844
H	-2.963745	-3.164736	3.241103
H	-3.720144	-3.963862	1.833484
H	-4.374785	-2.420399	2.433344
H	-2.563886	-1.249958	-0.638826
H	-4.164752	-1.414750	0.136056
H	-3.373591	-2.845226	-0.584454
H	2.571942	-1.267192	-0.811918
H	3.396253	-2.854383	-0.751735
H	4.197941	-1.404031	-0.086785
H	3.802434	-3.940654	1.668265
H	3.106760	-3.107768	3.087558
H	4.493541	-2.392599	2.214350
H	3.163271	3.749255	2.911225
H	3.879565	4.247081	1.352173
H	4.482768	2.792188	2.178351
H	3.338072	2.828799	-0.792917
H	2.391666	1.322965	-0.612584
H	4.047517	1.419009	0.051785
Cu	0.006772	0.035353	-0.911799
N	-0.017866	-0.074209	-2.809288
C	-0.041876	-0.137016	-5.577658
C	-0.007159	1.067020	-3.518430
C	-0.040492	-1.266431	-3.444581
C	-0.052791	-1.317115	-4.839547
C	-0.018627	1.083403	-4.905313
H	0.011071	1.995899	-2.940890
C	-0.052693	-2.501286	-2.601133
H	-0.070974	-2.288394	-5.339085
H	-0.009287	2.035477	-5.440018
H	-0.051338	-0.170526	-6.670868
H	-0.059631	-3.410272	-3.220582
H	-0.942239	-2.521371	-1.947055
H	0.833184	-2.537278	-1.942687

Table S11: Cartesian coordinates (in Å) for the $T_{LC,Dipp}$ geometries of compound **2b** in DCM

C	0.576230	4.414141	-0.771642	H	-4.446896	2.830700	-1.131303
C	-0.683598	4.760025	-1.250447	H	-2.586817	1.557808	1.907756
C	-1.761098	3.891056	-1.097203	H	-4.164417	1.038836	1.261092
C	-1.608673	2.660031	-0.452127	H	-3.760483	2.779212	1.341073
C	-0.325452	2.344212	0.033508	H	-2.510368	-3.234817	2.964450
C	0.784971	3.193285	-0.120396	H	-3.132959	-4.410286	1.770993
N	-0.126324	1.092088	0.699747	H	-3.975709	-2.860677	2.010677
C	0.039406	-0.087331	0.048937	H	-2.200083	-2.240798	-1.251825
N	0.242546	-0.981070	1.048011	H	-3.807770	-2.337115	-0.467877
C	0.196432	-0.385134	2.291761	H	-2.887243	-3.830275	-0.814326
C	-0.033393	0.935950	2.070621	H	2.707278	-1.403642	-1.632137
C	0.436336	-2.375708	0.809857	H	3.752378	-2.828566	-1.371073
C	1.693206	-2.831248	0.507642	H	4.358946	-1.197037	-0.974684
C	1.838164	-4.280050	0.175354	H	4.365124	-3.459106	1.167078
C	0.717606	-5.152703	0.259911	H	3.601938	-2.506826	2.471467
C	-0.517159	-4.674187	0.593150	H	4.854733	-1.767000	1.432407
C	-0.730588	-3.213731	0.835831	H	2.529631	4.537243	1.568113
C	2.917050	-1.959394	0.466531	H	3.332580	4.591456	-0.027919
C	3.992101	-2.456284	1.440330	H	3.976186	3.537729	1.248780
C	-2.124814	-2.668105	0.886110	H	3.042859	2.602241	-1.660552
C	-2.794520	-2.777151	-0.493026	H	2.264771	1.096720	-1.080534
C	2.170377	2.766525	0.334620	H	3.847516	1.593498	-0.423404
C	2.868888	1.968265	-0.772319	Cu	-0.084860	-0.454697	-1.832799
C	-2.773835	1.701316	-0.277937	N	-0.664349	0.832604	-3.290980
C	-3.348764	1.773808	1.141266	C	-1.398584	2.736260	-5.180597
C	-2.979268	-3.335121	1.970496	C	0.060101	1.945710	-3.465489
C	-3.883777	1.897259	-1.307587	C	-1.766194	0.639442	-4.042526
C	3.043650	3.927243	0.805339	C	-2.155738	1.582627	-4.997365
C	3.464145	-1.843679	-0.961290	C	-0.262411	2.923322	-4.397676
H	0.335306	-0.948868	3.211232	H	0.931545	2.061609	-2.815796
H	-0.129121	1.773602	2.757894	C	-2.559269	-0.603783	-3.793680
H	-1.367674	-5.352901	0.693610	H	-3.055663	1.404225	-5.590926
H	2.820564	-4.668878	-0.097920	H	0.362936	3.813735	-4.491895
H	0.859869	-6.221654	0.071417	H	-1.696399	3.481756	-5.923667
H	-2.736343	4.177095	-1.496635	H	-3.396658	-0.697290	-4.501415
H	1.411705	5.103949	-0.913096	H	-2.972826	-0.593398	-2.769494
H	-0.827317	5.717565	-1.759849	H	-1.917025	-1.496738	-3.879400
H	-2.064760	-1.594253	1.131709	N	0.316439	-2.212424	-2.604535
H	-2.371180	0.682679	-0.423092	C	0.578478	-3.298261	-2.901294
H	2.047384	2.086541	1.194093	C	0.905794	-4.661492	-3.262085
H	2.624772	-0.945799	0.787488	H	0.333363	-5.354759	-2.624191
H	-4.604239	1.063870	-1.241280	H	1.982181	-4.837153	-3.102001
H	-3.487609	1.927386	-2.336676	H	0.659236	-4.845931	-4.320511

Table S12: Cartesian coordinates (in Å) for the $T_{LC/MLCT}$ geometries of compound **1** in DCM

C	1.173528	4.458840	0.409110	H	-3.476789	2.946056	-0.697719
C	-0.046073	5.089398	0.175969	H	-3.039923	3.429870	3.075164
C	-1.243046	4.433286	0.451834	H	-4.418692	2.591242	2.306313
C	-1.247634	3.136218	0.975630	H	-3.830121	4.132628	1.636046
C	-0.000668	2.534084	1.213409	H	-2.976411	-3.292839	3.177512
C	1.224102	3.162513	0.932264	H	-3.771071	-3.968385	1.727806
N	0.022093	1.196218	1.724200	H	-4.368648	-2.449423	2.438837
C	0.018185	0.106618	0.924821	H	-2.515072	-1.181474	-0.592576
N	0.041204	-0.942662	1.777275	H	-4.118372	-1.290882	0.182536
C	0.059363	-0.521732	3.089706	H	-3.403228	-2.733048	-0.597379
C	0.047242	0.840186	3.055717	H	2.523600	-1.145895	-0.642599
C	0.040977	-2.299829	1.319759	H	3.429934	-2.686101	-0.689377
C	1.276684	-2.916837	1.061723	H	4.151570	-1.242081	0.081424
C	1.247068	-4.217328	0.547085	H	3.884034	-3.938414	1.609428
C	0.037719	-4.864306	0.306105	H	3.125233	-3.288438	3.089863
C	-1.169966	-4.225470	0.575137	H	4.483982	-2.420002	2.318808
C	-1.196218	-2.925041	1.090233	H	3.086802	3.498083	2.964518
C	2.594767	-2.195511	1.272788	H	3.810182	4.211880	1.495867
C	3.572615	-3.010344	2.120019	H	4.452207	2.683963	2.147260
C	-2.514352	-2.214151	1.333705	H	3.394493	3.011739	-0.821048
C	-3.174649	-1.835895	0.005183	H	2.458809	1.489244	-0.838801
C	2.552571	2.454977	1.119925	H	4.091309	1.524630	-0.112952
C	3.158691	2.101472	-0.241368	Cu	-0.008389	0.047096	-0.951651
C	-2.553797	2.401366	1.209369	N	-0.023512	-0.015075	-2.811028
C	-3.510548	3.186478	2.106998	C	-0.038382	-0.210588	-5.685027
C	-3.456446	-3.030917	2.218864	C	-0.038871	1.077638	-3.554091
C	-3.202702	2.039150	-0.129758	C	-0.019292	-1.305126	-3.507663
C	3.526077	3.261131	1.980124	C	-0.024657	-1.348382	-4.929268
C	3.209440	-1.797174	-0.071749	C	-0.047641	1.068353	-4.959332
H	0.079140	-1.220577	3.922704	H	-0.042963	2.035367	-3.021776
H	0.054122	1.580012	3.852774	C	-0.011915	-2.489111	-2.632324
H	-2.110704	-4.745370	0.372816	H	-0.018653	-2.335308	-5.401535
H	2.186157	-4.730892	0.322469	H	-0.059843	2.020214	-5.494062
H	0.036422	-5.879801	-0.100725	H	-0.043197	-0.229308	-6.775410
H	-2.192648	4.936370	0.247813	H	-0.013584	-3.424717	-3.211852
H	2.104362	4.981781	0.171434	H	-0.890984	-2.497006	-1.952746
H	-0.064050	6.103615	-0.233936	H	0.874657	-2.494516	-1.962482
H	-2.300778	-1.274155	1.869127				
H	-2.326230	1.454966	1.727362				
H	2.362700	1.505799	1.647889				
H	2.388088	-1.263032	1.823858				
H	-4.119176	1.444962	0.031527				
H	-2.514491	1.441084	-0.754530				

Table S13: Cartesian coordinates (in Å) for the S_0 geometries of MeCN in DCM

N	0.495960	0.995390	-6.368660
C	0.755080	1.220310	-7.474380
C	1.082210	1.502750	-8.861950
H	1.286850	0.564190	-9.402490
H	1.974970	2.146700	-8.918220
H	0.240860	2.018720	-9.352670

Table S14: Cartesian coordinates (in Å) for the S_0 geometries of MeCN in MeCN

N	0.495354	0.995483	-6.369085
C	0.756010	1.220351	-7.474573
C	1.082317	1.502791	-8.862209
H	1.286721	0.563979	-9.402268
H	1.975014	2.146795	-8.918093
H	0.240504	2.018662	-9.352143

References

[1] I. H. M. van Stokkum, D. S. Larsen, R. van Grondelle, *Biochim. Biophys. Acta, Bioenerg.* **2004**, *1657*, 82-104.

[2] A. Liske, L. Wallbaum, T. Hölzel, J. Föller, M. Gernert, B. Hupp, C. Ganter, C. M. Marian, A. Steffen, *Inorg. Chem.* **2019**, *58*, 5433-5445.

Online Resource:

References for Small Fluorescence Quantum Yields

*Mahbobeh Morshedi[1], Simon L. Zimmermann[1], David Klaverkamp[1], and Peter Gilch[*1]*

[1]Institut für Physikalische Chemie, Heinrich-Heine-Universität Düsseldorf, Universitätsstr. 1,

40225 Düsseldorf, Germany

Corresponding Author
*E-mail: gilch@hhu.de

Transition dipole representation

Mirror-image relationships between absorption and fluorescence spectra are best investigated relying on the transition dipole representation [1, 2]. This representation corrects absorption and fluorescence signals for trivial frequency dependencies. To arrive at this representation, absorption and fluorescence signals recorded as a function of the wavelength λ were plotted as a function of the wavenumber $\tilde{\nu}$. This conversion of the fluorescence spectrum entailed a λ^2 factor (see main text). In the transition dipole representation, the absorption signals are plotted as $\varepsilon(\tilde{\nu})/\tilde{\nu}$ and the fluorescence ones as $S_{fl}(\tilde{\nu})/\,\tilde{\nu}^3$ (see Fig. S1, S2, S3, S4).

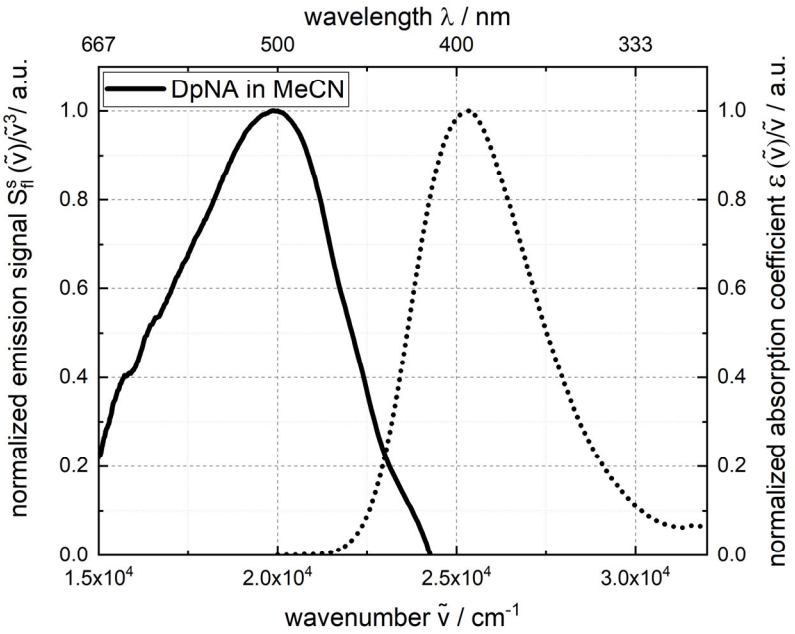

Fig. S1 Absorption (coefficient, black dotted line) and fluorescence (smoothed black solid line) spectra of DpNA in acetonitrile in transition dipole representation. The spectra were converted into the transition dipole representation and then normalized. To record the fluorescence spectrum, the excitation wavelength was set to 400 nm

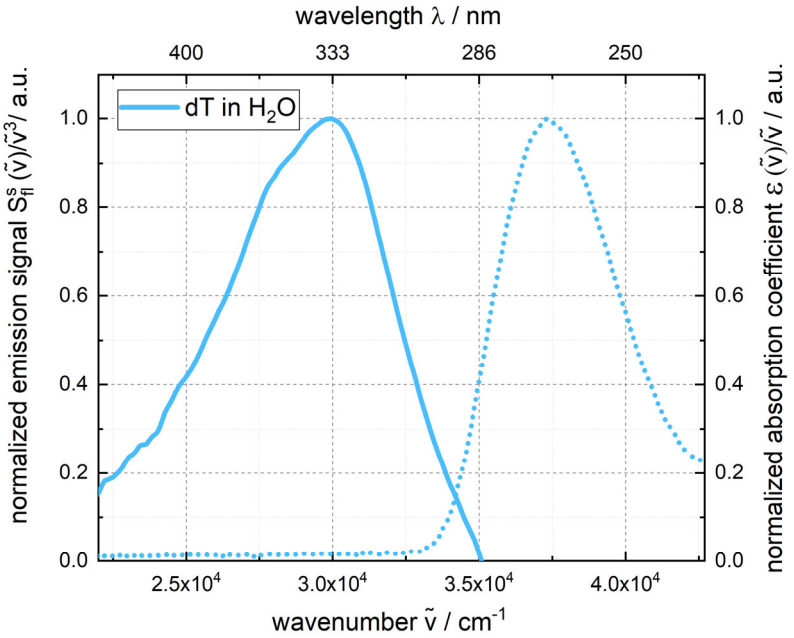

Fig. S2 Absorption (coefficient, blue dotted line) and fluorescence (smoothed blue solid line) spectra of dT in water in transition dipole representation. The spectra were converted into the transition dipole representation and then normalized. To record the fluorescence spectrum, the excitation wavelength was set to 255 nm

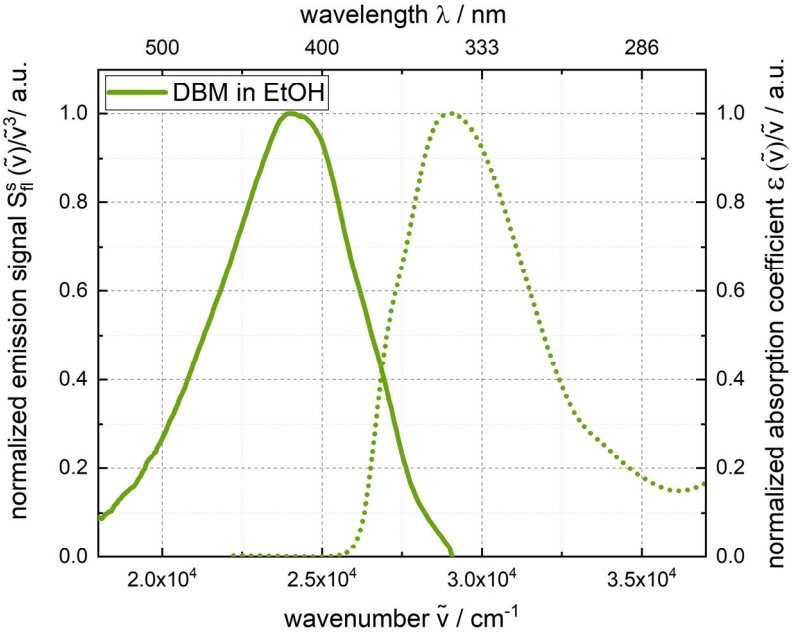

Fig. S3 Absorption (coefficient, green dotted line) and fluorescence (smoothed green solid line) spectra of DBM in ethanol in transition dipole representation. The spectra were converted into the transition dipole representation and then normalized. To record the fluorescence spectrum, the excitation wavelength was set to 330 nm

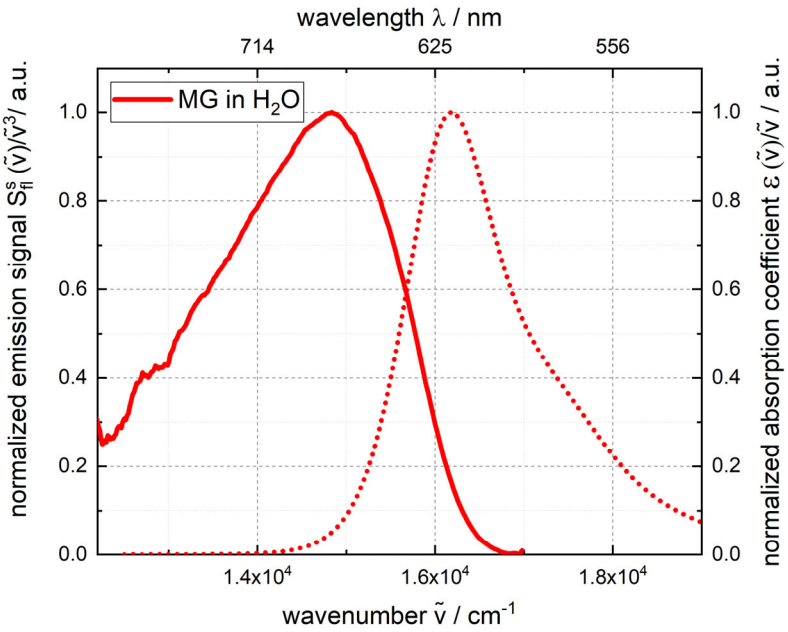

Fig. S4 Absorption (coefficient, red dotted line) and fluorescence (smoothed red solid line) spectra of MG in water in transition dipole representation. The spectra were converted into the transition dipole representation and then normalized. To record the fluorescence spectrum, the excitation wavelength was set to 535 nm

References

1. Angulo G, Grampp G, Rosspeintner A (2006) Recalling the appropriate representation of electronic spectra. Spectrochimica Acta Part A: Molecular Biomolecular Spectroscopy 65:727-731. https://doi.org/10.1016/j.saa.2006.01.007

2. Parson W W (2007) Modern optical spectroscopy. Springer, Berlin.